

UC Berkeley

UC Berkeley Electronic Theses and Dissertations

Title

Design and Application of Photoinduced-Electron Transfer-Based Voltage-Sensitive Dyes to Biological Imaging

Permalink

<https://escholarship.org/uc/item/5991p9hq>

Author

Kulkarni, Rishikesh U

Publication Date

2018

Peer reviewed|Thesis/dissertation

Design and Application of Photoinduced-Electron Transfer-Based Voltage-Sensitive Dyes to
Biological Imaging

By
Rishikesh Kulkarni

A dissertation submitted in partial satisfaction of the
requirements for the degree of
Doctor of Philosophy
in
Chemistry
in the
Graduate Division
of the
University of California, Berkeley

Committee in charge:

Professor Evan W. Miller, Chair
Professor Matthew B. Francis
Professor Helen S. Bateup

Summer 2018

Design and Application of Photoinduced-Electron Transfer-Based Voltage-Sensitive Dyes to
Biological Imaging

Copyright © 2018

By: Rishikesh Kulkarni

Abstract

Design and Application of Photoinduced-Electron Transfer-Based Voltage-Sensitive Dyes to Biological Imaging

by

Rishikesh Kulkarni

Doctor of Philosophy in Chemistry

University of California, Berkeley

Professor Evan W. Miller, Chair

Voltage-sensitive dyes have provided recent promise for affording new methods to interrogate the electrical activity of biological circuits. In particular, small-molecule based approaches have proven useful for designing sensitive molecules that can observe neuronal activity in a noninvasive, highly-parallel manner. However, currently-available voltage-sensitive dyes are marred by low sensitivity, brightness, and/or poor solubility. In order to overcome these challenges, we designed and synthesized voltage-sensitive dyes based on a new family of photoinduced-electron transfer-based voltage sensors, or VoltageFluors. Using the VoltageFluor scaffold, we designed two new families of rhodol- and rhodamine-based voltage-sensitive dyes optimized for two-photon voltage imaging in thick biological tissues, such as brain slices and intact brains. Using these dyes, we characterized the neuronal phenotype associated with the epileptic disorder tuberous sclerosis and monitored spiking activity in awake, behaving mice. We then developed a synergistic computational and experimental approach to guide the rational design of new VoltageFluor dyes. Through this approach, we design and test the most voltage-sensitive VoltageFluor dye to date and also the brightest, highest signal-to-noise fluorescein-based VoltageFluor dye. This work lays the foundation for the diverse array of biological applications of VoltageFluor dyes and develops the guiding principles for future dye design.

Dedicated to my friends and family.
You push me to ever-greater heights.

Table of Contents

Chapter 1: Small Molecule Probes for Voltage Imaging Applications

1.1 Voltage Imaging to Probe Biological Activity.....	2
1.2 Small-Molecule Fluorescent Voltage Indicators.....	4
1.3 Fluorescent Protein-based Voltage Indicators.....	5
1.4 Opsin-based Voltage Indicators	5
1.5 Dual Opsin-Fluorescent Protein Strategies	6
1.6 Universal Challenges for Voltage Imaging.....	7
1.7 Conclusion and Overview	10
1.8 References	12

Chapter 2: A Voltage-Sensitive Rhodol with Enhanced Two-Photon Brightness

2.1 Voltage Imaging for Two-Photon and Long-Term Imaging Applications	16
2.2 Synthesis and Characterization of RVF5	17
2.3 Imaging TSC1 Knockout Neurons with RVF5.....	26
2.4 Imaging Neuronal Activity in Mouse Brain Slices with RVF5	31
2.5 Conclusions and Future Outlook.....	33
2.6 Methods and Materials	34
2.7 References	42

Chapter 3: *In vivo* Voltage Imaging Using a Sulfonated Rhodamine Voltage Reporter

3.1 <i>In vivo</i> Voltage Imaging and Electrophysiology	46
3.2 Design and synthesis of sRhoVR dyes	47
3.3 Cellular Characterization and Performance of sRhoVRs.....	50
3.4 Two-Photon Performance and Imaging of sRhoVR in Neurons.....	53
3.5 Conclusions and Future Outlook.....	60
3.6 Methods and Materials	60
3.7 References	80

Chapter 4: A Rational-Designed Strategy for Membrane Orientation of Photoinduced Electron-Transfer-Based Voltage-Sensitive Dyes

4.1 Dye Membrane Orientation as a Factor in Voltage Sensitivity	83
4.2 Molecular Modeling of VoltageFluor Dyes	84
4.3 Synthesis and Characterization of Doubly-Sulfonated VoltageFluor Dyes.....	88
4.4 Imaging Voltage in Neurons Using Doubly-Sulfonated VoltageFluors	96

4.5 Conclusions and Future Outlook.....	97
4.6 Methods and Materials	98
4.7 References	131

Chapter 5: Isomerized Xanthene PeT-Based Chromophores with Increased Brightness and Signal-to-Noise

5.1 Dye Membrane Orientation and Donor-Acceptor Energy Matching as a Factor in PeT ...	135
5.2 Computational Modeling of isoVF2.2(OMe).Cl.....	137
5.3 Synthesis and Characterization of isoVF2.2(OMe).Cl.....	139
5.4 Neuronal Imaging with isoVF2.2(OMe).Cl	143
5.5 Conclusions and Future Outlook.....	147
5.6 Methods and Materials	148
5.7 References	154

Appendices

Appendix 1. Protocol for Two-Photon Voltage Imaging	156
Appendix 2. Protocol for Density Functional Theory Calculations.....	157

Acknowledgements

First and foremost, I would like to thank Evan Miller for all the mentorship and guidance he provided over the course of my PhD. I imagine that taking on four graduate students as your first class must have been a challenge, but your management of all of us was admirable. Evan was always supportive of my new project ideas and encouraged me to participate in many fruitful collaborations. Evan's enthusiasm for the science we were doing pushed me through many bumps in the road as has served as the driving force for the lab in general.

My work could not have been possible without my hardworking and talented collaborators. Over the course of my time at UC Berkeley, I worked with Dr. Maroof Adil and Goncalo Rodrigues in David Schaffer's group, Dan Kramer in Helen Bateup's group, Dr. Abigail Knight and Rachel Bisiewicz in Matt Francis's group, Hang Yin in Yi Wang's group, and Martin Thunemann in Anna Devor's group. Each and every one of these collaborators brought indispensable expertise to our projects and I am incredibly thankful to have worked with each of you during my graduate career.

Perhaps the largest influencers on my graduate career were my coworkers in the Miller lab. All of them contributed in their own way to the work I did. There are a few people I will acknowledge in particular – when I first joined the lab, my cohort of Parker, Vince, and Alisha made the lab feel like a welcoming place. We all struggled to find ourselves and figure out our research projects as newly-minted second year students in a brand-new laboratory, but I am glad to have shared that experience with the three of you. I hope we can remain friends after graduation.

As one of the senior students in the lab, I had many opportunities to interact with new hires over the years. One of the first additions to the lab after I joined was Dr. Alison Walker, a postdoctoral scholar that we were lucky to have. Ali's biological expertise filled a conspicuously-empty niche in our lab and I doubt that our in-house cell culture facility would have gotten off the ground without her. Ali's creative analysis of how our dyes could be applied to biology made her an exceptional mentor and her sense of humor made her an incredible friend. Before leaving, Ali trained another fantastic researcher in regards to cell culture – Julia. Julia always provided a helpful ear when I was brainstorming solutions to research problems and I was also happy to provide one in return when she was in need. I am glad that we could become friends over those many afternoon conversations while she was culturing cells next to my desk. I wish her the best during her final year as a graduate student, but I honestly do not worry about her finding success.

The remaining group of students in the Miller group's second class – Pei, Steven, Gloria, and Jenna have also all proven to be wonderful friends and coworkers. While I did not work closely with any of them on any of my projects, I had many opportunities to exercise my muscles as a mentor when all of you joined the lab. All of you are excellent scientists and people and I know that the culture of the lab will remain welcoming as you become the senior members of the group.

My projects could not have succeeded without the help of the students that I affectionately refer to as “team Rishi.” It is hard for me to express in words how much working with you has meant to me, but I will attempt to do my best. My first direct mentorship experience was working with an Amgen scholar, Ben Raliski. Ben was a talented and hardworking undergraduate with a good sense of humor and incredible taste in music. I can only assume that he enjoyed working with me, as well, because he returned to UC Berkeley after graduation and joined to Miller group as a graduate

student. I look forward to seeing what amazing work you put out after I am gone. My next students were Narges Pourmandi and Feroz James, who worked as synthetic chemists on my projects. While the two of you were very different, your kindness, enthusiasm, and general cleverness made my years in graduate school particularly enjoyable. The two of you were pleasures to work with and I know that I am forever grateful to the two of you.

An important friend-turned-collaborator that defined my experience at UC Berkeley was Dr. Abigail Knight in the Francis group. I rotated with her in my first year and, as a result, we created a new class of fluorescent heavy metal sensors based on her favorite scaffold, peptoids. Abby is one of the most ambitious and clever scientists that I have met and I am glad that we have remained close friends despite her graduation. She is now beginning a professorship at UNC Chapel Hill and I hope that we can work together again in the future. Our collaboration managed to continue after Abby's graduation with the addition of Rachel Bisiewicz. I met Rachel when she was a prospective student visiting UC Berkeley and I was her graduate student host. I was happy to hear that she decided to come to UC Berkeley and I was even more pleased when she joined the Francis group and began working with Abby. After Abby's graduation, Rachel and I began working together on the next evolution of fluorescent heavy metal sensors and I am excited to see what the future holds for peptoids. I am happy to call Rachel a friend and collaborator and I hope that the future brings her success.

My most steadfast supporters are, of course, my family members. My late grandfather always hoped that I would, like him, attain a PhD in Chemistry from an American university. My father, despite not following in his father's footsteps, has always been a source of support and inspiration. My mother has always pushed me to fulfill my potential, even when my own motivation was low. My brother, who has become a businessman, has always reminded me of the value of my work. I am grateful for their love of support.

Finally, and most importantly, I would like to thank my fiancé, Kate. I met her in my second year of graduate school and, as a fellow graduate student, she understood the trials and tribulations associated with navigating a PhD. She was always open to listening to my half-baked theories about my work and she gave useful advice when my projects overlapped with her field of study, neuroscience. I consider myself incredibly lucky to have met her and I look forward to our life together. Her input inspired many of the applications of my work described below.

Chapter 1

Small Molecule Probes for Voltage Imaging Applications

Abstract

Optical methods to interrogate membrane potential changes in neurons promise to revolutionize our ability to dissect the activity of individual cells embedded in neural circuits underlying behavior and sensation. A number of voltage imaging strategies have emerged in the last few years. Developments in both small molecule and genetically-encoded fluorescent indicators of membrane potential have afforded unique benefits to the field of voltage imaging. In particular, recent advances in small molecule fluorescent indicators that rely on photoinduced electron transfer (PeT) to sense voltage as well as refinements of voltage-sensitive fluorescent proteins and new opsin-based strategies for monitoring voltage changes have enabled fast, sensitive measurement of transmembrane potential in a variety of biological preparations. Several engineering challenges associated with voltage sensing have yet to be overcome, however. In this chapter, I compare the requirements of fluorescent voltage indicators to those for more canonical Ca^{2+} sensing as a way to illuminate the particular challenges associated with voltage imaging.

This chapter is based on the publication in *Biochemistry* entitled “Voltage Imaging: Pitfalls and Potential.”

1.1. Voltage Imaging to Probe Biological Activity

Neuronal membrane voltage changes drive signaling in the brain and are a key component of the emergent properties of the human experience. Despite the importance of membrane voltage to neurobiology, most of the knowledge we have about the electrophysiological behavior of neurons arises from electrode-based methods, which usually involve the observation of single neurons at a time. Deeper understanding of neural circuits requires the ability to make simultaneous measurements of large numbers of neurons without compromising temporal or spatial resolution. A popular method for interrogating neuronal circuit behavior is calcium imaging; however, it remains an indirect measure of neuronal activity complicated by the slow intrinsic kinetics of calcium transients relative to underlying membrane potential dynamics. While small-molecule and genetically-encoded calcium sensors have transformed our ability to indirectly measure neuronal activity,¹ deconvolution of detected calcium transients into the underlying voltage changes remains a difficult problem.

Direct fluorescence imaging of voltage presents an attractive method for studying neural circuits, complementary to traditional electrode-based methods and imaging modalities that rely on Ca^{2+} fluxes. The field of voltage imaging with fluorescent indicators spans nearly four decades. There has been a recently flurry of activity in the development of new methods to optically monitor voltage. These new indicators, both small molecule and genetically-encoded, have made strides towards realizing the potential of voltage imaging. In this perspective, we provide a brief overview of recent chemical and genetic strategies employed for voltage imaging. We then discuss universal constraints on optical voltage determination that apply to all sensor designs, with the hope of providing a perspective on upcoming challenges.

Pioneering work in the 1970s identified several different classes of small molecules that possessed voltage-sensitive optical properties, and this work is extensively reviewed elsewhere.²⁻⁴ Small molecule voltage-sensitive fluorescent indicators generally fall into two classes: electrochromic-type dyes (**Figure 1.1a**), which possess response speeds sufficient to track action potentials, but with low sensitivity;⁵ and oxonols, which have larger fractional fluorescence responses to voltage, but respond so slow as to prohibit visualization of discrete action potentials.⁶ Recent work in our lab has employed photoinduced electron transfer (PeT) as a voltage sensitive trigger that achieves both fast (sub-millisecond response times) and sensitive ($>60\% \Delta F/F$ per 100 mV) monitoring of membrane potential dynamics.

In contrast, genetically-encoded strategies were first employed about 20 years ago. The first genetically-encoded voltage sensitive fluorescent proteins were fusions of native ion channels or voltage sensing domains and fluorescent proteins. The first indicators were in principle voltage sensitive, but suffered from severe trafficking defects that prohibited efficient expression at the cell surface. Poor membrane targeting limited their utility for detecting action potentials in neurons. Recent iterations have improved trafficking, kinetics and sensitivity. A complementary

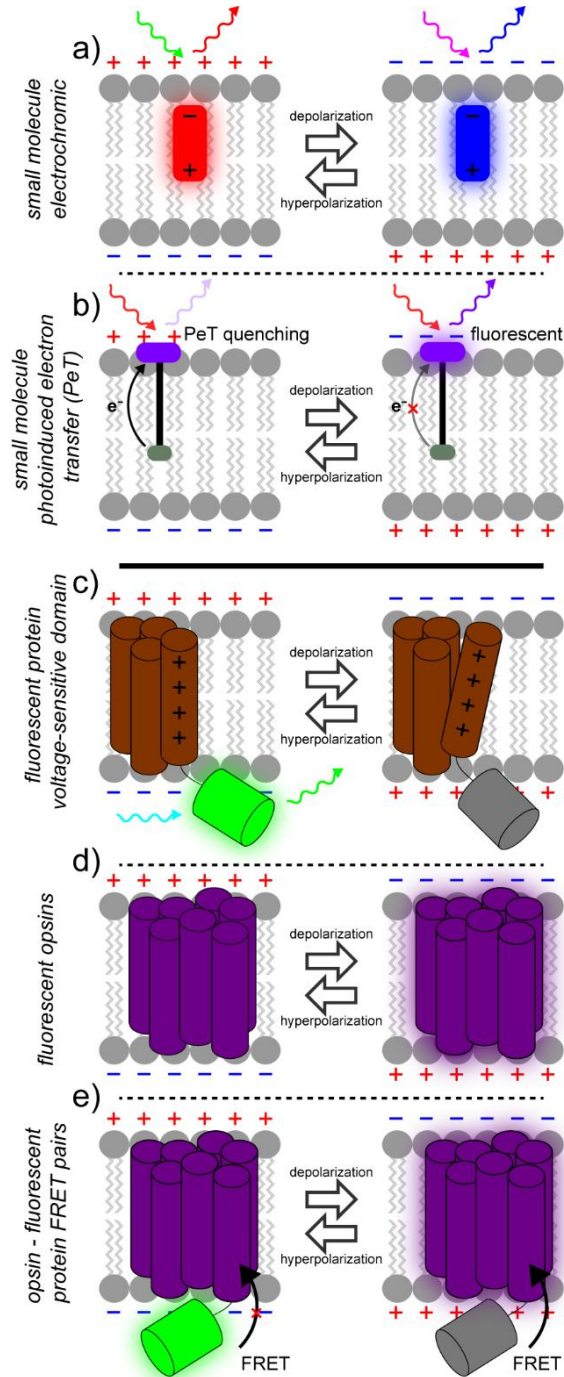


Figure 1.1. Fluorescent voltage indicators. Numerous strategies for optically sensing voltage changes in living cells exist. Small molecule fluorophore platforms (upper panels) include electrochromic dyes (a) and photo-induced electron transfer (PeT) approaches (b). Genetically encoded strategies (lower panels) include fusions of fluorescent proteins to voltage-sensing domains (c), use of opsins (d), and hybrid opsin – fluorescent protein pairs (e).

addition to the genetically encoded toolkit makes use of light-sensitive opsins. This is a new mechanism for sensing voltage and has helped to reinvigorate the field of voltage sensing by enabling opsin or opsin-fluorescent protein hybrid voltage sensing strategies. Comprehensive reviews of voltage-sensitive fluorescent proteins are available.⁷⁻¹⁰ Below, we will first discuss recent dye-based voltage-sensing strategies followed by new protein-based strategies.

1.2. Small-Molecule Fluorescent Voltage Indicators

Our lab has been exploring photoinduced electron transfer (PeT) as a platform for optical voltage sensing. The general scaffold of these PeT-based voltage sensors, or VoltageFluors, consists of a fluorescent reporter molecule covalently linked to an electron-rich molecular wire-donor moiety that quenches the fluorescent reporter via photoinduced electron transfer (PeT). The rate of PeT is sensitive to the presence of an external electric field, enabling it to be used as a voltage-sensitive mechanism of fluorescence quenching. By orienting the dye in the membrane so that the electron-rich donor is intercalated into the plasma membrane, the resting membrane potential accelerates the rate of PeT, quenching the fluorophore. Depolarization inhibits PeT, resulting in an increase in fluorescence (**Figure 1.1b**).

The use of PeT as a voltage-sensing mechanism affords unique opportunities important for voltage imaging. In the context of a VoltageFluor, the rate of PeT must occur within the nanosecond lifetime of the fluorophore excited state. This makes PeT processes approximately 6 orders of magnitude faster than an action potential and allows VF dyes to effectively resolve AP kinetics. Additionally, PeT modulates the fluorescence efficiency of the dye in a voltage-dependent fashion, making all of the emitted photons voltage-sensitive and useful for imaging. Finally, moving an electron over a relatively long distance (approximately half-way across a typical 4 nm plasma membrane), results in high sensitivity, without sacrificing response kinetics. We control the orientation of VoltageFluors dyes in the membrane using a combination of a hydrophobic molecular wire coupled with an anionic anchoring group, usually a sulfonate¹¹ or a tertiary amide.¹² After bath application of the VoltageFluor, the hydrophobic wire partitions into the plasma membrane, but the water-soluble anchor prevents the dye from crossing the membrane, ensuring that the dye is uniformly oriented in the outer leaflet of the plasma membrane.

Sensitivity of VF dyes can be improved by tuning the relative redox potentials of the donor/acceptor pairs¹³ or by improving dye orientation in the plasma membrane.¹⁴ Because the reporter (fluorescent dye) is chemically orthogonal to the voltage sensing domain (molecular wire/aniline) the VF scaffold enables ready exchange the fluorophore acceptor to access a wide range of the visible and near-infrared portions of the electromagnetic spectrum,^{12, 15} as well as optimized VoltageFluors for two-photon voltage imaging.¹⁶ Although VoltageFluors are bright, sensitive, and employ a fast and non-disruptive mechanism of voltage sensing, their pan-membrane localization introduces a source of background noise in heterogeneous samples, limiting sensitivity.^{13, 16} We have developed a small-molecule photoactivatable optical sensor of transmembrane potential, or SPOT, a photocaged voltage sensor based on the first generation VoltageFluor molecules that enables cellular contrast via a photoactivation mechanism.¹⁷ Other strategies we are exploring involve the use of enzymatically cleavable masking groups and self-labeling enzyme/ligand pairs to target VoltageFluors to specific neuronal subtypes.

1.3. Fluorescent Protein-based Voltage Indicators

A voltage-sensitive fluorescent protein was first reported in 1997, when Iscoff and Siegel fused the green fluorescent protein (GFP) to the Shaker potassium channel.¹⁸ Although the kinetics of the optical response to voltage were too slow to enable action potential tracking, this study showed that membrane potential-induced conformational changes could alter the fluorescence of GFP. In 2001, Knopfel and co-workers showed that voltage sensitivity could be achieved by using just the voltage-sensing domain of a potassium channel and coupled this movement to changes in FRET efficiency between cyan fluorescent protein (CFP) and yellow fluorescent protein (YFP).¹⁹ In 2002, Pieribone fused GFP to a sodium channel to achieve fast kinetics.²⁰ This first generation of voltage-sensitive fluorescent proteins represent an important first step, but combinations of slow response kinetics, poor membrane localization, and/or low sensitivity hindered their wide-spread use.

In 2007, Knopfel and co-workers discovered that the use of the voltage-sensing domain from the voltage-sensitive phosphatase (VSP) from *Ciona intestinalis* improved membrane localization, response kinetics, and sensitivity.²¹ Most of the recently-deployed FP-only strategies (**Figure 1.1c**) make use of the *C. intestinalis* VSP domain (CiVSD). Pieribone, Cohen, and co-workers demonstrated that insertion of super-ecliptic pHluorin to an intracellular loop of the CiVSD, results in a voltage-sensitive fluorescent protein. This construct, ArcLight, displays high sensitivity to membrane potential changes and sufficient kinetics and brightness to detect action potentials in neurons.²² Although the precise molecular mechanisms by which CiVSD transduces fluorescence changes in FPs remain incompletely characterized, for the case of ArcLight, depolarization causes a turn-off response. ArcLight has been used *in vivo* for dissecting neural circuits underlying odor perception in the fly.²³ Recently, Pieribone and co-workers uncovered mutations in ArcLight which reverses the polarity of response. This new indicator, Marina, gives fluorescence increases upon depolarization and maintains the response magnitude and kinetics of the parent ArcLight.²⁴

Use of non-canonical FPs, such as super-ecliptic pHluorin, have proved a useful strategy for generating voltage-sensitive fluorescent proteins. Another example is the use of circularly permuted GFPs (cpGFPs). A screen of CiVSD and cpGFP insertions yielded ElectricPk, which had exceptional kinetics and good trafficking to plasma membranes. This study showed that cpGFPs and CiVSDs enable fast detection of voltage changes in an FP-only sensor.²⁵ Building off of this work, Lin and co-workers described the development of ASAP, in which cpGFP is inserted into an extracellular loop of the CiVSD. The ASAP family of indicators maintains the rapid kinetics and turn-off response of the ElectricPk construct while improving voltage sensitivity by an order of magnitude. This enables detection of action potentials in single trials in cultured neurons. Improved versions of ASAP have been employed in intact flies.²⁶ Insertion of circularly-permuted mApple (cpmApple), a red-fluorescent protein, into an intracellular loop of CiVSD enabled the development of FlicR1 (fluorescent indicator for voltage imaging red), which provides a turn-on response to action potentials and retains good response magnitude and kinetics.²⁷

1.4. Opsin-based Voltage Indicators

Genetically encoding sensors of transmembrane potential typically rely on the fusion of a fluorescent protein (or two) to an ion channel or voltage sensing domain. A more recent approach uses the natural electrochromism of bacteriorhodopsins. Light-gated ion pumps and channels find wide application in neurobiology for optical activation or silencing of neurons, since cells which express these membrane-bound proteins now pass ions in response to light, thereby changing their

membrane potential.²⁸ In 2011, Cohen’s group showed that these opsin proteins could be “run in reverse,” that is, changes in membrane potential causes a change in their fluorescence.^{29, 30} The reversible electric field-induced deprotonation event in bacteriorhodopsins modulates their fluorescence and makes these proteins an attractive candidate for genetically-encoded voltage indicators (**Figure 1.1d**). Cohen and coworkers developed the Arch system, based on the light-gated proton pump Archaeorhodopsin 3 (Arch),²⁹ and showed that the weak fluorescence of the all-*trans*-retinal (ATR) cofactor of Arch was modulated by changes in membrane potential. By deactivating the proton pumping mechanism with a single amino acid mutation (D95N) and taking advantage of the improved eukaryotic membrane localization of Arch 3, Arch(D95N) can effectively report on voltage changes in cells without the induction of a photocurrent. Despite the high voltage sensitivities and turn-on responses of rhodopsin-based voltage indicators, they require high light power to achieve sufficient fluorescence, as a result of their complex photocycle.³¹ Mutational screens identified a few mutations that improve brightness³² (Archer, or Arch with enhanced radiance) or kinetics,³³ relative to Arch(D95N). Focused screening to improve brightness and reduce photocurrent, while retaining the fast kinetics of Arch resulted in the development of QuasAr1 and QuasAr2 (Quality superior to Arch).³⁴ With improvements in brightness and further bathochromic excitation shifts, QuasAr1 can be used in conjunction with optogenetic actuators to faithfully report neuronal action potentials. More recently, synthetic analogs of ATR, merocyanine retinals (MCR), coupled with evolved Arch mutants with binding preferences for MCR over ATR provide access to brighter and red-shifted variants of Arch.³⁵ The most promising Arch mutant, Mero-6, displays strong, membrane-associated, near-infrared fluorescence in *E. coli* expressing Mero-6 and treated with MCR. Trafficking to the plasma membrane in eukaryotic cells is poor relative to *E. coli*. Despite this, the Mero-6/MCR pair displays some voltage sensitivity and may be a promising platform for future development.

1.5. Dual Opsin-Fluorescent Protein Strategies

In addition to improving the intrinsic brightness of the opsin indicators, another solution is to couple opsin voltage indicators with a brighter reporter via energy transfer (**Figure 1.1e**). Decoupling the voltage sensing component (opsin) from the optical reporter (fluorescent protein), conceptually similar to the sensor/reporter decoupling in VoltageFluor dyes, allows for flexibility in choosing both the voltage sensor and optical reporter. This strategy was initially used to investigate the photocycle of opsins,³⁶ because changes in the absorption spectrum of the opsin alter the efficiency of fluorescence resonance energy transfer (FRET) from a nearby fluorophore. Changes in FRET efficiency indicate changes in the absorption spectrum of the opsin. If the spectrum of the opsin is altered by changes in transmembrane potential, the fluorescence of the FRET donor provides a convenient signal for monitoring voltage.³⁷ This approach, variously described as FRET-opsin³⁸ or electrochromic FRET (eFRET),³⁹ has been implemented across a number of opsins—including Arch,³⁷ QuasAR (Arch parent),³⁹ Mac (*L. maculans*),³⁸ and Ace (*A. acetabulum*)⁴⁰—paired with assorted fluorescent proteins—mOrange2,³⁹ mCitrine,³⁸ or mNeon.⁴⁰ The proposed mechanism is that depolarization of the plasma membrane results in an increase in the absorption spectrum of the opsin, making it a better FRET acceptor and quenching fluorescence from the fluorescent protein donor. This results in a fluorescence decrease upon membrane depolarization – whereas the opsin fluorescence itself increases upon depolarization. FRET-opsin or eFRET efficiency is governed by the usual FRET parameters: both distance and spectral overlap between donor and acceptor influence FRET efficiency. Recently, a FRET-opsin hybrid, Ace2-mNeon, was deployed to optically record spikes in intact mouse and fly brains.⁴⁰ The improved

performance of Ace2-mNeon pair is, in part, aided by the hypsochromic spectral shift of the Ace chromophore relative to Mac, providing enhanced overlap with the bright fluorescent protein, mNeon.⁴¹ Matching rhodopsins (and mutants) with desirable photocycle kinetics and spectral overlap with fluorescent reporters may be source of enhanced sensitivity and/or brightness. Enhancing trafficking to cell membrane and substantially reducing photocurrents while maintaining response kinetics offer pathways for improvement of these indicators.

1.6 Universal Challenges for Voltage Imaging

Whether chemically-synthesized or genetically encoded, optical voltage determination faces inherent challenges. We outline a few of these considerations below and compare them to considerations for fluorescent Ca^{2+} indicators (**Figure 1.2**), which are the most prevalent functional imaging modality in neurobiology.

The first consideration is the speed of the biological event of interest: the neuronal action potential (**Figure 1.2a**). The electric field reorientation that occurs during an action potential occurs on timescale of one to two milliseconds with the fastest component, the rising phase, occurring over the course of approximately $250 \mu\text{s}$.⁴² Therefore the response kinetics of a voltage indicator must be able to resolve changes on the sub-millisecond timescale. Achieving sufficiently fast response speed while maintaining high sensitivity is the primary hurdle for voltage indicators. While

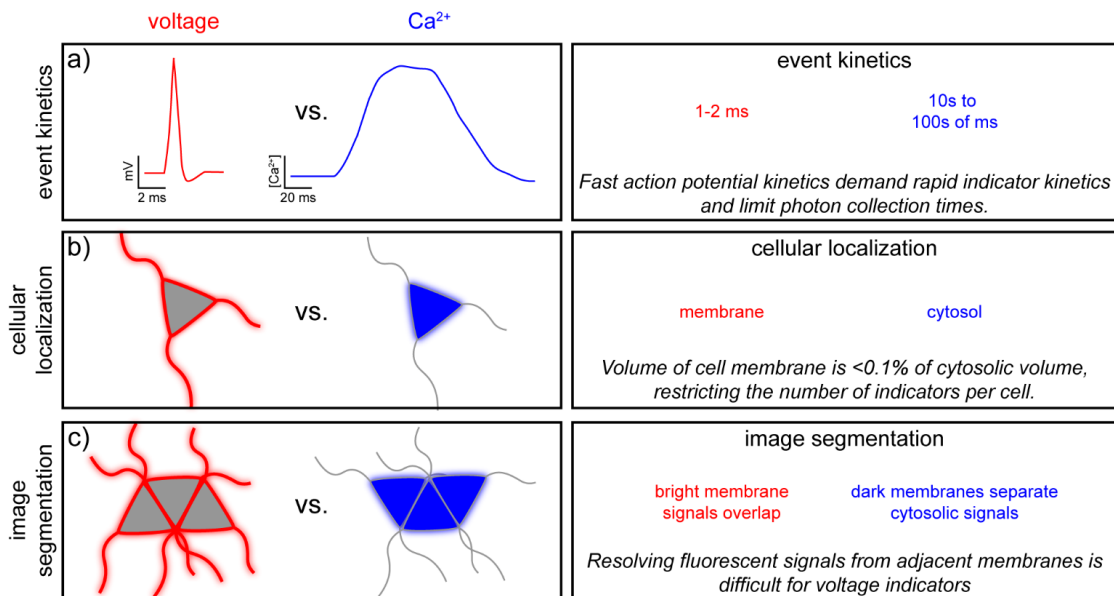


Figure 1.2. Design challenges encountered in the development of fluorescent voltage indicators. Constraints for the design of fluorescent voltage indicators (red) are contrasted against the requirements of fluorescent Ca^{2+} indicators (blue).

neuronal action potentials have a fleeting duration, on the order of several milliseconds, Ca^{2+} concentration increases can persist for 10s to 100s of milliseconds inside of a neuron. The consequences of this are several-fold. First, image acquisition must be fast, on the order of 1000 Hz to accurately sample action potentials. Acquisition speeds for Ca^{2+} imaging can be in the 1 to 10 Hz range. Relative to Ca^{2+} indicators, voltage indicators therefore have less time to deliver

photons to the imaging detector, making each measurement inherently noisier. To compensate, voltage indicators need to have higher inherent brightness than Ca^{2+} indicators. One cannot bypass this restriction by acquiring images at lower rates, because slower sampling frequencies will result in “missed” events. Achieving fast acquisition speeds (>1 kHz) while maintaining a large field of view is a related hurdle faced uniquely by voltage imaging. For imaging modalities well-suited for thick tissues, like raster-scanning two-photon microscopy, acquiring large fields of view at fast rates is difficult for voltage imaging, but less problematic for Ca^{2+} imaging. A number of promising strategies are pushing the limits of acquisition rate during two-photon imaging.⁴³ Future progress in this area will be required to capitalize on the full potential of voltage imaging.

The second universal constraint is indicator localization (**Figure 1.2b**). Ca^{2+} indicators function by translating the rise in intracellular Ca^{2+} concentration into changes in fluorescence intensity or color. Mediated through ionotropic receptors, voltage-gated Ca^{2+} channels or release from internal stores, cytosolic Ca^{2+} concentration can increase by one to two orders of magnitude over their resting 50-100 nM resting concentration. Ca^{2+} indicators work best when localized to cytosolic compartments. In contrast, voltage indicators must localize to the plasma membrane in order to properly sense voltage. Improperly localized voltage indicator erodes sensitivity by raising the level of background fluorescence from non-response indicator. However, even given perfect localization, the total amount of voltage indicator that can “fit” in the volume of the plasma membrane on the order of $<0.1\%$ of the amount of Ca^{2+} indicator that can fit in the cytosol (based on the relative volumes of plasma membrane and cytosol for a perfectly spherical cell with a 10 μm radius and 4 nm plasma membrane). This restriction places a further design challenge on voltage indicators if they are to match the performance of a typical Ca^{2+} indicator.

Finally, image analysis and segmentation must be considered for voltage imaging (**Figure 1.2c**). One aspect of the appeal of optical indicators is the ability to record from multiple neurons simultaneously. Ca^{2+} indicator-stained neurons appear as bright islands, segmented by the plasma membrane of adjacent cells. Voltage indicators, in contrast, give a “chicken wire” staining pattern when cell bodies abut one another. Optically resolving two adjacent membranes using just their fluorescent signals is difficult and presents a unique challenge that must be solved by all optical voltage-sensing modalities. In areas like the CA1 region of the hippocampus, where cell bodies are positioned in ordered arrays, this represents a particular challenge. In brain regions like the cortex, where cell bodies can be more sparsely scattered, this may be less of an issue. Nonetheless, registering signals from hundreds of neurons with cytosolic Ca^{2+} indicators is challenging and the problem is compounded with voltage imaging, where fluorescence signals overlap in space.

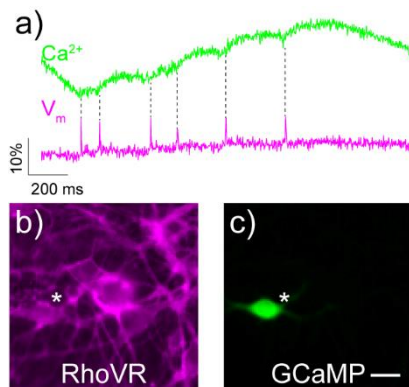


Figure 1.3. Comparison of voltage and Ca^{2+} imaging in neurons. a) Ca^{2+} (green) and voltage (magenta) responses to single, spontaneously-arising action potentials in the same rat hippocampal neuron, as recorded by GCaMP6s (green) and the voltage-sensitive dye, RhoVR 1 (magenta). Panels b and c depict the neuron (white star) analyzed in part a. Scale bar is 20 μm . Figure adapted from Deal, et al., 2017.

Overall, compared to Ca^{2+} imaging, voltage imaging requires acquiring data at 100-1000 times faster speeds, resulting in 100 to 1000-fold fewer photons collected per cycle. Voltage imaging must be done with concentrations of indicators limited to just the plasma membrane, resulting in 1000-fold fewer indicators per cell. Finally, because fluorescent signals from voltage indicators come from the plasma membrane rather than cytosol, segmentation of images and resolving individual cells is more difficult than for cytosolic Ca^{2+} indicators. Despite having to do “more with less”, voltage indicators can achieve good success in detecting single action potentials. For example, the red voltage indicator developed in our lab, RhoVR 1 shows excellent signal to noise and good $\Delta F/F$, in addition to far superior kinetics for single action potentials when compared to the genetically encoded Ca^{2+} indicator GCaMP (**Figure 1.3**).¹²

In addition to the universal constraints or design challenges of all voltage indicators, there are some specific considerations related to particular methods of voltage sensing. First, because voltage indicators must reside in the plasma membrane to sense voltage, it is important to consider delivery routes for a particular indicator to the plasma membrane. For small molecule approaches, this means developing amphipathic indicators that can exist in aqueous environments en route to the cell of interest, reside in the hydrophobic cell membrane environment, and avoid internalization once reaching the membrane of interest. VoltageFluor dyes do both of these well, and bath application of VF dyes gives membrane localized fluorescence.^{12, 14} However, small molecule voltage indicators display poor selectivity for particular cell types and stain all membranes, making cellular resolution difficult.^{13, 16} We have developed photoactivation methods to address the problem of contrast,¹⁷ and development of complementary approaches with genetically encoded components is underway in our lab.

Genetically-encoded voltage indicators offer cell-type specificity but face similar challenges in proper targeting to the cell membrane. Indeed, the very first generation of fluorescent protein- and opsin-based voltage indicators suffered from poor membrane trafficking in mammalian cells, limiting their performance.^{19, 30} Trafficking to the plasma membrane has improved with both the use of voltage sensing domains from CiVSD and targeting sequences that can, in some cases,

improve membrane trafficking. Poor trafficking of genetically encoded voltage sensitive fluorescent proteins results, at best, in intracellular fluorescence that is not voltage sensitive and, at worst, in indicators that do not function in mammalian cells.³⁰ Optimal trafficking signals remain an empirically determined choice and improvements in this area are needed.

Second, with any indicator, care must be taken that use of an indicator does not alter the observed event itself. Ca^{2+} indicators can buffer native Ca^{2+} fluxes. All voltage indicators can, depending on the mechanism of sensing, change the excitability of neurons in a number of ways. Added capacitance coming from charges moving within the membrane on the same time scale as biological charges perturbs the intrinsic properties of the neuron under study—this is most problematic for “slow response” dyes⁶ and is not encountered for electrochromic or PeT-based dyes. For genetically encoded indicators, the gating charges on the voltage sensing domains (VSDs) used in fluorescent protein-based indicators could also increase capacitance. If high concentrations of electrochromic or oxonol indicators are required, this can alter neuronal responses by potentiating the GABA-A receptor.⁴⁴ Phototoxicity—often through generation of singlet oxygen and other reactive oxygen species—can compromise membrane integrity. Another perturbation specific to opsin-based approaches is the generation of a photocurrent. For sensing methodologies based on opsins, removal of the native light-induced charge transport function of the proteins must be mitigated while maintaining voltage sensitivity and response kinetics. For each of the approaches discussed above, these disruptive properties must be considered during any imaging application.

1.7. Conclusion and Overview

In summary, voltage imaging presents a unique opportunity to peer into the inner workings of neural systems with unprecedented spatial and temporal resolution. Yet, despite the clear promise of voltage imaging, widespread application of voltage imaging lags behind techniques like Ca^{2+} imaging. This gap is due, in part, to a lack of methods that can faithfully record neuronal action potentials with the required speed and sensitivity. As discussed in this Perspective, the requirements for voltage imaging are more demanding than the requirements for Ca^{2+} imaging. Voltage indicators must respond orders of magnitude more quickly and occupy a small fractional volume of cell bodies. These constraints place sharp demands on fluorescent voltage indicators, which must be faster, brighter, and more sensitive than corresponding Ca^{2+} indicators. Despite these challenges, in the last few years, several complementary approaches have emerged, offering new promise for voltage imaging. Small molecule PeT-based indicators, fluorescent protein-CiVSD fusions, voltage-sensitive opsins, and opsin-fluorescent protein hybrid all address aspects of the challenges outlined above. In future years, these approaches, and others, will need to address the pitfalls outlined here in order to reach the full potential of voltage imaging.

It is our opinion that while current-generation voltage sensors can always be further optimized in terms of sensitivity, the next generation of challenges that confront the field are not solely synthetic. Each of the three classes of voltage indicators we discussed are compatible for in vivo imaging in some regard – however, in order to construct imaging experiments that provide meaningful data, due consideration must be given to imaging configuration and analytical techniques.

Most proof of concept voltage imaging experiments thus far have been performed with wide-field one-photon epifluorescence microscopy, which is well-suited for the high-framerate imaging required for action potential detection. While these experiments have borne fruit in terms of

achieving voltage imaging in biological systems at many different levels of complexity, the traditional workhorse technique for in vivo imaging in systems neuroscience has and will be multiphoton microscopy. Two-photon microscopy is attractive due to fundamental differences in terms of excitation volume and light frequency, resulting in less scattering and less out-of-focus light, enabling imaging of deep brain regions. Traditional 2P microscopy systems, however, are limited in acquisition speed in comparison to wide-field systems, reaching framerates of up to 30 fps using commercially available sensors and scan geometries. However, imaging depths of several hundred micrometers have been demonstrated using newly popular adaptive optics technologies and the use of acousto-optic deflectors rather than galvanometers has enabled kilohertz-frequency 2P imaging in vivo.⁴³ The field of voltage imaging should engender the naturally mutualistic relationship with the high-speed imaging field in order to reap the benefits of 2P imaging technologies with framerates sufficient for voltage imaging in mammalian systems.

A major selling point of voltage imaging is the ability to gather data from several neurons simultaneously. However, as these imaging experiments become more and more ambitious, the imaging data sets will also grow more difficult to parse. It is critical to be able to extract the meaningful data across populations of cells and be able to correlate spiking activity between cells and with the behavioral output of the animal. While many sophisticated analytical methods have been developed for analyzing calcium imaging data, several of them focus on spike deconvolution from the calcium transients, making them unsuitable for analyzing voltage imaging data. Current approaches involve the usage of simple thresholding or linear regression.¹⁶ The incorporation of machine-learning based schemes and algorithms used in other image analysis applications could help develop the computational aspect of voltage imaging into an indispensable software package for interpreting the vast amount of data that can be acquired by voltage imaging experiments.

The development of fluorescent voltage indicators has gone a long way toward addressing the engineering challenges associated with voltage sensing, resulting in a collection of indicators that can detect action potentials with high sensitivity and specificity using conventional imaging setups that are readily available to many research groups. Furthermore, the variety of colors available has enabled multiplexed imaging in conjunction with other powerful optical tools, permuting the possible avenues of investigation using voltage sensors many-fold. There remain improvements to be made in regards to targeting, photophysical properties, sensitivity indices, and kinetics for the various classes of voltage sensors, which will better enable spike detection under low-light, two-photon, and/or long-term imaging settings. However, confronting the next generation of technical challenges for voltage imaging in the form of high-speed microscopy technology and developing analytical tools will play a fundamental role in ensuring that voltage imaging will be an indispensable technology for the interrogation of neuronal circuits.

Herein, the design of several new VoltageFluors based on a modular synthetic platform to address some of the above-described challenges is reported. These dyes are designed with a combined experimental and rational design approach aimed to optimize voltage sensitivity, signal-to-noise, and loading parameters of the dyes to their biological application of interest. This is followed by the application of these VoltageFluor dyes to a variety of biological systems, including voltage imaging in mouse brain slices, cultured rat hippocampal neurons, human embryonic and induced pluripotent stem cell-derived neurons, and awake, behaving mice. These studies demonstrate the capabilities of VoltageFluor dyes as tools for probing transmembrane potential in complex biological systems and highlight the value of using small molecule design principles to optimize dye properties and function in biological systems.

1.8. References

1. Grienberger, C., and Konnerth, A. (2012) Imaging calcium in neurons, *Neuron* 73, 862-885.
2. Loew, L. M. (2015) Design and Use of Organic Voltage Sensitive Dyes, In *Membrane Potential Imaging in the Nervous System and Heart* (Canepari, M., Zecevic, D., and Bernus, O., Eds.), pp 27-53, Springer-Verlag Berlin, Berlin.
3. Miller, E. W. (2016) Small molecule fluorescent voltage indicators for studying membrane potential, *Curr Opin Chem Biol* 33, 74-80.
4. Braubach, O., Cohen, L. B., and Choi, Y. (2015) Historical Overview and General Methods of Membrane Potential Imaging, In *Membrane Potential Imaging in the Nervous System and Heart* (Canepari, M., Zecevic, D., and Bernus, O., Eds.), pp 3-26, Springer International Publishing, Cham.
5. Fluhler, E., Burnham, V. G., and Loew, L. M. (1985) Spectra, membrane binding, and potentiometric responses of new charge shift probes, *Biochemistry* 24, 5749-5755.
6. Gonzalez, J. E., and Tsien, R. Y. (1995) Voltage sensing by fluorescence resonance energy transfer in single cells, *Biophys J* 69, 1272-1280.
7. Inagaki, S., and Nagai, T. (2016) Current progress in genetically encoded voltage indicators for neural activity recording, *Curr Opin Chem Biol* 33, 95-100.
8. [Lin, M. Z., and Schnitzer, M. J. (2016) Genetically encoded indicators of neuronal activity, *Nat Neurosci* 19, 1142-1153.
9. Xu, Y., Zou, P., and Cohen, A. E. (2017) Voltage imaging with genetically encoded indicators, *Curr Opin Chem Biol* 39, 1-10.
10. Yang, H. H., and St-Pierre, F. (2016) Genetically Encoded Voltage Indicators: Opportunities and Challenges, *J Neurosci* 36, 9977-9989.
11. Miller, E. W., Lin, J. Y., Frady, E. P., Steinbach, P. A., Kristan, W. B., Jr., and Tsien, R. Y. (2012) Optically monitoring voltage in neurons by photo-induced electron transfer through molecular wires, *Proc Natl Acad Sci U S A* 109, 2114-2119.
12. Deal, P. E., Kulkarni, R. U., Al-Abdullatif, S. H., and Miller, E. W. (2016) Isomerically Pure Tetramethylrhodamine Voltage Reporters, *J Am Chem Soc* 138, 9085-9088.
13. Woodford, C. R., Frady, E. P., Smith, R. S., Morey, B., Canzi, G., Palida, S. F., Araneda, R. C., Kristan, W. B., Jr., Kubiak, C. P., Miller, E. W., and Tsien, R. Y. (2015) Improved PeT molecules for optically sensing voltage in neurons, *J Am Chem Soc* 137, 1817-1824.
14. Kulkarni, R. U., Yin, H., Pourmandi, N., James, F., Adil, M. M., Schaffer, D. V., Wang, Y., and Miller, E. W. (2017) A Rationally Designed, General Strategy for Membrane Orientation of Photoinduced Electron Transfer-Based Voltage-Sensitive Dyes, *ACS Chem Biol* 12, 407-413.
15. Huang, Y. L., Walker, A. S., and Miller, E. W. (2015) A Photostable Silicon Rhodamine Platform for Optical Voltage Sensing, *J Am Chem Soc* 137, 10767-10776. Kulkarni, R. U., Kramer, D. J., Pourmandi, N., Karbasi, K., Bateup, H. S., and Miller, E. W. (2017) Voltage-

- sensitive rhodol with enhanced two-photon brightness, *Proc Natl Acad Sci U S A* 114, 2813-2818.
16. Grenier, V., Walker, A. S., and Miller, E. W. (2015) A Small-Molecule Photoactivatable Optical Sensor of Transmembrane Potential, *J Am Chem Soc* 137, 10894-10897.
 17. Siegel, M. S., and Isacoff, E. Y. (1997) A genetically encoded optical probe of membrane voltage, *Neuron* 19, 735-741.
 18. Sakai, R., Repunte-Canonigo, V., Raj, C. D., and Knopfel, T. (2001) Design and characterization of a DNA-encoded, voltage-sensitive fluorescent protein, *Eur J Neurosci* 13, 2314-2318.
 19. Ataka, K., and Pieribone, V. A. (2002) A genetically targetable fluorescent probe of channel gating with rapid kinetics, *Biophys J* 82, 509-516.
 20. Dimitrov, D., He, Y., Mutoh, H., Baker, B. J., Cohen, L., Akemann, W., and Knopfel, T. (2007) Engineering and characterization of an enhanced fluorescent protein voltage sensor, *PLoS One* 2, e440.
 21. Jin, L., Han, Z., Platisa, J., Wooltorton, J. R., Cohen, L. B., and Pieribone, V. A. (2012) Single action potentials and subthreshold electrical events imaged in neurons with a fluorescent protein voltage probe, *Neuron* 75, 779-785.
 22. Cao, G., Platisa, J., Pieribone, V. A., Raccuglia, D., Kunst, M., and Nitabach, M. N. (2013) Genetically targeted optical electrophysiology in intact neural circuits, *Cell* 154, 904-913.
 23. Platisa, J., Vasan, G., Yang, A., and Pieribone, V. A. (2017) Directed Evolution of Key Residues in Fluorescent Protein Inverses the Polarity of Voltage Sensitivity in the Genetically Encoded Indicator ArcLight, *ACS Chem Neurosci* 8, 513-523.
 24. Barnett, L., Platisa, J., Popovic, M., Pieribone, V. A., and Hughes, T. (2012) A fluorescent, genetically-encoded voltage probe capable of resolving action potentials, *PLoS One* 7, e43454.
 25. Yang, H. H., St-Pierre, F., Sun, X., Ding, X., Lin, M. Z., and Clandinin, T. R. (2016) Subcellular Imaging of Voltage and Calcium Signals Reveals Neural Processing In Vivo, *Cell* 166, 245-257.
 26. Abdelfattah, A. S., Farhi, S. L., Zhao, Y., Brinks, D., Zou, P., Ruangkittisakul, A., Platisa, J., Pieribone, V. A., Ballanyi, K., Cohen, A. E., and Campbell, R. E. (2016) A Bright and Fast Red Fluorescent Protein Voltage Indicator That Reports Neuronal Activity in Organotypic Brain Slices, *J Neurosci* 36, 2458-2472.
 27. Deisseroth, K. (2015) Optogenetics: 10 years of microbial opsins in neuroscience, *Nat Neurosci* 18, 1213-1225.
 28. Kralj, J. M., Douglass, A. D., Hochbaum, D. R., Maclaurin, D., and Cohen, A. E. (2011) Optical recording of action potentials in mammalian neurons using a microbial rhodopsin, *Nat Methods* 9, 90-95.
 29. Kralj, J. M., Hochbaum, D. R., Douglass, A. D., and Cohen, A. E. (2011) Electrical spiking in *Escherichia coli* probed with a fluorescent voltage-indicating protein, *Science* 333, 345-348.
 30. Maclaurin, D., Venkatachalam, V., Lee, H., and Cohen, A. E. (2013) Mechanism of voltage-sensitive fluorescence in a microbial rhodopsin, *Proc Natl Acad Sci U S A* 110, 5939-5944.

31. Flytzanis, N. C., Bedbrook, C. N., Chiu, H., Engqvist, M. K., Xiao, C., Chan, K. Y., Sternberg, P. W., Arnold, F. H., and Gradinaru, V. (2014) Archaeorhodopsin variants with enhanced voltage-sensitive fluorescence in mammalian and *Caenorhabditis elegans* neurons, *Nat Commun* 5, 4894.
32. Gong, Y., Li, J. Z., and Schnitzer, M. J. (2013) Enhanced Archaeorhodopsin Fluorescent Protein Voltage Indicators, *PLoS One* 8, e66959.
33. Hochbaum, D. R., Zhao, Y., Farhi, S. L., Klapoetke, N., Werley, C. A., Kapoor, V., Zou, P., Kralj, J. M., Maclaurin, D., Smedemark-Margulies, N., Saulnier, J. L., Boulting, G. L., Straub, C., Cho, Y. K., Melkonian, M., Wong, G. K., Harrison, D. J., Murthy, V. N., Sabatini, B. L., Boyden, E. S., Campbell, R. E., and Cohen, A. E. (2014) All-optical electrophysiology in mammalian neurons using engineered microbial rhodopsins, *Nat Methods* 11, 825-833.
34. Herwig, L., Rice, A. J., Bedbrook, C. N., Zhang, R. K., Lignell, A., Cahn, J. K., Renata, H., Dodani, S. C., Cho, I., Cai, L., Gradinaru, V., and Arnold, F. H. (2017) Directed Evolution of a Bright Near-Infrared Fluorescent Rhodopsin Using a Synthetic Chromophore, *Cell Chem Biol* 24, 415-425.
35. Bayraktar, H., Fields, A. P., Kralj, J. M., Spudich, J. L., Rothschild, K. J., and Cohen, A. E. (2012) Ultrasensitive measurements of microbial rhodopsin photocycles using photochromic FRET, *Photochem Photobiol* 88, 90-97.
36. Cohen, A. E., Kralj, J. M., and Douglass, A. D. (2012) Optogenetic probes for measuring membrane potential, Google Patents.
37. Gong, Y., Wagner, M. J., Zhong Li, J., and Schnitzer, M. J. (2014) Imaging neural spiking in brain tissue using FRET-opsin protein voltage sensors, *Nat Commun* 5, 3674.
38. Zou, P., Zhao, Y., Douglass, A. D., Hochbaum, D. R., Brinks, D., Werley, C. A., Harrison, D. J., Campbell, R. E., and Cohen, A. E. (2014) Bright and fast multicoloured voltage reporters via electrochromic FRET, *Nat Commun* 5, 4625.
39. Gong, Y., Huang, C., Li, J. Z., Grewe, B. F., Zhang, Y., Eismann, S., and Schnitzer, M. J. (2015) High-speed recording of neural spikes in awake mice and flies with a fluorescent voltage sensor, *Science* 350, 1361-1366.
40. Shaner, N. C., Lambert, G. G., Chamma, A., Ni, Y., Cranfill, P. J., Baird, M. A., Sell, B. R., Allen, J. R., Day, R. N., Israelsson, M., Davidson, M. W., and Wang, J. (2013) A bright monomeric green fluorescent protein derived from *Branchiostoma lanceolatum*, *Nat Methods* 10, 407-409.
41. Hodgkin, A. L., and Huxley, A. F. (1952) The components of membrane conductance in the giant axon of *Loligo*, *J Physiol* 116, 473-496.
42. Ji, N., Freeman, J., and Smith, S. L. (2016) Technologies for imaging neural activity in large volumes, *Nat Neurosci* 19, 1154-1164.
43. Mennerick, S., Chisari, M., Shu, H. J., Taylor, A., Vasek, M., Eisenman, L. N., and Zorumski, C. F. (2010) Diverse voltage-sensitive dyes modulate GABA_A receptor function, *J Neurosci* 30, 2871-2879.

Chapter 2

A Voltage-Sensitive Rhodol with Enhanced Two-Photon Brightness

Abstract

We have designed, synthesized, and applied a new rhodol-based chromophore to a photoinduced electron transfer (PeT)-based platform for voltage sensing to achieve fast, sensitive, and bright voltage sensing using two-photon (2P) illumination. Rhodol VoltageFluor-5 (RVF5) is a new voltage-sensitive dye with improved 2P cross section for use in thick tissue or brain samples. RVF5 features a dichlororhodol core with pyrrolidyl substitution at the nitrogen center. In mammalian cells under one-photon (1P) illumination, RVF5 demonstrates high voltage sensitivity (28% $\Delta F/F$ per 100 mV) and improved photostability relative to first-generation voltage sensors. This photostability enables multi-site optical recordings from neurons lacking Tsc1, in a mouse model of genetic epilepsy. Using RVF5, we show that Tsc1 KO neurons exhibit increased activity relative to wild type neurons and additionally show that the proportion of active neurons in the network increases with the loss of Tsc1. The high photostability and voltage sensitivity of RVF5 is recapitulated under 2P illumination. Finally, the ability to chemically tune the 2P absorption profile through the use of rhodol scaffolds affords the unique opportunity to image neuronal voltage changes in acutely prepared mouse brain slices using 2P illumination. Stimulation of the CA1 region of the mouse hippocampus evoked spiking activity that was readily discerned with bath-applied RVF5, demonstrating the utility of RVF5 and PeT-based voltage sensors with 2P-optimized fluorophores for imaging voltage in intact brain tissue.

This chapter is based on the publication in the *Proceedings of the National Academy of Sciences* entitled “Voltage-sensitive rhodol with enhanced two-photon brightness.”

2.1 Voltage Imaging for Two-Photon and Long-Term Imaging Applications

Neurons communicate by translating electrical signals (membrane potential) into chemical signals (neurotransmitter release). Neuronal membrane potential dynamics drive neurotransmitter release and are therefore responsible for the unique physiology associated with neurons at cellular, circuit, and organismal levels. Despite the central importance of proper neuronal firing to human health, an integrated understanding of neuronal activity in the context of larger brain circuits remains elusive, due in part to a lack of methods for interrogating membrane potential dynamics with sufficient spatial and temporal resolution.

Traditional methods for monitoring membrane potential rely heavily on the use of invasive electrodes, through one of two methods. The first method, patch-clamp electrophysiology, uses a single electrode to make contact with or puncture a cell to record changes in membrane potential, sacrificing throughput and spatial resolution to achieve a comprehensive description of a single cellular electrophysiological profile. A second method utilizes multi-electrode arrays (MEAs), in which patterned arrays of electrodes introduced to cells or tissues report on electrical changes. Spatial resolution of MEAs depends on the number and positioning of the electrodes within the array. Although throughput is improved relative to patch clamp electrophysiology, recorded signals are typically less sensitive than whole-cell methods and can be an amalgamation of several cells, making deconvolution of recorded signals and precise correlation to specific cells difficult or impossible. Additionally, it is impossible to tell if a “silent” MEA channel is a result of poor electrode positioning (i.e. not near or within a cell) or because the neuron itself is silent.¹

Direct imaging of voltage changes with fluorescent probes is an attractive solution to these challenges because voltage imaging can provide the spatial and temporal resolution needed to match signals to cells with high throughput and fidelity.²⁻⁴ The challenge of achieving optical voltage sensing is a long-standing goal within the scientific community,^{5, 6} and recent approaches have included fluorinated styryl dyes,⁷ annulated hemicyanines,^{8, 9} and cyanines,¹⁰ lipophilic anions,¹¹⁻¹³ hybrid small molecule/fluorescent protein probes,¹⁴⁻¹⁶ porphyrins,¹⁷ and nanoparticles.^{18, 19} However, combinations of poor sensitivity, slow kinetics, ineffective membrane localization, rapid photobleaching, and/or limited two photon cross section, which is important for imaging in thick tissue have hampered rapid progress towards a general solution for optical voltage imaging. Small molecule voltage sensors in particular are plagued by tradeoffs in speed and sensitivity. More recently, genetically encoded fluorescent voltage sensors also show promise in terms of both speed and sensitivity,²⁰⁻²³ but current methods are similarly limited by low brightness and low two photon absorption brightness.²⁴

We were therefore drawn to a new method for voltage sensing that makes use of a photoinduced electron transfer (PeT)(25) through a molecular wire as a voltage-sensitive trigger.²⁶ PeT-based molecular wire voltage sensors, or VoltageFluors, intercalate into the plasma membrane so that the direction of PeT aligns perpendicular to the plane of the plasma membrane (**Figure 2.1a**).²⁷ PeT within a VF dye is enhanced under hyperpolarized cellular conditions (negative intracellular charge) and decreased during cellular depolarization (positive intracellular charge). Because the rate of PeT competes with the rate of fluorescence, cellular hyperpolarization, corresponding to typical resting neuronal membrane potential, results in a dim fluorescent state from the VF dye, while depolarization gives fluorescence enhancement, enabling the detection of fast spiking action potentials in a variety of neuronal contexts.

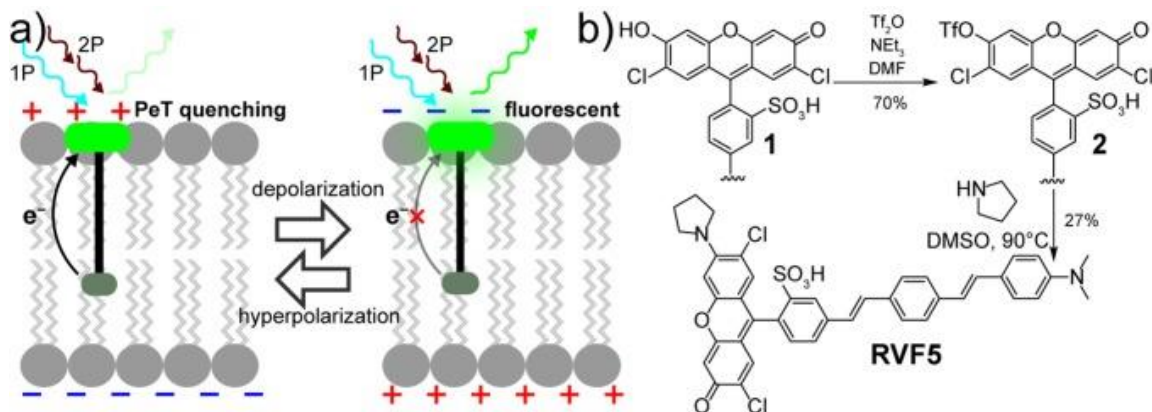


Figure 2.1. Voltage Sensing via Photoinduced Electron Transfer (PeT) using 1 or 2 Photon Excitation and Synthesis of RVF5 a) At hyperpolarized or resting potentials (left), fluorescence is quenched via PeT, while at depolarized potentials (right), PeT is inhibited by the electric field across the membrane, enhancing fluorescence. Voltage sensitivity can be achieved under traditional one-photon illumination with blue light (1P, cyan arrow) or with two photons of infrared light (2P, dark red arrow). b) Synthesis of RVF5.

Small molecule fluorescent voltage sensors based on a PeT trigger show promise for interrogating membrane potential dynamics in neuronal systems because these VoltageFluors, or VF dyes, display good sensitivity, excellent response times, and avoid complications associated with added capacitance. Additionally, because VF dyes are small molecules, they should be readily tunable to a number of different chromophores²⁸ to select for desired properties, such as wavelength,²⁹ improved photostability, or enhanced two photon cross section.³⁰ In this manuscript, we describe the design, synthesis, characterization, and application of Rhodol VoltageFluor-5 (RVF5), a new voltage-sensitive small molecule in the VoltageFluor family with enhanced photostability and improved two-photon optical cross section relative to the parent fluorescein-based VF dyes. We use RVF5 to show for the first time that PeT-based voltage sensors can operate under two photon illumination and to probe neuronal excitability in a mouse model of the human genetic epilepsy disorder Tuberous Sclerosis Complex (TSC), both in cultured neurons and in acutely-prepared brain slices.

2.2 Synthesis and Characterization of RVF5

We reasoned that the conversion of fluorescein-based VF dyes into unsymmetrical rhodol-based reporters, in which one of the oxygen atoms at the 3'- and 6'-position of the xanthene chromophore is replaced to a substituted nitrogen, would improve photostability and two photon absorbance (σ^2). Introduction of asymmetry in the chromophore axis increases the extent of intramolecular charge transfer (ICT), enhancing efficiency of σ^2 (measured in Göppert-Mayer units of $10\text{-}50\text{ cm}^4\text{ s photon}^{-1}\text{ molecule}^{-1}$).³⁰ Furthermore, rhodols exhibit higher photostability than their oxygen-substituted xanthene counter parts.³¹

Both properties—improved photostability and σ^2 —would significantly improve our ability to monitor changes in neuronal voltage for extended periods of time and in thick, optically opaque tissues. RVF5 is available in two steps from a first generation VF dye (**Figure 2.1b**). Triflation of the original VF dye, VF2.1.Cl, **1** with triflic anhydride and pyridine in CH_2Cl_2 provided

intermediate **2** in 70% yield, following silica gel chromatography. Subsequent nucleophilic aromatic substitution (S_NAr) with pyrrolidine at 90 °C provided RVF5 in 27% yield, following purification by reversed-phase semi-preparative HPLC.

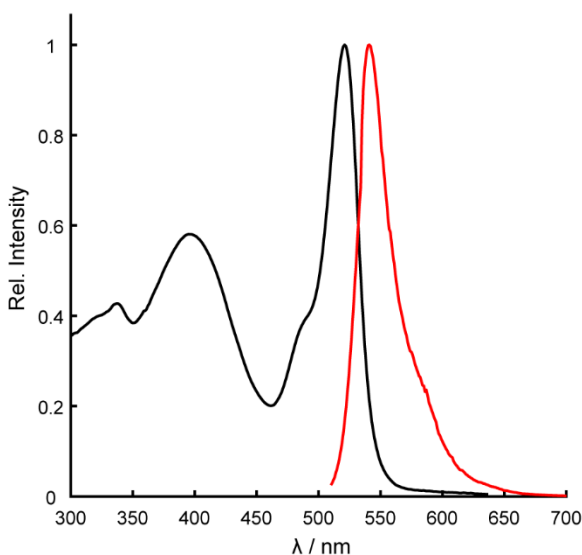


Figure 2.2. Spectroscopic properties of RVF5. The excitation and emission spectra of RVF5 in PBS, pH 7.4 with 0.1% Triton-X.

RVF5 displays excitation and emission profiles centered in the visible range, with a λ_{max} of 520 nm ($\epsilon_{520} = 83,000 \text{ cm}^{-1} \text{ M}^{-1}$, PBS, pH 7.4) and a secondary absorbance at 380 nm ($\epsilon_{380} = 45,000 \text{ cm}^{-1} \text{ M}^{-1}$) corresponding to the phenylene-vinylene molecular wire (**Figure 2.2**) RVF5 emits at 535 nm ($\Phi_{\text{fl}} = 0.27$, PBS, pH 7.4 **Figure 2.2**). Bath application of RVF5 to HEK cells at 37 °C for 15 minutes results in clear fluorescence intensity associated with the membrane, confirming cellular localization of this new rhodol-based voltage sensitive dye.

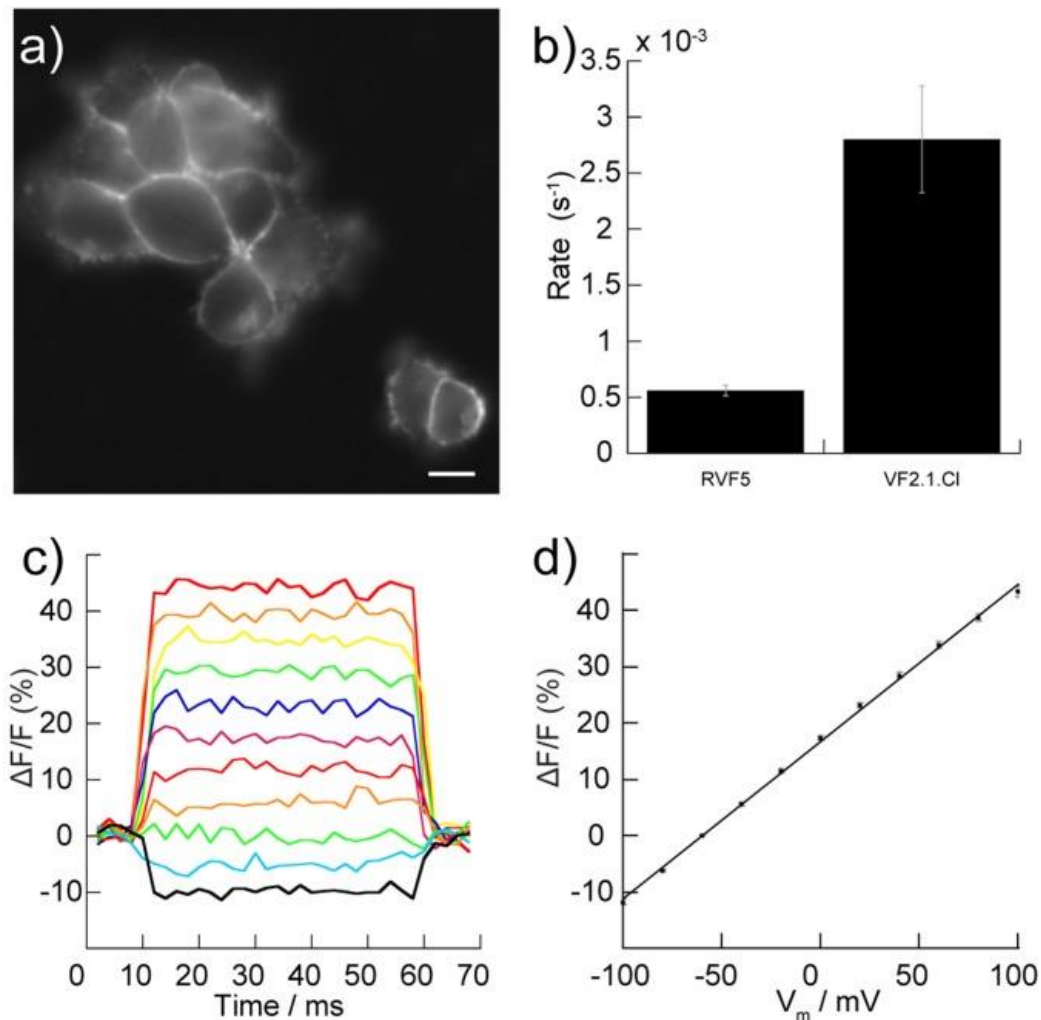


Figure 2.3. One photon characterization of RVF5 in HEK cells. a) Widefield fluorescence image of HEK cells stained with 200 nM RVF5 for 15 min at 37 °C. b) Relative photostability of RVF5 compared to VF2.1.Cl. Error bars are \pm SEM for $n = 5$ experiments. Voltage sensitivity of RVF5 in HEK cells was assayed by patch clamp electrophysiology. c) Fractional change in RVF5 fluorescence ($\Delta F/F$) vs. time in a HEK cell held under voltage clamp at -60 mV and then subjected to potentials ranging from +100 mV to -100 mV for 50 ms in 20 mV increments. Concatenated traces shown in c) are representative of a single experiment. d) Fractional change in fluorescence ($\Delta F/F$) vs. final membrane potential (V_m), in mV. Error bars are \pm SEM for $n = 7$ experiments. Scale bar is 10 μ m.

To assess the photostability of RVF5 under cellular illumination conditions, we loaded HEK cells with either RVF5 or VF2.1.Cl and monitored membrane-associated fluorescence over time. (510 nm, 15 W/cm²). Under illumination conditions 8-fold more intense than those used for typical imaging experiments with RVF5, RVF5 exhibits approximately 8-fold greater photostability compared to VF2.1.Cl (**Figure 2.3b**), with a bleach rate of $1.2(\pm 0.1) \times 10^{-6} \text{ s}^{-1}$ for RVF5 and $4.3(\pm 0.3) \times 10^{-6} \text{ s}^{-1}$ for VF2.1.Cl (**Figure 2.4**).

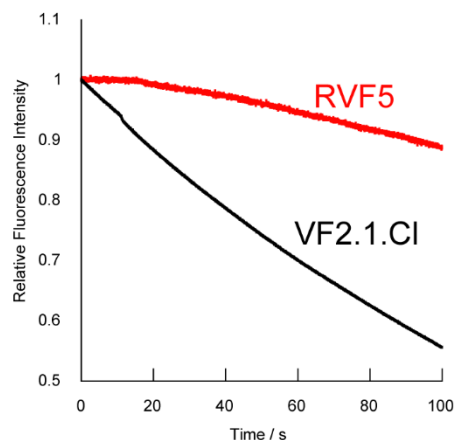


Figure 2.4. Photostability of RVF5 and VF2.1.Cl in HEK cells. The fluorescence bleaching curves of RVF5 and VF2.1.Cl in HEK cells under 475 nm light at a power of 15 W/cm². RVF5 bleaches with a time constant four-fold smaller than that of VF2.1.Cl. Traces represent the average of n = 9 experiments.

To confirm that membrane-associated RVF5 fluorescence in HEK cells is voltage sensitive, HEK cells were stained with RVF5 (200 nM) and subjected to whole-cell patch-clamp electrophysiology under voltage clamp conditions. Cells were held at a membrane potential of -60 mV to simulate resting potential for a typical mammalian neuron and then hyper- and depolarized to various potentials ranging from -100 mV to +100 mV in 20 mV increments (**Figure 2.3c**). As predicted, and as demonstrated for previous classes of PeT-based voltage sensors,^{26, 27, 29} depolarization results in fluorescence enhancement from the cell membrane while hyperpolarization decreases membrane fluorescence (**Figure 2.3c**). Plotting fractional change in fluorescence ($\Delta F/F$) vs. potential gives a linear voltage sensitivity of 28% ($\pm 1\%$) $\Delta F/F$ per 100 mV over a range spanning ± 100 mV, comparable to the voltage sensitivity of the first generation of xanthene-based VF dyes (27% $\Delta F/F$ per 100 mV) (**Figure 2.3d**).

We next sought to determine the two-photon optical properties of RVF5. Two-photon absorption relies on the essentially instantaneous delivery of two low-energy photons to promote a chromophore from the ground state to the excited state,³⁰ and is beneficial for imaging in thick tissue because lower energy photons scatter less, cause less tissue damage, and, in the case of two-photon microscopy, reduce out-of-plane illumination because of the quadratic dependence of two-photon absorbance on incident light intensity.^{32, 33} We measured the two-photon cross section of RVF5 and VF2.1.Cl in vitro by normalizing to a fluorescein or rhodamine B standard.³⁴⁻³⁶ A plot of two-photon cross section vs. excitation wavelength reveals an absorption maximum of 120 GM at 820 nm for RVF5 (**Figure 2.5b**). For comparison, VF2.1.Cl displays a weaker two-photon absorbance, approximately 40 GM at its λ_{max} of 780 nm.

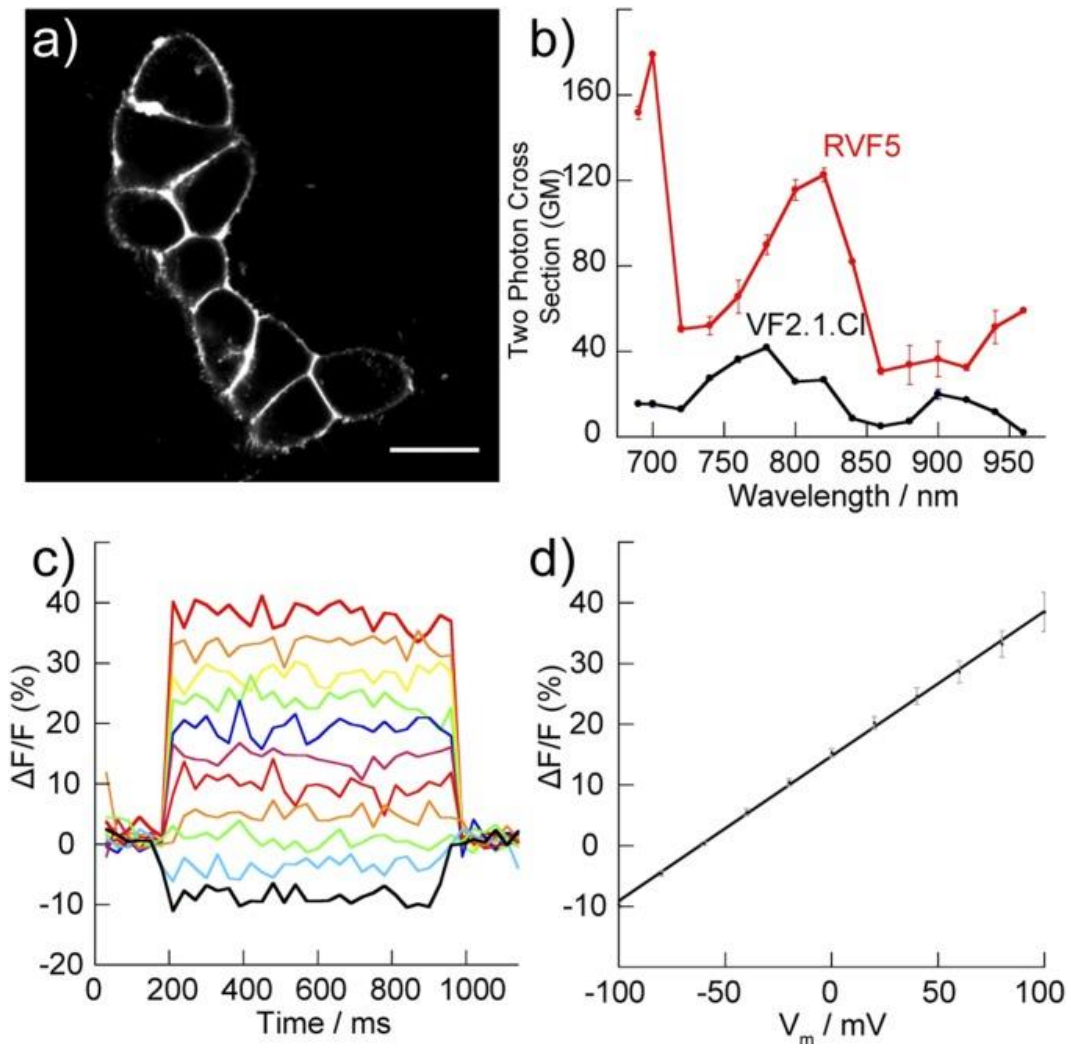


Figure 2.5. Two photon characterization of RVF5 in HEK cells. a) Two-photon scanning laser microscopy image of HEK cells stained with 1 μ M RVF5 for 15 min at 37 $^{\circ}$ C. b) Comparison of two-photon cross section of RVF5 (red) and VF2.1.Cl (black) vs. wavelength in vitro (PBS, pH 7.4). Error bars are \pm SEM for $n = 3$ experiments. c) Fractional change in fluorescence ($\Delta F/F$) vs. time in a patch-clamped HEK cells under 2P illumination (820 nm), held at -60 mV and then stepped to potentials ranging from \pm 100 mV in 20 mV increments. Traces shown are for a single cell. d) $\Delta F/F$ vs. final membrane potential (V_m) in mV. Error bars are \pm SEM for $n = 3$ experiments. Scale bar is 10 μ m.

Other voltage-sensitive fluorophores like the widely-used ANEPPS family display maximum two photon absorbance values in the range of 5-10 GM,³⁷ and eGFP has maximum two photon absorbance value of 30-40 GM at 925 nm.³³ The two photon absorbance value for VF2.1.Cl at 820 nm is 27 GM, which is in agreement with previously reported values for fluorescein that range from 30 to 50 GM.^{34, 35, 38} HEK cells loaded with RVF5 and imaged using two photon laser scanning microscopy ($\lambda_{ex} = 820$ nm) displayed clear membrane-localized fluorescence (**Figure 2.5a**) that showed a quadratic dependence on illumination intensity, consistent with pure two photon absorbance (**Figure 2.6**).

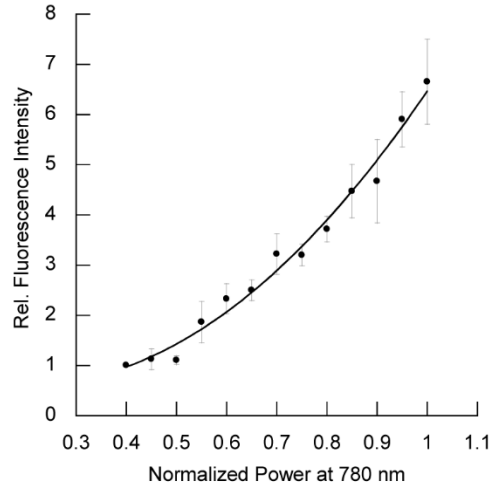


Figure 2.6. Two photon characterization of RVF5. Quadratic dependence of fluorescence on illumination intensity. The fluorescence of RVF5 displays a quadratic dependence on illumination power (780 nm). Error bars are \pm standard deviation for $n = 3$ independent measurements. The points were best fit by the following equation: $y = 9.2x^2 - 3.7x + 0.99$ with an R^2 value of 0.985.

Under two photon illumination, voltage sensitivity of RVF5 in HEK cells was approximately 24% ($\pm 7\%$, SEM for $n = 3$ separate experiments) $\Delta F/F$ per 100 mV, when considering pixels only at the cell membrane (**Figure 2.5c, d**) These results establish that RVF5, a PeT-based voltage indicator, can sense voltage under two-photon illumination. When a region of interest (ROI) included pixels within the dark cytosol, the calculated voltage sensitivity was lower, at 17% $\Delta F/F$ per 100 mV (**Figure 2.7**).

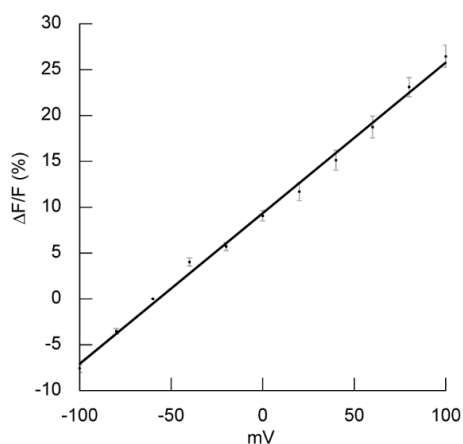


Figure 2.7. Voltage sensitivity of RVF5 in HEK cells under two-photon illumination. The fractional change in fluorescence vs. final membrane potential is plotted. Values represent regions of interest that include the *membrane and cytosol*. Error bars are \pm SEM for $n = 3$ experiments.

In HEK cells, RVF5 showed enhanced 2P photostability when compared to VF2.1.Cl or ASAP 1,²¹ a genetically encoded voltage-sensitive green fluorescent protein (**Figure 2.8**). Both VF2.1.Cl and ASAP 1 showed rapid bleaching under 820 nm illumination. After approximately 30 seconds, a typical timeframe for imaging under 2P illumination, RVF5 fluorescence remains at 50% ($\pm 6\%$) of its original value, while VF2.1.Cl bleached substantially to 8% ($\pm 1\%$) and ASAP 1 drops to 20% ($\pm 6\%$). The improved photostability of RVF5 under 2P illumination mirrors our measurements under 1P illumination and agrees with reports in the literature.^{24, 31}

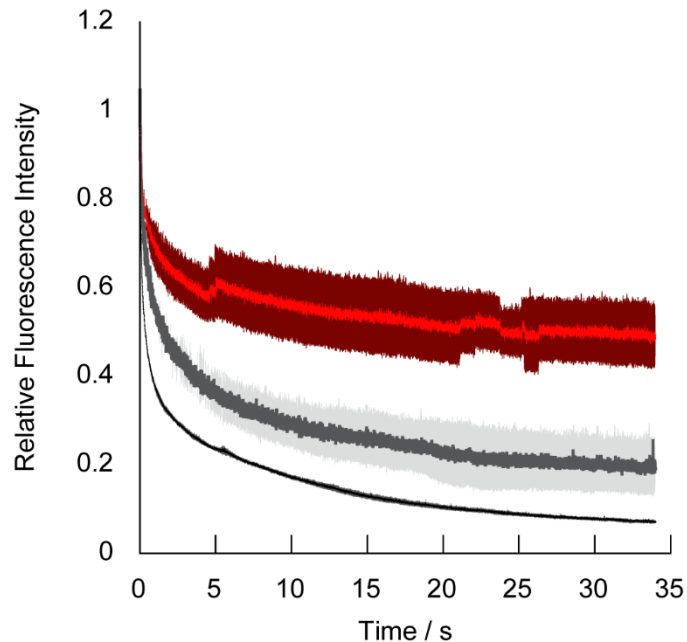


Figure 2.8. 2P photostability of R VF5, VF2.1.C1 and ASAP 1. R VF5 (red trace, upper), VF2.1.C1 (black trace, lower), and ASAP 1 (grey trace, middle) were loaded or transfected into HEK293T cells and bleached under 820 nm light from a Chameleon Compact OPO laser at 100% laser intensity. Images were collected using the BiG-2 detector on a Zeiss LSM 880 Axio Examiner. The traces represent average values and the shaded regions indicate the standard error of the mean from $n = 3$ trials.

With enhanced photostability and voltage sensitivity on par with previous generations of VF dyes, R VF5 should be well-suited to observing membrane voltage changes in neurons. Cultured rat hippocampal neurons bathed with R VF5 (200 nM) displayed clear membrane fluorescence when examined using one photon, wide-field fluorescence microscopy (**Figure 2.9a**).

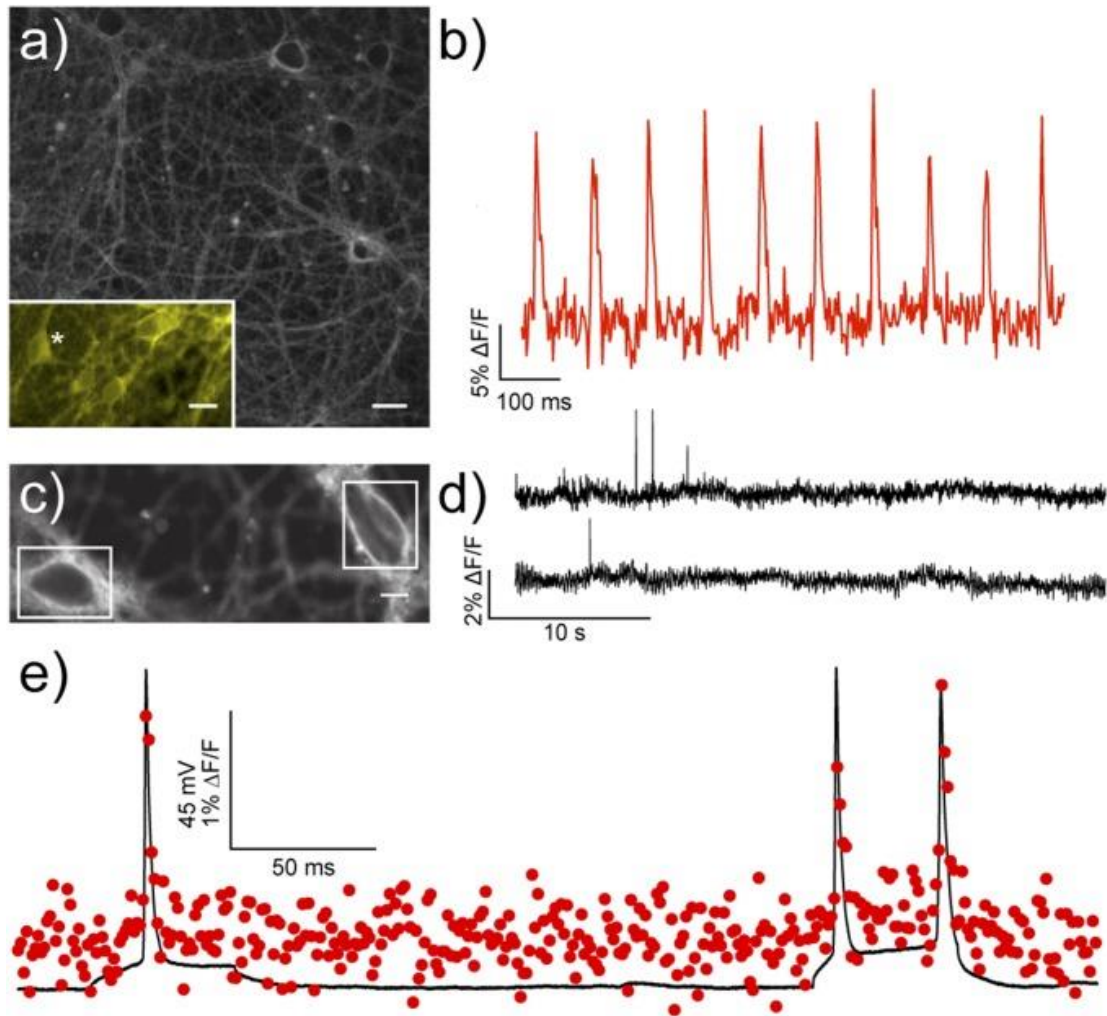


Figure 2.9. One-photon characterization of RVF5 in neurons. a) Dissociated rat hippocampal neurons stained with RVF5 and imaged under widefield fluorescence microscopy conditions. Inset shows image used for acquisition of data in panel b. Scale bars are 20 μm . b) Trains of action potentials evoked by extracellular stimulation of neurons in panel a, inset. Plot shows the average intensity from the neuron indicated by (*). c and d) Imaging spontaneous activity in rat hippocampal neurons stained with RVF5. Traces on the right show the spontaneous activity in the boxed neurons in panel c. Scale bar is 8 μm . e) Dual electrophysiological and optical recording of action potentials in cultured hippocampal neurons. Action potentials were evoked under current clamp mode and recorded electrophysiologically (black trace; 50 kHz sampling rate) and optically (red dots, 1 kHz sampling rate).

Field stimulation of neurons loaded with RVF5 resulted in optically recorded transients displaying approximately 11% $\Delta\text{F}/\text{F}$ per spike ($\pm 1\%$, $n = 10$ AP each from $n = 3$ neurons) with a signal-to-noise ratio (SNR) of 10:1 (± 1) (**Figure 2.9b**). The improved photostability of RVF5 relative to VF2.1.Cl enabled longer recording from neurons and therefore imaging of spontaneous activity. Optical recording of rat hippocampal neurons stained with RVF5 (**Figure 2.9c**) for 40 second periods revealed sparse spiking events, which could be collected from multiple cells

simultaneously (**Figure 2.9d**). Rat hippocampal neurons loaded with RVF5 were also subjected to whole-cell patch clamp electrophysiology under current-clamp mode to evoke action potentials. Dual optical (red circles) and electrophysiological recording (black line) establish that RVF5 exactly follows the electrophysiological recording (**Figure 2.9e**). Comparison of action potential parameters recorded electrophysiologically in cultured mouse hippocampal neurons with and without RVF5 show no significant difference in action potential duration, rise, or decay time (**Figure 2.10**), suggesting that RVF5 does not perturb cellular physiology.

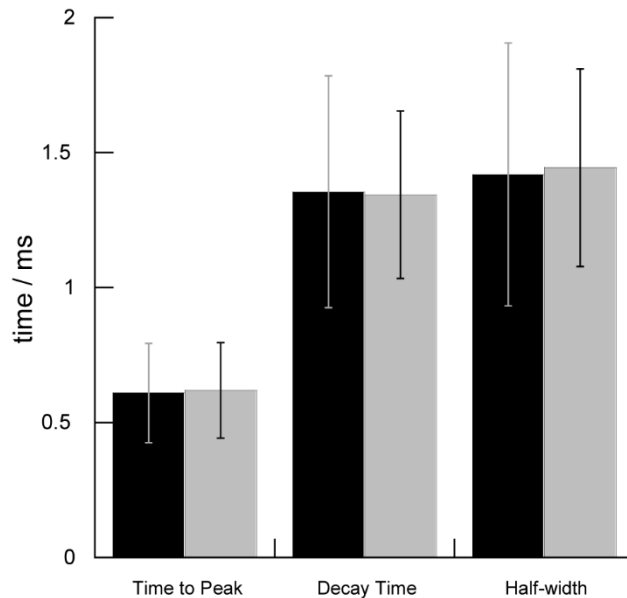


Figure 2.10. Comparison of AP parameters in mouse hippocampal neurons with and without RVF5. Mouse hippocampal neurons were subjected to patch clamp electrophysiology under current clamp mode in the whole-cell configuration, with or without loading of RVF5. Trains of action potentials were evoked (10 AP, 5 Hz) by current injection. Values are mean values for $n = 70$ AP from 7 different cells for each condition (\pm RVF5). Error bars are standard deviation and all p values are > 0.05 (Student's t -test, two-tailed).

2.3 Imaging *TSC1* Knockout Neurons with RVF5

The ability to monitor neural activity with cellular resolution for extended recording periods is important for deciphering the role individual neurons play in the context of larger networks. This would be especially useful for elucidating disease mechanisms in models of human disorders characterized by altered neuronal activity, such as epilepsy. For example, the human neurodevelopmental disorder tuberous sclerosis is characterized by epilepsy, autism spectrum disorder, and cognitive disability³⁹ and resulting from loss of function mutations in the *TSC1* or *TSC2* genes. The protein products of these genes form a complex that negatively regulates mTOR signaling, however the mechanisms by which changes in mTOR signaling lead to deregulated neural activity are not well understood.⁴⁰⁻⁴² In mice, loss of *Tsc1* leads to imbalances in synaptic excitation/inhibition, increased overall network activity, and seizures, which are a hallmark of this

disorder.⁴³ Previously, MEA recordings from control and Tsc1 knock-out (KO) neurons in hippocampal cultures^{43,44} showed a clear difference in the activity of Tsc1 KO neurons, with Tsc1 KO cultures displaying higher rates of activity and burst firing (groups of action potentials) relative to controls.⁴³ However, MEA recordings cannot provide the spatial information required to match bursting patterns to individual cells, precluding sub-type specific characterization or further analysis of how single cells may affect the properties of the entire network. Additionally, MEAs cannot give a concrete measure of the number of silent cells within a particular network, which may play an important role in determining overall network properties.

To address these open questions, dissociated hippocampal neuronal cultures were prepared from mice with conditional alleles of Tsc1 (Tsc1^{fl/fl}) flanked by LoxP,^{43,44} cultured in vitro and treated with a lentivirus encoding mCherry-tagged Cre recombinase to delete the Tsc1 gene. This strategy provided paired sets of neurons from the same mouse that differed in their expression of Tsc1 (WT or KO). Following infection, neurons showed nuclear-localized mCherry signal, identifying Tsc1 KO neurons (**Figure 2.11b**). After 14 days in vitro (DIV), neurons were incubated with RVF5 (**Figure 2.11a**) and imaged for 40 s intervals to determine the spontaneous firing rate of the paired WT and Tsc1 KO samples. Optical records of spontaneous activity were acquired for over 50 individual neurons for both WT (n = 72, Fig. 5c, black trace) and Tsc1 KO (n = 54, **Figure 2.11c**, red trace). We developed a custom script to enable rapid processing and extraction of spike timings from the acquired data. Briefly, the fluorescence intensity vs. time for each neuron was plotted, and the standard deviation for a non-spiking period of the recording was determined. Any time point 3 standard deviations above the mean baseline was considered a spike. Tsc1 KO neurons show a significantly higher average firing rate ($9.2 \text{ Hz} \pm 1.6 \text{ Hz}$, SEM) than their matched WT counterparts ($4.3 \text{ Hz} \pm 0.8 \text{ Hz}$, $p < 0.01$, Student's t-test) (**Figure 2.11d**, **e Figure 2.12**), not including silent cells (see below). This result is consistent with previously reported observations from MEA data (approximately 13 and 5 Hz per electrode for WT and KO cultures, respectively).⁴³ Voltage imaging with RVF5 represents an improvement in cellular resolution over MEA recording, because spikes are sorted per neuron, as opposed to per electrode. Control experiments indicate that treatment with tetrodotoxin (TTX, 1 μM), a sodium channel blocker, completely abolishes spontaneous spiking activity, establishing that these spikes reflect action potentials (**Figure 2.13**).

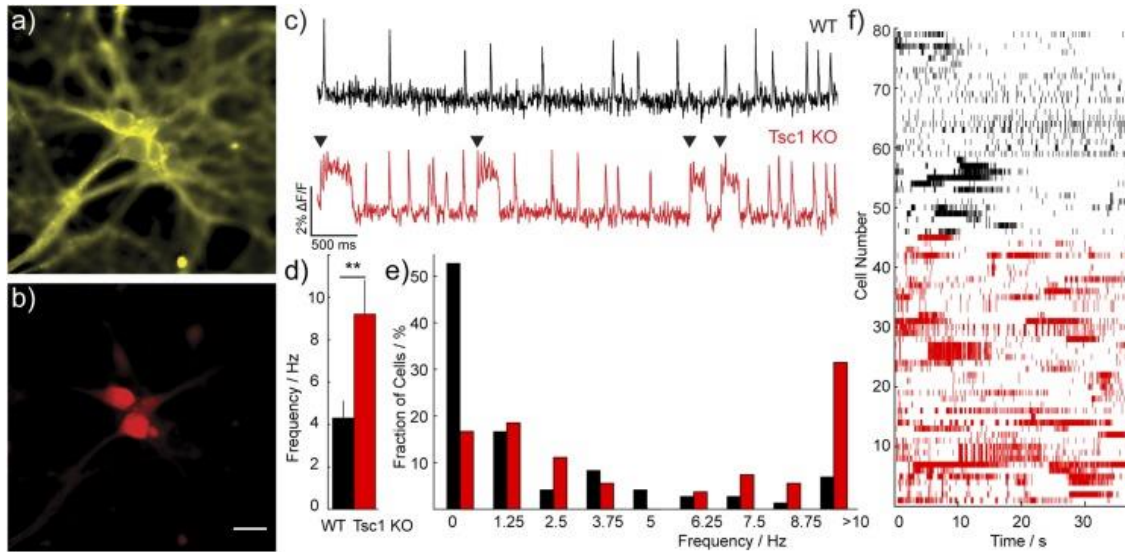


Figure 2.11. Assessing differences in spontaneous activity in WT and Tsc1 KO neurons with RVF5. Widefield fluorescence image of RVF5 staining a) in DIV 14 cultured Tsc1fl/fl mouse hippocampal neurons infected with a virus encoding mCherry-Cre to knockout the Tsc1 gene (Tsc1 KO). b) mCherry labels Cre-expressing Tsc1 KO neurons. Scale bar is 20 μm . c) Representative optical recordings of spontaneous activity in pairs of wild-type (WT, upper, black trace) and Tsc1 KO cultures (Tsc1 KO, lower, red trace). Arrowheads (▼) indicate periods of “burst” firing in the Tsc1 KO neuron. d) Average spiking frequency, in Hz, for active WT and Tsc1 KO neurons. Error bars are SEM for $n = 72$ and 54 neurons for WT and Tsc1 KO, respectively. ** indicates $p < 0.01$, Student’s two-tailed t-test. e) Histogram displaying fraction of total cells vs. firing frequency during a recording session for both WT (black) and Tsc1 KO (red) neurons. f) Raster plot depicting spiking activity for all spontaneously active neurons. Each line represents a single spike detected in a given cell during the 40 s recording window for both WT (black) and Tsc1 KO (red) neurons. Each horizontal row depicts the spiking activity of a single neuron over time.

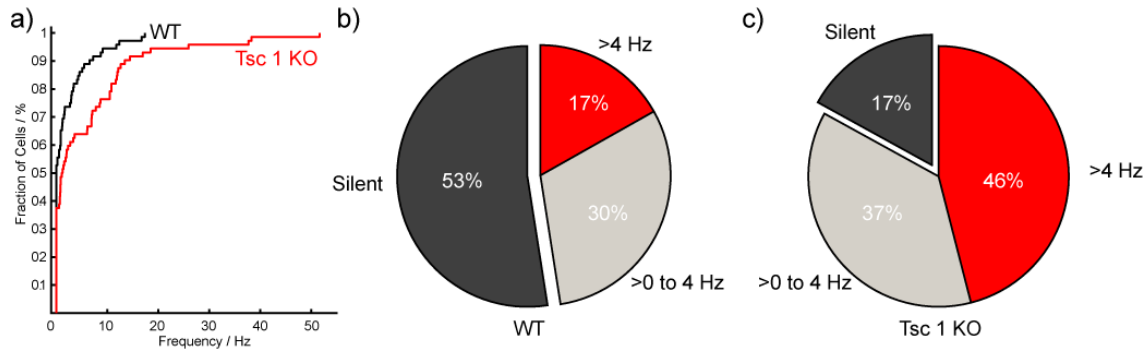


Figure 2.12. Quantification of spiking activity in WT and Tsc1 KO neurons. a) Cumulative frequency plot of WT and Tsc1 KO neuronal firing rate for all imaged neurons. b and c) Proportion of “Silent” (no detected spikes, black), intermediate firing (up to 4 Hz average spike rate, grey), and highly active neurons (>4 Hz average spike rate, red) for b) WT and c) Tsc1 KO neurons.

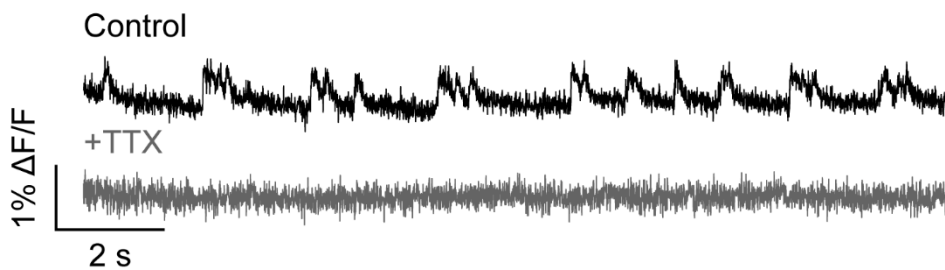


Figure 2.13. Imaging spontaneous activity in cultured mouse neurons with RVF5. Addition of TTX (1 μ M) abolishes activity. Traces are single trials and are not filtered or corrected for bleaching.

A raster plot displaying all spikes from across all imaging experiments clearly shows the higher density of action potentials in neurons lacking Tsc1 (**Figure 2.11e, f**). Interestingly, over half (38 of 72, 53%) of WT neurons were silent (**Figures 2.11e, 2.14a, b**), while only 9 of 54 (17%) Tsc1 KO neurons were silent (**Figures 2.11e, 2.14c, d**) across all trials. The proportion neurons firing at intermediate rates (>0 to 4 Hz) was similar across both WT and Tsc1 KO neurons at 30% and 37%, respectively (n = 72 for WT, 54 for KO, **Figures 2.11e, 2.12b,c**), while the proportion of highly active (>4 Hz) neurons increases in the Tsc1 KO condition (17% WT vs. 46% KO, **Figure 2.12b,c**). These results show, for the first time, that loss of Tsc1 increases not only the firing rate, but the proportion of cells within the network that are spontaneously active. Voltage imaging with RVF5 offers an expedient method for assessing global network properties (such as spike rate) while maintaining cellular specificity and resolution; studies are underway to probe the identity and molecular profile of both active and non-spontaneously active neurons in the context of Tsc1 loss.

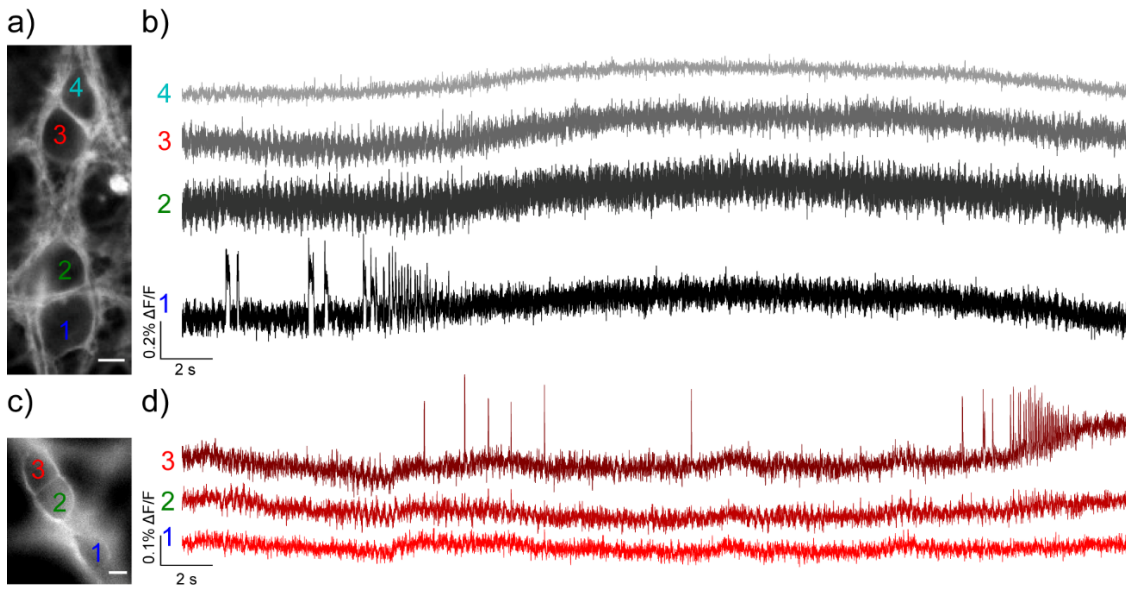


Figure 2.14. Example traces of spontaneous activity imaging with RVF5 in cultured hippocampal neurons from WT or Tsc1 KO mice. Cultured hippocampal neurons from *Tsc1^{fl/fl}* mice a) alone (control, WT) or treated with virus encoding c) synapsin-mCherry-IRES-Cre (Tsc1 KO) and stained with RVF5. Traces to the right are the optical recordings (200 Hz frame rate) from the b) WT or d) Tsc1 KO cells. All traces are single trial recordings. Scale bars are 10 μm .

2.4 Imaging Neuronal Activity in Mouse Brain Slices with RVF5

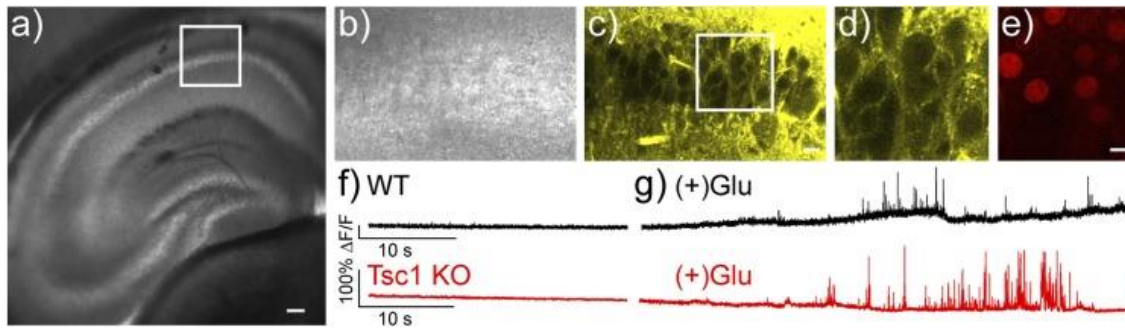


Figure 2.15. Two-photon voltage imaging in mouse brain slices. Transmitted light images of mouse hippocampal brain slice stained with 10 μM RVF5 in oxygenated ACSF show a) the entire hippocampus and b) a zoomed region of CA1. c) Fluorescence signals from RVF5 (10 μM , oxygenated ACSF) from the same region in panel (b) show membrane-localized staining. d and e) A zoomed-in region from panel (c) shows RVF5 fluorescence primarily in cellular membranes and excluded from the cytosol and e) nuclear-localized mCherry-Cre indicating Tsc1 KO neurons. Functional imaging was performed by creating a 8 x 64 pixel region over an area of CA1 and imaging at ~ 200 Hz for 20-40 s, first in the absence of glutamate (panel f) and then following addition of glutamate to the perfusate (panel g (+)Glu). Responses were recorded from neurons in the sham injected (control, “WT”, black traces) and mCherry-Cre injected (“Tsc1 KO”, red traces) hemispheres. Scale bars are 100 μm for panel a and 20 μm for panels b-e. Fluorescence traces are single-trial $\Delta\text{F}/\text{F}$ values from single pixels and are uncorrected for photobleaching.

To lay the groundwork for further exploration of the roles of Tsc1 in neuronal excitability in the context of intact circuits, we assessed the ability of RVF5 to monitor neuronal activity *ex vivo* in mouse brain slices. Bath application of 10 μM RVF5 to brain slices acutely prepared from mice injected unilaterally with the mCherry-Cre virus (Tsc1 KO) or a sham (WT) into hippocampal area CA1 results in clearly-defined membrane staining (**Figure 2.15c and d, 2.16a,b**). The fluorescence staining closely matched the cellular anatomy of the local brain region. For example, in cortical slices stained with RVF5, cell bodies of neurons appeared as dark cavities against a bright background of fluorescent membrane (**Figure 2.16b**). In the hippocampus, the highly stratified neuroanatomy (**Figure 2.15a-c**) is easily visualized at ~ 50 μm below the surface, in particular in the CA1 region where the cell bodies appear as a single dark band, highlighted by RVF5 staining of the membranes separating distinct cell bodies (**Figure 2.15c,d, 2.16a**). Above and below the cell body layer, the basal and apical dendrites appear as a homogeneous stain, indicating the non-specific uptake of RVF5 into cellular membranes. The expression of nuclear-localized mCherry confirmed successful infection into the CA1 hippocampal subfield (**Figure 2.15d,e**).

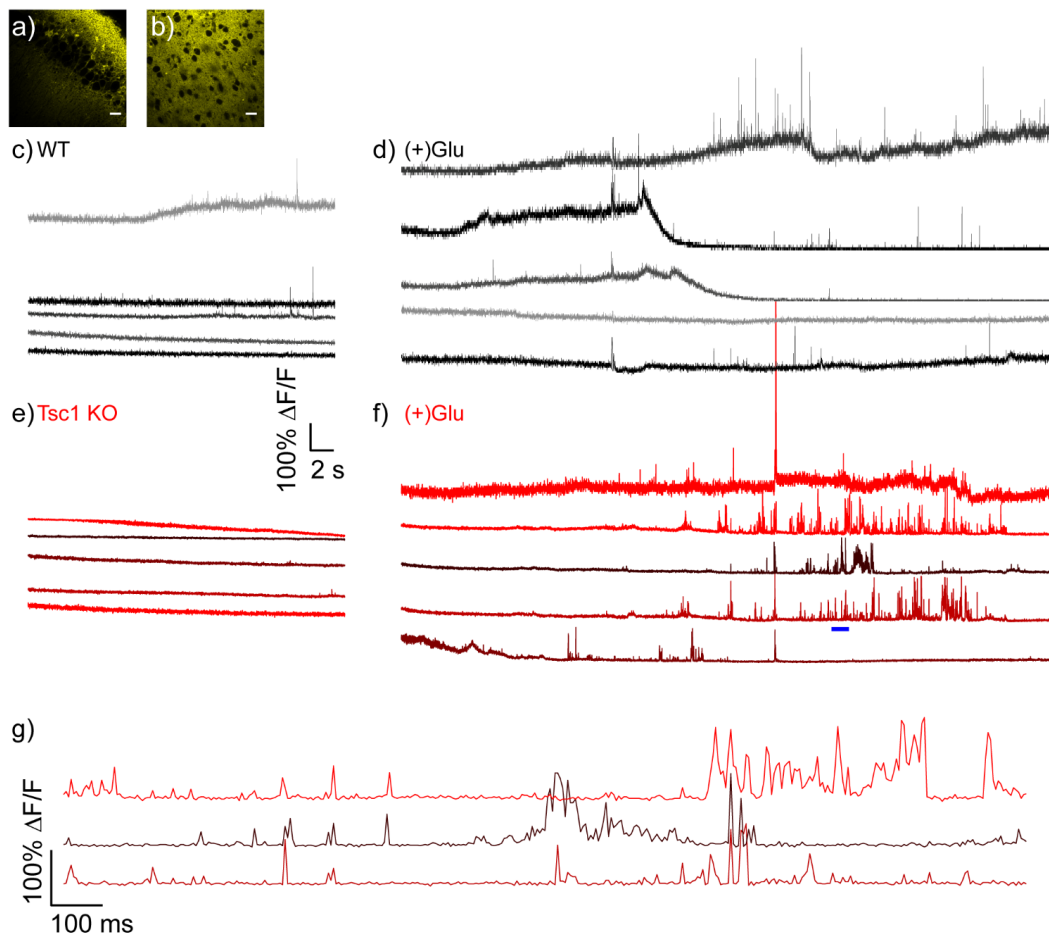


Figure 2.16. Representative traces from 2P imaging in mouse brain slices. 2P laser scanning fluorescence image of RVF5-stained mouse brain slice in the a) CA1 region of the hippocampus and in the b) somatosensory cortex. Scale bar is 20 μm . c-f) Each trace represents a single pixel in the CA1 region of a mouse hippocampal brain slice stained with 10 μM RVF5 and then imaged under 2P illumination. Each trace represents $\Delta F/F$ plotted vs. time. For panel f), the upper three traces are all from adjacent pixels, yet have distinct firing patterns. Panel g) shows an expanded time scale of the region indicated by a blue bar.

We made optical recordings under 2P illumination for 20-40 s in the CA1 region of the hippocampus. In single-trial, single-pixel (6.6 μm^2) optical recordings in oxygenated ACSF, both WT and Tsc1 KO slices show minimal activity, as measured by fractional changes in RVF5 fluorescence (**Figure 2.15f, 2.16**). Addition of the excitatory neurotransmitter glutamate to the slices results in robust induction of spiking behavior in both the WT and Tsc1 KO slices due to strong activation of excitatory synapses (**Figure 2.15g, 2.16**), similar to what we observe in single-unit, whole-cell electrophysiological recordings in neurons from CA1 in hippocampal slices (**Figure 2.17**). Our imaging field of view, comprising approximately $425 \times 52 \mu\text{m}$, allows us to sample a large number of neurons within the CA1; however, the fast sampling rates required for voltage imaging (>200 Hz), required trade-offs in spatial resolution, making distinguishing single

cells in the functional imaging data difficult. This is further complicated by the fact that RVF5 efficiently stains all membranes, obscuring the assignment of fluorescence signals to single cells. Despite this challenge, at our current resolution and speed, we can clearly observe distinct firing patterns even in adjacent pixels (**Figure 2.16c-f**, Tsc1 KO traces), providing sub-10 μm resolution of neuronal activity at a rate of approximately 200 Hz. These results demonstrate the utility of RVF5 for profiling neuronal activity in the context of thick, opaque tissues.

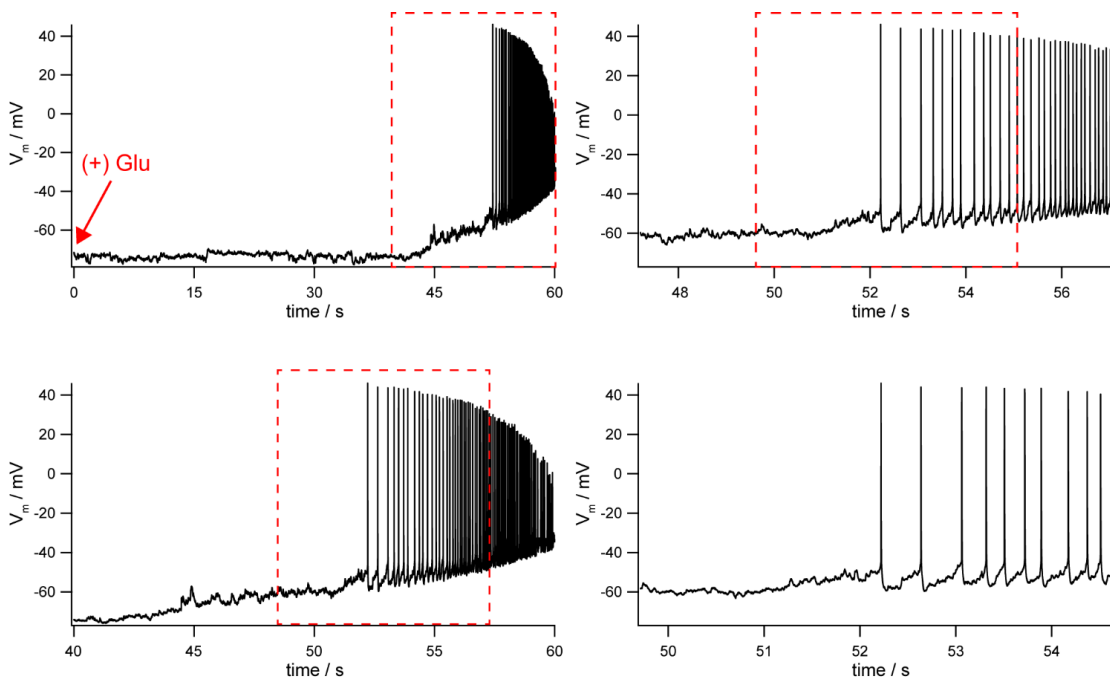


Figure 2.17. Whole-cell electrophysiological recordings from a CA1 neuron in the mouse hippocampus. Bath application of glutamate (Glu, 5 mM) results in robust spiking. Expanded time scales are shown, beginning in the upper left and proceeding in a counter-clockwise direction.

2.5 Conclusions and Future Outlook

In summary, we present the design, synthesis, and applications of RVF5, a PeT-based molecular wire voltage-sensitive dye that features a rhodol scaffold for improved photostability and two photon absorption. Under both 1P and 2P illumination, RVF5 shows good voltage sensitivity and improved photostability when compared to first-generation VF dyes. Additionally, we demonstrate, for the first time, that PeT-based voltage sensors efficiently report membrane potential dynamics under two photon illumination.

Incorporation of a rhodol fluorophore into a molecular wire voltage-sensing platform dramatically improves the two photon performance of VF-type dyes. Under two photon illumination, RVF5 displays an approximately 4-fold increase in two photon absorption cross section (20-fold in two photon excitation brightness) relative to VF2.1.Cl, while maintaining high voltage sensitivity. Previous studies on the 2P voltage sensitivity of both small molecule⁴⁵ and genetically encoded voltage indicators²⁴ reveal that the voltage sensing behavior under 2P illumination is not always identical to properties under 1P illumination. This study provides evidence that the voltage

sensitivity of RVF5 is largely similar under both 1P and 2P conditions ($28\pm 1\%$ vs. $24\pm 7\%$ $\Delta F/F$ per 100 mV, respectively).

Small molecule voltage-sensitive dyes have been previously employed under 2P illumination conditions.⁴⁶ However, styryl dyes used in these studies typically have σ_{TPA} values in the range of 5-10 GM, and maximal voltage sensitivity is only achieved by excitation at the very far edge of the 1P excitation spectrum,^{45, 47} necessitating the loss of many incident photons and increasing photo-toxicity. In contrast, PeT-based probes, like RVF5, can be excited at or near their excitation peaks, maximizing the useful number of photons delivered to tissue. This mitigates phototoxicity and is critically important for voltage imaging, because the high optical sampling rates required to image fast spiking events restrict photon collection time, severely hampering sensitivity.

The improved photostability of RVF5 enables long-term recording of network activity with cellular resolution in a mouse model of epilepsy disorder TSC. Our voltage imaging results are consistent with MEA recordings and further reveal that *Tsc1* KO alters network properties by increasing the proportion of highly active cells relative to WT neurons. Simultaneously, voltage imaging with RVF5 provides a means to correlate recorded activity to individual cells for post hoc analysis (e.g. for cell type confirmation). Finally, the increased two photon absorption cross section of RVF5 enables deep tissue imaging of voltage dynamics in hippocampal brain slices. Studies are underway to improve cell-type staining and understand the contributions membrane potential fluctuations make to neurological disease, especially in the context of genetic epilepsy disorders.

2.6 Methods and Materials

General method for chemical synthesis and characterization

Chemical reagents and anhydrous solvents were purchased from commercial suppliers and used without further purification. All reactions were carried out in oven-dried flasks under an inert atmosphere of N_2 . Thin layer chromatography (TLC) (Silicycle, F254, 250 μm) was performed on glass backed plates pre-coated with silica gel and were visualized by fluorescence quenching under UV light. Flash column chromatography was performed on Silicycle Silica Flash F60 (230–400 Mesh) using a forced flow of air at 0.5–1.0 bar. NMR spectra were measured on a Bruker AV-600 MHz, 150 MHz. Chemical shifts are expressed in parts per million (ppm) and are referenced to *d*₆-DMSO, 2.50 ppm. Coupling constants are reported as Hertz (Hz). Splitting patterns are indicated as follows: s, singlet; d, doublet; sep, septet; dd, doublet of doublet; ddd, doublet of doublet of doublet; dt, doublet of triplet; td, triplet of doublet; m, multiplet. High-resolution mass spectra (ESI EI) were measured by the QB3/Chemistry mass spectrometry service at University of California, Berkeley. High performance liquid chromatography (HPLC) and low resolution ESI Mass Spectrometry were performed on an Agilent Infinity 1200 analytical instrument coupled to an Advion CMS-L ESI mass spectrometer. Columns used for the analytical and semi-preparative HPLC were Phenomenex Luna C18(2) (4.6 mm I.D. \times 150 mm) and Phenomenex Luna 5 μ C18(2) (10 mm I.D. \times 150 mm) columns with a flow rate of 1.0 and 3.0 mL/min, respectively. The mobile phase were MQ-H₂O with 0.05% formic acid (eluent A) and HPLC grade acetonitrile with 0.05% formic acid (eluent B). Signals were monitored at 254 and 460 nm in 20 min with gradient 5-100% eluent B.

Spectroscopic studies

Stock solutions of RVF5 were prepared in DMSO (1.0–10 mM) and diluted with PBS (100 mM Na_2HPO_4 , pH 7.4, 0.1% Triton-X). UV-Vis absorbance and fluorescence spectra were recorded

using a Shimadzu 2501 Spectrophotometer (Shimadzu) and a Quantamaster Master 4 L-format scanning spectrofluorometer (Photon Technologies International). The fluorometer is equipped with an LPS-220B 75-W xenon lamp and power supply, A- 1010B lamp housing with integrated igniter, switchable 814 photon-counting/analog photomultiplier detection unit, and MD5020 motor driver. Samples were measured in 1-cm path length quartz cuvettes (Starna Cells).

Measurement of Two-Photon Cross Section

The two-photon excitation (TPE) cross section of RVF5 was determined according to procedures described in the literature.⁴⁸⁻⁵⁰ We first measured the fluorescence signal generated by the two-photon absorbance (TPA) and the following equation:

$$\sigma_{TPE} = \eta_2 * \sigma_{TPA}$$

Where η_2 is the two-photon fluorescence quantum yield of RVF5. However, the measured fluorescence depends strongly on several factors regarding the optical field, such as temporal coherence. Accurately calculating the TPE cross section requires knowledge of these factors. The complications of determining these factors were avoided by using either fluorescein or rhodamine B, fluorophores of known TPE cross section and spectra, as a standard calibration sample. Fluorescence signals from RVF5 were calibrated relative both to the fluorescence of fluorescein and rhodamine b; i.e. the ratio of measured fluorescence signals determined the value of the σ_{TPA} for RVF5. This was performed by preparing samples at the same concentration of fluorophore and using the same incident power for both samples. Then, by assuming that the two-photon fluorescence quantum yield is the same as the one-photon fluorescence quantum yield and that the fluorescence collecting efficiency of the microscope is equal for fluorescein and RVF5, σ_{TPE} at each wavelength for RVF5 was calculated using the following equation:

$$\sigma_{TPE RVF5} = \frac{\varphi_{fluo} * \sigma_{TPE fluo}}{\varphi_{RVF5}} * \frac{F_{RVF5}}{F_{fluo}}$$

Where F_{RVF5} and F_{fluo} are the measured fluorescence signal from RVF5 and fluorescein or rhodamine b, respectively. The values for σ_{TPE} at different wavelengths for fluorescein and rhodamine b were obtained from Albota, et al.⁴⁹

Two-photon absorbance cross section (σ_{TPA}) measurements were obtained by comparison to fluorescein standards, as previously reported.⁴⁹ A brief explanation follows.

Two photon absorbance (TPA) cross section (σ_{TPA}) is difficult to determine directly because it requires measuring the amount of light absorbed in a two-photon process, which is negligible relative to high incident power needed to generate a two-photon signal. A generally accepted alternative is to measure the two photon excitation (TPE) cross section σ_{TPE} , which is the product of the two-photon quantum efficiency (η_2) and σ_{TPA} .

The photons detected during fluorescence emission from a sample or calibrant is related to the intrinsic properties of the dye as well as the instrumentation and optics, in the following manner:

$$\frac{F(t)_{cal} = \phi_{cal} \eta_{2cal} \sigma_{TPAcal} C_{cal} (P_{cal}(t))^2 n_{cal}}{F(t)_{new} = \phi_{new} \eta_{2new} \sigma_{TPAnew} C_{new} (P_{new}(t))^2 n_{new}} \quad (1)$$

where $F(t)$ is the photons collected, ϕ is the fluorescence collection efficiency of the instrument, η_2 is the two-photon quantum fluorescence quantum yield, C is the concentration of dye, $P(t)^2$ is the time-averaged power of the incident illumination, and n is the refractive index of solution. The σ_{TPE} of a new fluorophore can then be determined in the following manner:

$$\eta_{2new} \sigma_{TPAnew} = \eta_{2cal} \sigma_{TPAcal} \frac{\phi_{cal} C_{cal}}{\phi_{new} C_{new}} \frac{\langle P_{cal}(t) \rangle^2 n_{cal}}{\langle P_{new}(t) \rangle^2 n_{new}} \frac{F(t)_{new}}{F(t)_{cal}} \quad (2)$$

Assuming that the collection efficiency (ϕ), power ($P(t)^2$), and refractive index (n) remain constant across samples, and that $\eta_2 = \eta_1$ (quantum yield under one photon illumination), the σ_{TPA} for a given fluorophore (in this case RVF5) can be determined by comparison to fluorescein, using the following relationship:

$$\sigma_{TPA-RVF5} = \frac{\eta_{2-fluorescein} \sigma_{TPA-fluorescein}}{\eta_{2-RVF5}} \frac{F(t)_{RVF5}}{F(t)_{fluorescein}} \quad (3)$$

Cell Culture and Brain Slice Preparation

All animal procedures were approved by the UC Berkeley Animal Care and Use Committees and conformed to the NIH Guide for the Care and Use of Laboratory Animals and the Public Health Policy.

Human embryonic kidney 293T (HEK) cells were passaged and plated onto 12 mm glass coverslips pre-coated with Poly-D Lysine (PDL; 1 mg/ml; Sigma-Aldrich) to provide a confluency of ~15% and 50% for electrophysiology and imaging, respectively. HEK cells were plated and maintained in Dulbecco's modified eagle medium (DMEM) supplemented with 4.5 g/L D-glucose, 10% FBS and 1% Glutamax.

Primary dissociated hippocampal cultures were prepared from P0-P1 *Tsc1^{fl/fl}* mice⁵¹ using standard protocols⁵². Neurons were counted using a hemocytometer and plated at $0.8-1 \times 10^5$ cells per well into 24-well plates containing Poly-D Lysine (PDL – Sigma P7886-50mg) and Laminin (Gibco – 23017015) coated acid-washed coverslips (Fisher Scientific – 12-545-82). Neuronal cultures were maintained in Neurobasal media (Gibco 21103-049) supplemented with glutamine, pen/strep, and B-27 supplement (Gibco – 17504-044) with one third media changes every 4 days. Custom adenoassociated virus (AAV) expressing mCherry-tagged Cre recombinase from the CBA promoter was prepared by the Penn Vector Core and added to half of the wells at 2 days *in vitro* (DIV) to knock out the *Tsc1* gene. Functional imaging was performed on mature neurons at 13-20 DIV. Electrophysiological experiments were performed at 12-15 DIV.

Coronal slices containing cortex (275 μ m thick) or hippocampus (300 μ m), were prepared from P14-P16 (cortex) or P27-30 (hippocampus) *Tsc1^{fl/fl}* mice.⁵¹ Slices were cut in an ice-cold choline-based external solution and transferred to 34°C ACSF for a 15 minute recovery. Slices were then incubated for 30 minutes in oxygenated, room-temperature ACSF with 10 μ M RVF5 (from a 100x stock in DMSO). The slice was transferred to a slide chamber, perfused with oxygenated, room-temperature ACSF for 2P recording. Spontaneous activity was recorded for 6000 frames at 5ms/frame. Action potentials were driven by adding 5mM L-glutamic acid (Tocris – 0218, final concentration) to the ACSF. Neurons were reimaged for 12,000 frames at 5ms/frame following L-glutamic acid perfusion.

Stereotaxic injections into mouse brain

Unilateral stereotaxic injections into the CA1 region of the hippocampus were done at M/L +/- 3.4mm, A/P -3.0mm, and D/V-2.3 relative to Bregma. The left hemisphere was injected with 1 μ L of AAV-mCherry-Cre (1.04×10^{13} genome copy/mL). The right hemisphere was injected with 1 μ L of sterile saline as a sham control. Injections were performed in P13-P15 mice. Mice were used for experiments 13-16 days following viral injection.

Imaging Parameters

Epifluorescence imaging was performed on an AxioExaminer Z-1 (Zeiss) equipped with a Spectra-X Light engine LED light (Lumencor), controlled with Slidebook (v6, Intelligent Imaging

Innovations). Images were acquired with either a W-Plan-Apo 20x/1.0 water objective (20x; Zeiss) or a W-Plan-Apo 63x/1.0 water objective (63x; Zeiss). Images were focused onto either an OrcaFlash4.0 sCMOS camera (sCMOS; Hamamatsu) or an eVolve 128 EMCCD camera (EMCCD; Photometrix).

Two-photon imaging was performed with either a Zeiss LSM 780 NLO AxioExaminer or a Zeiss LSM 880 NLO AxioExaminer equipped with either a Mai Tai HP Laser (Spectra Physics) or a Chameleon Ultra I laser (Coherent Inc.) Fluorescence images were acquired using a Zeiss BiG-2 GaAsP detector.

More detailed imaging information for each experimental application is expanded below.

Voltage sensitivity in HEK cells

Functional imaging of RVF5 was performed using a 20x objective paired with image capture from the EMCCD camera at a sampling rate of 0.5 kHz. RVF5 was excited using the 488 nm LED with an intensity of 2.5 W/cm². For initial voltage characterization emission was collected with the QUAD filter (430/32, 508/14, 586/30, 708/98 nm) after passing through a quadruple dichroic mirror (432/38, 509/22, 586/40, 654 nm LP). For two-photon voltage sensitivity, RVF5 was excited using 820 nm light with a laser attenuation percentage of 4% and the emission was collected using the Zeiss BiG-2 detector with a 690+ dichroic.

Imaging groups of cells

Imaging experiments looking for functional responses from many (>5) neurons required a larger field of view which were obtained using the sCMOS camera with a 20x objective. RVF5 was excited using a 475 nm LED with an intensity of 2.3 W/cm² and emission was collected with a QUAD filter. Images were binned 4x4 to allow sampling rates of 0.25 kHz. To identify Tsc1 knockout neurons, mCherry was excited by the 540 nm LED and emission was collected with the QUAD filter and dichroic.

Imaging of RVF5 in patch-clamped hippocampal neurons

Functional imaging of patched neurons was performed using a sCMOS camera and a 20x objective. This objective has a larger working distance and allowed for positioning of the patch electrode. RVF5 was excited using a 488 nm LED with an intensity of 2.5 W/cm² and emission was collected with QUAD filter and dichroic. For optical assessment of the action potential waveform the sampling rate was increased to 1.0 kHz.

Imaging of RVF5 in brain slices

Imaging experiments in brain slices were performed using the Zeiss LSM 880 AxioExaminer equipped with a BiG-2 detector with a 690+ dichroic. RVF5 was excited using 820 nm light with a laser attenuation percentage between 2 and 5%. The brain slices were loaded with dye via incubation in oxygenated ACSF with 10 μM RVF5 and 0.1% DMSO. The slices were then transferred to a perfusion chamber and perfused with a constant supply of oxygenated, room temperature ACSF at a drip rate of 3 mL/minute. In order to evoke electrophysiological activity, perfusion was switched to ACSF with 5 mM glutamate while a small area was imaged in a 64x8 array at an exposure time of 4.95 ms per frame.

Electrophysiology

For electrophysiological experiments, pipettes were pulled from borosilicate glass (Sutter Instruments, BF150-86-10), with a resistance of 5–8 MΩ, and were filled with an internal solution; (in mM) 115 potassium gluconate, 10 BAPTA tetrapotassium salt, 10 HEPES, 5 NaCl, 10 KCl, 2 ATP disodium salt, 0.3 GTP trisodium salt (pH 7.25, 275 mOsm).

Recordings were obtained with an Axopatch 200B amplifier (Molecular Devices) at room temperature. The signals were digitized with Digidata 1332A, sampled at 50 kHz and recorded with pCLAMP 10 software (Molecular Devices) on a PC. Fast capacitance was compensated in the on-cell configuration. For all electrophysiology experiments, recordings were only pursued if series resistance in voltage clamp was less than 30 M Ω . For whole-cell, voltage clamp recordings in HEK 293T cells, cells were held at -60 mV and 100 ms hyper- and de-polarizing steps applied from -100 to +100 mV in 20 mV increments. For whole-cell, current clamp recordings in hippocampal neurons, following membrane rupture, resting membrane potential was assessed and recorded at $I = 0$ and monitored during the data acquisition. Neurons were switched to current clamp mode if they displayed series resistance in voltage clamp less than 30 megaohms. Pipette tip resistance was corrected by performing a bridge balance compensation.

To test if loading RVF5 onto the membrane of neurons has any effect on action potential firing, ten 500 ms current steps were injected into neurons in increments of 0.05 pA. The action potentials for each sweep were analyzed in Clampfit 10 software (Molecular Devices) to give amplitude and kinetic data.

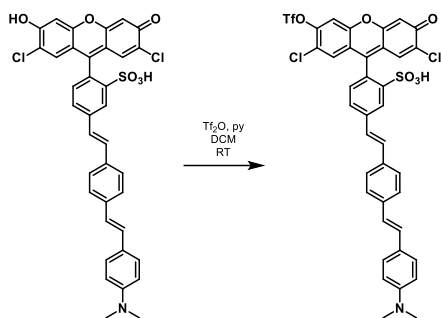
Image analysis

Analysis of voltage sensitivity in HEK cells was performed using custom Matlab routines. Briefly, a region of interest (ROI) was selected automatically based on fluorescence intensity and applied as a mask to all image frames. Fluorescence intensity values were calculated at known baseline and voltage step epochs. For analysis of RVF5 voltage responses in neurons, regions of interest encompassing cell bodies were drawn in ImageJ and the mean fluorescence intensity for each frame extracted. The photostability of RVF5 means that over short traces, no or minor linear bleach correction was required. For longer experiments (40 sec), the bleaching was corrected using the automatic baseline correction in Clampfit 10 (Molecular Devices).

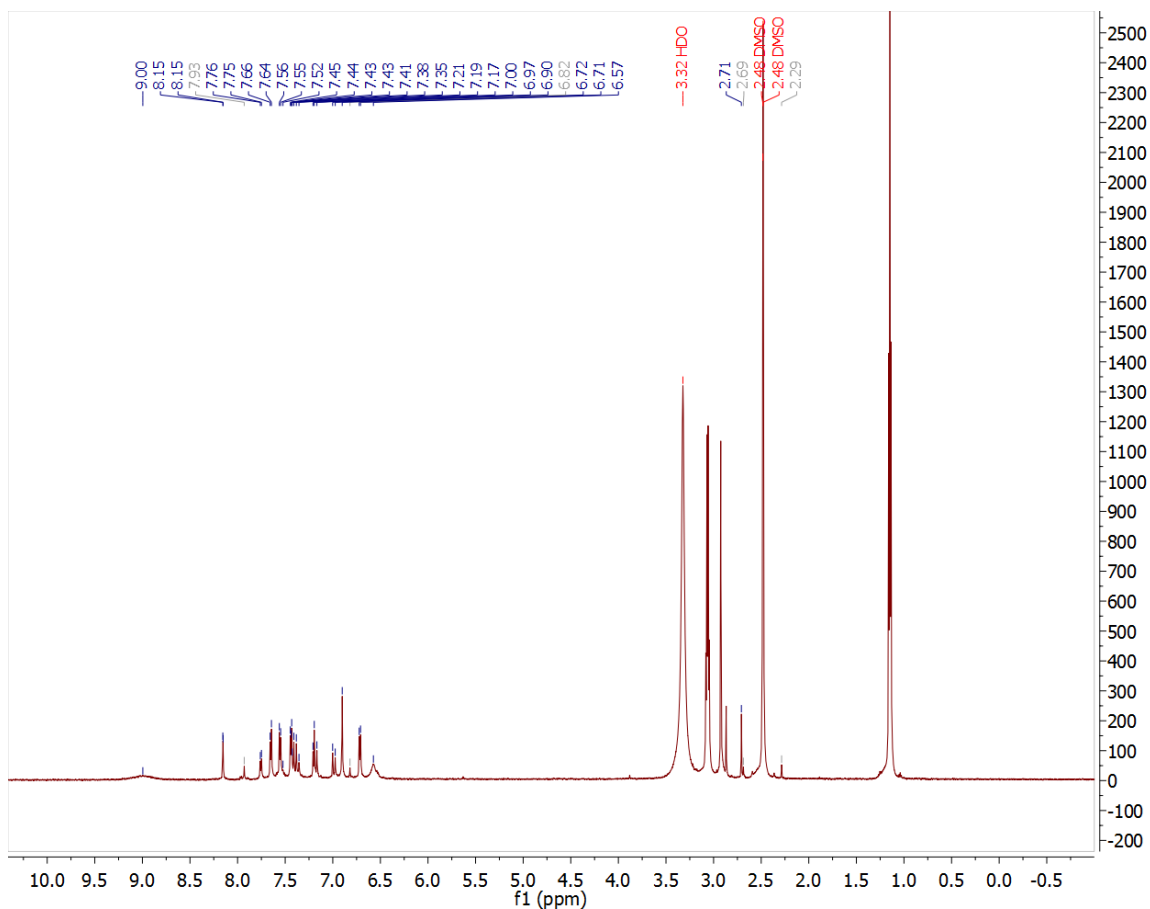
For detection of action potentials recorded electrophysiologically and optically, imaging traces were analyzed using threshold-based spike detection algorithms in the Clampfit 10 software (Molecular Devices).

For automated spike detection, a custom Matlab routine (“SpikeMapper”, which is available upon request, please email evanwmiller@berkeley.edu) was employed. In summary, a TIFF stack was imported into Matlab and the intensity values for each pixel, or if desired, a user-designated block of pixels, was extracted. The intensity over time for each block was then baseline corrected by fitting to a 2nd degree polynomial and then each block was heat-mapped by counting the number of frames that the intensity of the block at any particular time exceeds the standard deviation (3x of the intensity values over the entire trace). Cells were selected by drawing regions of interest around “active” blocks of pixels, outputting the bleach-corrected trace as an Excel file and spike times as a text file.

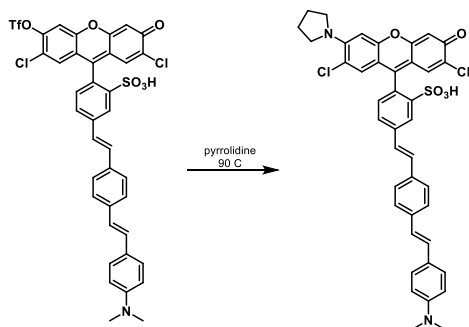
Synthetic Details



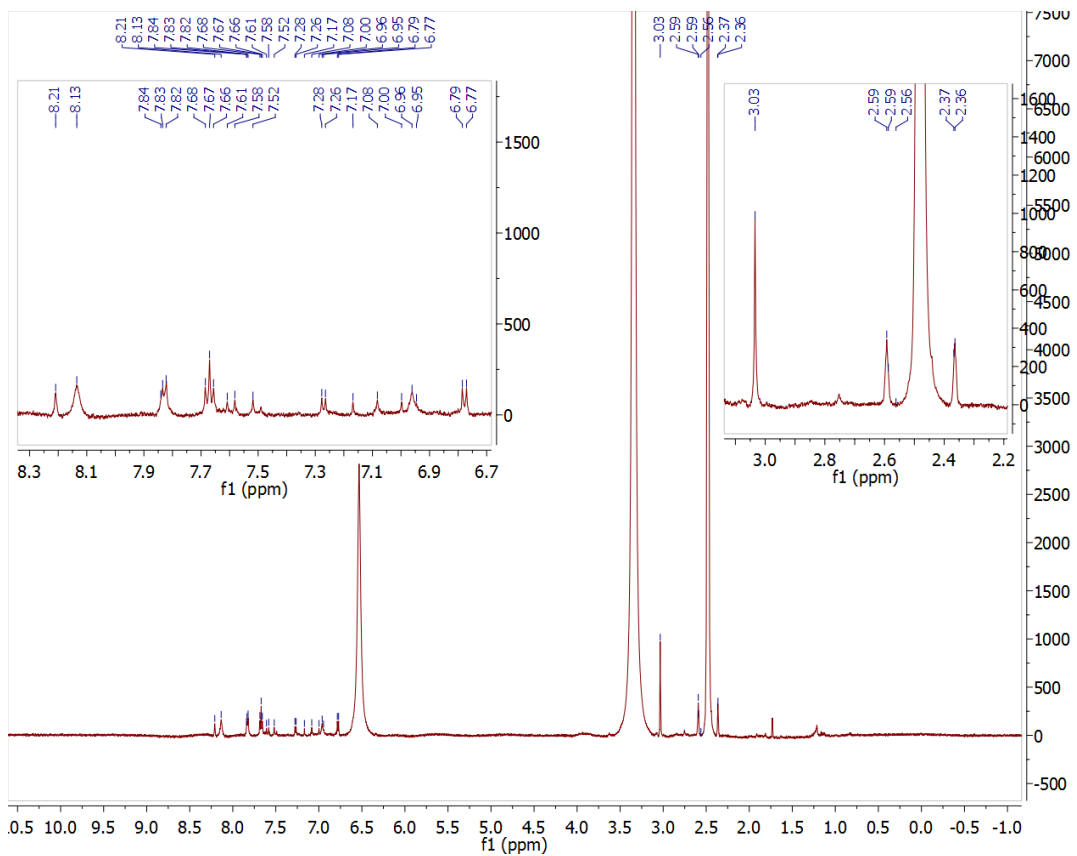
VF2.1.Cl (0.1 g, 0.28 mmol) was suspended in CH_2Cl_2 (5 mL) and cooled to 0 °C. Pyridine (2 mL) and trifluoromethanesulfonic anhydride (0.3 mL) were added dropwise, and the ice bath was removed. The yellow-red color of the solution disappeared as triflic anhydride was added. The reaction was stirred at room temperature for 2 hours. It was subsequently diluted with water and extracted with CH_2Cl_2 (2×). The combined organic extracts were washed 3 times (brine, 1 M HCl), dried (MgSO_4), filtered, and concentrated in vacuo. Product was run over a thin silica plug in 100% CH_2Cl_2 and then concentrated via rotary evaporation. The product Tf-VF2.1.Cl was isolated as a light brown solid (83 mg, 69.6%). ^1H NMR (600 MHz, DMSO-d_6) δ 8.15 (d, $J = 1.8$ Hz, 1H), 7.78 – 7.72 (m, 1H), 7.65 (d, $J = 8.1$ Hz, 2H), 7.55 (d, $J = 8.1$ Hz, 4H), 7.43 (dd, $J = 7.0, 4.7$ Hz, 2H), 7.42 – 7.35 (m, 2H), 7.22 – 7.14 (m, 2H), 6.99 (d, $J = 16.3$ Hz, 1H), 6.90 (s, 2H), 6.72 (d, $J = 8.5$ Hz, 2H), 2.92 (s, 6H). (ESI-HR, Calculated: 814.0429, Determined: 814.0634)



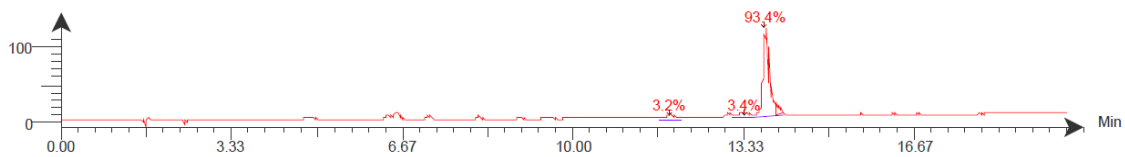
¹H NMR of Tf-VF2.1.Cl



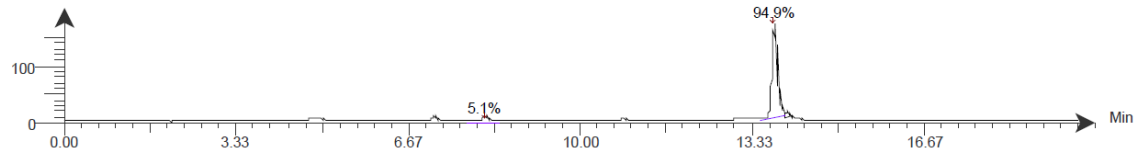
A (25 mg) was added to pyrrolidine (1 mL) and stirred at 90 °C overnight. Upon addition, a deep orange color developed immediately. The reaction mixture was then dried under high vacuum and taken up in 0.5 mL of DMSO. The product was then isolated by RP-HPLC to give an orange solid (6 mg, 26.6%). ¹H NMR (600 MHz, DMSO-d₆) δ 8.21 (s, 1H), 7.83 (d, J = 7.3 Hz, 4H), 7.67 (t, J = 8.6 Hz, 3H), 7.59 (d, J = 15.9 Hz, 2H), 7.52 (s, 1H), 7.27 (d, J = 7.8 Hz, 1H), 7.17 (s, 1H), 7.08 (s, 1H), 7.00 (s, 1H), 6.96 (s, 2H), 6.78 (d, J = 8.6 Hz, 2H), 3.03 (s, 6H), 2.59 (d, J = 3.3 Hz, 4H), 2.37 (d, J = 2.4 Hz, 4H). (ESI-HR, Calculated: 735.1593, Determined: 735.1803)



¹H NMR of RVF5



254 nm LCMS of RVF5



460 nm LCMS of RVF5

2.7 References

1. Spira ME & Hai A (2013) Multielectrode array technologies for neuroscience and cardiology. *Nat Nanotechnol* 8(2):83-94.
2. Scanziani M & Hausser M (2009) Electrophysiology in the age of light. *Nature* 461(7266):930-939.
3. Peterka DS, Takahashi H, & Yuste R (2011) Imaging voltage in neurons. *Neuron* 69(1):9-21.
4. Miller EW (2016) Small molecule fluorescent voltage indicators for studying membrane potential. *Curr Opin Chem Biol* 33:74-80.
5. Davila HV, Salzberg BM, Cohen LB, & Waggoner AS (1973) A large change in axon fluorescence that provides a promising method for measuring membrane potential. *Nat New Biol* 241(109):159-160.
6. Braubach O, Cohen LB, & Choi Y (2015) Historical Overview and General Methods of Membrane Potential Imaging. *Membrane Potential Imaging in the Nervous System and Heart, Advances in Experimental Medicine and Biology*, eds Canepari M, Zecevic D, & Bernus O, 859, pp 3-26.
7. Yan P, et al. (2012) Palette of fluorinated voltage-sensitive hemicyanine dyes. *Proc Natl Acad Sci U S A* 109(50):20443-20448.
8. Kuhn B & Fromherz P (2003) Anellated hemicyanine dyes in a neuron membrane: Molecular Stark effect and optical voltage recording. *J Phys Chem B* 107(31):7903-7913.
9. Hubener G, Lambacher A, & Fromherz P (2003) Anellated hemicyanine dyes with large symmetrical solvatochromism of absorption and fluorescence. *J Phys Chem B* 107(31):7896-7902.
10. Treger JS, Priest MF, Iezzi R, & Bezanilla F (2014) Real-Time Imaging of Electrical Signals with an Infrared FDA-Approved Dye. *Biophysical Journal* 107(6):L9-L12.
11. Fink AE, Bender KJ, Trussell LO, Otis TS, & DiGregorio DA (2012) Two-photon compatibility and single-voxel, single-trial detection of subthreshold neuronal activity by a two-component optical voltage sensor. *PLoS One* 7(8):e41434.
12. Bradley J, Luo R, Otis TS, & DiGregorio DA (2009) Submillisecond optical reporting of membrane potential in situ using a neuronal tracer dye. *J Neurosci* 29(29):9197-9209.
13. Gonzalez JE & Tsien RY (1995) Voltage Sensing by Fluorescence Resonance Energy-Transfer in Single Cells. *Biophysical Journal* 69(4):1272-1280.
14. Sjulson L & Miesenbock G (2008) Rational optimization and imaging in vivo of a genetically encoded optical voltage reporter. *J Neurosci* 28(21):5582-5593.
15. Chanda B, et al. (2005) A hybrid approach to measuring electrical activity in genetically specified neurons. *Nat Neurosci* 8(11):1619-1626.
16. Ghitani N, Bayguinov PO, Ma Y, & Jackson MB (2015) Single-trial imaging of spikes and synaptic potentials in single neurons in brain slices with genetically encoded hybrid voltage sensor. *J Neurophysiol* 113(4):1249-1259.
17. Reeve JE, et al. (2013) Porphyrins for probing electrical potential across lipid bilayer membranes by second harmonic generation. *Angew Chem Int Ed Engl* 52(34):9044-9048.
18. Park K, Deutsch Z, Li JJ, Oron D, & Weiss S (2012) Single molecule quantum-confined Stark effect measurements of semiconductor nanoparticles at room temperature. *ACS Nano* 6(11):10013-10023.
19. Marshall JD & Schnitzer MJ (2013) Optical Strategies for Sensing Neuronal Voltage Using Quantum Dots and Other Semiconductor Nanocrystals. *ACS Nano* 7(5):4601-4609.

20. Gong YY, et al. (2015) High-speed recording of neural spikes in awake mice and flies with a fluorescent voltage sensor. *Science* 350(6266):1361-1366.
21. St-Pierre F, et al. (2014) High-fidelity optical reporting of neuronal electrical activity with an ultrafast fluorescent voltage sensor. *Nat Neurosci* 17(6):884-889.
22. Hochbaum DR, et al. (2014) All-optical electrophysiology in mammalian neurons using engineered microbial rhodopsins. *Nature Methods* 11(8):825-833.
23. Jin L, et al. (2012) Single Action Potentials and Subthreshold Electrical Events Imaged in Neurons with a Fluorescent Protein Voltage Probe. *Neuron* 75(5):779-785.
24. Brinks D, Klein AJ, & Cohen AE (2015) Two-Photon Lifetime Imaging of Voltage Indicating Proteins as a Probe of Absolute Membrane Voltage. *Biophysical Journal* 109(5):914-921.
25. Li LS (2007) Fluorescence probes for membrane potentials based on mesoscopic electron transfer. *Nano Lett* 7(10):2981-2986.
26. Miller EW, et al. (2012) Optically monitoring voltage in neurons by photo-induced electron transfer through molecular wires. *Proc Natl Acad Sci U S A* 109(6):2114-2119.
27. Woodford CR, et al. (2015) Improved PeT molecules for optically sensing voltage in neurons. *J Am Chem Soc* 137(5):1817-1824.
28. Lavis LD & Raines RT (2008) Bright ideas for chemical biology. *ACS Chem Biol* 3(3):142-155.
29. Huang YL, Walker AS, & Miller EW (2015) A Photostable Silicon Rhodamine Platform for Optical Voltage Sensing. *J Am Chem Soc* 137(33):10767-10776.
30. Kim HM & Cho BR (2015) Small-Molecule Two-Photon Probes for Bioimaging Applications. *Chem Rev* 115(11):5014-5055.
31. Whitaker JE, Haugland RP, Ryan D, Hewitt PC, & Prendergast FG (1992) Fluorescent rhodol derivatives: versatile, photostable labels and tracers. *Anal Biochem* 207(2):267-279.
32. Weissleder R (2001) A clearer vision for in vivo imaging. *Nat Biotechnol* 19(4):316-317.
33. Drobizhev M, Makarov NS, Tillo SE, Hughes TE, & Rebane A (2011) Two-photon absorption properties of fluorescent proteins. *Nat Methods* 8(5):393-399.
34. Xu C, Zipfel W, Shear JB, Williams RM, & Webb WW (1996) Multiphoton fluorescence excitation: new spectral windows for biological nonlinear microscopy. *Proc Natl Acad Sci U S A* 93(20):10763-10768.
35. Makarov NS, Drobizhev M, & Rebane A (2008) Two-photon absorption standards in the 550-1600 nm excitation wavelength range. *Opt Express* 16(6):4029-4047.
36. Albota MA, Xu C, & Webb WW (1998) Two-photon fluorescence excitation cross sections of biomolecular probes from 690 to 960 nm. *Appl Optics* 37(31):7352-7356.
37. Fisher JA, Salzberg BM, & Yodh AG (2005) Near infrared two-photon excitation cross-sections of voltage-sensitive dyes. *J Neurosci Methods* 148(1):94-102.
38. Mutze J, et al. (2012) Excitation spectra and brightness optimization of two-photon excited probes. *Biophys J* 102(4):934-944.
39. Prather P & de Vries PJ (2004) Behavioral and cognitive aspects of tuberous sclerosis complex. *J Child Neurol* 19(9):666-674.
40. Fryer AE, et al. (1987) Evidence that the gene for tuberous sclerosis is on chromosome 9. *Lancet* 1(8534):659-661.
41. Cheadle JP, Reeve MP, Sampson JR, & Kwiatkowski DJ (2000) Molecular genetic advances in tuberous sclerosis. *Hum Genet* 107(2):97-114.
42. Kwiatkowski DJ & Manning BD (2005) Tuberous sclerosis: a GAP at the crossroads of multiple signaling pathways. *Hum Mol Genet* 14:R251-R258.

43. Bateup HS, et al. (2013) Excitatory/Inhibitory Synaptic Imbalance Leads to Hippocampal Hyperexcitability in Mouse Models of Tuberous Sclerosis. *Neuron* 78(3):510-522.
44. Kwiatkowski DJ, et al. (2002) A mouse model of TSC1 reveals sex-dependent lethality from liver hemangiomas, and up-regulation of p70S6 kinase activity in Tsc1 null cells. *Hum Mol Genet* 11(5):525-534.
45. Kuhn B, Fromherz P, & Denk W (2004) High sensitivity of Stark-shift voltage-sensing dyes by one- or two-photon excitation near the red spectral edge. *Biophys J* 87(1):631-639.
46. Fisher JAN, et al. (2008) Two-photon excitation of potentiometric probes enables optical recording of action potentials from mammalian nerve terminals in situ. *J Neurophysiol* 99(3):1545-1553.
47. Loew LM (2015) Design and Use of Organic Voltage Sensitive Dyes. *Membrane Potential Imaging in the Nervous System and Heart, Advances in Experimental Medicine and Biology*, eds Canepari M, Zecevic D, & Bernus O, 859, pp 27-53.
48. Xu C & Webb WW (1996) Measurement of two-photon excitation cross sections of molecular fluorophores with data from 690 to 1050 nm. *J Opt Soc Am B* 13(3):481-491.
49. Albota MA, Xu C, & Webb WW (1998) Two-photon fluorescence excitation cross sections of biomolecular probes from 690 to 960 nm. *Appl Optics* 37(31):7352-7356.
50. Xu C, Zipfel W, Shear JB, Williams RM, & Webb WW (1996) Multiphoton fluorescence excitation: new spectral windows for biological nonlinear microscopy. *Proc Natl Acad Sci U S A* 93(20):10763-10768.
51. Kwiatkowski DJ, et al. (2002) A mouse model of TSC1 reveals sex-dependent lethality from liver hemangiomas, and up-regulation of p70S6 kinase activity in Tsc1 null cells. *Hum Mol Genet* 11(5):525-534.
52. Beaudoin GMJ, et al. (2012) Culturing pyramidal neurons from the early postnatal mouse hippocampus and cortex. *Nat Protoc* 7(9):1741-1754.

Chapter 3

In vivo Voltage Imaging Using a Sulfonated Rhodamine Voltage Reporter

ABSTRACT

Optical methods that rely on fluorescence for mapping changes in neuronal membrane potential in the brains of awake animals provide a powerful way to interrogate the activity of neurons that underlie neural computations ranging from sensation and perception to learning and memory. To achieve this goal, fluorescent indicators should be bright, highly sensitive to small changes in membrane potential, non-toxic, and excitable with infra-red light. We report a new class of fluorescent, voltage-sensitive dyes: sulfonated Rhodamine Voltage Reporters (sRhoVR), synthetic fluorophores with high voltage sensitivity, excellent two-photon performance, and compatibility in intact mouse brains. sRhoVR dyes are based on a tetramethyl rhodamine fluorophore coupled to a phenylenevinylene molecular wire/diethyl aniline voltage-sensitive domain. When applied to cells, sRhoVR dyes localize to the plasma membrane and respond to membrane depolarization with a fluorescence increase. The best of the new dyes, sRhoVR 1, displays a 44% $\Delta F/F$ increase in fluorescence per 100 mV change, emits at 570 nm, and possesses excellent two-photon absorption of approximately 200 GM at 840 nm. sRhoVR 1 can detect action potentials in cultured rat hippocampal neurons under both single- and two-photon illumination with sufficient speed and sensitivity to report on action potentials in single trials, without perturbing underlying physiology or membrane properties. The combination of speed, sensitivity and brightness under two-photon illumination makes sRhoVR 1 a promising candidate for *in vivo* imaging in intact brains. We show sRhoVR powerfully complements electrode-based modes of neuronal activity recording in the mouse brain by recording neuronal transmembrane potentials from the neuropil of layer 2/3 of the mouse barrel cortex in concert with extracellularly recorded local field potentials (LFPs). sRhoVR imaging reveals robust depolarization in response to whisker stimulation; concurrent electrode recordings reveal negative deflections in the LFP recording, consistent with the canonical thalamocortical response. Importantly, sRhoVR 1 can be applied in mice with chronic optical windows, presaging its utility in dissecting and resolving voltage dynamics using two-photon functional imaging in awake, behaving animals.

3.1 *In vivo* Voltage Imaging and Electrophysiology

Emergent brain properties arise from the coordinated firing of neurons. The flux of ions in and out of these specialized cells give rise to transmembrane potentials fluctuations. Intracellular electrophysiological recordings provide the most accurate determination of membrane potential in single neurons, offering resolution of large action potential spikes or even synaptic currents, but are difficult to implement in parallel (i.e. more than one neuron) for measurements of circuit activity *in vivo*.¹ A partial solution to the problem of recording from large numbers of neurons intracellularly is to record extracellular potentials resulting from transmembrane ionic currents in neuronal populations.² These extracellular electrical signals, reflecting contributions from multiple neurons, have the advantage that they can be readily obtained *in vivo* and modern fabrication methods enable massively multiplexed recordings.^{3, 4}

The slow component of the extracellularly recorded signals, local field potentials, or LFPs, provide an integration of the synaptic events of large numbers of neurons, enabling high density recordings across a variety of species for use in understanding fundamental neurobiology and driving brain-machine interfaces. Despite the utility of LFP recordings for measuring ensemble neuronal activity in diverse brain contexts, they suffer from ambiguity in interpretation of the underlying membrane potential dynamics. For example, excitatory inputs and depolarization close to the cortical surface can produce the same LFP as inhibitory inputs and hyperpolarization in deep cortical layers. Resolving this ambiguity requires prior knowledge of underlying neuronal architecture and physiology, complementary functional imaging approaches, and computational models. Further, LFP signals in cerebral cortex lack a true depth resolution, because a signal recorded from the surface can arise due to synaptic inputs to the deep layers and vice versa.⁵

Fluorescence imaging of neuronal activity with offers a promising strategy for complementing LFP recordings. LFP recordings have been combined with activity imaging using both small molecule^{6, 7} and genetically encoded^{8, 9} Ca²⁺ indicators as well as small molecule^{10, 11} and genetically encoded voltage indicators.¹² Voltage imaging with voltage-sensitive fluorescent indicators provides a direct readout of the local transmembrane potential and an important complement for interpreting LFPs. However, most studies employ single-photon excitation coupled with widefield, epifluorescence imaging in the cortex. This type of imaging results in depth-averaged voltage signals that lack the depth resolution require to calibrate the interpretation of LFP.¹⁰⁻¹⁴ Additionally, the use of powerful electrochromic voltage-sensitive dyes like the popular RH-1691 or RH-1692¹⁵⁻¹⁷ compounds requires off-peak excitation and emission, resulting in approximately 99% photon loss compared to on-peak dye excitation and emission.¹⁸ A recent study employed a genetically encoded voltage indicator targeted to defined cells, coupled with single-photon fiber photometry, to optically measure transmembrane potential in concert with electrophysiological field recordings.¹⁹ By constraining indicator expression to specific cells, some depth resolution could be achieved, even in the absence of an imaging approach. We envisioned that two-photon imaging with untargeted voltage sensitive dyes would offer a generalizable approach, without the need for transgenic animals. In contrast to single-photon excitation, two-photon excitation offers optical sectioning due to a sharp fall of fluorescence intensity with distance from the focal plane. Therefore, to achieve the full potential of voltage imaging, especially in the context of existing technologies for recording extracellularly from large populations of neurons, requires indicators that are bright, excellent two-photon absorbers, highly voltage sensitive, and efficient with excitation and emission photons.

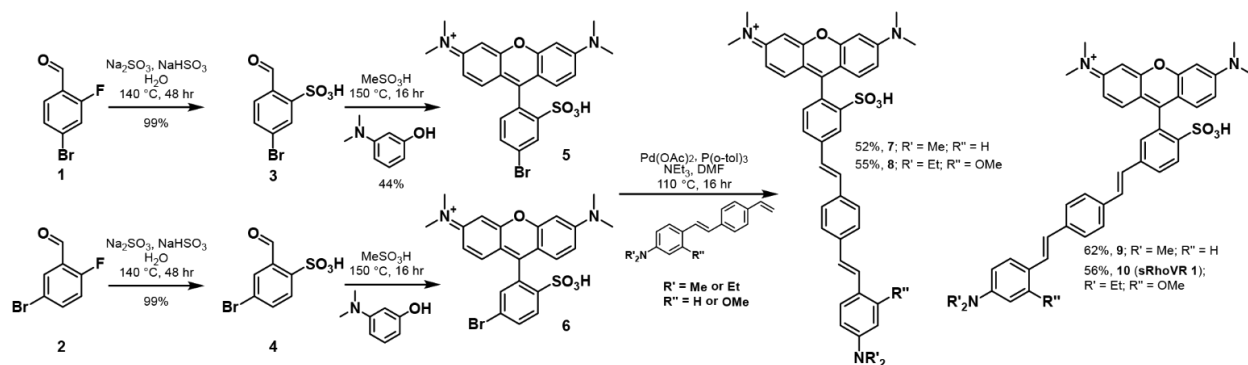
To address these challenges, we recently initiated a program to develop voltage-sensitive fluorescent indicators with sufficient speed, sensitivity, and brightness to monitor rapid changes in membrane potential. Our strategy relies on the use of photoinduced electron transfer, or PeT, as a voltage-sensitive trigger. Voltage-sensitive fluorophores, which we generically refer to as VoltageFluors or VF dyes, are designed to partition into the outer leaflet of the plasma membrane. Their fluorescence is diminished when cells are hyperpolarized. Correspondingly, when cells depolarize, VF fluorescence brightens. We hypothesize this is a result of the changing transmembrane electrochemical potential altering the rate of PeT and therefore modulating fluorescence.²⁰ Consistent with this hypothesis, VF dyes display rapid response kinetics, enabling them to detect action potentials in single-trial optical recordings, possess sensitivities of up to 63% $\Delta F/F$ per 100 mV,²¹ can be tuned across a range of wavelength spanning the color palette from blue to far-red,²²⁻²⁵ and operate efficiently using two-photon illumination.²³

A recent VF dye based on a rhodol chromophore, RhodolVoltageFluor-5, or RVF5, made use of a chlorinated, pyrrolidine-based rhodol. RVF5 possessed good photostability and voltage sensitivity, enabling detection of action potentials in cultured hippocampal neurons under conventional wide-field illumination and spiking events in mouse brain slices using two-photon illumination.²³ Building on this result, we wondered whether we could access VF dyes that made use of fluorophores with even higher two-photon absorption cross sections and even longer wavelength emission for use in *in vivo* applications. In this regard, rhodamine dyes, with symmetrical nitrogen substitution at the 3' and 6' positions of the xanthene chromophore present themselves as an ideal choice because they have large two-photon absorption cross sections (σ_{TPA}), emission profiles bathochromically separated from typical fluoresceins and rhodols, and good photostability.

We recently disclosed the synthesis of the Rhodamine Voltage Reporter (RhoVR) family of tetramethylrhodamine (TMR)-based voltage sensors, which incorporate an *ortho*-carboxamide group to prevent spirocyclization of the rhodamine fluorophore and ensure localization of RhoVRs to the outer leaflet of the plasma membrane.²⁴ We hypothesized that the sulfonated version of RhoVR would retain the essential characteristics of the carboxamide dye, but with improved solubility and fewer overall synthetic steps. We now disclose the design, synthesis, characterization, and application of sulfonated Rhodamine Voltage Reporters, or sRhoVRs. This study is enabled by a new synthetic route to *ortho*-sulfonated rhodamine dyes that provides regioisomerically-pure sulfonated rhodamines in good yields and in just three steps from readily available starting materials. The best of the new indicators, sRhoVR 1, features good voltage sensitivity in HEK cells (44% $\Delta F/F$ per 100 mV), possesses a large σ_{TPA} (>200 GM at 840 nm), can detect action potentials in rat neurons in a single trial under widefield, confocal and two-photon microscopy, and can be employed *in vivo* in both anesthetized and awake mice to report on the evolution of voltage changes during sensory stimulation.

3.2 Design and synthesis of sRhoVR dyes

Preparation of sRhoVR dyes can be achieved through a Pd-catalyzed Heck coupling reaction between halogenated, sulfonated rhodamines (**5** or **6**) and substituted styrenes. We accessed sulfonated rhodamines dyes²⁶ from readily prepared 4-bromo-2-sulfobenzaldehyde²¹ (**3**) and a novel 5-bromo-2-sulfobenzaldehyde (**4**). Both **3** and **4** could be generated in quantitative yield via reaction of bisulfite²⁷ onto commercially available fluorinated bromobenzaldehydes **1** and **2** (**Scheme 3.1**).



Scheme 3.1. Synthesis of sulfonated Rhodamine Voltage Reporters (sRhoVRs)

Sulfonated benzaldehydes **3** and **4** were condensed with 3-(dimethylamino)phenol to afford the sulfoTMR dyes **5** (*para*-isomer) and **6** (*meta*-isomer) in 35% and 44% yield. Subsequent Pd-catalyzed Heck coupling with previously reported styrene molecular wires²¹ gave sRhoVR dyes (**7-10**) in isolated crude yields ranging from 52 to 62%. Compared to carboxamide-substituted RhovR, which requires 6 synthetic steps from commercially available starting materials,²⁴ sRhoVR can be accessed in just 3 steps, representing a 50% reduction in step count. Small amounts of the sRhoVR molecules were purified via preparative HPLC for spectroscopic characterization.

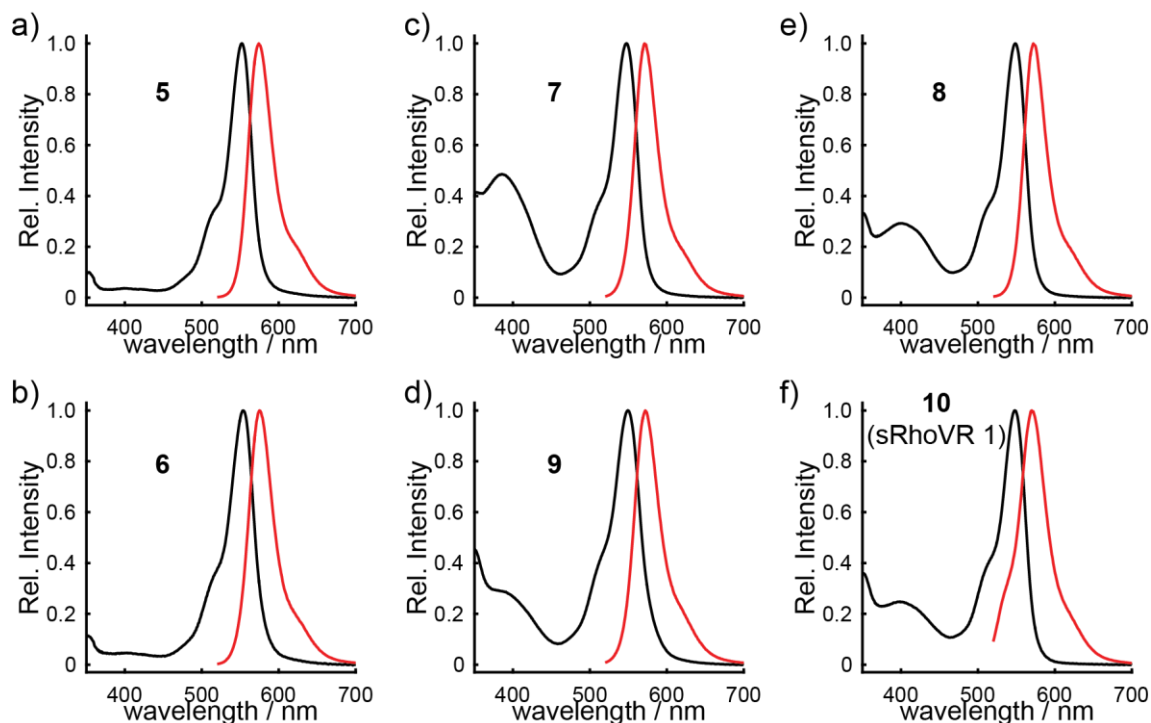


Figure 3.1. Absorption (UV/vis) and fluorescence emission spectra of compounds **5** through **10**. Black lines indicate the UV/vis absorption spectra. Red lines indicate the fluorescence emission spectra. Spectra were acquired in ethanol. For fluorescence emission spectra, excitation was provided at 10 nm longer wavelength than the respective absorbance maximum.

The use of sulfonated benzaldehydes provides ready access to regioisomerically pure sulfonated rhodamines and may be a general strategy for creation of analogous fluoresceins and carbo- and silicon-substituted xanthene dyes. The SulfoTMR dyes **5** and **6**, as well as the final sRhoVR dyes (**7-10**) demonstrate absorption maxima centered between 548 and 553 nm ($\epsilon = 60,000$ to $88,000$ $M^{-1} \text{ cm}^{-1}$; **Figure 3.1**), similar to those of classic tetramethylrhodamine dyes. The sRhoVR compounds also possess a strong secondary absorption band near 400 nm due to the presence of the phenylene vinylene molecular wires, with the *para*-sRhoVR (**7, 8**; **Figure 3.1**) secondary band slightly red-shifted relative to that of the *meta*-SulfoRhoVRs (**9, 10**; **Figure 3.1**). Fluorescence emission from all of the compounds was centered between 570 and 574 nm ($\Phi = 0.24$ - 0.57 ; **Table 3.1**).

Table 3.1. Photophysical properties of sRhoVR dyes

Compound	$\epsilon / M^{-1} \text{ cm}^{-1} (\lambda_{\text{max}}/\text{nm})^a$	$\Phi (\lambda_{\text{max}}/\text{nm})^a$	$\Delta F/F (\%)^b$	SNR ^b
5	69000 (552)	0.52 (574)	N/A	N/A
6	88000 (553)	0.57 (575)	N/A	N/A
7	75000 (548)	0.29 (571)	$3 \pm 0.01\%$	6:1
8	83000 (548)	0.24 (572)	$24 \pm 2\%$	10:1
9	77000 (549)	0.33 (572)	$8 \pm 0.02\%$	19:1
10 (sRhoVR 1)	60000 (547)	0.30 (570)	$44 \pm 0.02\%$	91:1

^a 100% ethanol. ^b per 100 mV in voltage-clamped HEK cells.

3.3 Cellular Characterization and Performance of sRhoVRs

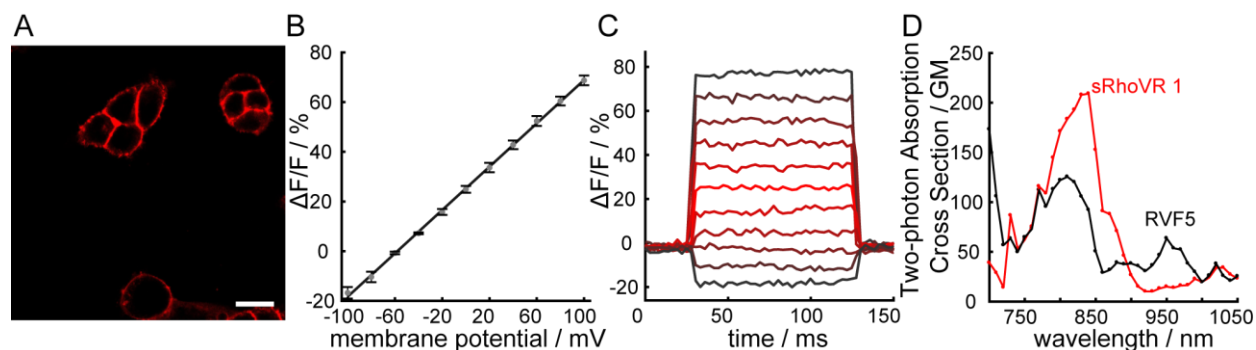


Figure 3.2. Characterization of SulfoRhoVR 1 (sRhoVR 1) in HEK Cells. A Confocal fluorescence image of SulfoRhoVR 1 (compound 10). SulfoRhoVR 1 clearly localizes to the outer membrane of HEK293T cells. Scale bar is 20 μm . B Plot of the percentage change in fluorescence vs. membrane potential summarizing data from five separate cells, resulting in an average voltage sensitivity of 44% per 100 mV. Error bars are \pm SEM. C Plot of fractional change in fluorescence vs. time for 100 ms hyper- and depolarizing steps from +100 mV to -100 mV in 20 mV increments from a holding potential of -60 mV for single HEK293T cells under whole-cell voltage-clamp mode. D Two-photon cross section of sRhoVR 1 vs. RhodolVoltageFluor 5 (RVF5), acquired in PBS, pH 7.4.

Live-cell imaging reveals that sRhoVR dyes localize to the plasma membrane of cells. Incubation of HEK cells with sRhoVR dyes (7-10) at a concentration of 200 nM results in clear membrane-localized fluorescence, as determined by confocal laser scanning fluorescence microscopy (**Figure 3.2A**, **Figure 3.3**). The apparent membrane staining was brighter for the *meta*-sRhoVR dyes (9 and 10) than for the *para*-sRhoVR dyes (7 and 8). The membrane staining of sRhoVR dyes indicates that the *ortho*-sulfonate is sufficient to prevent internalization of tetramethylrhodamine-based voltage indicators. We assessed the voltage sensitivity of each sRhoVR dye in HEK cells using patch-clamp electrophysiology in whole-cell voltage-clamp mode. Hyper- and depolarizing steps from +100 to -100 mV in 20 mV increments from a baseline potential of -60 mV demonstrated a range of voltage sensitivities from 3 to 44%, depending on the combination of fluorophore (*para* 5 or *meta* 6) and molecular wire (**Table 3.1**, **Figure 3.2B,C**, and **Figure 3.4**). The voltage sensitivities of sRhoVR compounds tracked well with previously reported RhoVR counterparts,²⁴ suggesting that the replacement of the carboxyl group associated with classical rhodamines with a sulfonate group minimally perturbed the electronic properties of the voltage reporters. Voltage-sensitive dyes with *meta*-substitution patterns (9 and 10) were both more voltage-sensitive and demonstrated higher signal-to-noise ratios (SNR) than their *para*-substituted counterparts.

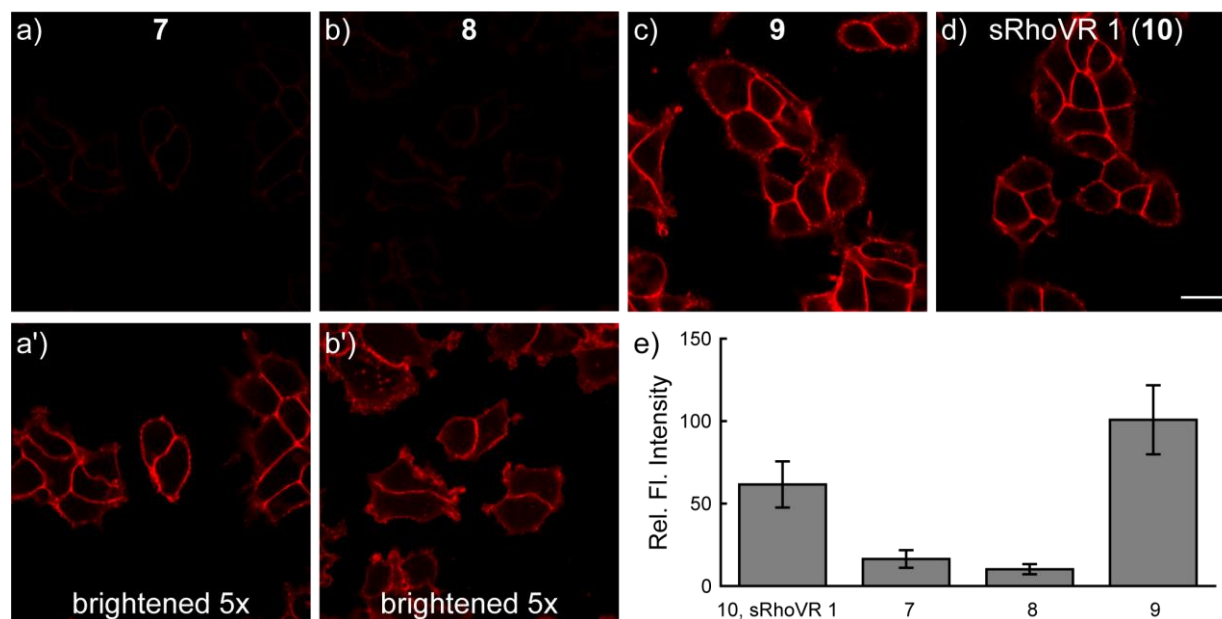


Figure 3.3. Confocal imaging of sRhoV dyes in HEK cells. HEK cells were stained with 200 nM in HBSS sRhoVR derivative 7 (a), 8 (b), 9 (c), or 10 (d, also known as sRhoVR 1) for 15 minutes at 37 °C. Cell were transferred to fresh HBSS (without any dye) and imaged via confocal laser scanning microscopy. All imaging parameters are identical. Histogram display values are identical; panels a' and b' have been brightened 5x to indicate the staining patterns of compounds 7 and 8. Scale bar is 20 μm . The fluorescence intensity of the membrane staining is quantified in panel e). Values represent the mean fluorescence of membrane ROIs containing HEK cells stained with compounds 7-10. $n = 15$. Error bars are \pm standard deviation.

We are currently undertaking studies to probe the molecular mechanisms underlying this difference. One simple explanation is that for the *meta*-sRhoVRs, the alignment of the sulfonate with the long axis of the molecular wire improves the alignment between the electron transfer vector and the transmembrane electric field, which should enhance sensitivity.²¹ Given its high sensitivity and brightness in cells (**Figure 3.3**), we chose compound **10**, which we call sRhoVR 1, for further characterization in subsequent experiments. Importantly, for use in imaging in tissue and *in vivo*, the solubility of sRhoVR 1 (0.92 mM) was nearly 3-fold the solubility of RVF5 (0.29 mM) and 5-fold greater than RhoVR 1 (0.17 mM).

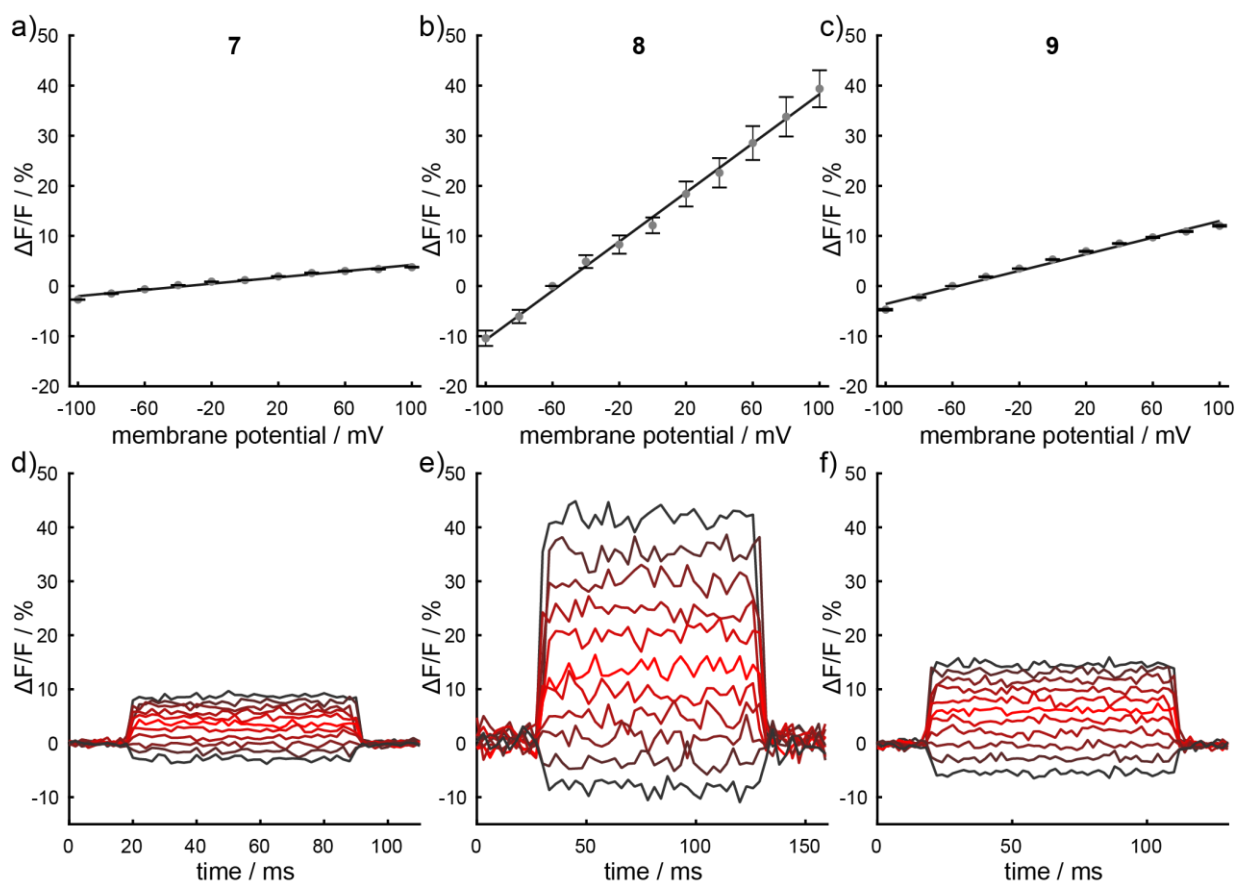


Figure 3.4. Voltage sensitivity of compounds **7** to **9**, determined by fluorescence microscopy and electrophysiology. Average voltage sensitivity plots of percentage change in fluorescence vs. membrane potential values from whole-cell voltage-clamp electrophysiology of 5 HEK cells each for dyes **7** (a), **8** (b), and **9** (c). Error bars indicate standard error of the mean for $n = 5$ different cells. Summaries reveal average voltage sensitivities of 3%, 24%, and 8%, respectively. Representative traces of fractional change in fluorescence vs. time from whole-cell voltage-clamp electrophysiology for compounds **7** (d), **8** (e), and **9** (f).

Cultured rat hippocampal neurons incubated with sRhoVR 1 (**10**, 500 nM) and imaged using confocal laser scanning fluorescence microscopy display clear membrane staining (**Figure 3.5A**). Rat hippocampal neurons were subjected to whole-cell patch-clamp electrophysiology under current-clamp mode to record spontaneous and evoked action potentials. Dual optical and electrophysiological recording of spontaneous action potentials demonstrate that sRhoVR 1 exactly follows the electrophysiology recording (**Figure 3.5B**). We recorded evoked action potentials in hippocampal neurons under whole-cell current clamp mode, in the presence or absence of sRhoVR 1 (500 nM). The presence of sRhoVR 1 did not significantly alter the time to peak, half-width, rise tau, rise time, or decay time of the action potential, nor overall cell capacitance ($n = 7$ cells, 10 spikes each), suggesting that sRhoVR 1 does not significantly perturb cellular physiology and membrane properties (**Figure 3.6**). Spontaneous activity recordings in cultured rat neurons revealed a SNR of 20:1 ($n = 30$ APs) with a $\Delta F/F$ of 5% per spike (**Figure 3.5C**). Cultured rat neurons were also subjected to external field stimulation and SNR for a single action potential was determined to be 11:1 ($n = 50$ APs) with a $\Delta F/F$ of 3% per spike (**Figure 3.5D**).

3.4 Two-Photon Performance and Imaging of sRhoVR in Neurons

We evaluated the ability of sRhoVR to monitor membrane potential changes under two-photon illumination. Two-photon absorption relies on the essentially simultaneous absorption of two lower-energy photons to promote a chromophore to a singlet excited state. Due to the use of longer-wavelength light,^{28, 29} two-photon microscopy enables imaging in thick tissue samples such as brain slices and intact brains. We showed previously that rhodol-based voltage indicators display voltage sensitivity in both traditional single-photon and two-photon microscopy contexts.²³ Rhodamines have high two-photon absorption cross sections,²⁸ suggesting that sRhoVR 1, with its large voltage sensitivity (44% $\Delta F/F$ per 100 mV) and yellow to orange emission profile (570 nm), would be a promising two-photon voltage indicator. We measured the two-photon absorption cross section (σ_{TPA}) of SulfoTMR dyes **5** and **6** (in ethanol) as well as sRhoVR 1 and RVF5 (in PBS, pH 7.4) by normalizing to a rhodamine B standard.^{23, 30} A plot of two-photon absorption cross-section vs. excitation wavelength reveals σ_{TPA} maxima of approximately 210 GM (830 – 840 nm), which is in good agreement with literature values for rhodamine B (a very similar fluorophore) in ethanol (204 GM at 830 nm)³⁰ (**Figure 3.7**). By comparison, RVF5 displays an almost 2-fold lower value, 125 GM at its maximum of 820 nm (**Figure 3.7D**) and the previously reported VF2.1.Cl has a much weaker 40 GM at its maximum of 780 nm.²³ Consistent with two-photon absorption, sRhoVR 1 emission under two-photon illumination demonstrates a quadratic dependence on illumination intensity (**Figure 3.8**).

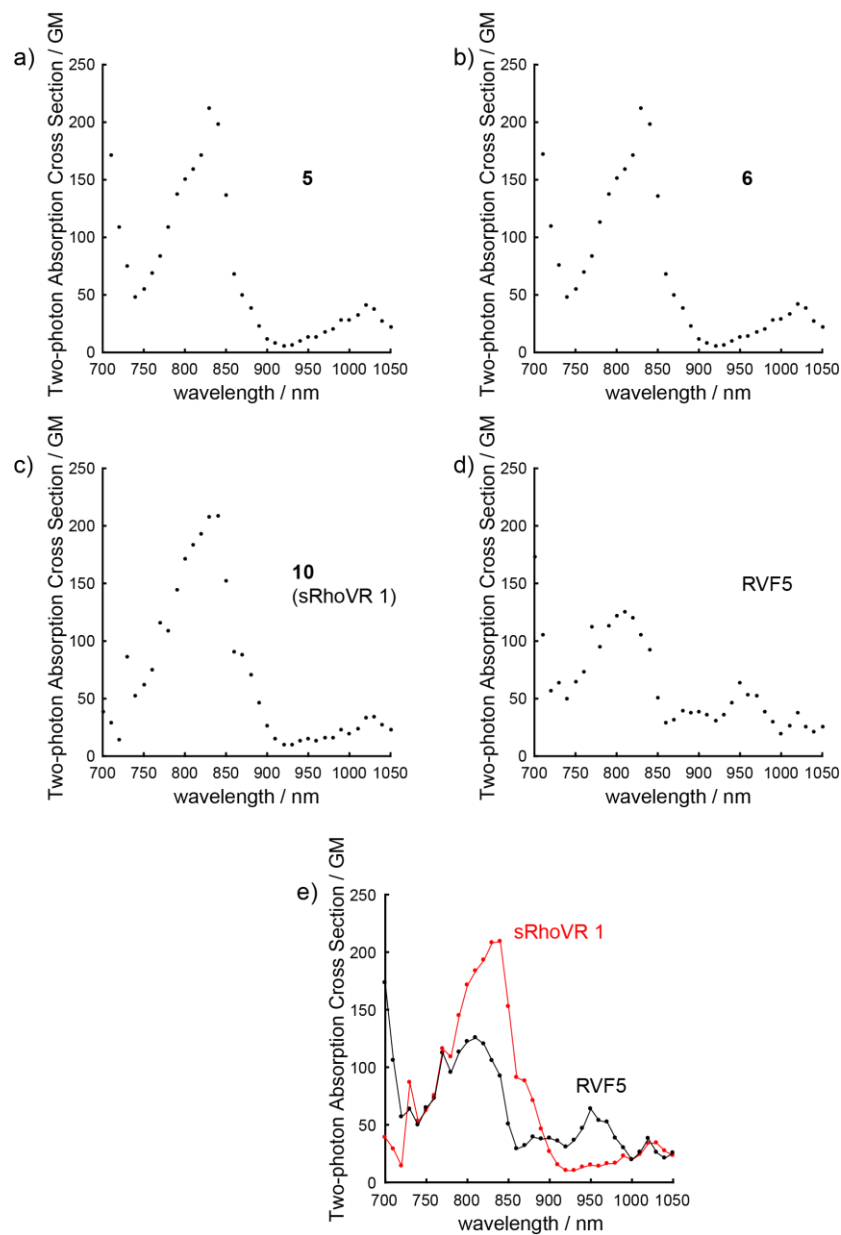


Figure 3.7. Two-photon absorption cross sections of sulfoTMR dye heads (5 and 6), sRhoVR 1 (10), and RVF5. SulfoTMR spectra are taken in 100% ethanol, while RVF5 and sRhoVR 1 are in PBS (pH 7.4). Panel e) directly compares the spectra of sRhoVR 1 and RVF5.

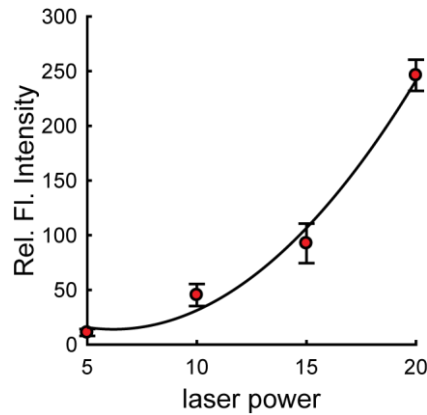


Figure 3.8. Quadratic Dependence of SulfoRhoVR 1 2P Brightness on Laser Power. Plot of fluorescence intensity vs. percentage laser power reveals a quadratic dependence of fluorescence on laser power for SulfoRhoVR 1. Line of best fit via least squares regression is $y = 1.19x^2 - 14.78x + 59.73$. $R^2 = 0.987$. Error bars are \pm standard deviation for $n = 3$ experiments.

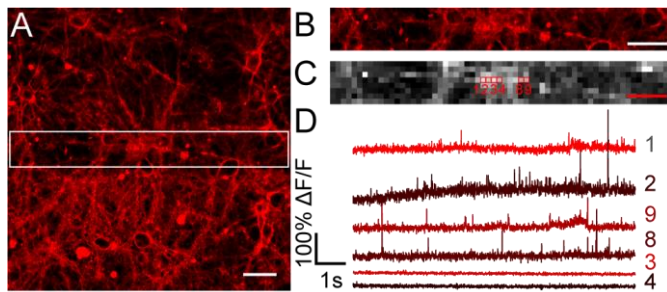


Figure 3.9. Two-photon voltage imaging of sRhoVR 1 in rat hippocampal neurons. A sRhoVR 1 brightly stains the plasma membrane of rat hippocampal neurons under two-photon illumination. Scale bar is 50 μm for all images. B Zoomed version of boxed region in panel A. C Still frame from a video recording (200 Hz, 425 x 52 μm , 64 x 8 pixels) of the neurons from panel B. D Fluorescence responses demonstrate robust spontaneous activity. Fluorescence traces are single-trial $\Delta F/F$ values from single pixels, are unfiltered, and uncorrected for bleaching.

With bright two-photon emission and high voltage sensitivity, we expected that sRhoVR 1 could be used for two-photon voltage imaging. To lay the groundwork for these studies, we assessed the ability of sRhoVR 1 to measure neuronal activity in cultured rat hippocampal neurons under two-photon illumination. Bath application of sRhoVR 1 (200 nM) resulted in well-defined membrane staining (**Figure 3.9A and B**). In single-trial, single-pixel (6.6 μm^2) optical recordings (**Figure 3.9C**), the rat neurons showed robust spontaneous activity that could be detected without *post-hoc* filtering, averaging, or photobleach correction (**Figure 3.9D**). To confirm that the activity we observed was due to action potentials, we treated active cultures with tetrodotoxin (TTX, 1 μM), to inhibit spontaneous action potential firing. In TTX-treated cultures, we did not observe spiking activity (**Figure 3.10**). Together these results establish that sRhoVR 1 can detect neuronal voltage changes under two-photon illumination.

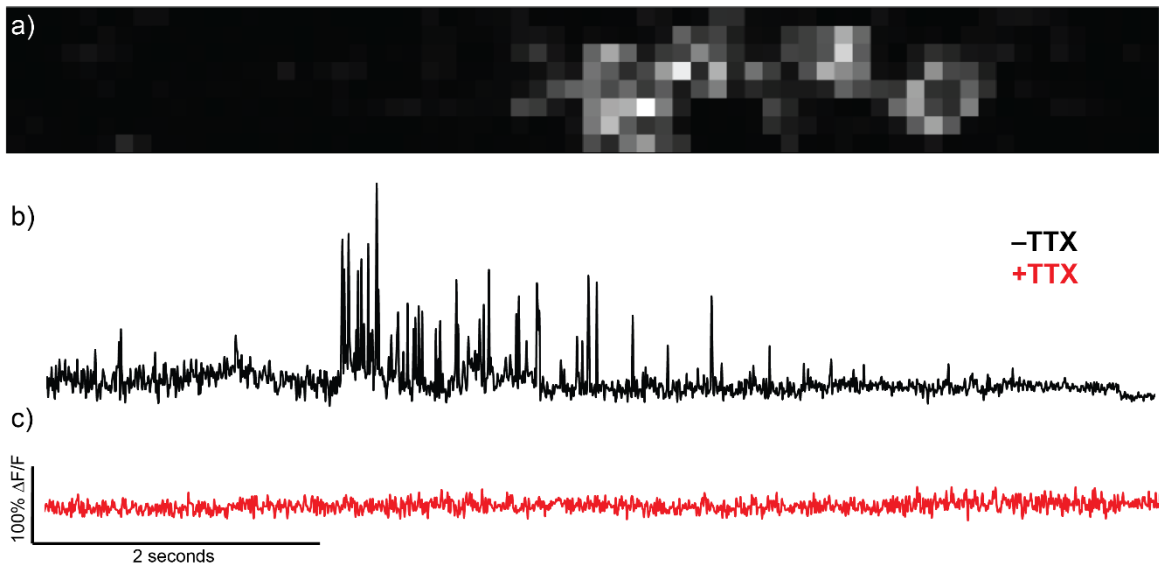


Figure 3.10. 2P imaging of spontaneous activity in cultured mouse neurons with SulfoRhoVR 1. (a) Sample still frame from spontaneous activity imaging. (b-c) Robust spontaneous spiking is observed via 2P imaging of SulfoRhoVR 1. Addition of TTX (1 μ M) abolishes activity. Traces are single trials and are not filtered.

in vivo imaging with sRhoVR 1

We next sought to deploy sRhoVR 1 for imaging voltage changes in the brains of live mice. sRhoVR is a promising candidate for *in vivo* brain imaging because it possesses a nearly 2-fold larger two-photon cross section than RvF5, shows a 50% improvement in voltage sensitivity over RvF5 (44% vs 28%), and an emission peak red-shifted by 35 nm. In particular, the ability to use two-photon illumination for voltage imaging allows the interrogation of voltage dynamics from neuronal membranes localized to a particular two-photon focal plane of approximately 2 μ m. This is in contrast to classically-employed widefield voltage imaging techniques as well as extracellular electrophysiological recordings of local field potential (LFP) and multi-unit activity (MUA). LFP reflects a current dipole that often extends hundreds of micrometers throughout a number of cortical layers,^{5, 31} while MUA reflects spiking of many neurons within \sim 100 μ m of the recording electrode tip.² Therefore, use of electrodes alone cannot resolve differences in layer-specific activity recorded by LFP. Similarly, pairing widefield epifluorescence microscopy with electrode-based recording cannot resolve layer-specific responses due to out-of-plane fluorescence collected during epifluorescence microscopy. We envisioned two-photon imaging with sRhoVR 1 would be a generalizable solution to this problem: bulk loading of sRhoVR 1 would widely label cells *in vivo*, and optical sectioning with two-photon microscopy would enable depth resolution for complementing LFP recordings.

We performed two-photon sRhoVR 1 imaging in layer 2/3 of the barrel cortex of anesthetized mice (**Figure 3.12A**). Pressure injection of sRhoVR 1 through a glass pipette at \sim 200 μ m below the surface (**Figure 3.12B**, asterisk, 100 to 200 μ M in ACSF) resulted in diffuse fluorescence staining across an area approximately 500 μ m in diameter (**Figure 3.12B**, red is sRhoVR 1 fluorescence,

cyan is fluorescein isothio cyanate-conjugated dextran labeling of the vasculature). Typical staining patterns reveal comprehensive labeling of neuropil, with cell bodies appearing as dark silhouettes (**Figure 3.12C and D**). In general, the staining was uniform, although occasionally we observed brighter cells, which are currently unidentified and may be microglia (**Figure 3.12C**, arrowheads). RVF5 did not perform as well as sRhoVR: injection of rhodol-based voltage indicator RVF5 did not give staining over as large of an area, which may be partially explained by the lower solubility of RVF5 relative to sRhoVR (0.29 mM vs. 0.92 mM). Extracellular recordings of LFP and MUA were acquired simultaneously with two-photon imaging using a tungsten microelectrode inserted near the site of sRhoVR 1 injection (**Figure 3.12B**, white arrowhead). Optical recordings were acquired under two-photon excitation from a region of interest (ROI) shaped as a horizontal strip approximately $200 \times 25 \mu\text{m}$ in size (**Figure 3.12D**, black rectangle), at a framerate of approximately 20 Hz. Weak electrical stimulation of the contralateral whisker pad in anesthetized mice resulted in clear, single-trial optical responses from sRhoVR 1 (**Figure 3.12E**). The fluorescence increase ranged from 4 to 10% $\Delta F/F$, with a signal to noise ratio (SNR) of 5.9 ± 3.2 in single trials and 11.6 after averaging 8 trials (**Figure 3.12F**). The time course of the externally-recorded field potential (LFP, **Figure 3.12E,F**) precisely matches the time course of the optically-measured transmembrane potential (sRhoVR 1, **Figure 3.12E,F**). The positive deflection in sRhoVR 1 fluorescence indicates membrane depolarization. Combined with the negative deflections in the LFP, this confirms excitatory currents across neuronal membranes at a depth of 200 μm , resulting in depolarization. Because the sign of the LFP can vary with the position of the electrode, two-photon imaging of transmembrane potential with sRhoVR 1 provides an important calibration for interpreting the extracellularly-recorded LFP.

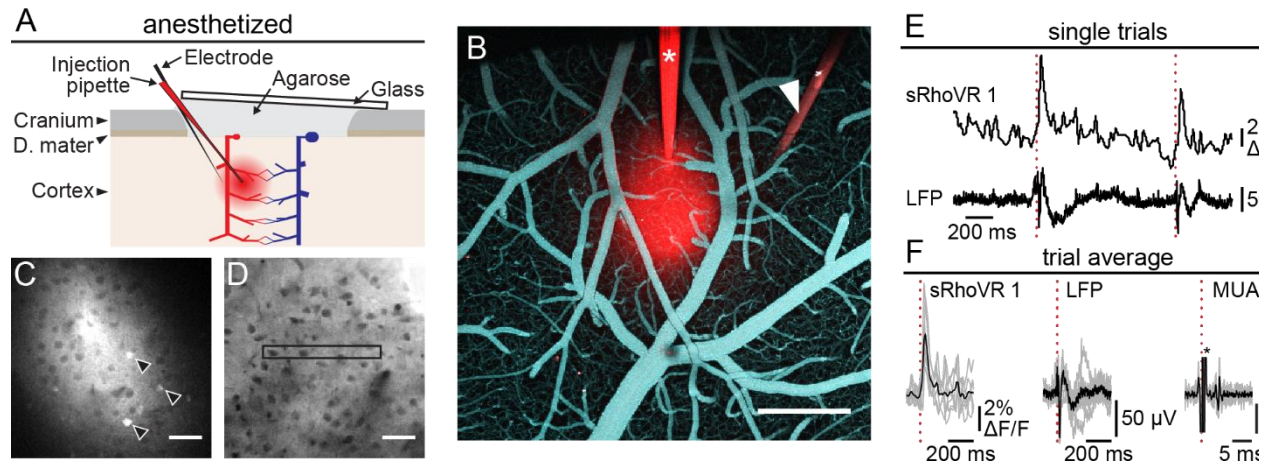


Figure 3.11. *In vivo*, two-photon voltage imaging in layer 2/3 of the barrel cortex of anesthetized mice using SulfoRhoVR 1. A Schematic of *in vivo* imaging experimental setup. Cranial bone and dura mater were removed above the barrel cortex. The brain was covered with 0.7% agarose and on top, a coverslip was placed in a way that allowed access to the brain from one side of the preparation. SulfoRhoVR 1 (100 to 200 μM in ACSF) was pressure-injected through a glass or quartz micropipette; local field potentials (LFP) and multi-unit activity (MUA) were recorded in close vicinity to the injection site with a tungsten electrode (impedance: 5-7 $\text{M}\Omega$). B A view from the top on the cortical surface after intracortical injection of SulfoRhoVR 1 (red) and intravascular injection of fluorescein isothiocyanate-conjugated dextran (green); the SulfoRhoVR 1-filled glass pipette (asterisk) and tungsten electrode (white arrowhead) are visible. Scale bar, 500 μm . C and D Typical two-photon images of tissue staining with SulfoRhoVR 1 in cortical layer 2/3; the majority of cell bodies appeared dark indicating the lack of SulfoRhoVR 1 in the intracellular compartment; arrowheads indicate a few exceptions. The rectangle in (d) depicts a typical region of interest (ROI) for data acquisition (approximately $200 \times 25 \mu\text{m}$). Scale bars, 50 μm . E Time-course of SulfoRhoVR 1 fluorescence, relative to baseline ($\Delta\text{F}/\text{F}$), and LFP traces acquired simultaneously. Dotted red lines indicate timing of contralateral whisker pad stimulation with a single 300 μs weak electrical pulse. F Single trials (gray) and trial average (black) for SulfoRhoVR1 fluorescence, LFP, and MUA; 8 trials from one ROI are overlaid. Dotted red lines indicate timing of contralateral whisker pad stimulation; asterisk in the MUA trace indicates artifact of electrical stimulation. For panels E and F SulfoRhoVR 1 fluorescence was acquired in frame scan mode at a frequency of ~ 20 Hz and normalized to mean fluorescence over the entire time course to obtain $\Delta\text{F}/\text{F}$. All fluorescence time-courses are unfiltered, and uncorrected for bleaching.

To further establish the utility of sRhoVR 1 for bridging neuronal transmembrane potential dynamics to behavior in living organisms, we performed similar *in vivo* imaging experiments in awake mice (**Figure 3.12**). Mice were implanted with chronic cranial windows that also allowed loading of sRhoVR 1, or other fluorescent indicators, through a silicon injection port (**Figure 3.12A**). Mice were briefly anesthetized with isoflurane for intracortical injection of sRhoVR 1 (100 to 200 μM) using a quartz pipet positioned at $\sim 200 \mu\text{m}$ below the surface (**Figure 3.12A**). The staining pattern was similar to that in acute experiments (**Figure 3.12B**): sRhoVR 1 comprehensively labeled neuropil, with cell bodies appearing as dark shadows (representative

images, **Figure 3.12C and D**). Following recovery from isoflurane, we imaged responses to brief air puffs to the contralateral whisker pad. **Figure 3.12E** shows sRhoVR 1 signal time-courses from five different ROIs in layer 2/3 imaged consecutively at different depths (130-300 μm). In each case, the time-course was computed as an average from all pixels within the ROI ($\sim 200 \times 25 \mu\text{m}$ imaged at 20 Hz). Robust increases in fluorescence were observed in response to each air puff. Positive sRhoVR 1 responses indicate depolarizations in shallow (130 μm), intermediate (200 μm) and deeper cortical layers (300 μm , **Figure 3.12E**), providing a critical depth resolution constraint for the interpretation of LFP recordings in the cortex.⁵ Following imaging sessions, mice recovered fully and could be again treated with sRhoVR 1 for voltage imaging. Together, these experiments establish the compatibility of sRhoRV-type dyes for *in vivo* imaging in mice and demonstrate the utility of sRhoVR 1 for recording optical transmembrane potential responses with depth resolution in the cortex.

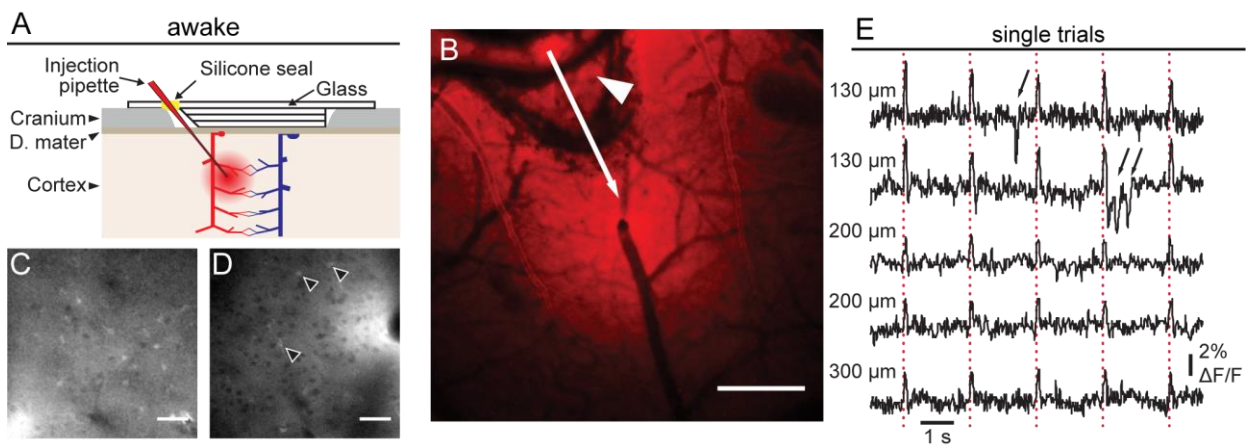


Figure 3.12. *In vivo*, two-photon voltage imaging in the barrel cortex of awake mice using sRhoVR 1. **A** The chronic “cranial window,” made by fusing a stack of three 3-mm and one 5-mm glass coverslips, was used to close the exposure. As injection port, a 0.5-mm hole was drilled into the 5-mm coverslip and covered with silicone. During implantation surgery, the cranial bone was removed while dura mater was left intact. After 3-4 weeks following implantation, sRhoVR 1 (0.1-0.2 mM in ACSF) was pressure-injected with a quartz pipette inserted through the silicone injection port while the animal was under isoflurane anesthesia; imaging started after recovery from anesthesia (20-30 min after injection). **B** A view from the top on the cortical surface after intracortical injection of SulfoRhoVR1 (red); arrow indicates the injection path, the arrowhead points towards the injection port. Scale bar, 500 μm . **C** and **D** Typical two-photon images of tissue staining with SulfoRhoVR1 in cortical layer 1 (**c**) and 2/3 (**d**). Arrowheads indicate bright cell bodies. Scale bars, 50 μm . **E** Time-courses of sRhoVR 1 fluorescence relative to baseline ($\Delta F/F$); each traces corresponds to a different ROIs in the same animal at the indicated cortical depth. Dotted red lines indicate timing of contralateral whisker pad stimulation with a single air puff. Black arrows point to motion artifacts. sRhoVR 1 fluorescence was acquired in frame scan mode at a frequency of ~ 20 Hz and normalized to mean fluorescence over the entire time course. All fluorescence time-courses are unfiltered, and uncorrected for bleaching.

3.5 Conclusions and Future Outlook

In summary, we present the design, synthesis, and application of sulfonated Rhodamine Voltage Reporter 1 (sRhoVR 1). sRhoVR 1 represents the best of a new class of sulfonated rhodamine that uses PeT as a voltage-sensing trigger. With short synthetic route from commercially-available starting materials (3 steps), high voltage sensitivity (44% $\Delta F/F$ per 100 mV), an emission maximum centered at 570 nm, enhanced solubility (3- to 5-fold over RhoVR 1 or RVF5), improved two-photon cross section ($\sim 2x$ over RVF5 and $\sim 5x$ over VF2.1.Cl), and fast response kinetics capable of tracking action potentials under both single-photon and two-photon conditions, sRhoVR is a promising candidate for use *in vivo*. We show that sRhoVR 1 can be deployed in intact mouse brains for two-photon imaging *in vivo*. By coupling optical recording of sRhoVR 1 responses in layer 2/3 of the barrel cortex of mouse, sRhoVR 1 can provide important depth resolution of LFP records. In this case, depolarizations measured via optical sRhoVR 1 signals provide direct evidence for excitatory synaptic transmission at multiple, optically-resolved cortical depths, and were accompanied by negative deflections in LFP recording at the same depth, consistent with a canonical thalamocortical response. Importantly, sRhoVR 1 is applicable for imaging in awake, head-fixed mice with implanted cranial imaging windows, opening the door for longitudinal *in vivo* two-photon membrane potential studies in behaving animals.

3.6 Methods and Materials

General methods for chemical synthesis and characterization

Chemical reagents and anhydrous solvents were purchased from commercial suppliers and used without further purification. All reactions were carried out in oven-dried flasks under an inert atmosphere of N_2 . Thin layer chromatography (TLC) (Silicycle, F254, 250 μm) was performed on glass backed plates pre-coated with silica gel and were visualized by fluorescence quenching under UV light. NMR spectra were measured on a Bruker AV-900 MHz, 226 MHz. Chemical shifts are expressed in parts per million (ppm) and are referenced to d_6 -DMSO, 2.50 ppm or $CDCl_3$, 7.26 ppm. Coupling constants are reported as Hertz (Hz). Splitting patterns are indicated as follows: s, singlet; d, doublet; sep, septet; dd, doublet of doublet; ddd, doublet of double of doublet; dt, doublet of triplet; td, triplet of doublet; m, multiplet. High-resolution mass spectra (ESI EI) were measured by the QB3/Chemistry mass spectrometry service at University of California, Berkeley. High performance liquid chromatography (HPLC) and low resolution ESI Mass Spectrometry were performed on an Agilent Infinity 1200 analytical instrument coupled to an Advion CMS-L ESI mass spectrometer. Columns used for the analytical and preparative HPLC were Phenomenex Luna C18(2) (4.6 mm I.D. \times 150 mm) and Waters XBridge 10 μ C18 (19 mm I.D. \times 250 mm) columns with a flow rate of 1.0 and 30.0 mL/min, respectively. The mobile phase were MQ- H_2O with 0.05% trifluoroacetic acid (eluent A) and HPLC grade acetonitrile with 0.05% trifluoroacetic acid (eluent B). Signals were monitored at 254, 350, and 580 nm in 20 min with gradient 10-100% eluent B.

Imaging Parameters

Epifluorescence imaging was performed on an AxioExaminer Z-1 (Zeiss) equipped with a Spectra-X Light engine LED light (Lumencor), controlled with Slidebook (v6, Intelligent Imaging Innovations). Images were acquired with either a W-Plan-Apo 20x/1.0 water objective (20x; Zeiss) or a W-Plan-Apo 63x/1.0 water objective (63x; Zeiss). Images were focused onto either an OrcaFlash4.0 sCMOS camera (sCMOS; Hamamatsu). The sCMOS was used to acquire large fields of view for recording from multiple neurons (i.e. Figure 4a-d). Two-photon imaging was

performed with a Zeiss LSM 880 NLO AxioExaminer equipped with a Chameleon Ultra I laser (Coherent Inc.) Fluorescence images were acquired using a Zeiss BiG-2 GaAsP detector.

Spectroscopic studies

Stock solutions of VF dyes were prepared in DMSO (1.0–10 mM) and diluted with PBS (100 mM Na₂HPO₄, pH 7.4, 0.1% Triton-X) or with absolute ethanol. UV-Vis absorbance and fluorescence spectra were recorded using a Shimadzu 2501 Spectrophotometer (Shimadzu) and a Quantamaster Master 4 L-format scanning spectrofluorometer (Photon Technologies International). The fluorometer is equipped with an LPS-220B 75-W xenon lamp and power supply, A- 1010B lamp housing with integrated igniter, switchable 814 photon-counting/analog photomultiplier detection unit, and MD5020 motor driver. Samples were measured in 1-cm path length quartz cuvettes (Starna Cells). For solubility studies, 5 mg each of SulfoRhoVR 1, RVF5, and RhoVR 1 were dissolved in 10 mL of distilled water. Over the course of seven days, and while stirring, 1 mg of each of the dyes was added daily until no more solid went into solution. The resulting suspensions were then filtered through a 0.22-micron polytetrafluoroethylene filter into a scintillation vial. The resulting filtrates were then used to determine the amount of voltage dye in solution via UV-Vis absorbance by dilution into ethanol for sulfoRhoVR 1 and PBS for RVF5 and RhoVR 1. Molar extinction coefficient values were used to determine concentration (RVF5: 83,000 cm⁻¹M⁻¹, RhoVR 1: 87,000 cm⁻¹M⁻¹).

Cell Culture

All animal procedures were approved by the UC Berkeley Animal Care and Use Committees and conformed to the NIH Guide for the Care and Use of Laboratory Animals and the Public Health Policy. Human embryonic kidney 293T (HEK) cells were passaged and plated onto 12 mm glass coverslips pre-coated with Poly-D Lysine (PDL; 1 mg/ml; Sigma-Aldrich) to provide a confluency of ~15% and 50% for electrophysiology and imaging, respectively. HEK cells were plated and maintained in Dulbecco's modified eagle medium (DMEM) supplemented with 4.5 g/L D-glucose, 10% FBS and 1% Glutamax.

Voltage sensitivity in HEK cells

Functional imaging of VF dyes was performed using a 20x objective paired with image capture from the EMCCD camera at a sampling rate of 0.5 kHz. SulfoRhoVR dyes were excited using the 550 nm LED with an intensity of 9.7 W/cm². For initial voltage characterization emission was collected with the QUAD filter (430/32, 508/14, 586/30, 708/98 nm) after passing through a quadruple dichroic mirror (432/38, 509/22, 586/40, 654 nm LP).

Electrophysiology

For electrophysiological experiments, pipettes were pulled from borosilicate glass (Sutter Instruments, BF150-86-10), with a resistance of 5–8 MΩ, and were filled with an internal solution; (in mM) 115 potassium gluconate, 10 BAPTA tetrapotassium salt, 10 HEPES, 5 NaCl, 10 KCl, 2 ATP disodium salt, 0.3 GTP trisodium salt (pH 7.25, 275 mOsm).

Recordings were obtained with an Axopatch 200B amplifier (Molecular Devices) at room temperature. The signals were digitized with Digidata 1332A, sampled at 50 kHz and recorded with pCLAMP 10 software (Molecular Devices) on a PC. Fast capacitance was compensated in the on-cell configuration. For all electrophysiology experiments, recordings were only pursued if series resistance in voltage clamp was less than 30 MΩ. For whole-cell, voltage clamp recordings

in HEK 293T cells, cells were held at -60 mV and 100 ms hyper- and de-polarizing steps applied from -100 to +100 mV in 20 mV increments. For whole-cell, following membrane rupture, resting membrane potential was assessed and recorded at $I = 0$ and monitored during the data acquisition. Neurons were switched to current clamp mode if they displayed series resistance in voltage clamp less than 30 megaohms. Pipette tip resistance was corrected by performing a bridge balance compensation.

To test if loading SulfoRhoVR 1 onto the membrane of neurons has any effect on action potential firing, ten 500 ms current steps were injected into neurons in increments of 0.05 pA. The action potentials for each sweep were analyzed in Clampfit 10 software (Molecular Devices) to give amplitude and kinetic data.

Image analysis

Analysis of voltage sensitivity in HEK cells was performed using custom Python scripts. Briefly, a region of interest (ROI) was selected based on fluorescence intensity and applied as a mask to all image frames. Fluorescence intensity values were calculated at known baseline and voltage step epochs.

Two-Photon Excitation Cross Section Measurement

The two-photon excitation (TPE) cross section of SulfoTMR dyes and SulfoRhoVR 1 was determined according to previously reported procedures.²³ We first measured the fluorescence signal generated by two-photon excitation of a rhodamine b standard using a Zeiss BiG-2 GaAsP detector on a Zeiss LSM 880 NLO AxioExaminer equipped with a Chameleon Ultra I laser. We then determined the one-photon quantum yield of the dyes of interest and measured the fluorescence signal generated by two-photon excitation of the dyes of interest. We then calculated the TPE of the dyes of interest via the following equation:

$$\sigma_{TPE\ DYE} = \frac{\phi_{Rho\ B} * \sigma_{TPE\ Rho\ B}}{\phi_{DYE}} * \frac{F_{DYE}}{F_{Rho\ B}}$$

Where F_{DYE} and $F_{Rho\ B}$ are the measured fluorescence signal from the dye of interest and rhodamine b, respectively. The values for σ_{TPE} at different wavelengths for rhodamine b were obtained from Xu and Webb.²⁸

Animal procedures for imaging under anesthesia

All experimental procedures were performed in accordance with the guidelines established by the UCSD Institutional Animal Care and Use Committee (IACUC). Adult wild-type C57Bl/6 or ICR mice (age: 3-6 months) were used for *in vivo* imaging experiments.

Mice were anesthetized with isoflurane (2% initially, 1-1.5% for maintenance) in 100% oxygen during surgical procedures. A cannula was inserted into the femoral artery, tracheotomy was performed, and a metal holding bar was glued to the temporal bone for immobilization of the head during imaging. An area of skull overlying whisker pad and forepaw region of the primary somatosensory cortex (SI) contralateral to the holding bar was exposed and the dura mater removed. A ~5x3 mm cranial window was kept moist with artificial cerebrospinal fluid (ACSF) containing 142 mM NaCl, 5 mM KCl, 10 mM glucose, 10 mM HEPES, 3.1 mM CaCl₂, 1.3 mM MgCl₂, pH 7.4. A drop of agarose (0.7% wt/vol, A9793, Sigma) in ACSF was applied on the brain surface, and the exposure was covered with a round glass coverslip (8 mm, WPI) cut straight on one side, and sealed with dental acrylic. A gap was left in the seal to allow insertion of recording microelectrodes and/or glass pipettes. To avoid herniation of the exposed brain due to excessive

intracranial pressure, the dura mater over the IVth cerebral ventricle was punctured, thus allowing cerebrospinal fluid drainage. After the exposure was closed, the drainage hole was sealed with agarose.

After closing the exposure, mice were left to rest under 1% isoflurane for 45 min. Then, isoflurane was discontinued, and anesthesia was maintained with α -chloralose (50 mg/kg/h, C0128, Sigma or 100459, MP Biochemicals). Mice were paralyzed with pancuronium bromide (0.4 mg/kg/h, P1918, Sigma) and ventilated ($\sim 110 \text{ min}^{-1}$) with 100% O₂. Expired CO₂ was measured continuously using a micro-capnometer (CI240, Columbus instruments). Heart rate, blood pressure, and body temperature were monitored continuously. α -chloralose, pancuronium, and 5% dextrose (all in saline) were supplied through the femoral line every 30 min for the duration of data acquisition. At the end of each imaging experiment, fluorescein isothiocyanate (FITC)-labeled dextran (MW=2 MDa, FD-2000S, Sigma) was injected (50-100 μL of a 5% (w/v) solution in phosphate-buffered saline) to visualize the vasculature and to control for the integrity of the capillary bed.

The stock solution of the voltage probe sRhoVR 1 (10 mM in DMSO) was diluted in ACSF yield a final probe concentration of 90-180 μM . 20% Pluronic F-127 in DMSO (P3000MP, Thermo-Fisher Scientific) was added to the solution to yield a final concentration of 0.35-0.7% Pluronic. The solution was filtered and pressure-microinjected into the cortical tissue using a glass or quartz micropipette. The microinjection pipette was guided under the glass coverslip and positioned $\sim 200 \mu\text{m}$ below the cortical surface using a Luigs & Neumann translation stage (380FM-U) and manipulation equipment integrated into the 2-photon imaging system. The fluorescence of sRhoVR 1 was used to visualize the micropipette during manipulation and to provide visual feedback during pressure-microinjection into the cortical tissue. The pressure was manually adjusted to ensure visible spread of sRhoVR 1 while avoiding movement of tissue, which would indicate excessive pressure.

Animal procedures for imaging awake mice

For imaging in awake mice, three weeks prior to the first imaging session, mice underwent surgery for implantation of a chronic cranial window and headpost for repeated immobilization of the head. During surgery, mice were anesthetized with isoflurane (2% initially followed by 1-1.5% during surgery) in 100% oxygen; their body temperature was maintained at 37 °C. A custom-made holding bar was glued to the skull overlaying the right hemisphere. Over the Barrel cortex of the left hemisphere, a 3-mm diameter area of skull was removed and replaced by a premade glass window assembly with silicon injection port. The glass window was fixed along the perimeter with dental acrylic. Additional dental acrylic was applied around the holding bar joining to the perimeter of the window to reinforce the overall assembly. Animals received 4.8 mg/kg Dexamethasone via intraperitoneal injection 2-4 h before surgery, and 0.05 mg/kg Buprenorphine via subcutaneous injection for 1-3 days after surgery. Ibuprofen (20 mg/ml) and Sulfatrim (5 ml/250 ml) were supplied via the drinking water 1 day before until 5 days after surgery.

After surgical implantation of the bar and 5-7 days of recovery, mice were habituated in 1 session per day to accept increasingly longer periods of head restraint under the microscope objective (up to 2 h). During head restraint, the animal was placed on a suspended bed. A drop of sweetened condensed milk was offered every 15 min during the fixation as reward. Animals were free to readjust their body position and displayed natural grooming behavior. A video camera (Lifecam Studio, Microsoft; IR filter removed) with an NIR longpass filter (LP920-25.5, Midwest Optical)

was used for continuous observation of the mouse. Infrared illumination (M940L3-IR (940 nm) LED, Thorlabs) was invisible for the PMT photodetectors and generated no imaging artifacts. The camera frames were recorded and synchronized with 2-photon imaging during data analysis. Periods of extensive body movement (e.g., grooming behavior) were excluded during data analysis.

Two-photon imaging

Images were obtained using an Ultima 2-photon laser scanning microscopy system (Bruker Fluorescence Microscopy). Excitation light was delivered by an Ultra II mode-locked Ti:Sapphire femtosecond laser (Coherent) tuned to 840 nm. Green (FITC) and red (sRhoVR 1) fluorophores were imaged using a cooled GaAsP (H7422P-40, Hamamatsu) and a multialkaline PMT (H7422-01, Hamamatsu) detectors, respectively. We used a combination of Zeiss 5x (Plan-NEOFLUAR, NA=0.16) and Olympus 20x (UMPlanFI, NA=0.5) objectives for a coarse approach and fine manipulation under the glass coverslip, respectively. The laser beam diameter was adjusted to overfill the back aperture. The laser power after the objective was ~30 mW. Time-resolved imaging was performed in frame-scan mode using ~200x25 pixel ROIs (~100x20 μm) acquired at ~20 Hz, ~4 μs dwell time. Image data was analyzed with custom-written software in MATLAB (MathWorks Inc.).

Extracellular electrophysiological recordings

Extracellular recordings of LFP and MUA were acquired using a tungsten microelectrode (FHC, 6-8 M Ω). The recorded potential was amplified and filtered into two signals: a low-frequency part (0.1–500 Hz, sampled at 2 kHz with 16 bits) and a high-frequency part (150-5,000 Hz, sampled at 20 kHz with 12 bits). The low-frequency part is referred to as the LFP. The high-frequency part was further filtered digitally between 750 and 5,000 Hz using a zero phase-shift second-order Butterworth filter to provide the MUA.

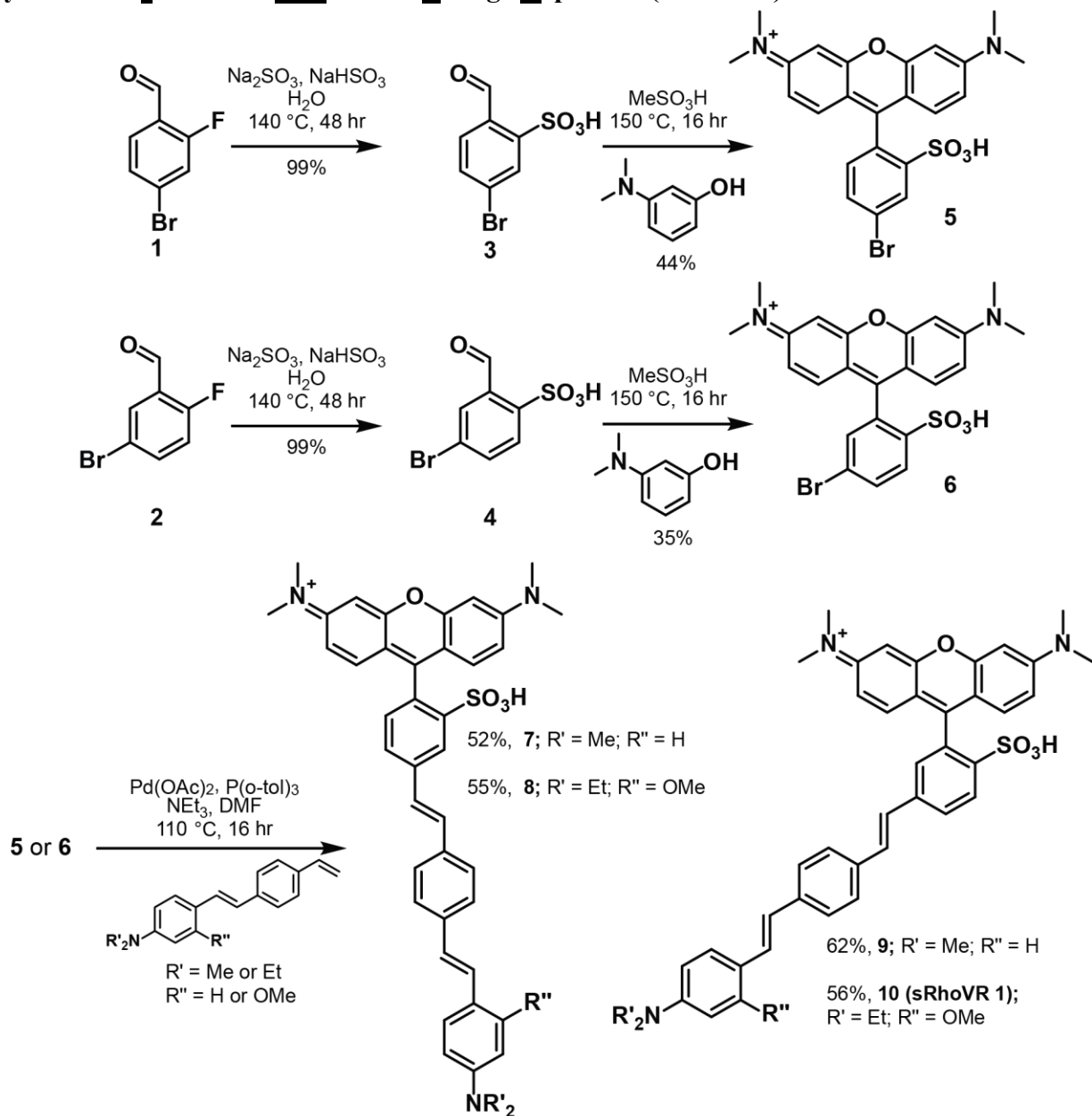
Microelectrodes were guided under the glass coverslip and positioned in cortical layer II/III within 200 μm from the imaged ROI using Luigs & Neumann translation stage (380FM-U) and manipulation equipment integrated into the Ultima system. Simultaneous 2-photon imaging and electrophysiological recordings from exactly the same location is not possible because of the photovoltaic artifact resulting from direct exposure of the metal microelectrode to focused Ti:Sapphire laser light.

Sensory stimulation and synchronization with data acquisition

In experiments under anesthesia, sensory stimulation was delivered to forepaw or whisker pad contralateral to the cortical exposure through a pair of thin needles inserted under the skin using weak electrical pulses (300 μs , 1 mA). In awake mice, the sensory stimulus consisted of air puffs onto the whiskers contralateral to the cortical window. We used 100-ms puffs delivered through a plastic tube (2 mm inner diameter). The tube was positioned behind the whiskers to minimize the eye blink reflex.

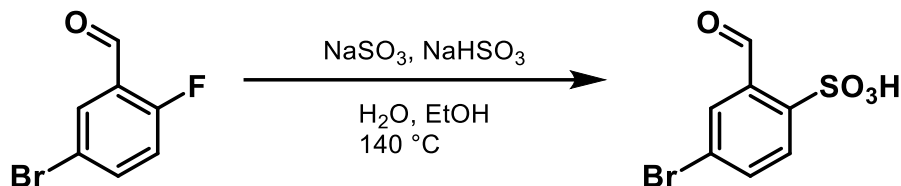
Stimulation devices (A365 stimulus isolator or PV830 picopump, WPI) were triggered using a separate PC that also acquired timing signals for data acquisition (“trigger out” signals for each frame/line) and physiological readings using a National Instruments IO DAQ interface (PCI-6229) controlled by custom-written software in MATLAB. The timing of each frame/line relative to the stimulus onset was determined during data analysis based on acquired triggering signals.

Synthesis of sulfonated Rhodamine Voltage Reporters (sRhoVRs)



Synthetic Details

Preparation of sulfobenzaldehydes:



Synthesis of 5-bromo-2-sulfobenzaldehyde

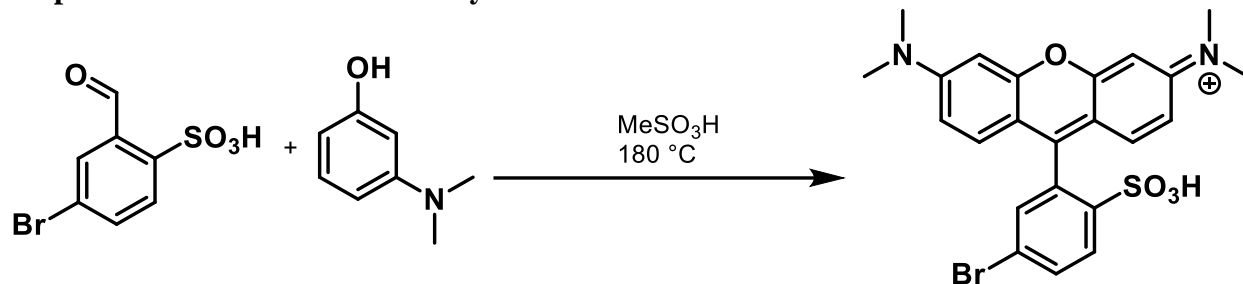
5-bromo-2-fluorobenzaldehyde (3.0 g, 14.78 mmol) was placed in a long-necked bomb flask and dissolved in a 1:1 mixture of ethanol and water. Sodium sulfite (1.49 g, 11.82 mmol) and sodium bisulfite (123 mg, 1.18 mmol) were added and the reaction was stirred for 48 hours at 140 degrees Celsius. The reaction mixture, after cooling, was poured into methanol while stirring so as to make 20% aqueous content of the whole volume. This process precipitated the inorganic salts, which were then removed by vacuum filtration. The solvent from the filtrate was removed under reduced pressure to obtain a solid residue, which was triturated with methanol/ethyl ether to produce a fluffy white solid (3.9 g, 99%).

¹H NMR (900 MHz, DMSO-*d*₆) δ 10.80 (s, 1H), 7.83 – 7.82 (m, 2H), 7.76 (d, *J* = 8.1 Hz, 1H).

¹³C NMR (226 MHz, DMSO-*d*₆) δ 192.31, 148.83, 135.64, 134.14, 129.29, 128.91, 122.43.

HR-ESI-MS *m/z* for C₇H₄BrO₄S⁻ calculated: 263.9092 found: 262.9021 (M-H).

Preparation of Sulfonated TMR dyes:



Synthesis of *N*-(9-(5-bromo-2-sulfohenyl)-6-(dimethylamino)-3*H*-xanthen-3-ylidene)-*N*-methylmethanaminium (metaTMR)

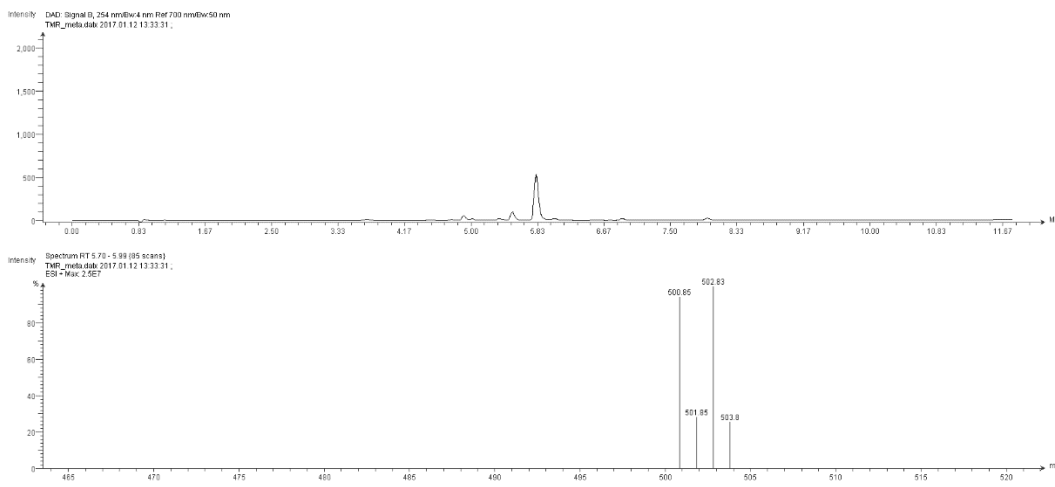
5-bromo-2-sulfobenzaldehyde (300 mg, 1.13 mmol) and 3-(dimethylamino)phenol (310 mg, 2.26 mmol) were placed in a roundbottom flask, dissolved in 3 mL of neat methanesulfonic acid, and stirred for 16 hours at 150 degrees Celsius. After cooling, the reaction mixture was diluted with 30mL water and basified with 10 mL 5M KOH. Products were extracted with ten 50 mL portions of 90:10 DCM:IPA, after which the organic layers were dried over sodium sulfate before being concentrated via rotary evaporation. The resulting dark purple oil was dissolved in 3-5 mL of DCM and then poured into an excess of diethyl ether, precipitating the product. The deep purple solid (250 mg, 44%) was collected via vacuum filtration.

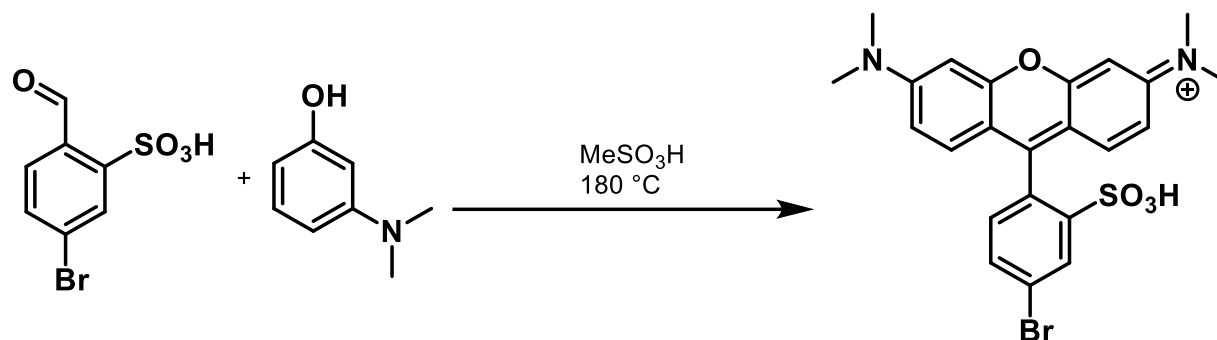
$^1\text{H NMR}$ (900 MHz, CDCl_3) δ 8.27 (d, $J = 8.6$ Hz, 1H), 7.76 (dd, $J = 8.6, 1.9$ Hz, 1H), 7.32 (d, $J = 9.4$ Hz, 2H), 7.24 (s, 1H), 6.80 (dd, $J = 9.4, 2.3$ Hz, 2H), 6.67 – 6.63 (m, 2H), 3.21 (s, 12H).

$^{13}\text{C NMR}$ (226 MHz, CDCl_3) δ 159.33, 157.83, 157.33, 145.49, 133.27, 133.09, 131.44, 131.42, 131.09, 123.21, 114.75, 113.77, 96.28, 40.99.

HR-ESI-MS m/z for $\text{C}_{23}\text{H}_{21}\text{BrN}_2\text{O}_4\text{SNa}^+$ calculated: 523.0298 found: 523.0309 (M+Na).

LR-ESI-MS m/z for $\text{C}_{23}\text{H}_{22}\text{BrN}_2\text{O}_4\text{S}^+$ calculated: 501.05 found: 500.85 (M)





Synthesis of *N*-(9-(4-bromo-2-sulfophenyl)-6-(dimethylamino)-3*H*-xanthen-3-ylidene)-*N*-methylmethanaminium (paraTMR)

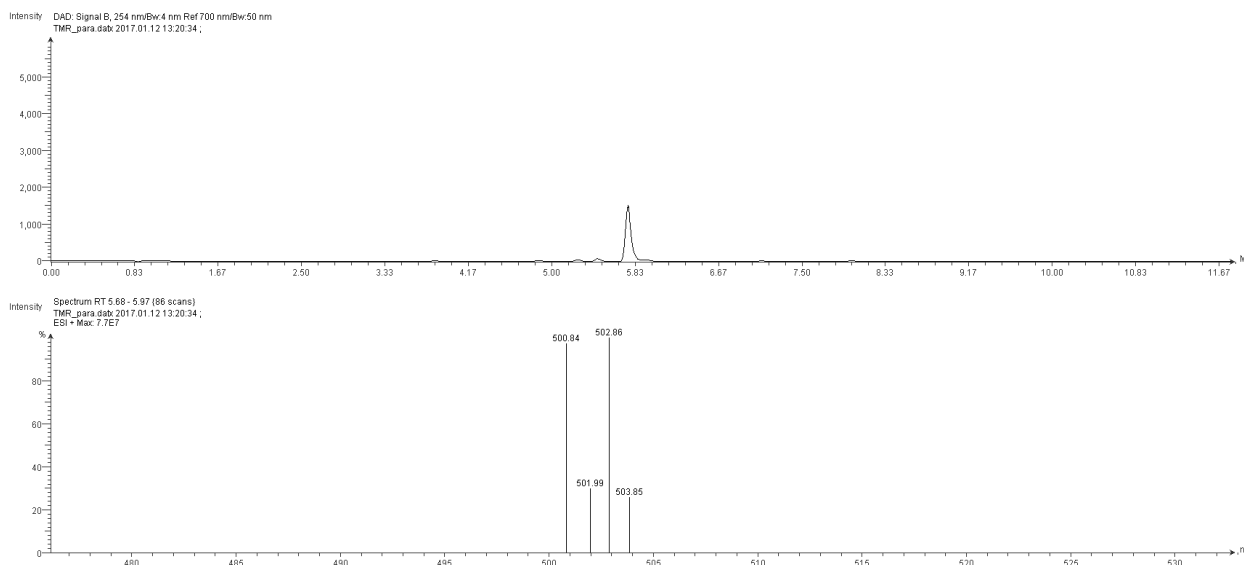
4-bromo-2-sulfobenzaldehyde (300 mg, 1.13 mmol) and 3-(dimethylamino)phenol (310 mg, 2.26 mmol) were placed in a roundbottom flask, dissolved in 3 mL of neat methanesulfonic acid, and stirred for 16 hours at 150 degrees Celsius. After cooling, the reaction mixture was diluted with 30mL water and basified with 10 mL 5M KOH. Products were extracted with ten 50 mL portions of 90:10 DCM:IPA, after which the organic layers were dried over sodium sulfate before being concentrated via rotary evaporation. The resulting dark purple oil was dissolved in 3-5 mL of DCM and then poured into an excess of diethyl ether, precipitating the product. The deep purple solid (201 mg, 35%) was collected via vacuum filtration.

¹H NMR (900 MHz, CDCl₃/MeOD) δ 8.43 – 8.42 (m, 1H), 7.61 (dd, *J* = 8.0, 2.0 Hz, 1H), 7.21 (d, *J* = 9.4 Hz, 2H), 6.92 (d, *J* = 8.0 Hz, 1H), 6.80 (dd, *J* = 9.4, 2.4 Hz, 2H), 6.65 (d, *J* = 2.4 Hz, 2H), 3.19 (s, 12H).

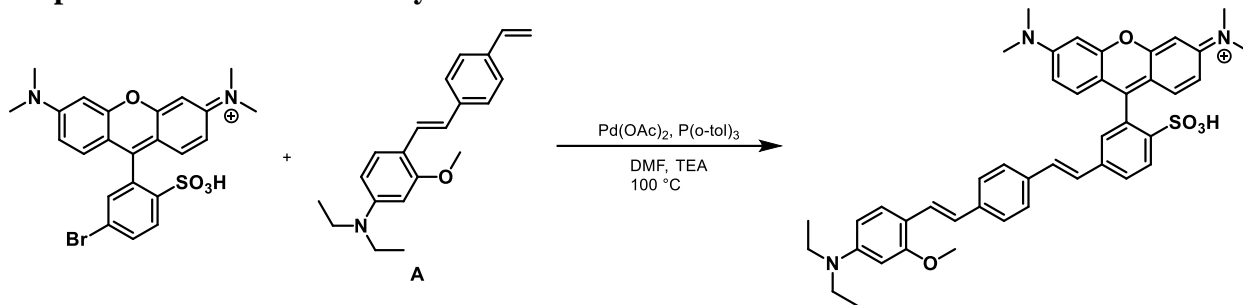
¹³C NMR (226 MHz, CDCl₃/MeOD) δ 157.80, 157.33, 132.96, 132.48, 132.10, 132.05, 131.87, 130.63, 128.76, 128.70, 128.39, 124.21, 114.69, 113.71, 96.10, 40.76.

HR-ESI-MS *m/z* for C₂₃H₂₂BrN₂O₄S⁺ calculated: 523.0298 found: 523.0305 (M+Na).

LR-ESI-MS *m/z* for C₂₃H₂₂BrN₂O₄S⁺ calculated: 501.05 found: 500.84 (M)



Preparation of SulfoRhoVR dyes:



Synthesis of metaSulfoRhoVR_OMe

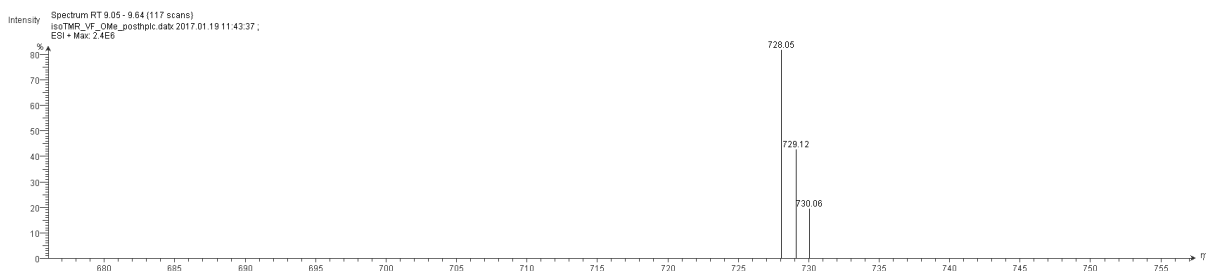
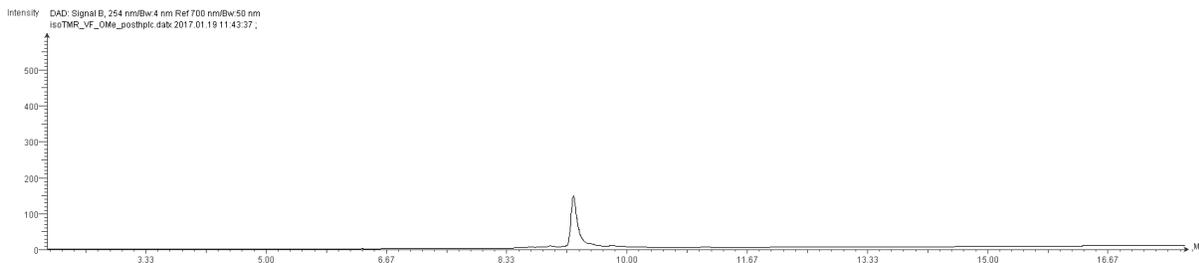
isoTMR (100 mg, 0.20 mmol), A (73 mg, 0.24 mmol), palladium acetate (2 mg, 0.008 mmol), and P(*o*-tol)₃ (5.4 mg, 0.018 mmol) were placed in an oven-dried Schlenk flask. The flask was sealed and evacuated/backfilled with nitrogen (3x). Anhydrous DMF (1 mL) and anhydrous Et₃N (1 mL) were added via syringe and the reaction was stirred for 16 hours at 100 degrees Celsius. After cooling, the reaction mixture was diluted with 10 mL dichloromethane and filtered through celite, which was then washed with methanol. The solvent was removed from the filtrate via rotary evaporation and the resulting residue was dissolved in 5 mL dichloromethane. The mixture was then poured into diethyl ether, resulting in precipitation of a violet solid. The crude solid was isolated via vacuum filtration (82 mg, 56%, 65% pure by HPLC). A small amount of material was purified via RP-HPLC for further characterization (12 mg, 8%).

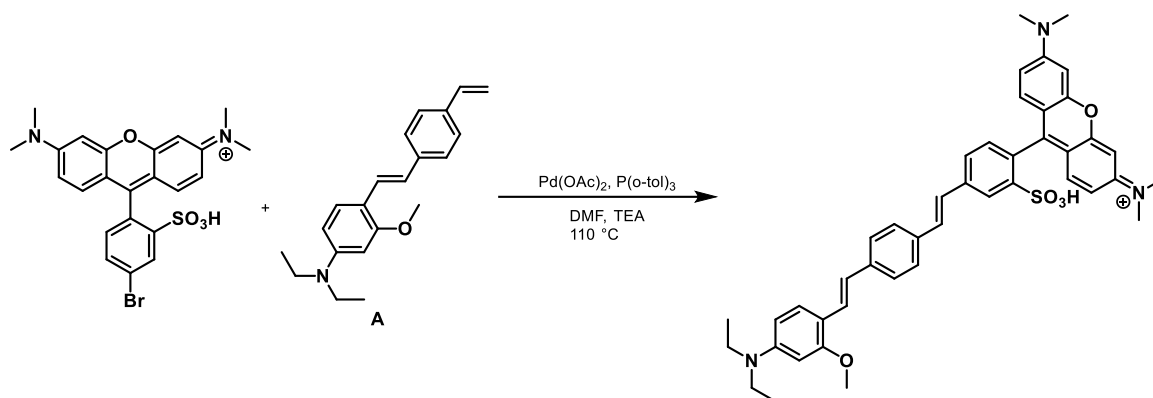
¹H NMR (900 MHz, CDCl₃) δ 8.19 (d, *J* = 9.4 Hz, 1H), 8.02 (s, 1H), 7.69 (d, *J* = 8.3 Hz, 1H), 7.38 (t, *J* = 10.2 Hz, 2H), 7.35 (d, *J* = 7.4 Hz, 3H), 7.31 – 7.29 (m, 2H), 7.15 (s, 1H), 7.06 (d, *J* = 16.2 Hz, 1H), 6.99 (d, *J* = 16.2 Hz, 1H), 6.84 (d, *J* = 16.4 Hz, 1H), 6.82 – 6.80 (m, 2H), 6.66 (d, *J* = 2.3 Hz, 2H), 6.27 (s, 1H), 6.17 (s, 1H), 3.80 (s, 3H), 3.32 (q, *J* = 8.3, 7.6 Hz, 4H), 3.19 (s, 12H), 1.12 (t, *J* = 7.0 Hz, 6H).

¹³C NMR (226 MHz, CDCl₃/MeOD) δ 166.12, 160.64, 158.33, 157.74, 157.21, 143.75, 138.70, 134.40, 134.11, 133.14, 132.23, 131.94, 131.90, 131.07, 129.85, 129.42, 129.08, 128.62, 128.57, 127.49, 127.41, 126.87, 126.61, 126.23, 125.28, 124.01, 114.73, 113.57, 95.82, 67.78, 55.38, 40.57, 29.59.

HR-ESI-MS *m/z* for C₄₄H₄₆N₃O₅S⁺calculated: 728.3153 found: 728.3175.

LR-ESI-MS *m/z* for C₄₄H₄₆N₃O₅S⁺calculated: 728.32 found: 728.05.





Synthesis of paraSulfoRhoVR_OMe

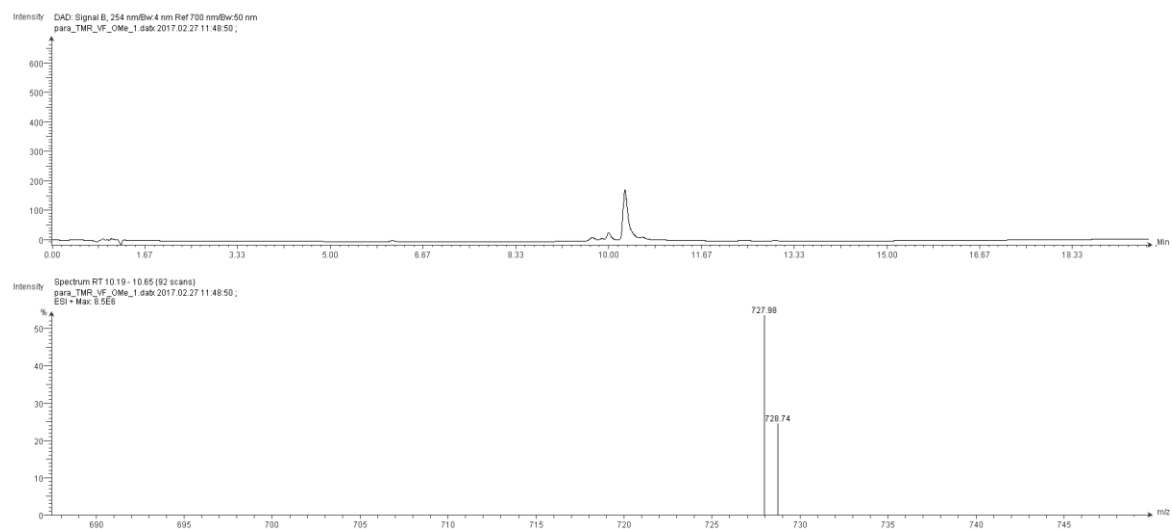
paraTMR (100 mg, 0.20 mmol), **A** (73 mg, 0.24 mmol), palladium acetate (2 mg, 0.008 mmol), and P(*o*-tol)₃ (5.4 mg, 0.018 mmol) were placed in an oven-dried Schlenk flask. The flask was sealed and evacuated/backfilled with nitrogen (3x). Anhydrous DMF (1 mL) and anhydrous Et₃N (1 mL) were added via syringe and the reaction was stirred for 16 hours at 110 degrees Celsius. After cooling, the reaction mixture was diluted with 10 mL dichloromethane and filtered through celite, which was then washed with methanol. The solvent was removed from the filtrate via rotary evaporation and the resulting residue was dissolved in 5 mL dichloromethane. The mixture was then poured into diethyl ether, resulting in precipitation of a violet solid. The crude solid was isolated via vacuum filtration (80 mg, 55%, 50% pure by HPLC). A small amount of material was purified via RP-HPLC for further characterization (8 mg, 6%).

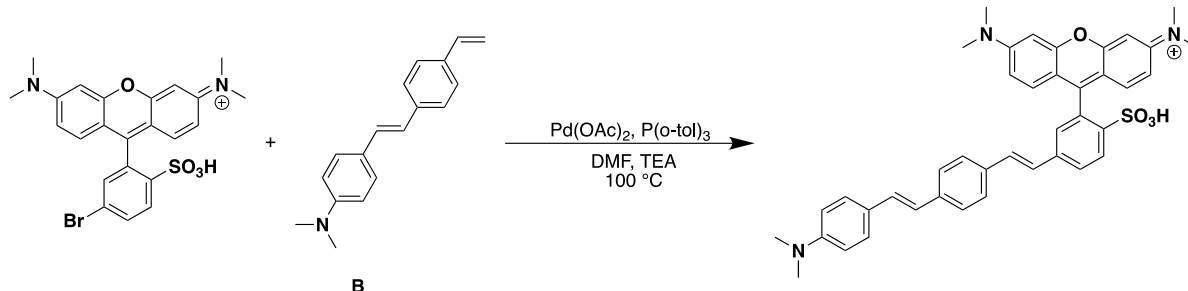
¹H NMR (900 MHz, CDCl₃/MeOD) δ 8.37 (s, 1H), 7.61 (d, *J* = 8.2 Hz, 1H), 7.59 – 7.57 (m, 1H), 7.56 (d, *J* = 9.4 Hz, 1H), 7.53 (dd, *J* = 12.1, 7.1 Hz, 1H), 7.48 (d, *J* = 4.0 Hz, 3H), 7.36 (d, *J* = 16.5 Hz, 1H), 7.25 (d, *J* = 9.6 Hz, 3H), 7.16 (d, *J* = 16.4 Hz, 1H), 7.06 (d, *J* = 16.5 Hz, 1H), 7.02 (d, *J* = 7.7 Hz, 1H), 6.85 (d, *J* = 8.2 Hz, 1H), 6.79 (dd, *J* = 9.5, 2.4 Hz, 1H), 6.64 (d, *J* = 2.4 Hz, 2H), 3.87 (s, 3H), 3.27 (m, 4H) 3.18 (s, 12H), 1.10 (t, *J* = 7.2 Hz, 6H).

¹³C NMR (226 MHz, CDCl₃/MeOD) δ 160.67, 158.08, 157.83, 157.33, 145.55, 139.45, 137.43, 136.34, 133.13, 132.38, 132.05, 130.89, 129.69, 128.76, 128.70, 128.19, 127.84, 127.25, 127.16, 126.74, 126.36, 122.08, 114.87, 113.62, 95.97, 56.11, 40.67, 34.68, 29.70.

HR-ESI-MS *m/z* for C₄₄H₄₆N₃O₅S⁺ calculated: 728.3153 found: 728.3156.

LR-ESI-MS *m/z* for C₄₄H₄₆N₃O₅S⁺ calculated: 728.32 found: 727.98.





Synthesis of metaSulfoRhoVR

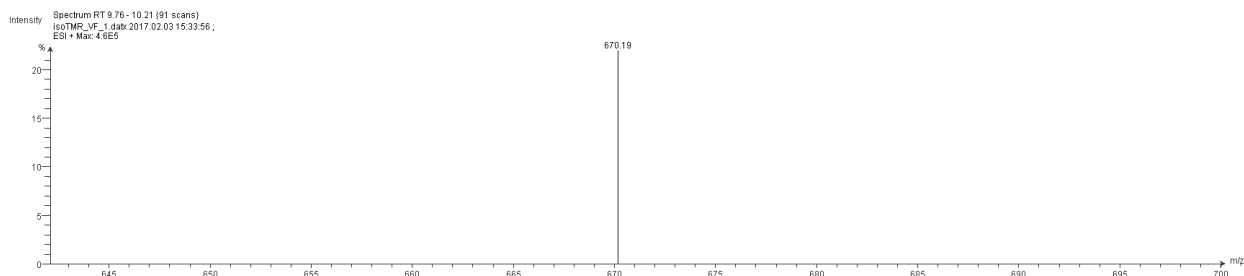
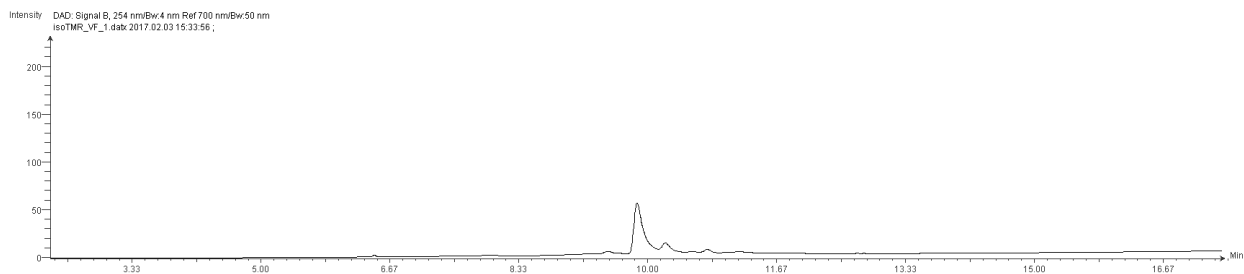
isoTMR (100 mg, 0.19 mmol), **B** (60 mg, 0.24 mmol), palladium acetate (2 mg, 0.008 mmol), and P(*o*-tol)₃ (5.4 mg, 0.018 mmol) were placed in an oven-dried Schlenk flask. The flask was sealed and evacuated/backfilled with nitrogen (3x). Anhydrous DMF (1 mL) and anhydrous Et₃N (1 mL) were added via syringe and the reaction was stirred for 16 hours at 100 degrees Celsius. After cooling, the reaction mixture was diluted with 10 mL dichloromethane and filtered through celite, which was then washed with methanol. The solvent was removed from the filtrate via rotary evaporation and the resulting residue was dissolved in 5 mL dichloromethane. The mixture was then poured into diethyl ether, resulting in precipitation of a brown solid. The crude solid was isolated via vacuum filtration (83 mg, 62%, 70% pure by HPLC). A small amount of material was purified via RP-HPLC for further characterization (9 mg, 7%).

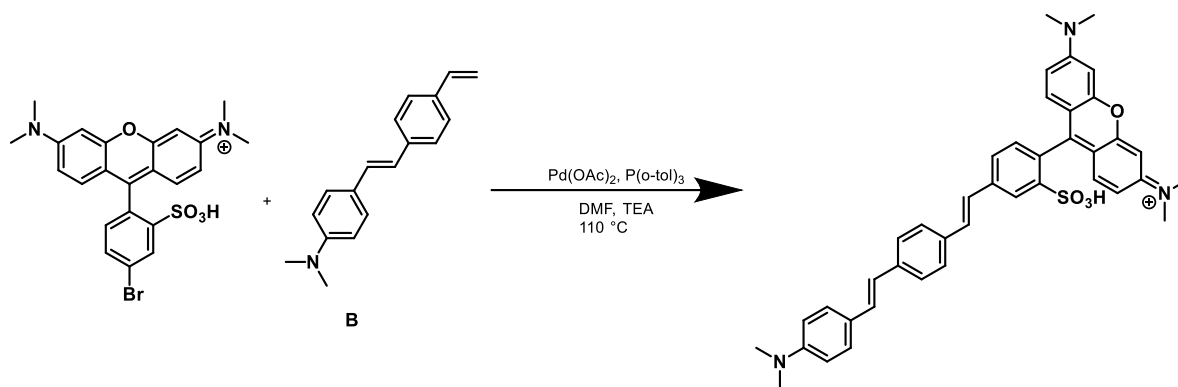
¹H NMR (900 MHz, CDCl₃/MeOD) δ 8.11 (d, *J* = 8.3 Hz, 2H), 7.66 (d, *J* = 9.6 Hz, 2H), 7.37 – 7.33 (m, 5H), 7.22 (d, *J* = 9.5 Hz, 2H), 7.14 (s, 1H), 7.04 (d, *J* = 16.2 Hz, 2H), 6.98 (d, *J* = 16.2 Hz, 1H), 6.96 (d, *J* = 16.2 Hz, 1H), 6.83 (d, *J* = 16.2 Hz, 1H), 6.78 (dt, *J* = 8.2, 4.1 Hz, 3H), 6.64 (d, *J* = 2.3 Hz, 1H), 3.24 (s, 12H), 3.16 (s, 6H).

¹³C NMR (226 MHz, CDCl₃/MeOD) δ 157.68, 157.20, 138.88, 137.94, 134.96, 132.88, 131.10, 129.91, 128.85, 128.63, 127.62, 127.47, 126.93, 126.81, 126.36, 125.54, 124.86, 114.57, 114.00, 113.54, 95.79, 41.38, 40.45.

HR-ESI-MS *m/z* for C₄₁H₄₀N₃O₄S⁺ calculated: 670.2734 found: 670.2738.

LR-ESI-MS *m/z* for C₄₁H₄₀N₃O₄S⁺ calculated: 670.27 found: 670.19.





Synthesis of paraSulfoRhoVR

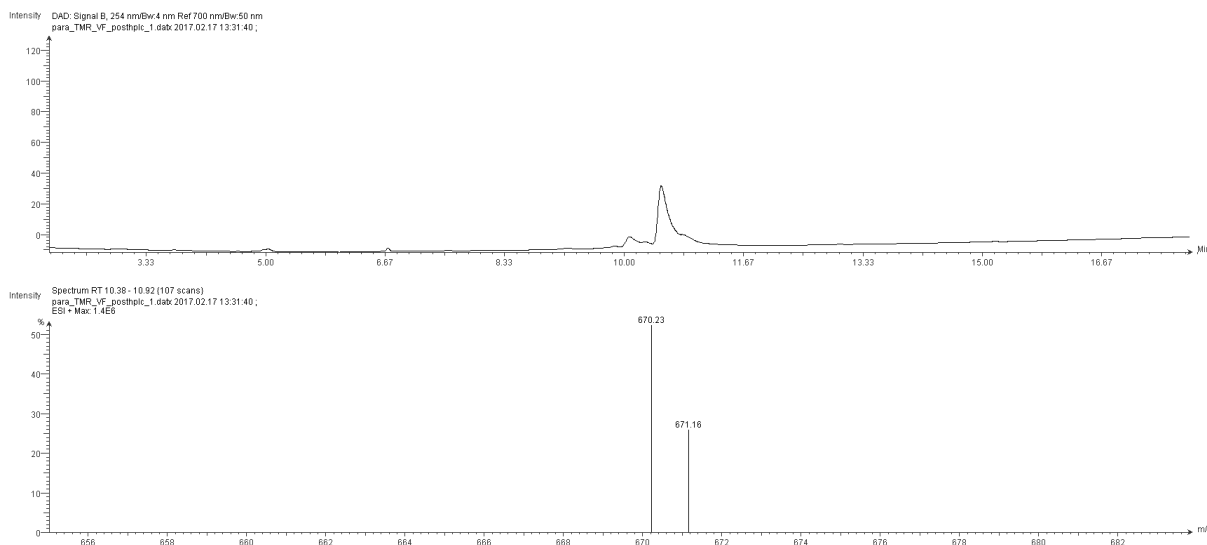
paraTMR (100 mg, 0.19 mmol), **B** (60 mg, 0.24 mmol), palladium acetate (2 mg, 0.008 mmol), and $P(o\text{-tol})_3$ (5.4 mg, 0.018 mmol) were placed in an oven-dried Schlenk flask. The flask was sealed and evacuated/backfilled with nitrogen (3x). Anhydrous DMF (1 mL) and anhydrous Et_3N (1 mL) were added via syringe and the reaction was stirred for 16 hours at 110 degrees Celsius. After cooling, the reaction mixture was diluted with 10 mL dichloromethane and filtered through celite, which was then washed with methanol. The solvent was removed from the filtrate via rotary evaporation and the resulting residue was dissolved in 5 mL dichloromethane. The mixture was then poured into diethyl ether, resulting in precipitation of a brown solid. The crude solid was isolated via vacuum filtration (70 mg, 52%, 85% pure by HPLC). A small amount of material was purified via RP-HPLC for further characterization (13 mg, 10%).

^1H NMR (900 MHz, $\text{CDCl}_3/\text{MeOD}$) δ 8.25 (s, 1H), 7.54 (d, $J = 7.4$ Hz, 1H), 7.40 (d, $J = 7.9$ Hz, 2H), 7.36 (d, $J = 7.9$ Hz, 2H), 7.33 (d, $J = 8.3$ Hz, 2H), 7.16 (d, $J = 9.3$ Hz, 2H), 7.08 (d, $J = 16.3$ Hz, 2H), 6.96 (dd, $J = 18.4, 12.1$ Hz, 3H), 6.83 (d, $J = 16.2$ Hz, 2H), 6.79 (d, $J = 8.1$ Hz, 2H), 6.74 – 6.71 (m, 1H), 6.60 (d, $J = 2.2$ Hz, 1H), 3.18 (s, 12H), 3.11 (s, 6H).

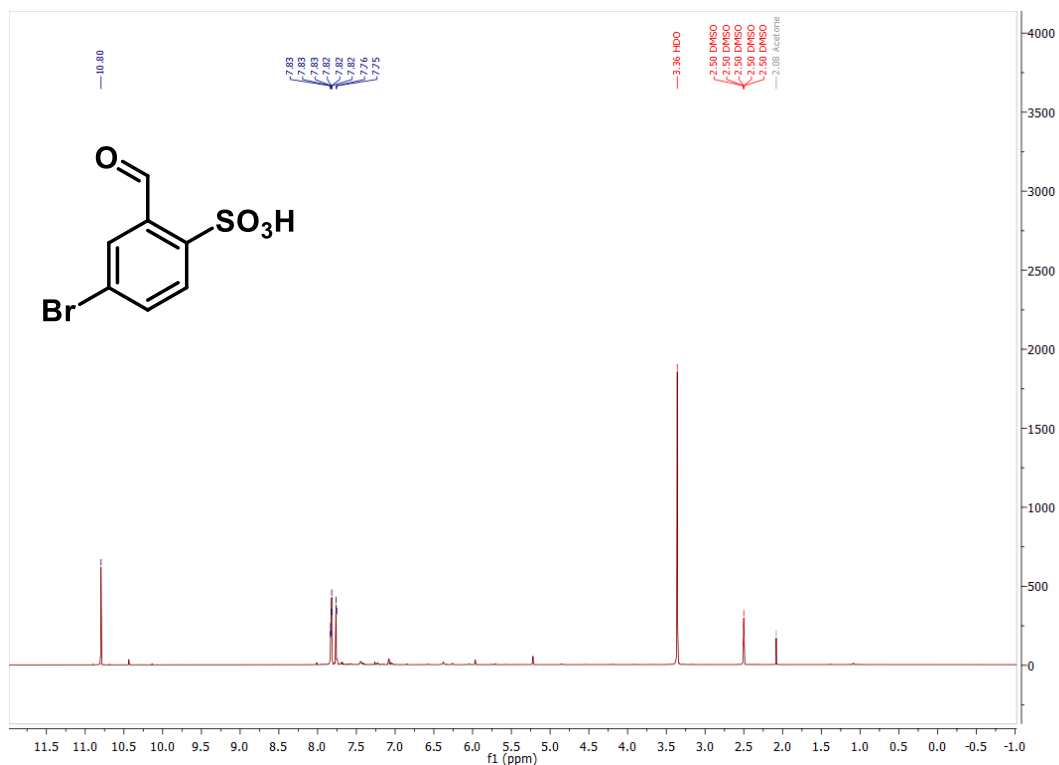
^{13}C NMR (226 MHz, $\text{CDCl}_3/\text{MeOD}$) δ 158.09, 157.62, 139.88, 138.20, 135.75, 133.24, 132.75, 132.25, 131.35, 130.26, 130.14, 129.04, 128.99, 128.79, 128.07, 127.45, 126.83, 126.40, 115.06, 113.87, 96.22, 46.67, 40.80.

HR-ESI-MS m/z for $\text{C}_{41}\text{H}_{40}\text{N}_3\text{O}_4\text{NaS}^+$ calculated: 692.2553 found: 692.2558 (M+Na).

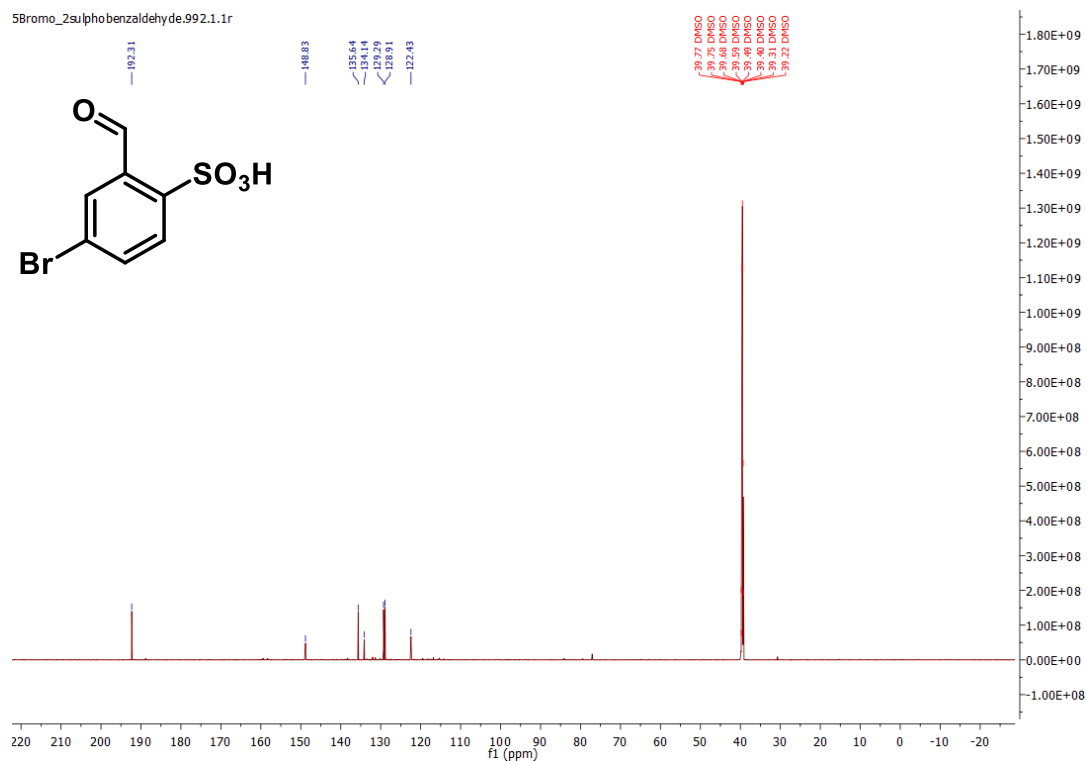
LR-ESI-MS m/z for $\text{C}_{41}\text{H}_{40}\text{N}_3\text{O}_4\text{S}^+$ calculated: 670.27 found: 670.23.



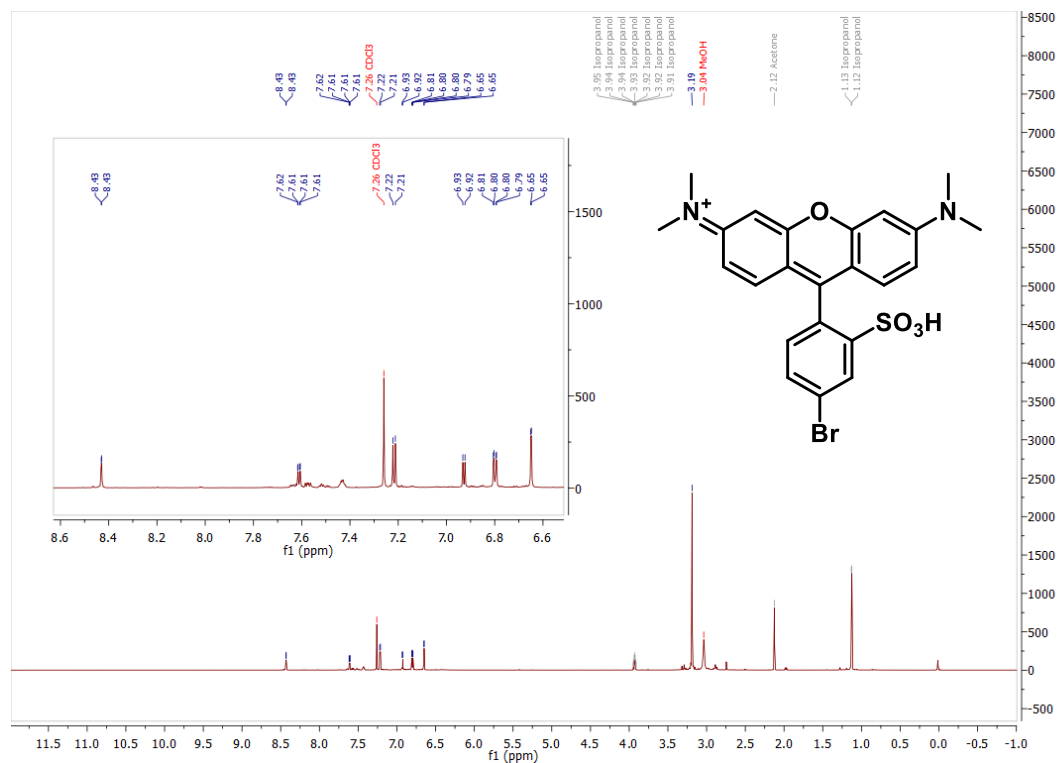
NMR Spectra



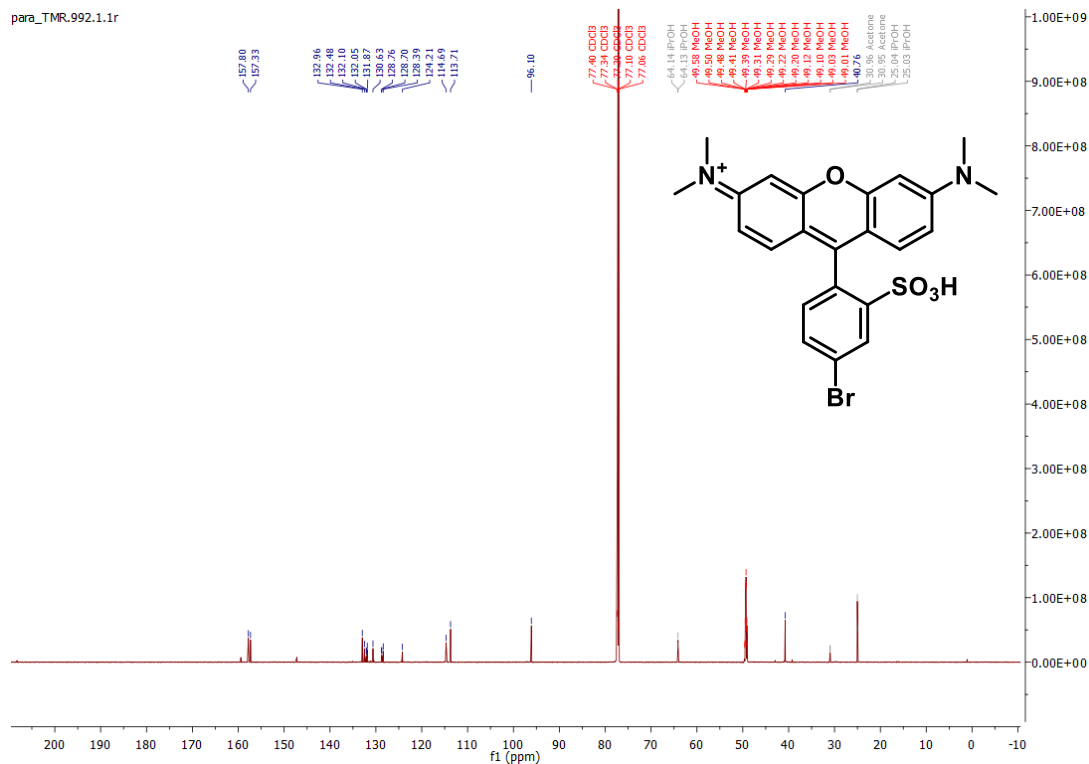
¹H NMR of 5-bromo-2-sulfobenzaldehyde



¹³C NMR of 5-bromo-2-sulfobenzaldehyde

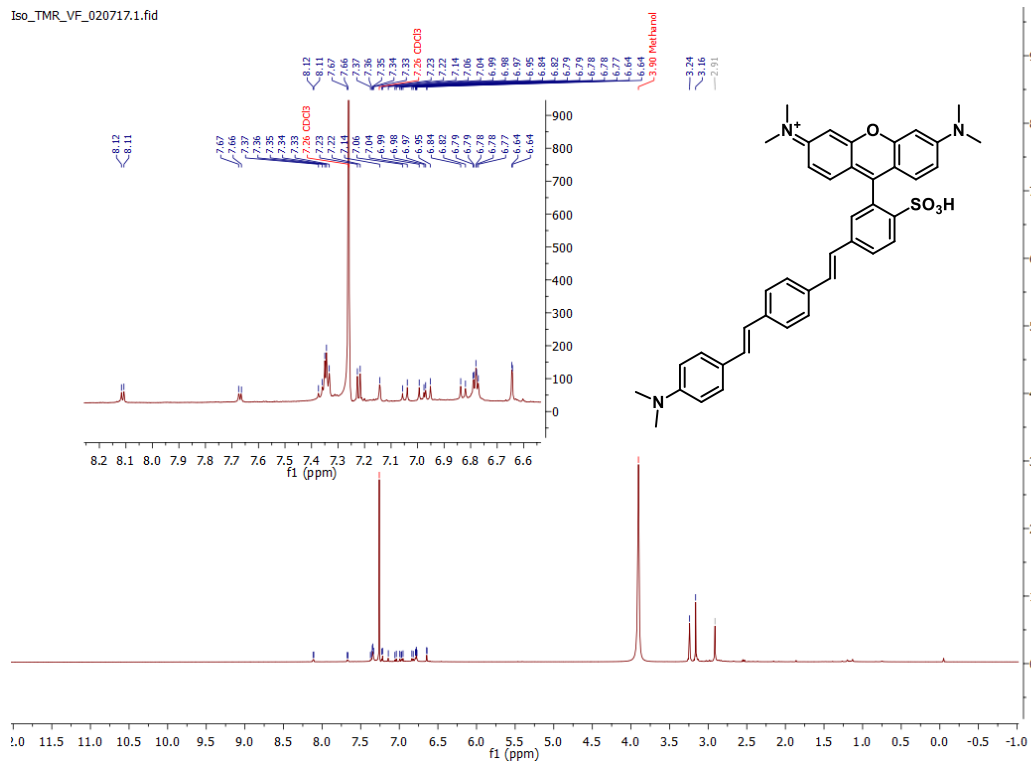


¹H NMR of para-sulfoTMR



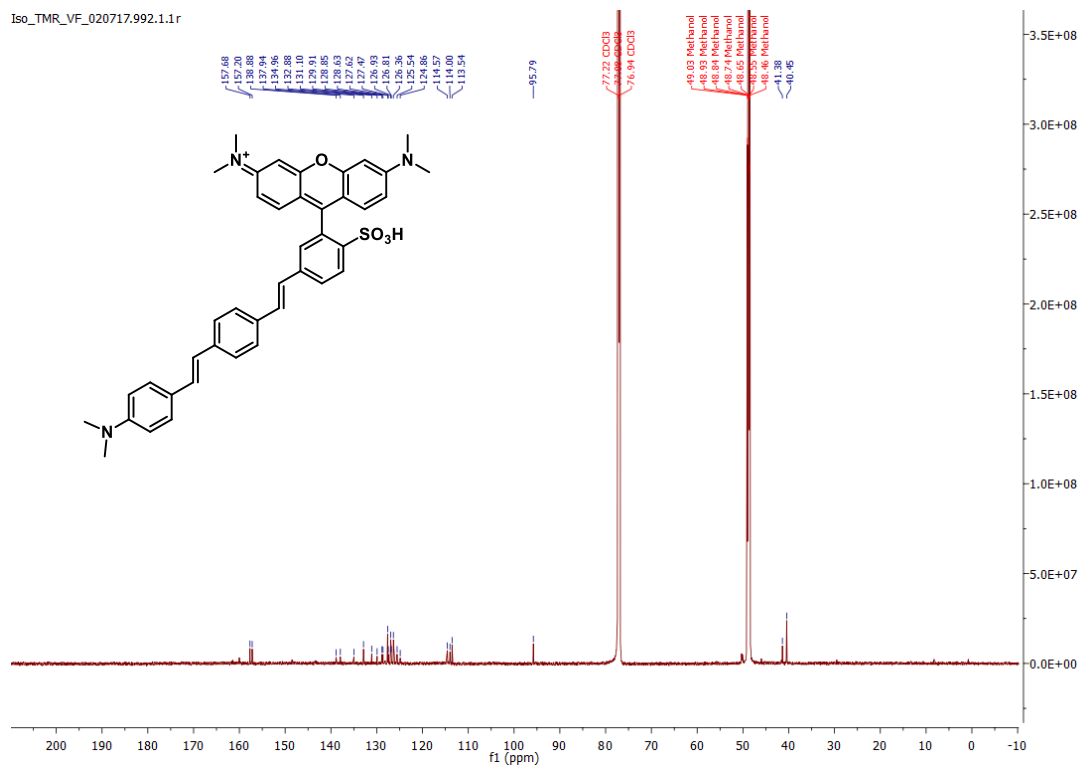
¹³C NMR of para-sulfoTMR

Iso_TMR_VF_020717.1.fid



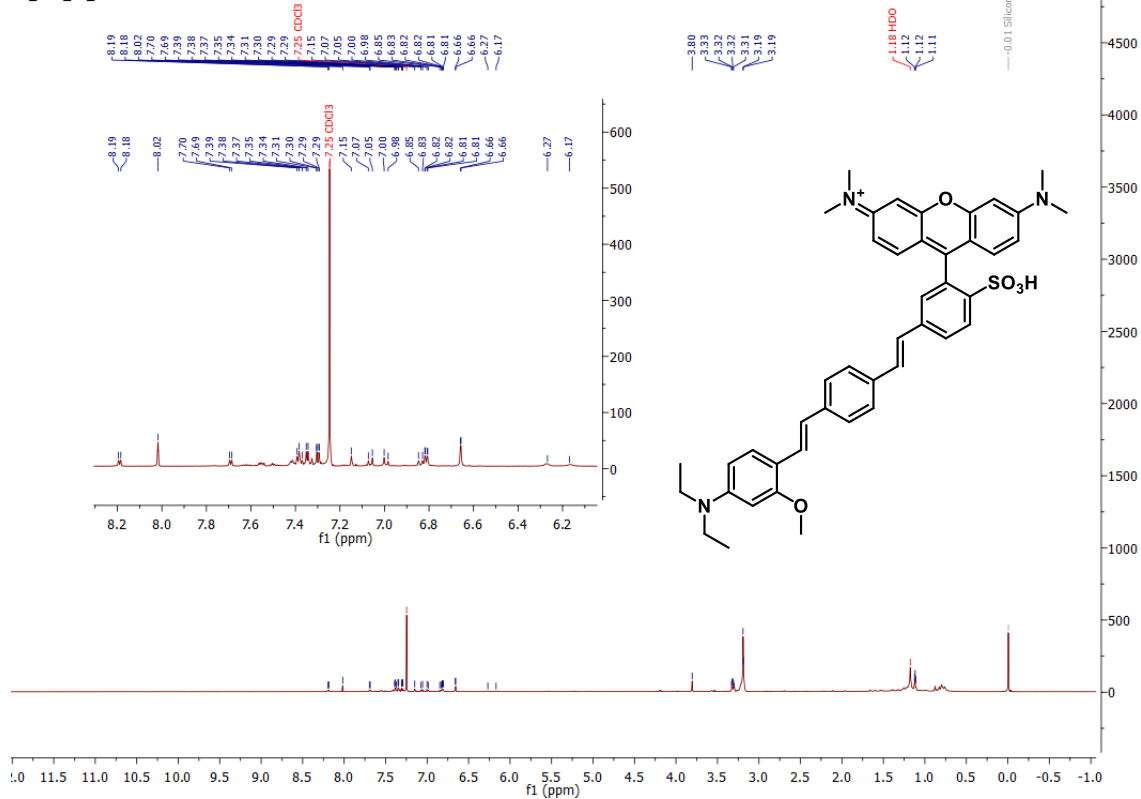
¹H NMR of metaSulfoRhoVR

Iso_TMR_VF_020717.992.1.1r



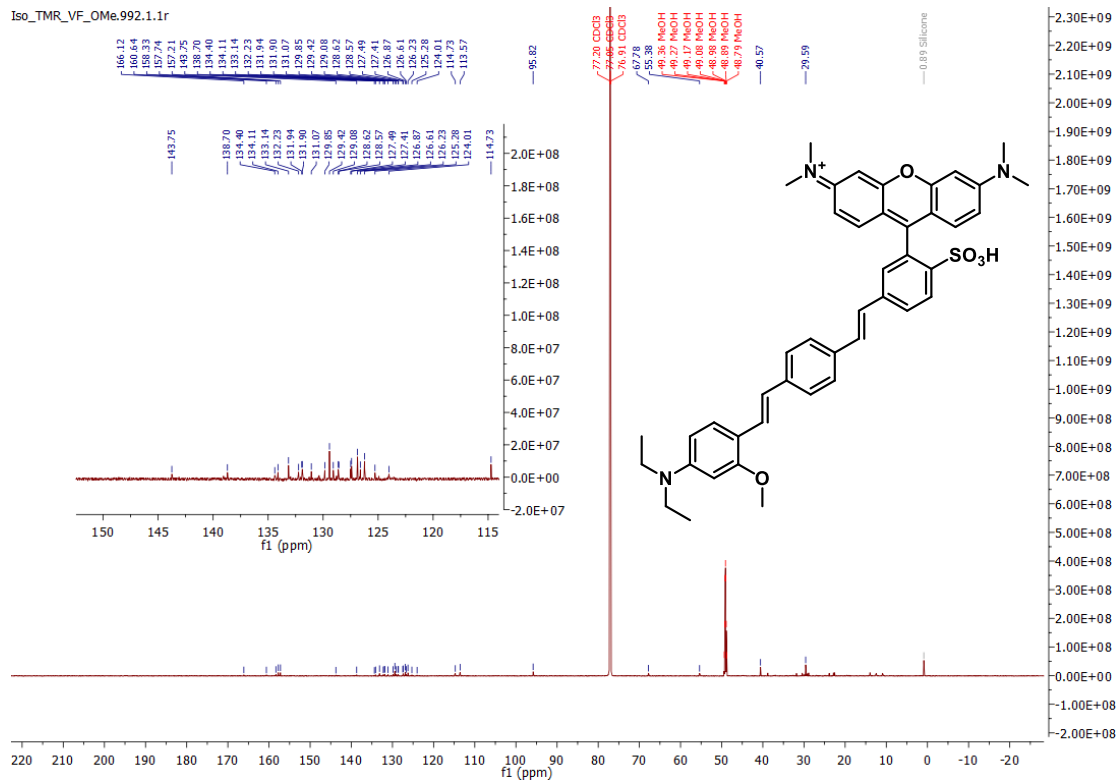
¹³C NMR of metaSulfoRhoVR

Iso_TMR_VF_OMe.1.fid



¹H NMR of metaSulfoRhoVR_OMe

Iso_TMR_VF_OMe.992.1.1r



¹³C NMR of metaSulfoRhoVR_OMe

3.7 References

1. Scanziani, M., and Hausser, M. (2009) Electrophysiology in the age of light, *Nature* 461, 930-939.
2. Buzsaki, G., Anastassiou, C. A., and Koch, C. (2012) The origin of extracellular fields and currents--EEG, ECoG, LFP and spikes, *Nat Rev Neurosci* 13, 407-420.
3. Buzsaki, G., Stark, E., Berenyi, A., Khodagholy, D., Kipke, D. R., Yoon, E., and Wise, K. D. (2015) Tools for probing local circuits: high-density silicon probes combined with optogenetics, *Neuron* 86, 92-105.
4. Jun, J. J., Steinmetz, N. A., Siegle, J. H., Denman, D. J., Bauza, M., Barbarits, B., Lee, A. K., Anastassiou, C. A., Andrei, A., Aydin, C., Barbic, M., Blanche, T. J., Bonin, V., Couto, J., Dutta, B., Gratiy, S. L., Gutnisky, D. A., Hausser, M., Karsh, B., Ledochowitsch, P., Lopez, C. M., Mitelut, C., Musa, S., Okun, M., Pachitariu, M., Putzeys, J., Rich, P. D., Rossant, C., Sun, W. L., Svoboda, K., Carandini, M., Harris, K. D., Koch, C., O'Keefe, J., and Harris, T. D. (2017) Fully integrated silicon probes for high-density recording of neural activity, *Nature* 551, 232-236.
5. Einevoll, G. T., Kayser, C., Logothetis, N. K., and Panzeri, S. (2013) Modelling and analysis of local field potentials for studying the function of cortical circuits, *Nat Rev Neurosci* 14, 770-785.
6. Shew, W. L., Bellay, T., and Plenz, D. (2010) Simultaneous multi-electrode array recording and two-photon calcium imaging of neural activity, *J Neurosci Methods* 192, 75-82.
7. Busche, M. A., Kekus, M., Adelsberger, H., Noda, T., Forstl, H., Nelken, I., and Konnerth, A. (2015) Rescue of long-range circuit dysfunction in Alzheimer's disease models, *Nat Neurosci* 18, 1623-1630.
8. Minderer, M., Liu, W., Sumanovski, L. T., Kugler, S., Helmchen, F., and Margolis, D. J. (2012) Chronic imaging of cortical sensory map dynamics using a genetically encoded calcium indicator, *J Physiol* 590, 99-107.
9. Rossi, L. F., Wykes, R. C., Kullmann, D. M., and Carandini, M. (2017) Focal cortical seizures start as standing waves and propagate respecting homotopic connectivity, *Nat Commun* 8, 217.
10. Petersen, C. C., Hahn, T. T., Mehta, M., Grinvald, A., and Sakmann, B. (2003) Interaction of sensory responses with spontaneous depolarization in layer 2/3 barrel cortex, *Proc Natl Acad Sci U S A* 100, 13638-13643.
11. Katzner, S., Nauhaus, I., Benucci, A., Bonin, V., Ringach, D. L., and Carandini, M. (2009) Local origin of field potentials in visual cortex, *Neuron* 61, 35-41.
12. Carandini, M., Shimaoka, D., Rossi, L. F., Sato, T. K., Benucci, A., and Knopfel, T. (2015) Imaging the awake visual cortex with a genetically encoded voltage indicator, *J Neurosci* 35, 53-63.
13. Mohajerani, M. H., Chan, A. W., Mohsenvand, M., LeDue, J., Liu, R., McVea, D. A., Boyd, J. D., Wang, Y. T., Reimers, M., and Murphy, T. H. (2013) Spontaneous cortical activity alternates between motifs defined by regional axonal projections, *Nat Neurosci* 16, 1426-1435.
14. Chen, Y., Palmer, C. R., and Seidemann, E. (2012) The relationship between voltage-sensitive dye imaging signals and spiking activity of neural populations in primate V1, *J Neurophysiol* 107, 3281-3295.
15. Shoham, D., Glaser, D. E., Arieli, A., Kenet, T., Wijnbergen, C., Toledo, Y., Hildesheim, R., and Grinvald, A. (1999) Imaging cortical dynamics at high spatial and temporal resolution with novel blue voltage-sensitive dyes, *Neuron* 24, 791-802.

16. Slovin, H., Arieli, A., Hildesheim, R., and Grinvald, A. (2002) Long-term voltage-sensitive dye imaging reveals cortical dynamics in behaving monkeys, *J Neurophysiol* 88, 3421-3438.
17. Lebeuf, R., Ferezou, I., Rossier, J., Arseniyadis, S., and Cossy, J. (2009) Straightforward synthesis of the near-infrared fluorescent voltage-sensitive dye RH1691 and analogues thereof, *Org Lett* 11, 4822-4825.
18. Kuhn, B., Fromherz, P., and Denk, W. (2004) High sensitivity of Stark-shift voltage-sensing dyes by one- or two-photon excitation near the red spectral edge, *Biophys J* 87, 631-639.
19. Marshall, J. D., Li, J. Z., Zhang, Y., Gong, Y., St-Pierre, F., Lin, M. Z., and Schnitzer, M. J. (2016) Cell-Type-Specific Optical Recording of Membrane Voltage Dynamics in Freely Moving Mice, *Cell* 167, 1650-1662 e1615.
20. Li, L. S. (2007) Fluorescence probes for membrane potentials based on mesoscopic electron transfer, *Nano Lett* 7, 2981-2986.
21. [21] Kulkarni, R. U., Yin, H., Pourmandi, N., James, F., Adil, M. M., Schaffer, D. V., Wang, Y., and Miller, E. W. (2017) A Rationally Designed, General Strategy for Membrane Orientation of Photoinduced Electron Transfer-Based Voltage-Sensitive Dyes, *ACS Chem Biol* 12, 407-413.
22. Woodford, C. R., Frady, E. P., Smith, R. S., Morey, B., Canzi, G., Palida, S. F., Araneda, R. C., Kristan, W. B., Jr., Kubiak, C. P., Miller, E. W., and Tsien, R. Y. (2015) Improved PeT molecules for optically sensing voltage in neurons, *J Am Chem Soc* 137, 1817-1824.
23. Kulkarni, R. U., Kramer, D. J., Pourmandi, N., Karbasi, K., Bateup, H. S., and Miller, E. W. (2017) Voltage-sensitive rhodol with enhanced two-photon brightness, *Proc Natl Acad Sci U S A* 114, 2813-2818.
24. Deal, P. E., Kulkarni, R. U., Al-Abdullatif, S. H., and Miller, E. W. (2016) Isomerically Pure Tetramethylrhodamine Voltage Reporters, *J Am Chem Soc* 138, 9085-9088.
25. Huang, Y. L., Walker, A. S., and Miller, E. W. (2015) A Photostable Silicon Rhodamine Platform for Optical Voltage Sensing, *Journal of the American Chemical Society* 137, 10767-10776.
26. Sandmeyer, T. (1896) Red dye, John R. Geigy & Co., Switz. .
27. Kovi, R., Nampalli, S., and Tharial, P. X. (2008) Process for preparation and purification of isosulfan blue, p 7pp.; Chemical Indexing Equivalent to 149:533918 (WO), Apicore, LLC, USA .
28. Xu, C., Zipfel, W., Shear, J. B., Williams, R. M., and Webb, W. W. (1996) Multiphoton fluorescence excitation: new spectral windows for biological nonlinear microscopy, *Proc Natl Acad Sci U S A* 93, 10763-10768.
29. Del Bonis-O'Donnell, J. T., Page, R. H., Beyene, A. G., Tindall, E. G., McFarlane, I. R., and Landry, M. P. (2017) Dual Near-Infrared Two-Photon Microscopy for Deep-Tissue Dopamine Nanosensor Imaging, *Adv Funct Mater* 27.
30. Xu, C., and Webb, W. W. (1996) Measurement of two-photon excitation cross sections of molecular fluorophores with data from 690 to 1050 nm, *J Opt Soc Am B* 13, 481-491.
31. Linden, H., Tetzlaff, T., Potjans, T. C., Pettersen, K. H., Grun, S., Diesmann, M., and Einevoll, G. T. (2011) Modeling the spatial reach of the LFP, *Neuron* 72, 859-872.

Chapter 4

A Rational-Designed Strategy for Membrane Orientation of Photoinduced Electron-Transfer-Based Voltage-Sensitive Dyes

Abstract

Voltage imaging with fluorescent dyes offers promise for interrogating the complex roles of membrane potential in coordinating the activity of neurons in the brain. Yet, low sensitivity often limits the broad applicability of optical voltage indicators. In this chapter, we use molecular dynamics (MD) simulations to guide the design of new, ultra-sensitive fluorescent voltage indicators that use photoinduced electron transfer (PeT) as a voltage-sensing switch. MD simulations predict an approximately 16% increase in voltage sensitivity resulting purely from improved alignment of dye with the membrane. We confirm this theoretical finding by synthesizing 9 new voltage-sensitive (VoltageFluor, or VF) dyes and establishing that all of them display the expected improvement of approximately 19%. This synergistic outworking of theory and experiment enabled computational and theoretical estimation of VF dye orientation in lipid bilayers and has yielded the most sensitive PeT-based VF dye to date. We use this new voltage indicator to monitor voltage spikes in neurons from rat hippocampus and human pluripotent stem cell-derived dopaminergic neurons.

This chapter is based on the publication in *ACS Chemical Biology* entitled “A rationally-designed, general strategy for membrane orientation of photoinduced electron transfer-based voltage-sensitive dyes.”

4.1. Dye Membrane Orientation as a Factor in Voltage Sensitivity

The development of fluorescent indicators for biological analytes has revolutionized our ability to interrogate biochemistry and biophysics in living cells. However, the design of fluorescent dyes and sensors remains an outstanding challenge in the field.¹⁻¹² Our group has recently initiated a program to build new chemical indicators for sensing membrane potential,¹³⁻¹⁵ in order to further understand the roles that membrane voltage plays, not only in excitable cells, such as neurons and cardiomyocytes, but also in non-excitable cells in the rest of the body. Traditional methods to measure membrane potential rely on invasive electrodes, introduced via pipette or on micro or nano-arrays. Voltage imaging with fluorescent probes is an attractive solution because such imaging circumvents problems of low-throughput, low spatial resolution, and high invasiveness associated with more traditional electrode-based techniques.¹⁶⁻¹⁸ Our lab is developing VoltageFluor, or VF, dyes which are a small molecule platform for voltage imaging that operates via a photoinduced electron transfer (PeT) quenching mechanism^{19,20} to directly image transmembrane voltage changes.^{13,14,21,22} Previously reported VF dyes have proven useful for measuring membrane potential in a number of biological contexts ranging from isolated synaptic vesicles²³ to intact leech neuronal ganglia^{24,25} to stem cell-derived cardiomyocytes,^{26,27} among others.^{28,29} However, a rational design scheme for VF dyes remains elusive, due in part to our incomplete understanding of the biophysical properties influencing voltage sensitivity in the VoltageFluor scaffolds.

We therefore desired to study and improve a single, key aspect of the PeT-quenching mechanism²⁰ of VF dyes. We propose that VF dyes sense voltage via a PeT-based mechanism where the transmembrane potential of the cell strongly influences the rate of PeT: at hyperpolarizing, or negative, potentials, PeT is accelerated and fluorescence is quenched. At depolarizing, or positive, voltages, fluorescence increases as the rate of PeT decreases. Pioneering work by Loew and co-workers modeled the voltage sensitivity of electrochromic voltage-sensitive dyes and proposed that the magnitude of the molecular Stark effect, or perturbation of the chromophore orbital energies, which gives rise to the voltage sensitivity of these compounds, is proportional to the following expression:^{30,31}

$$\Delta F/F \propto \Delta G = q\vec{r} \cdot \vec{E} \quad \text{Equation 4.1}$$

Where $\Delta F/F$ is the fractional voltage sensitivity of a dye, ΔG represents the change in energy associated with the shift in wavelength, q is the effective charge transferred, \vec{r} is the distance that quantity q travels and \vec{E} is the electric field. By extension to PeT-based voltage sensitive dyes, the voltage sensitivity should be proportional to the change in driving force for PeT, which may be modeled by a similar equation when the transmembrane potential is within a physiologically-relevant range.²⁰ Because the interaction between the transferred electron and the membrane potential is highest when the electron transfer vector and electric field vectors are aligned and at a minimum when perpendicular, equation 4.1 can be rewritten as

$$\Delta F/F \propto \Delta G = qrE \cos \theta \quad \text{Equation 4.2}$$

where θ is the angle of displacement, or tilt, between the electron transfer vector and the electric field vector (**Figure 4.1a-c**).

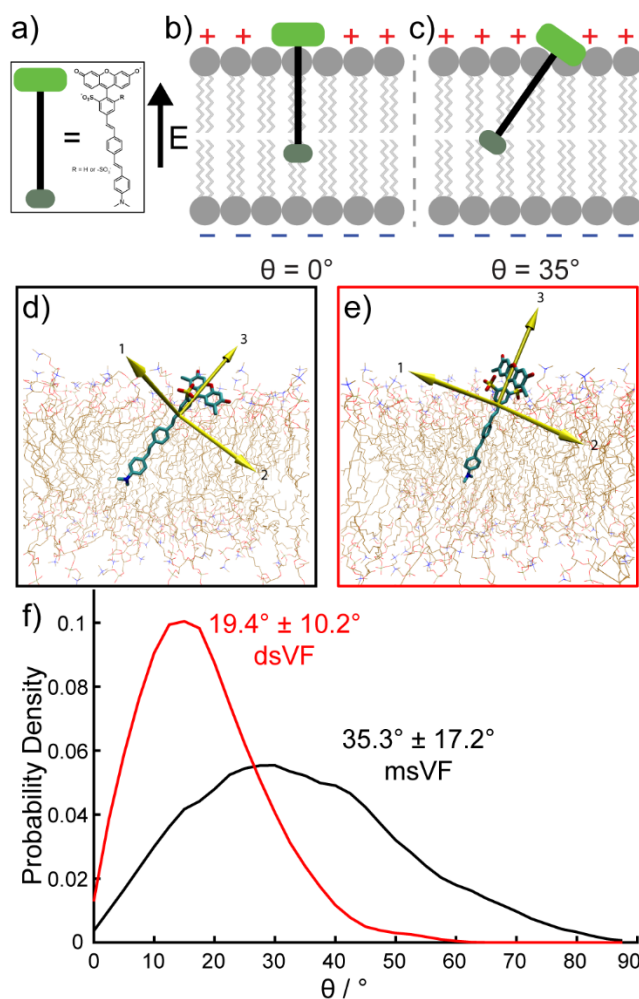


Figure 4.1. Orientation of ms and ds VF dyes. Schematic representation of a) VF dye alignment in the plasma membrane. b) Maximum voltage sensitivity is predicted when $\theta = 0^\circ$ (left) and is lowest when $\theta = 90^\circ$ (not shown). c) Intermediate values of θ (right) reduce voltage sensitivity. Snapshots of MD simulations in POPC lipid bilayers show d) msVF and e) dsVF. Yellow arrows indicate principal components. f) Plot of probability density vs. angle of displacement between the 3rd principle component (the long axis) of VF dyes and the membrane normal.

Our initial assumption was that the tilt angle θ was close to 0° , thus giving us the maximum voltage sensitivity for a given dye, where q , r , and E remain constant. To test this hypothesis, ascertain how VF dyes orient in the membrane, and propose new structural motifs for voltage sensing, we turned to molecular modeling to measure the tilt angle of VF2.1.Cl, a prototypical VF dye, in a simulated lipid bilayer.

4.2 Molecular Modeling of VoltageFluor Dyes

We parameterized VF2.1.Cl with the CHARMM general force field ³² (**Figure 4.2**) and then performed molecular dynamics (MD) simulations of the VF dye embedded in a 1-palmitoyl-2-

oleoyl-*sn*-glycerol-3-phosphocholine (POPC) lipid bilayer, as a simplified model of a mammalian cell membrane.^{33,34}

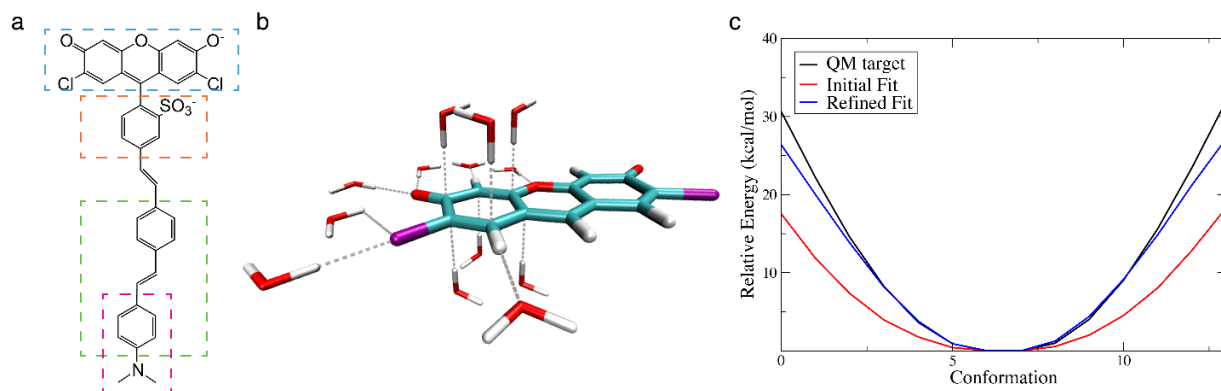


Figure 4.2. Parameterization of the msVF molecule in CHARMM general force field. (a) Division of msVF into four parts: xanthene derivative (blue), benzenesulfonate (orange), (E)-stilbene (green), and N,N-dimethylaniline (magenta). (b) Interaction energy calculation between atoms on the xanthene derivative and a TIP3p water. The calculation was performed at the MP2/6-31G* level for the two chlorine atoms (colored in purple) and at the HF/6-31G* level for the remaining ones. Due to the symmetry of the compound, calculation was only performed on half of the atoms. (c) Optimization of the dihedral OG312-CG2R61-CG2R61-CLGR1 (see topology and parameter files of msVF in the SI) through potential energy scan performed via ftk and Gaussian 09.

By modeling the behavior of VF2.1.Cl in a POPC lipid bilayer, we aimed to both make observations regarding the tilt angle and propose structural modifications that we could then synthesize to assess changes in voltage sensitivity. We performed three replicates of ~500 ns molecular dynamics simulations of VF2.1.Cl in a pure POPC membrane and sampled the tilt angle θ (between the long axis of VF and the membrane normal) every 5 ps via principle component analysis (PCA). As shown in **Figure 4.1d**, the 2' sulfonate of VF2.1.Cl localized primarily at the lipid:water interface, presumably to avoid burying the charged sulfonate in the non-polar lipid groups. Because the sulfonate of VF2.1.Cl is unsymmetrically positioned off the main axis of VF2.1.Cl, this results in a considerable tilt, with an average angle of 35° (**Figure 4.1d and f**). Furthermore, the molecule appeared to be rather “floppy” in the membrane, with a standard deviation in the tilt angle of 17° (**Fig. 4.1f**) and a correlation time of 9.7 ns (± 2.6 ns, \pm SEM, $n=3$ simulations) (**Figure 4.3**). An average tilt angle of 35° implies that the voltage sensitivity of VF2.1.Cl is only about 82% (cosine of 35°) of the theoretical maximum, assuming q and r remain the same. We wondered whether “straightening” VF dyes in the membrane would prove a general method for enhancing voltage sensitivity by approximately 22% ($1/\cosine 35^\circ$).

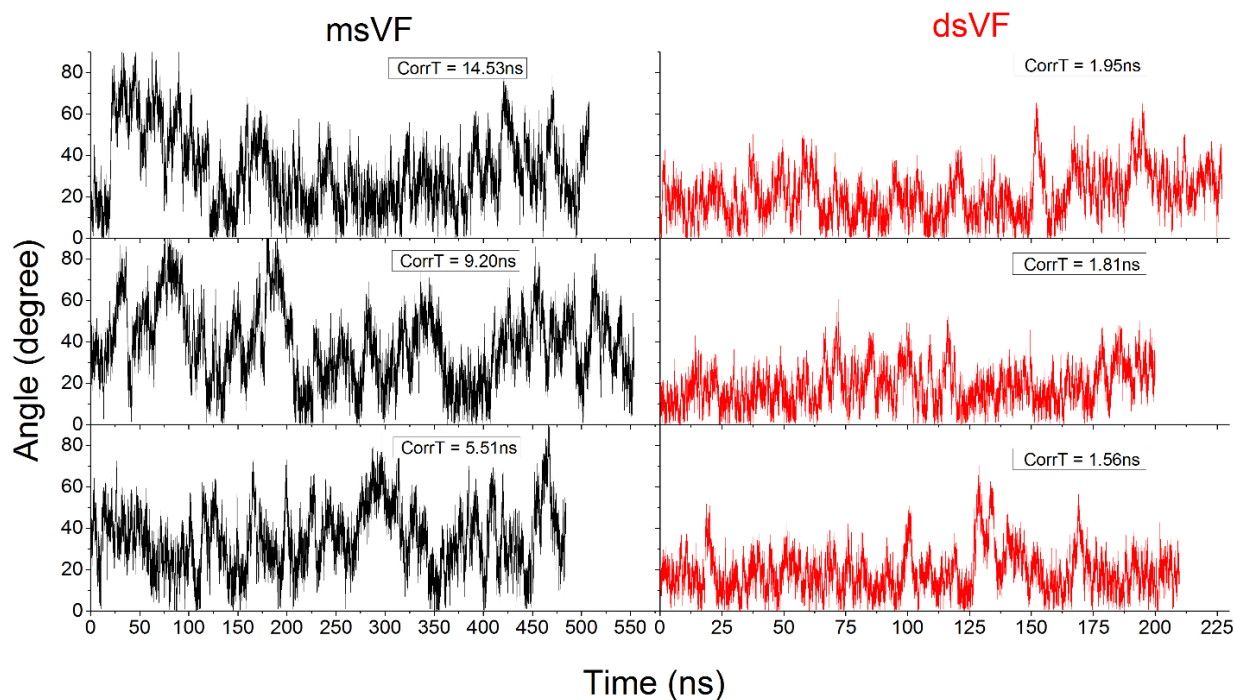


Figure 4.3. Time traces of the tilt angle measured from the three replicas of msVF (left) and dsVF (right) simulations. The correlation time (corrT) of the angle as determined from each simulation is labeled.

We reasoned that the tilt angle of the VF dye could be reduced in a straightforward manner by adding a second sulfonate group in the *ortho*-position on the meso-aryl ring of the xanthen chromophore (**Figure 4.1a-c**). We hoped the new, doubly-sulfonated, disulfoVF dyes (dsVF), with two opposing sulfonate groups at the 2'- and 6'-positions, would have both reduced overall tilt angle and increased rigidity since exposing one sulfonate to bulk water via tilting the whole molecule would require the other sulfonate to become buried in the non-polar lipid layer. Overall, we hypothesized that smaller fluctuations in the tilt angle of dsVF would cause an improvement in voltage sensitivity relative to monosulfoVF dyes (msVF).

We used MD simulations to test whether the proposed dsVF dye displays enhanced alignment within a model membrane relative to its monosulfo counterpart. MD simulations of dsVF2.1.Cl (**Figure 4.1d-e**) reveal a significant reduction in the tilt angle, θ , compared to msVF2.1.Cl: $19^\circ \pm 10^\circ$ for dsVF2.1.Cl and $35^\circ \pm 17^\circ$ for msVF2.1.Cl (**Figure 4.1f**). Compared to msVF, dsVF displays less conformational flexibility within the lipid bilayer, as reflected in the smaller standard deviation of θ values for dsVF2.1.Cl (10° for dsVF vs. 17° for msVF). Analysis of the correlation time for msVF2.1.Cl reveals a much longer periodicity in θ fluctuations (9.7 ± 2.7 ns; \pm SEM, $n = 3$ simulations) with larger magnitude swings away from the average orientation (**Figure 4.3**). In contrast, dsVF2.1.Cl has a much shorter period (1.8 ± 0.1 ns; \pm SEM, $n = 3$ simulations) characterized by smaller fluctuations in the average angle of displacement (**Figure 4.2b**).

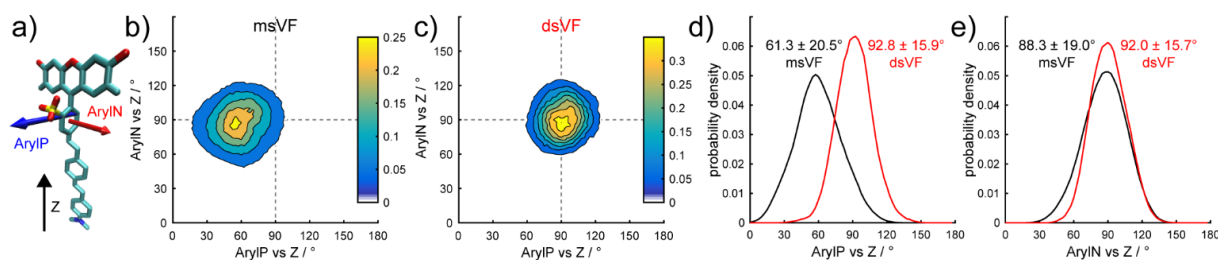


Figure 4.4. Calculated orientation of msVF and dsVF in a POPC lipid bilayer. a) Definition of vectors used to examine angles in VF dyes. “ArylP” describes the vector parallel to the *meso*-aryl ring; “ArylN” describes the vector normal to the plane of the aryl ring; and “Z” is the membrane normal. Contour plots describe the the ArylP vs Z and ArylN vs Z dihedral angles for a given snapshot of the simulation for b) msVF and c) dsVF. The dotted lines serve as a visual guide for a perfect 90° orientation between the dye and the membrane normal. The distribution of dihedral angles sampled during a simulation for d) ArylP vs Z and e) ArylN vs Z are plotted for both msVF (black) and dsVF (red).

The increased rigidity of the dsVF dye comes primarily from a restriction in the movement of the dye in a single plane. Molecular orientation in the plane of the sulfonates (defined as the angle between the vector parallel to the meso ring system, “ArylP,” and the membrane normal “Z” (**Figure 4.4a**) becomes more rigid upon going from msVF (61.3°) to dsVF (92.8°) (**Figure 4.4b-d**). In contrast, motion in the plane perpendicular to the sulfonates (defined as the angle between the vector normal to the meso ring system, “ArylN” and the membrane normal, **Figure 4.4a**) is relatively unchanged, shifting from 88.3° for msVF2.1.Cl to 92.0° for dsVF2.1.Cl (**Figure 4.4b-c and e**). This is consistent with the hypothesis that symmetric sulfonation rigidifies VF dyes in the plane parallel to the meso aromatic ring, ArylP, but has little effect on motion in the orthogonal coordinate, ArylN (**Figure 4.4b-c**).

Based on the MD simulations, we estimate an approximate 16% increase in voltage sensitivity upon going from the msVF to the dsVF dye scaffold, if molecular orientation, or θ , is the only change. This improvement represents a critical increase in the sensitivity of VF-type dyes. According to Equation 4.3, for a given msVF/dsVF pair, the change in voltage sensitivity should be proportional to the ratio between the cosine of θ for msVF and dsVF.

$$\frac{\Delta F/F_{dsVF}}{\Delta F/F_{msVF}} \propto \frac{\cos \theta_{dsVF}}{\cos \theta_{msVF}} \text{Equation 4.3}$$

Therefore, a change in θ from 35.4° to 19.4° should give a 16% increase in voltage sensitivity (cosine of 19.4°/cosine of 35.4° = 1.157).

Table 4.1. Properties of mono- and disulfo VoltageFluor dyes

Name	ID	R	R'	R''	Φ_{ff}^a	λ_{abs}^a	λ_{em}^a	$\Delta F/F^b$	Improvement (%) ^c
msVF2.1.Cl	11a	Cl	Me	H	0.06	522	536	30	---
dsVF2.1.Cl	11b	Cl	Me	H	0.08	520	539	36	21
msVF2.2(OMe).Cl	12a	Cl	Et	OMe	0.06	518	534	53	---
dsVF2.2(OMe).Cl	12b	Cl	Et	OMe	0.07	520	540	63	19
msVF2.1.H	13a	H	Me	H	0.10	507	528	17	---
dsVF2.1.H	13b	H	Me	H	0.14	509	540	20	17
msVF2.2(OMe).H	14a	H	Et	OMe	0.08	508	530	53	---
dsVF2.2(OMe).H	14b	H	Et	OMe	0.11	510	530	57	9
msVF2.1.F	15a	F	Me	H	0.09	508	524	27	---
dsVF2.1.F	15b	F	Me	H	0.13	507	529	33	25
msVF2.2(OMe).F	16a	F	Et	OMe	0.06	505	524	49	---
dsVF2.2(OMe).F	16b	F	Et	OMe	0.06	509	529	60	22

^a Measured in phosphate-buffered saline, pH 7.4 with 0.1% Triton X-100. ^b per 100 mV. Determined in HEK cells. ^c Relative to corresponding msVF.

4.3 Synthesis and Characterization of Doubly-Sulfonated VoltageFluor Dyes

To confirm the MD simulation results and experimentally test the hypothesis that improved orientation produces an increase in voltage sensitivity, we synthesized and characterized 6 new doubly-sulfonated VF dyes. Although the chromophores required for msVF are accessible via sulfonic acid anhydrides,³⁵ generation of the doubly-sulfonated precursors represented a synthetic challenge. To circumvent this problem, we devised a route from commercially available fluorobenzaldehydes (**1** and **2**) that enabled access to both singly and doubly sulfonated dye precursors. Sulfonated halobenzaldehydes **3** and **4** could be prepared via nucleophilic aromatic substitution (S_NAr) with sodium sulfite/bisulfite,³⁶ enabling us to bypass both the deactivating nature of the sulfonate group and any challenges in directing the sulfonate substitution pattern. Both 5-bromo-2-formyl-benzenesulfonic acid **3** and 5-bromo-2-formyl-1,3-benzenedisulfonic acid **4** were prepared in good yields (64-96%) on the gram scale from commercially available 4-bromo-mono- and di-fluorobenzaldehydes via S_NAr with sodium sulfite/bisulfite in a mixture of water and ethanol.

These aldehydes then condensed smoothly with unsubstituted and halogenated resorcinols in methanesulfonic acid (with *in situ* oxidation by air) to give an array of monosulfonated and disulfonated fluoresceins (**5-10**), with yields ranging from 40-84% (**Figure 4.5**).

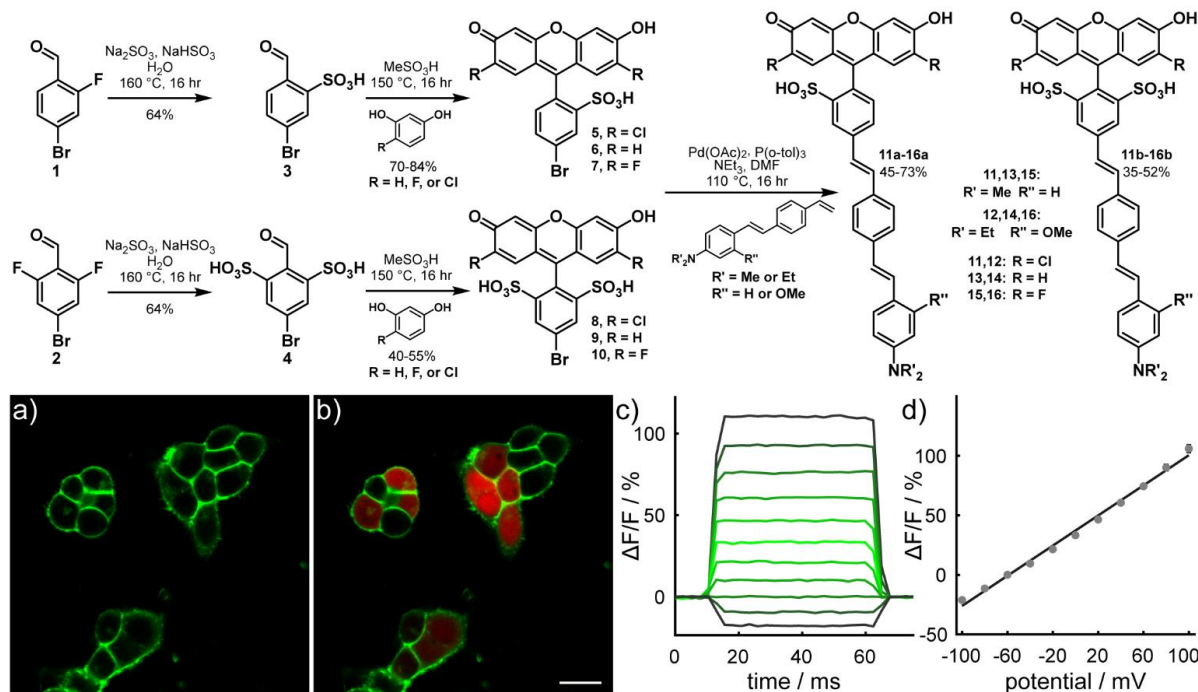


Figure 4.5. Synthesis and characterization of monosulfo and disulfoVF dyes. Upper panel: Synthesis of VF dyes. Lower panel: a) Confocal fluorescence images of dsVF2.2(OMe).Cl in HEK cells. Membrane-associated green fluorescence (panel a) shows clear membrane localization when compared with cytosolic mCherry (red, panel b). Scale bar is 20 μm . Membrane-localized dsVF2.2(OMe).Cl is voltage sensitive. c) The fractional change in fluorescence is plotted vs. time for 100 ms hyper- and depolarizing steps (± 100 mV, 20 mV increments) from a holding potential of -60 mV for a single HEK cells under whole-cell voltage-clamp mode. d) A plot of % $\Delta F/F$ vs. final membrane potential (mV), summarizing data from 8 separate cells, reveals a voltage sensitivity of approximately 63% per 100 mV ($\pm 1.6\%$). Error bars are \pm SEM.

Generally, yields of monosulfo-fluoresceins (70- 84%) were higher than for corresponding disulfo-fluoresceins (40-55%), which we attribute to the increased steric congestion of disulfo- vs. monosulfo-benzaldehydes. The new disulfo-fluoresceins show absorption and emission profiles similar to their mono-sulfo counterparts and display high fluorescence quantum yields (near unity, **Figure 4.6**) and aqueous solubility: up to 0.94 mM in H_2O with 0.1% DMSO for ds-dichlorofluorescein vs. only 0.41 mM for ms-dichlorofluorescein.

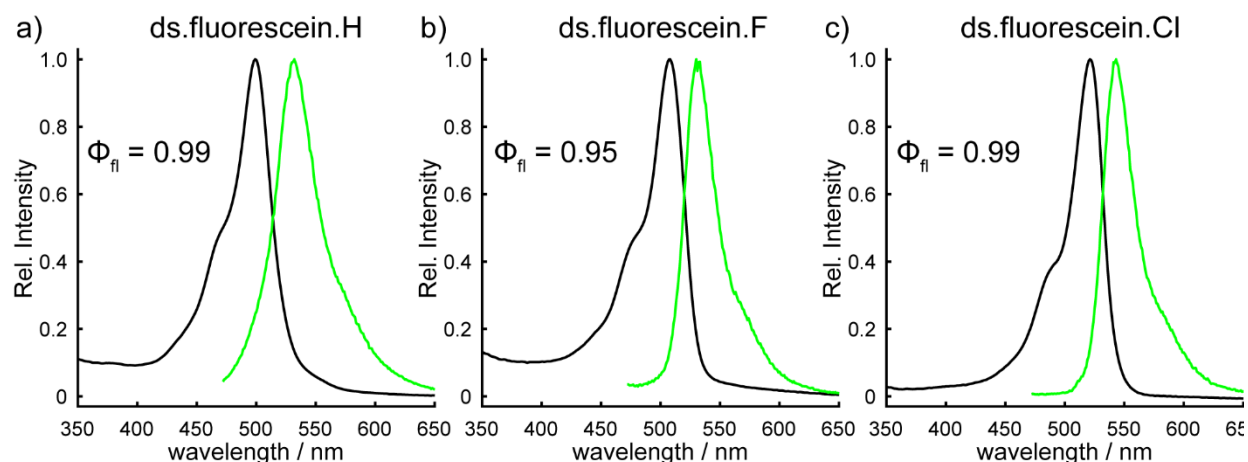


Figure 4.6. Absorption and emission spectra for disulfofluoresceins. Spectra were acquired in phosphate-buffered saline, pH 7.4 + 0.1% Triton X-100.

Methoxy-substituted anilines generally give the best voltage sensitivity in the context of a fluorescein-based voltage sensor,²² so we sought to make both 3-methoxy and unsubstituted aniline molecular wires to test if straightening via double sulfonation is a generalizable strategy. We used either a dimethyl aniline molecule wire or a N,N-diethyl-3-methoxyaniline wire as the two molecular wire scaffolds in this study. The N,N-diethyl-3-methoxyaniline was used in place of the previously described N,N-dimethyl-3-methoxyaniline wire because the diethyl derivative can be simply prepared from commercially available N,N-diethylsalicylaldehyde.³⁷ Heck coupling between the styrene molecular wires and corresponding mono- or di-sulfonated fluoresceins provided the ms- and dsVF dyes after purification via crystallization. Small amounts of dye were purified by semi-preparative HPLC for further analysis.

We synthesized a total of 9 new dyes: 6 new dsVF dyes and 3 new msVF dyes. Both msVF and dsVF dyes display similar excitation and emission profiles to previously reported msVF dyes (**Table 4.1, Figure 4.7**), and all localized to the plasma membrane when applied to HEK293T cells via bath loading. (**Figure 4.5a-b, 4.8**). In general, disulfonated fluorophores (**8-10**) and dsVF dyes (**11b-16b**) showed improved aqueous solubility relative to mono-sulfo derivatives (**5-7, 11a-16a**). Addition of a second sulfonate improved the aqueous solubility of fluorophore **8** 2.3-fold relative to monosulfo **5**, as determined either spectroscopically or gravimetrically. In the context of a full VF dye, a second sulfonate improved aqueous solubility by 22% for VF2.1.Cl and 55% for VF2.2(OMe).Cl (**11a vs 11b; 12a vs 12b; Figure 4.9**).

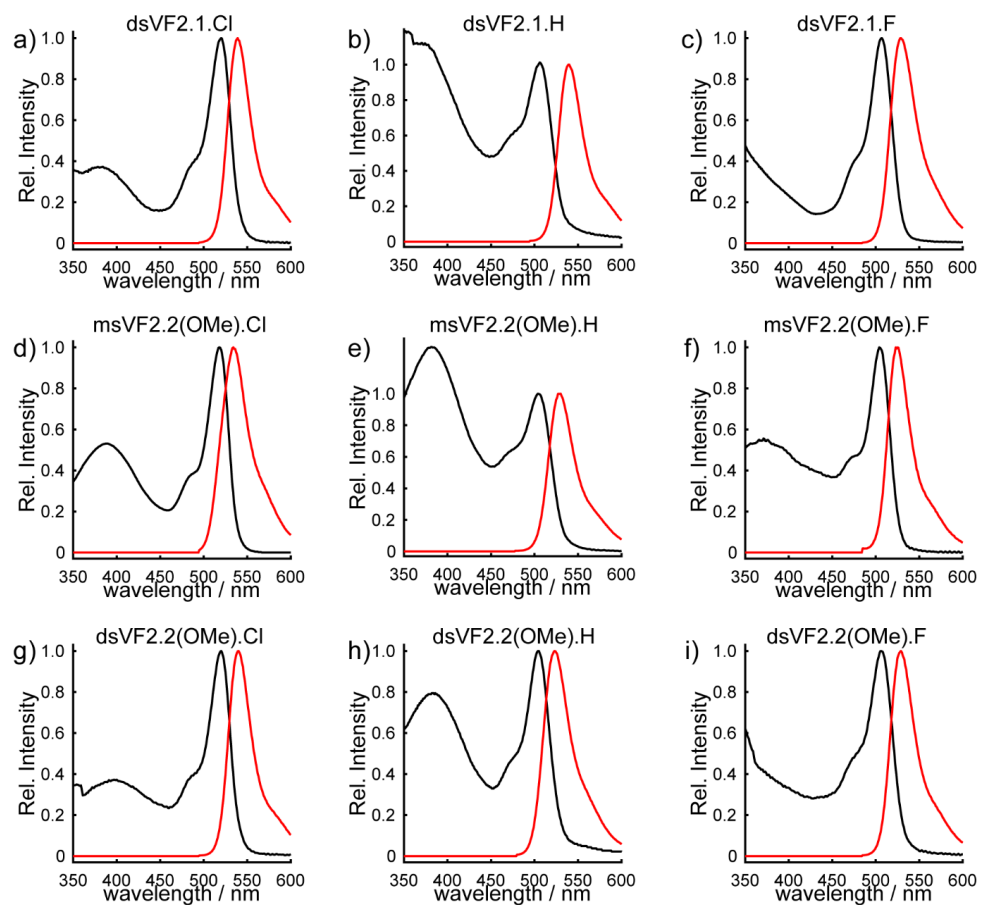


Figure 4.7. Absorption and emission spectra for msVF and dsVF dyes obtained in phosphate-buffered saline, pH 7.4 + 0.1% Triton X-100 as a surfactant.

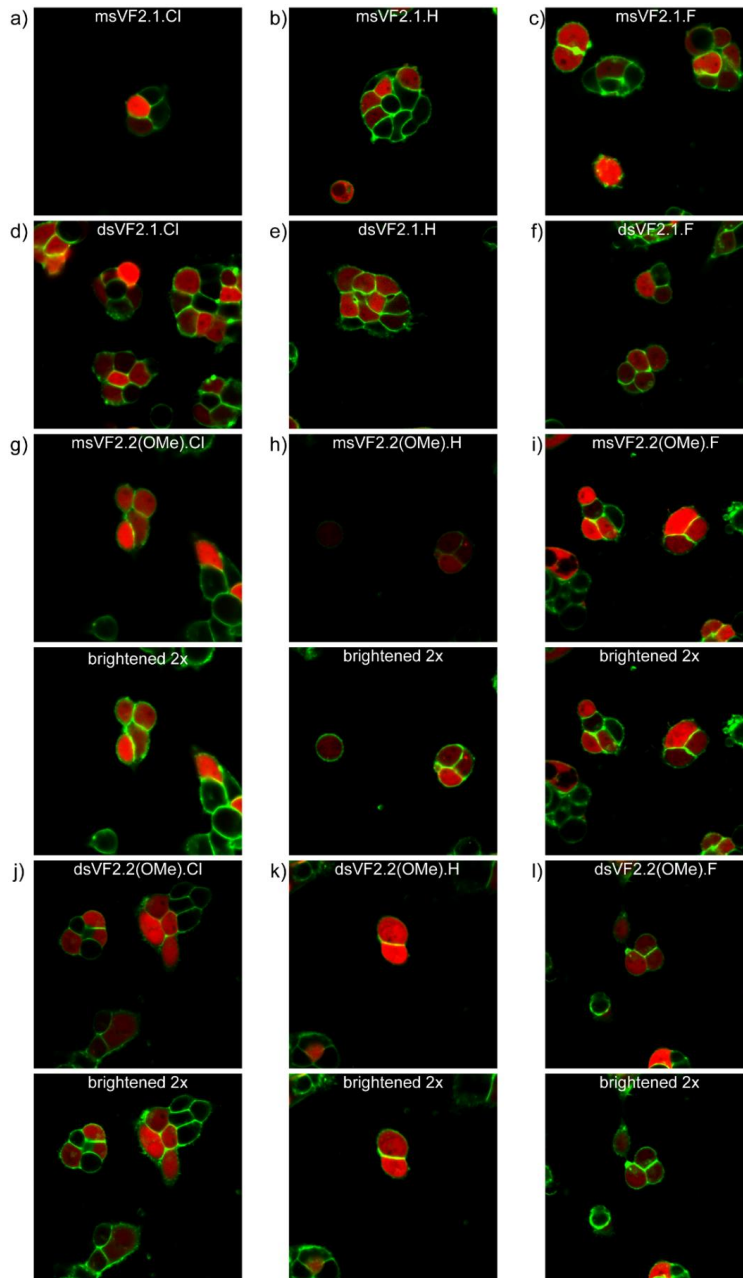


Figure 4.8. Laser-scanning confocal micrographs of HEK cells stained with the indicated msVF or dsVF dye. HEK cells also express cytosolic mCherry as marker of cytosol. The juxtaposition of red and green signals enables clear discrimination of membrane-localized staining of VF dyes.

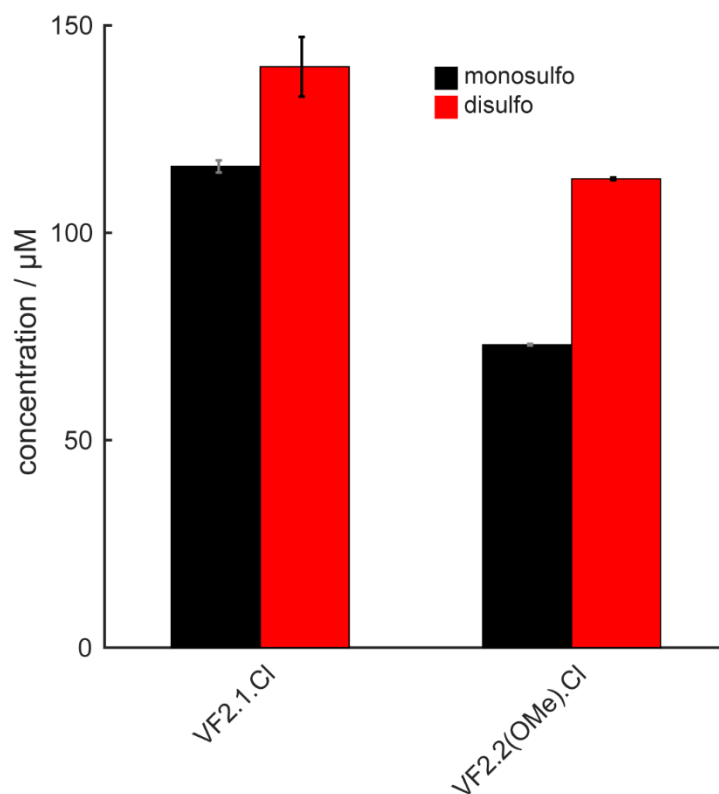


Figure 4.9. Solubility of msVF and dsVF derivatives in distilled water with 0.1% DMSO as determined by UV/Vis spectrophotometry. Data are from three trials for each dye. Error bars are \pm SEM.

To determine the voltage sensitivity of each of the dyes, we performed whole-cell patch clamp electrophysiology on HEK293T cells loaded with 200 nM VF (**Figure 4.5a-d**). Depolarization of the cell membrane in the presence of VF dye results in a large increase of fluorescence, while hyperpolarization results in lower levels of fluorescence (**Figure 4.5c-d, 4.10**). As an illustrative comparison, we found that msVF2.2(OMe).Cl (**12a**) had a voltage sensitivity of approximately $53\% \pm 1\% \Delta F/F$ per 100 mV, which is comparable to the previously reported msVF2.1(OMe).Cl, at 48% per 100 mV.²² The disulfoVF2.2(OMe).Cl (**12b**), when subjected to the same membrane depolarizations, had a voltage sensitivity of $63\% \pm 1\% \Delta F/F$ per 100 mV, representing a 19% improvement in voltage sensitivity over the monosulfonated VF analog, and the most sensitive VF dye to date.

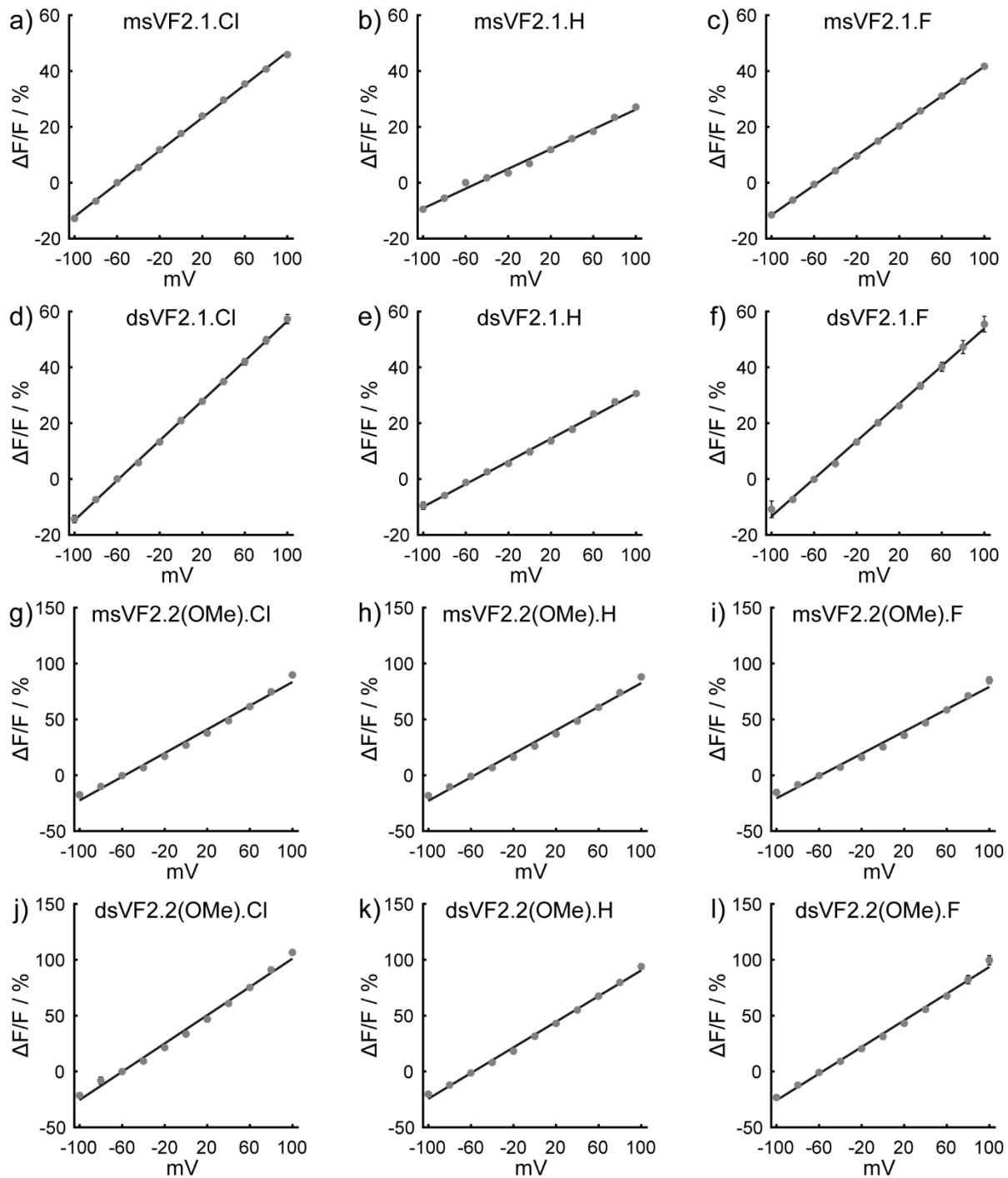


Figure 4.10. Voltage sensitivity of VF dyes in HEK cells. The fractional change in fluorescence is plotted vs. final membrane potential for 100 ms hyper- and depolarizing steps (± 100 mV, 20 mV increments) from a holding potential of -60 mV for a single HEK cells under whole-cell voltage-clamp mode. Data are from between 3 and 8 individual cells for each point. Error bars are \pm SEM.

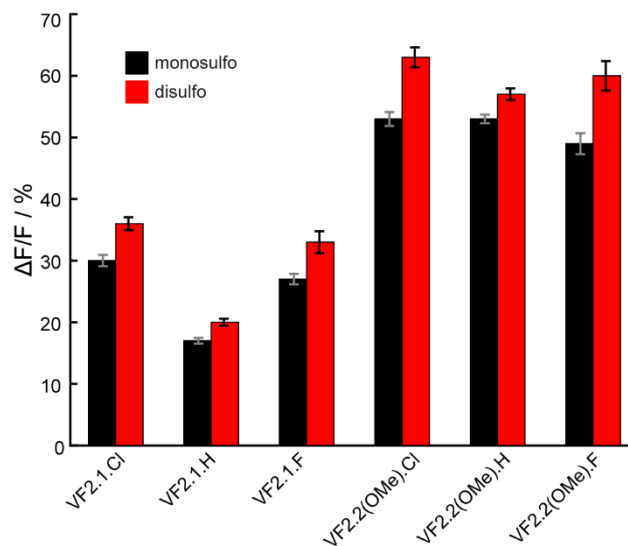


Figure 4.11. Comparison of voltage sensitivity of monosulfo- and disulfo-VoltageFluor. Black bars represent msVF dyes and red bars represent dsVF dyes. Voltage sensitivity is reported as $\Delta F/F$ per 100 mV as measured in patch-clamped HEK cells. Values represent 3-8 independent determinations and error bars are \pm SEM.

We determined the voltage sensitivity for the remaining 10 VF dyes using dual optical and electrophysiological recordings in HEK cells (3-8 separate cells per dye). All of the dyes—VF2.1.Cl (**11**), VF2.1.H (**13**), VF2.1.F (**15**), VF2.2(OMe).H (**14**), and VF2.2(OMe).F (**16**)—showed comparable improvements in voltage sensitivity when the second sulfonate group is added (**Table 4.1**, **Figure 4.11**). In all cases, we see an increase in voltage sensitivity upon transition to the dsVF dye. On average disulfoVF dyes show a $19\% \pm 2\%$ increase in voltage sensitivity over its monosulfonated counterpart (**Table 4.1**). The experimentally determined average increase in voltage sensitivity of 19% matches well with the computationally predicted value of 16% and provides a validation both of our MD simulation methodology and our hypothesis that the relative orientation of the VF dye influences voltage sensitivity. The small discrepancy may arise from differences in the electronic nature of ms- vs dsVF dyes, which is known to affect voltage sensitivity.²²

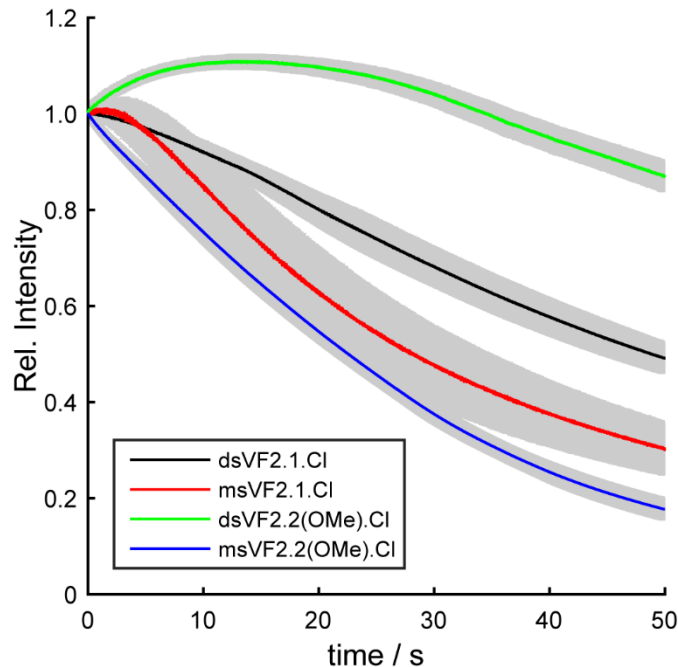


Figure 4.12. Bleaching curves for VoltageFluor dyes in HEK cells. The fractional change in fluorescence is plotted vs. time for each of the dyes under constant 488 nm illumination. Data are from 5 individual regions of interest. Shaded areas represent \pm standard deviation.

4.4 Imaging Voltage in Neurons Using Doubly-Sulfonated VoltageFluors

Due to its exceptional voltage sensitivity and good photostability compared to msVF2.2(OMe).Cl (**Figure 4.12**), we expected that disulfoVF2.2(OMe).Cl should be well-suited to observing membrane potential changes in neurons. Cultured rat hippocampal neurons bathed in disulfoVF2.2(OMe).Cl showed bright membrane staining, as confirmed by confocal microscopy (**Figure 4.13a**). We also used dsVF2.2(OMe).Cl to image neuronal activity in midbrain dopaminergic (mDA) neurons derived from cultured human pluripotent stem cells (hPSCs) in culture (**Figure 4.13b**) using differentiation conditions adapted from previously established protocols.³⁸ mDA neurons stained with dsVF2.2(OMe).Cl revealed distinct firing patterns (**Figure 4.13c,d**). Functional analysis of human- or patient-derived differentiated neurons in a simple, non-invasive manner enabled by dsVF2.2(OMe).Cl may be an important diagnostic tool alongside more conventional methods in ascertaining proper differentiation as well as in investigating human disease phenotypes.

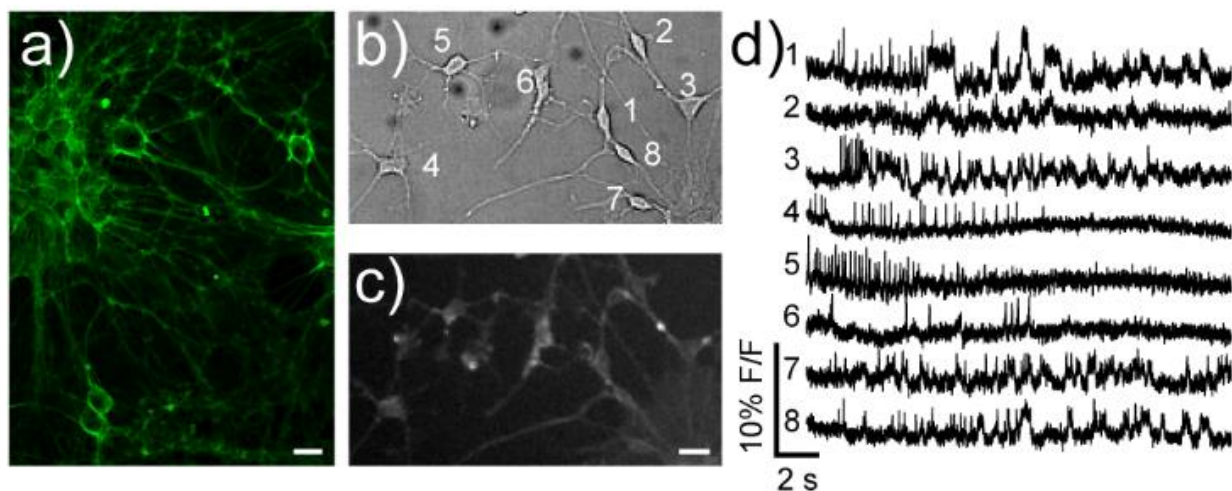


Figure 4.13. Imaging membrane potential changes in cultured rat hippocampal neurons and hPSC-derived midbrain dopaminergic (mDA) neurons using dsVF2.2(OMe).Cl. a) Confocal images of rat hippocampal neurons stained with 500 nM dsVF2.2(OMe).Cl. b) Transmitted light image (DIC) of hPSC-derived mDA neurons. c) Widefield fluorescence image of mDA neurons from panel b stained with 500 nM dsVF2.2(OMe).Cl. d) Fractional change in fluorescence vs. time for cells indicated in panels b. Each trace represents the fluorescence intensity from the indicated cell; all traces have been bleach corrected and are unfiltered. Scale bars are 20 μ m.

4.5 Conclusions and Outlook

In summary, we use a molecular modeling approach to study the effects of dye orientation within the plasma membrane on the voltage sensitivity of VoltageFluor dyes and use the model to propose the structure of a dye with enhanced voltage sensitivity over previous incarnations of VF dyes. Based on orientation effects observed in MD simulations, we predicted an approximate 16% increase in the voltage sensitivity of dsVF dyes.

To validate our computational results, we present the design and synthesis of disulfonated fluoresceins, a novel group of xanthene fluorophores with increased water solubility. The new disulfonated xanthene fluorophores may be useful in their own right as labeling agents due to their ease of synthesis in isomerically-pure form, high water solubility, and potential for derivatization. We then synthesize new, more rigid disulfo-VoltageFluor dyes based on these novel disulfonated fluoresceins. All of the dsVF dyes display enhanced voltage sensitivity relative to their msVF cognates, with an average increase in sensitivity of 19%, which matches well with our calculated improvement of 16%. In addition to providing excellent support for a PeT-based mechanism of voltage sensitivity, these results validate our hypothesis that proper orientation of a VF dye within the membrane significantly influences its voltage sensitivity. One of the new VF dyes, disulfoVF2.2(OMe).Cl shows the highest voltage sensitivity observed in PeT-based voltage sensors thus far (63% $\Delta F/F$ per 100 mV). Additionally, we demonstrate that disulfoVF2.2(OMe).Cl can be used to detect membrane potential changes in rat hippocampal neurons and in human-derived mid-brain dopaminergic neurons.

The improved voltage sensitivity of disulfoVF2.2(OMe).Cl facilitates voltage imaging under conditions that degrade signal-to-noise ratio and sensitivity, such as low-power illumination,

thicker tissue samples, and long-term imaging. Finally, the disulfonated VoltageFluor dyes represent a new scaffold for designing future dyes that have higher voltage sensitivity than first generation VF dyes. Efforts are currently underway in our lab to generalize this scaffold to other xanthene chromophores, such as rhodamines³⁷ and silicon-rhodamines.¹³

4.6 Methods and Materials

General method for chemical synthesis and characterization

Chemical reagents and anhydrous solvents were purchased from commercial suppliers and used without further purification. All reactions were carried out in oven-dried flasks under an inert atmosphere of N₂. Thin layer chromatography (TLC) (Silicycle, F254, 250 μm) was performed on glass backed plates pre-coated with silica gel and were visualized by fluorescence quenching under UV light. Flash column chromatography was performed on Silicycle Silica Flash F60 (230–400 Mesh) using a forced flow of air at 0.5–1.0 bar. NMR spectra were measured on a Bruker AV-600 MHz, 150 MHz. Chemical shifts are expressed in parts per million (ppm) and are referenced to *d*₆-DMSO, 2.50 ppm. Coupling constants are reported as Hertz (Hz). Splitting patterns are indicated as follows: s, singlet; d, doublet; sep, septet; dd, doublet of doublet; ddd, doublet of doublet of doublet; dt, doublet of triplet; td, triplet of doublet; m, multiplet. High-resolution mass spectra (ESI EI) were measured by the QB3/Chemistry mass spectrometry service at University of California, Berkeley. High performance liquid chromatography (HPLC) and low resolution ESI Mass Spectrometry were performed on an Agilent Infinity 1200 analytical instrument coupled to an Advion CMS-L ESI mass spectrometer. Columns used for the analytical and semi-preparative HPLC were Phenomenex Luna C18(2) (4.6 mm I.D. × 150 mm) and Phenomenex Luna 5 μm C18(2) (10 mm I.D. × 150 mm) columns with a flow rate of 1.0 and 3.0 mL/min, respectively. The mobile phase were MQ-H₂O with 0.05% formic acid (eluent A) and HPLC grade acetonitrile with 0.05% formic acid (eluent B). Signals were monitored at 254 and 460 nm in 20 min with gradient 5–100% eluent B.

Spectroscopic studies

Stock solutions of VF dyes were prepared in DMSO (1.0–10 mM) and diluted with PBS (100 mM Na₂HPO₄, pH 7.4, 0.1% Triton-X). UV-Vis absorbance and fluorescence spectra were recorded using a Shimadzu 2501 Spectrophotometer (Shimadzu) and a Quantamaster Master 4 L-format scanning spectrofluorometer (Photon Technologies International). The fluorometer is equipped with an LPS-220B 75-W xenon lamp and power supply, A- 1010B lamp housing with integrated igniter, switchable 814 photon-counting/analog photomultiplier detection unit, and MD5020 motor driver. Samples were measured in 1-cm path length quartz cuvettes (Starna Cells).

Differentiation of mDA neurons

mDA neurons were derived from H1 human embryonic stem cells (hESCs) using medium conditions adapted from previously established protocols.³⁹ On Day 25 of differentiation, cells were harvested from the culture platform and pipetted to generate small 50–100 μm clusters, and seeded on 12mm glass coverslips coated with 20 μg/ml Laminin (ThermoFischer Scientific). Cells were subsequently matured for 10 days before voltage sensitive imaging.

Voltage sensitivity in HEK cells

Functional imaging of VF dyes was performed using a 20x objective paired with image capture from the EMCCD camera at a sampling rate of 0.5 kHz. VF dyes were excited using the 488 nm LED with an intensity of 2.5 W/cm². For initial voltage characterization emission was collected

with the QUAD filter (430/32, 508/14, 586/30, 708/98 nm) after passing through a quadruple dichroic mirror (432/38, 509/22, 586/40, 654 nm LP).

Voltage imaging of neurons

Functional imaging of mDA cells was performed using a 20x objective paired with image capture from the ORCA-Flash4.0 camera (Hamamatsu) at a sampling rate of 100 Hz. VoltageFluor dye was excited using the 488 nm LED with an intensity of 2.5 W/cm². Light was collected with the QUAD filter (430/32, 508/14, 586/30, 708/98 nm) after passing through a quadruple dichroic mirror (432/38, 509/22, 586/40, 654 nm LP). For image analysis, a custom Matlab routine was employed. In summary, a TIFF stack was imported into Matlab and the intensity values a user-designated block of pixels was extracted as an array. The intensity over time for each block was then baseline corrected by fitting to a 2nd degree polynomial. Cells were selected by drawing regions of interest around cells in a DIC image corresponding to the video, outputting the bleach-corrected trace as an Excel file and spike times (frames in which the intensity was greater than 3x the standard deviation of the overall trace) as a text file.

Determination of Photostability

HEK cells were incubated separately with ms- and ds-VF2.1.Cl and VF2.2(OMe).Cl at 1 μ M in HBSS at 37 degrees Celsius for 15 minutes. Data were acquired with a W-Plan-Apo 63x/1.0 objective (Zeiss) and the ORCA-Flash4.0 camera (Hamamatsu). Images were exposed for 10 milliseconds each across 50 seconds with a constant illumination of the 488 nm LED (153 W/cm²). The excitation light was collected with the QUAD filter (430/32, 508/14, 586/30, 708/98 nm) after passing through a quadruple dichroic mirror (432/38, 509/22, 586/40, 654 nm LP). The fluorescence curves were background subtracted and then normalized to the fluorescence intensity at t = 0 and averaged across five cells of each dye.

Electrophysiology

For electrophysiological experiments, pipettes were pulled from borosilicate glass (Sutter Instruments, BF150-86-10), with a resistance of 5–8 M Ω , and were filled with an internal solution; (in mM) 115 potassium gluconate, 10 BAPTA tetrapotassium salt, 10 HEPES, 5 NaCl, 10 KCl, 2 ATP disodium salt, 0.3 GTP trisodium salt (pH 7.25, 275 mOsm).

Recordings were obtained with an Axopatch 200B amplifier (Molecular Devices) at room temperature. The signals were digitized with Digidata 1332A, sampled at 50 kHz and recorded with pCLAMP 10 software (Molecular Devices) on a PC. Fast capacitance was compensated in the on-cell configuration. For all electrophysiology experiments, recordings were only pursued if series resistance in voltage clamp was less than 30 M Ω . For whole-cell, voltage clamp recordings in HEK 293T cells, cells were held at -60 mV and 100 ms hyper- and de-polarizing steps applied from -100 to +100 mV in 20 mV increments. For whole-cell, following membrane rupture, resting membrane potential was assessed and recorded at I = 0 and monitored during the data acquisition.

Image analysis

Analysis of voltage sensitivity in HEK cells was performed using custom Matlab routines. Briefly, a region of interest (ROI) was selected automatically based on fluorescence intensity and applied as a mask to all image frames. Fluorescence intensity values were calculated at known baseline and voltage step epochs.

Solubility of VoltageFluor dyes

Suspensions of 5 milligrams each of solid mono- and disulfo-dichlorofluoresceins in 5 mL of distilled water were created. Over the course of three days, 5 milligrams of solid material was added at a time, ensuring that no visible particulates were present in the solution prior to addition. At the end of the experiment, the suspension was filtered through filter paper and then through a 0.22- μm polytetrafluoroethylene filter into a scintillation vial. 10 μL of this filtrate was used as a stock solution to determine the concentration of fluorescein present via UV-Vis spectrophotometry and the remainder was lyophilized and the amount of solid resulting was measured using an analytical microbalance. For VF dyes (VF2.1.Cl and VF2.2(OMe).Cl, both ms and ds versions), saturated solutions in distilled water were prepared via dilution from a 100 μM stock in DMSO for a resulting solution containing 0.1% DMSO. The solutions were allowed to sit overnight at 20 degrees Celsius and then filtered through 0.22- μm filters. The resulting filtrates were used as stock solutions to determine the amount of VF present via UV-Vis spectrophotometry.

Molecular dynamics simulation parameters and protocols

The msVF and dsVF molecules were parameterized in CHARMM General force field (CGenFF).⁴⁰ The CGenFF program^{40, 41} was used to obtain initial parameters, which were subsequently optimized with the Force Field Toolkit (fftk)⁴² and the program Gaussian 09.⁴³ Briefly, an entire VF molecule is divided into four parts during the parameterization (**SI Figure 1**). As benzenesulfonate and N,N-dimethylaniline were already in the CHARMM general force field, only the remaining two parts (xanthene derivative and (E)-stilbene) were submitted to the CGenFF program. Based on the resulting penalty scores, two dihedrals in (E)-stilbene were selected and optimized via fftk and Gaussian 09 following protocols outlined in ref.⁴⁴ For the -1 charged xanthene derivative, its atom typing and initial charge assignment was not based on the CGenFF program output. Instead, we first performed its geometry optimization at the MP2/6-31+G* level via Gaussian 09, which confirmed a symmetric and planar structure of the tricyclic ring, consistent with a previous density functional theory calculation.⁴⁵ We then assigned atom type and initial charges for the xanthene derivative based on the compounds phenoxazine, phenoxide and chlorobenzene from the CHARMM general force field and performed charge and dihedral optimization (**SI Figure 1**) following protocols outlined in ref.⁴⁴ The final topology and parameter files for both VF molecules are provided in the supporting information.

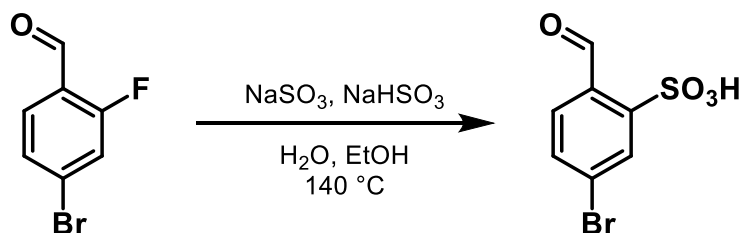
MD simulation system with either a msVF or a dsVF molecule was constructed by inserting it vertically inside the upper monolayer of a POPC bilayer, which was previously equilibrated in a 1- μs simulation⁴⁶ performed on the specialized machine Anton.⁴⁷ In each system, one lipid molecule overlapping with the inserted msVF or dsVF was removed. Using the autoionize plugin of VMD,⁴⁸ the systems were neutralized by adding sodium and chloride ions at a concentration of 0.1 mol/L. Final simulation systems contain $\sim 46,000$ atoms, with a size of approximately $75 \times 75 \times 73 \text{ \AA}^3$. Three replicas of ~ 500 ns simulations were performed to examine the orientation of msVF in the POPC bilayer, while three replicas of ~ 200 ns simulations were performed for the dsVF molecule in POPC. The longer simulation time for the former VF molecule is chosen based on its longer correlation time shown in **SI Figure 2**.

All simulations were performed with the 2.10 release of NAMD⁴⁹ and the CHARMM36 force field for lipids⁵⁰ as well as the CGenFF force field.⁴⁵ A time step of 2 fs was adopted in all simulations, with bonds involving hydrogen atoms constrained using RATTLE⁵¹ and water geometries maintained using SETTLE.⁵² The multiple-time-stepping algorithm was used, with

short-range forces calculated every step and long-range electrostatics calculated every two steps. The cutoff for short-range nonbonded interactions was set to 12 Å, with a switching distance of 10 Å. The CHARMM force switching was used for vdW forces, in order to be consistent with the CHARMM36 force field for lipids. Assuming periodic boundary conditions, the Particle Mesh Ewald (PME) method⁵³ with a grid density of at least $1/\text{Å}^3$ was employed for computation of long-range electrostatic forces. Langevin dynamics with a damping coefficient of 1 ps^{-1} was used to keep the temperature constant at 310 K, while a Nosé–Hoover–Langevin piston⁵⁴ was used to keep the pressure constant at 1 atm. The pressure control was performed semi-isotropically: the z axis of the simulation box, which is normal to the membrane, was allowed to fluctuate independently from the x and y axes.

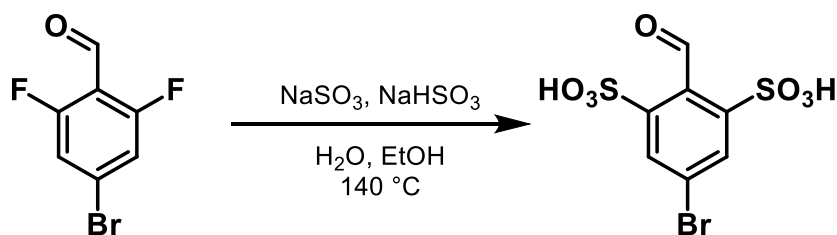
Synthetic Details

Preparation of formylbenzenesulfonic acids:



Synthesis of 5-bromo-2-formylbenzenesulfonic acid

4-bromo-2-fluorobenzaldehyde (3.0 g, 14.78 mmol) was placed in a long-necked bomb flask and dissolved in a 1:1 mixture of ethanol and water. Sodium sulfite (1.49 g, 11.82 mmol) and sodium bisulfite (123 mg, 1.18 mmol) were added and the reaction was stirred for 16 hours at 140 degrees Celsius. The reaction mixture, after cooling, was poured into methanol while stirring so as to make 20% aqueous content of the whole volume. This process precipitated the inorganic salts, which were then removed by vacuum filtration. The solvent from the filtrate was removed under reduced pressure to obtain a solid residue, which was triturated with methanol/ethyl ether to produce a fluffy white solid (2.82 g, 72%). ¹H NMR (400 MHz, DMSO-*d*₆) δ 10.85 (s, 1H), 8.09 (d, *J* = 1.7 Hz, 1H), 7.72 (d, *J* = 7.9 Hz, 1H), 7.66 (dd, *J* = 7.4, 1.5 Hz, 1H). ¹³C NMR (226 MHz, DMSO) δ 192.65, 151.31, 132.34, 131.46, 129.58, 128.88, 126.97. HR-ESI-MS *m/z* for C₇H₄BrO₄S⁻ calcd: 262.9092 found: 262.9017.

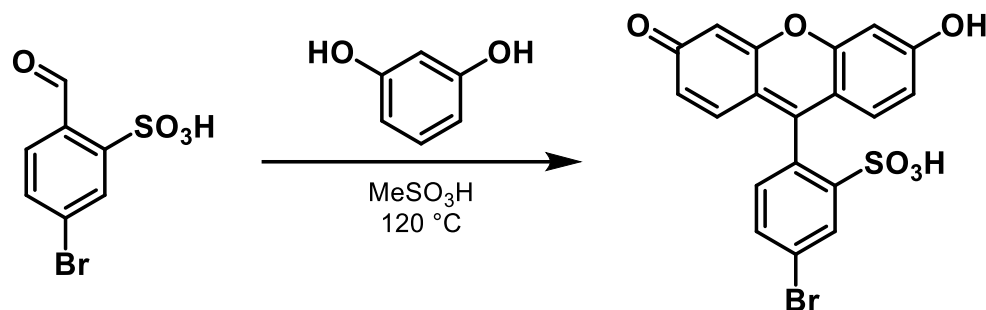


Synthesis of 5-bromo-2-formylbenzene-1,3-disulfonic acid

4-bromo-2,6-difluorobenzaldehyde (1.0 g, 4.52 mmol) was placed in a long-necked bomb flask and dissolved in 10 mL of a 1:1 mixture of ethanol and water. Sodium sulfite (1.14 g, 9.05 mmol) and sodium bisulfite (94 mg, 0.90 mmol) were added and the reaction was stirred for 16 hours at 140 degrees Celsius. The reaction mixture, after cooling, was poured into methanol

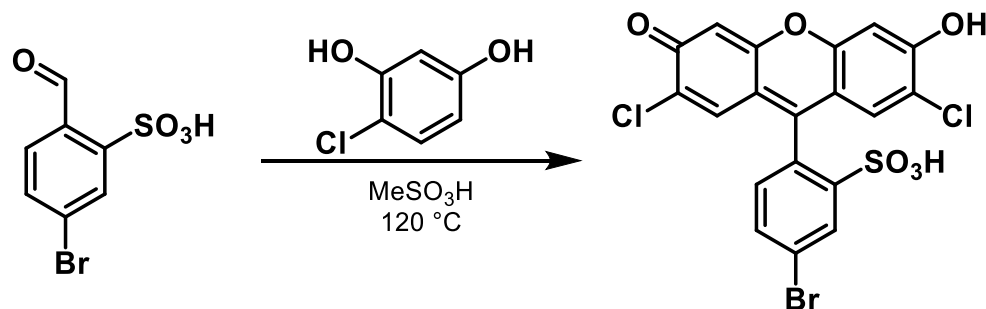
while stirring so as to make 20% aqueous content of the whole volume. This process precipitated the inorganic salts, which were then removed by vacuum filtration. The solvent from the filtrate was removed under reduced pressure to obtain a solid residue, which was triturated with methanol/ethyl ether to produce a fluffy white solid (1.19 g, 76%), which was judged to be pure by NMR. ^1H NMR (400 MHz, Methanol- d_4) δ 10.62 (s, 1H), 8.12 (s, 2H). ^{13}C NMR (226 MHz, DMSO) δ 186.45, 165.53, 155.33, 130.84. HR-ESI-MS m/z for $\text{C}_7\text{H}_4\text{BrO}_7\text{S}_2^-$ calcd: 342.8660 found: 342.8596.

Preparation of fluorescein dyes:



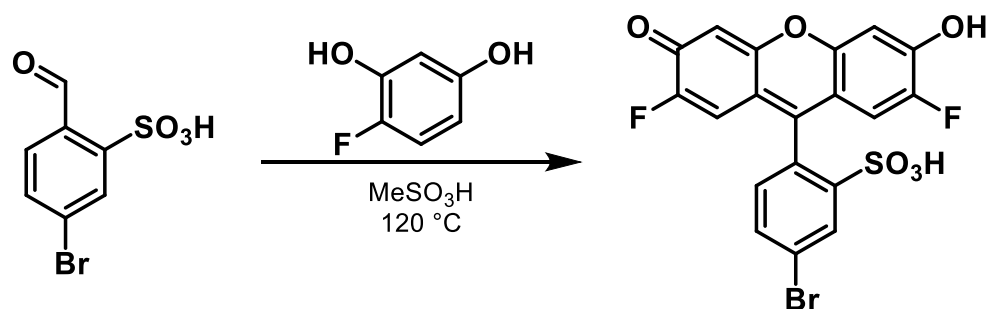
Synthesis of 5-bromosulfofluorescein

5-bromo-2-formylbenzenesulfonic acid (300 mg, 1.13 mmol) and resorcinol (249 mg, 2.26 mmol) were placed in a roundbottom flask dissolved in 3 mL of neat methanesulfonic acid and stirred for 16 hours at 120 degrees Celsius. After cooling, the reaction mixture was poured into 5 mL water, resulting in precipitation of a brown solid. The solid was isolated via vacuum filtration (400 mg, 79%) and judged to be pure by NMR. ^1H NMR (300 MHz, $\text{DMSO-}d_6$) δ 8.07 (s, 1H), 7.83 (d, $J = 6.8$ Hz, 1H), 7.44 (d, $J = 9.2$ Hz, 2H), 7.33 (s, 2H), 7.27 (d, $J = 8.3$ Hz, 1H), 7.18 (d, $J = 8.4$ Hz, 2H). ^{13}C NMR (226 MHz, DMSO) δ 170.84, 167.13, 158.57, 158.47, 148.63, 134.74, 131.77, 130.21, 119.48, 117.07, 106.24, 102.51, 101.72. HR-ESI-MS m/z for $\text{C}_{19}\text{H}_{10}\text{BrO}_6\text{S}^-$ calcd: 444.9460 found: 444.9379.



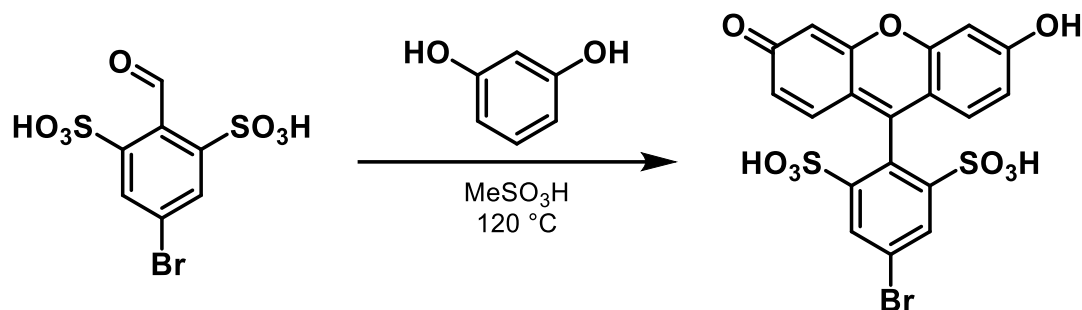
Synthesis of 5-bromo-2',7'-dichlorosulfofluorescein

5-bromo-2-formylbenzenesulfonic acid (250 mg, 0.94 mmol) and 4-chlororesorcinol (272 mg, 1.89 mmol) were placed in a roundbottom flask dissolved in 3 mL of neat methanesulfonic acid and stirred for 16 hours at 120 degrees Celsius. After cooling, the reaction mixture was poured into 5 mL water, resulting in precipitation of a reddish-brown solid. The solid was isolated via vacuum filtration (380 mg, 78%) and judged to be pure by NMR. ^1H NMR (400 MHz, $\text{DMSO-}d_6$) δ 8.06 (s, 1H), 7.75 (d, $J = 8.0$ Hz, 1H), 7.22 (d, $J = 8.1$ Hz, 1H), 6.89 (s, 2H), 6.73 (s, 2H). ^{13}C NMR (226 MHz, DMSO) δ 157.13, 153.54, 131.98, 131.89, 130.20, 129.81, 129.62, 122.76, 115.78, 109.47, 107.39, 103.68, 103.32. HR-ESI-MS m/z for $\text{C}_{19}\text{H}_8\text{BrCl}_2\text{O}_6\text{S}^-$ calcd: 512.8680 found: 512.8598.



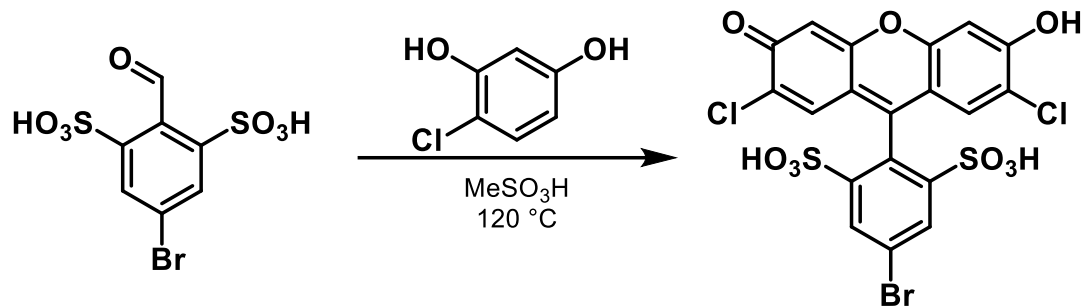
Synthesis of 5-bromo-2',7'-difluorosulfofluorescein

5-bromo-2-formylbenzenesulfonic acid (300 mg, 1.13 mmol) and 4-fluororesorcinol (290 mg, 2.26 mmol) were placed in a roundbottom flask dissolved in 3 mL of neat methanesulfonic acid and stirred for 16 hours at 120 degrees Celsius. After cooling, the reaction mixture was poured into 5 mL water, resulting in precipitation of a brown-black solid. The solid was isolated via vacuum filtration (463 mg, 85%) and judged to be pure by NMR. ^1H NMR (400 MHz, $\text{DMSO-}d_6$) δ 8.05 (d, $J = 2.0$ Hz, 1H), 7.73 (d, $J = 6.9$ Hz, 1H), 7.45 (d, $J = 8.2$ Hz, 1H), 6.78 (d, $J = 7.1$ Hz, 2H), 6.58 (d, $J = 11.4$ Hz, 2H). ^{13}C NMR (226 MHz, DMSO) δ 153.57, 151.96, 150.85, 148.58, 132.07, 131.76, 130.29, 128.27, 122.86, 115.24, 113.54, 113.45, 104.26. HR-ESI-MS m/z for $\text{C}_{19}\text{H}_8\text{BrF}_2\text{O}_6\text{S}^-$ calcd: 480.9271 found: 480.9187.



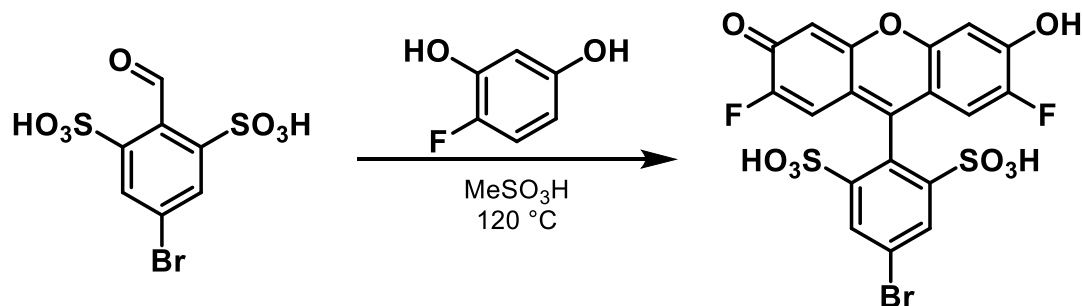
Synthesis of 5-bromodisulfofluorescein

5-bromo-2-formylbenzene-2,6-disulfonic acid (300 mg, 0.87 mmol) and resorcinol (191 mg, 1.74 mmol) were placed in a roundbottom flask dissolved in 3 mL of neat methanesulfonic acid and stirred for 16 hours at 120 degrees Celsius. After cooling, the reaction mixture was diluted with 3 mL dichloromethane and poured into 50 mL diethyl ether, resulting in precipitation of a brown solid. The solid was isolated via vacuum filtration (129 mg, 28%) and judged to be pure by NMR. ^1H NMR (600 MHz, $\text{DMSO-}d_6$) δ 8.11 (s, 2H), 7.36 (d, $J = 9.2$ Hz, 2H), 7.26 (s, 2H), 7.08 (d, $J = 6.4$ Hz, 2H). ^{13}C NMR (226 MHz, DMSO) δ 170.00, 157.81, 149.34, 149.32, 135.70, 133.36, 130.65, 123.69, 118.56, 118.17, 100.93. HR-ESI-MS m/z for $\text{C}_{19}\text{H}_{10}\text{BrO}_9\text{S}_2^-$ calcd: 524.9028 found: 524.8944.



Synthesis of 5-bromo-2',7'-dichlorodisulfofluorescein

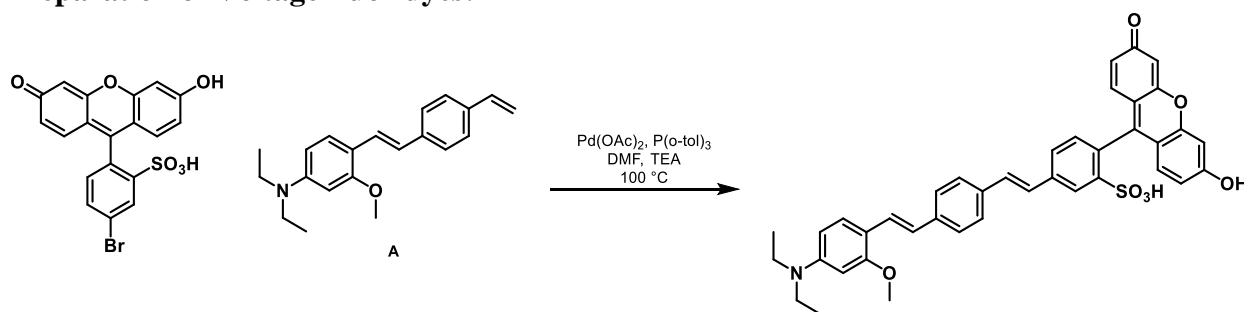
5-bromo-2-formylbenzene-2,6-disulfonic acid (250 mg, 0.72 mmol) and 4-chlororesorcinol (209 mg, 1.45 mmol) were placed in a roundbottom flask dissolved in 3 mL of neat methanesulfonic acid and stirred for 16 hours at 120 degrees Celsius. After cooling, the reaction mixture was diluted with 3 mL dichloromethane and poured into 50 mL diethyl ether, resulting in precipitation of a reddish-brown solid. The solid was isolated via vacuum filtration (200 mg, 46%) and judged to be pure by NMR. ^1H NMR (600 MHz, DMSO- d_6) δ 8.11 (s, 2H), 6.82 (s, 2H), 6.67 (s, 2H). ^{13}C NMR (226 MHz, DMSO) δ 155.04, 149.45, 131.49, 130.81, 124.17, 123.49, 122.48, 117.72, 102.47. HR-ESI-MS m/z for $\text{C}_{19}\text{H}_8\text{BrCl}_2\text{O}_9\text{S}_2^-$ calcd: 592.8248 found: 522.8157.



Synthesis of 5-bromo-2',7'-difluorodisulfofluorescein

5-bromo-2-formylbenzene-2,6-disulfonic acid (300 mg, 0.87 mmol) and 4-fluororesorcinol (222 mg, 1.74 mmol) were placed in a roundbottom flask dissolved in 3 mL of neat methanesulfonic acid and stirred for 16 hours at 120 degrees Celsius. After cooling, the reaction mixture was diluted with 3 mL dichloromethane and poured into 50 mL diethyl ether, resulting in precipitation of a reddish-brown solid. The solid was isolated via vacuum filtration (330 mg, 67%) and judged to be pure by NMR. ^1H NMR (300 MHz, DMSO- d_6) δ 8.11 (s, 2H), 7.16 (d, J = 6.7 Hz, 2H), 6.84 (d, J = 11.1 Hz, 2H). ^{13}C NMR (226 MHz, DMSO) δ 161.45, 161.37, 154.30, 151.48, 150.37, 149.45, 131.27, 124.34, 123.26, 118.05, 118.01, 116.10, 116.01, 103.66. HR-ESI-MS m/z for $\text{C}_{19}\text{H}_8\text{BrF}_2\text{O}_9\text{S}_2^-$ calcd: 560.8839 found: 560.8752.

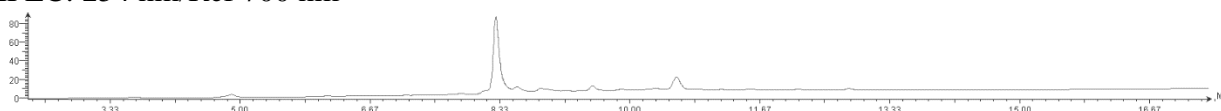
Preparation of VoltageFluor dyes:

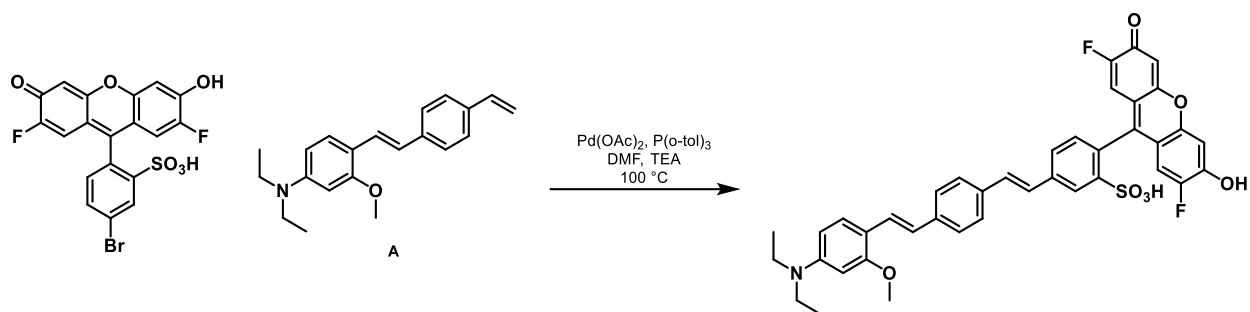


Synthesis of monosulfoVF2.2(OMe).H

5-bromosulfofluorescein (100 mg, 0.22 mmol), **A** (83 mg, 0.27 mmol), palladium acetate (1 mg, 0.045 mmol), and P(*o*-tol)₃ (2.7 mg, 0.09 mmol) were placed in an oven-dried Schlenk flask. The flask was sealed and evacuated/backfilled with nitrogen (3x). Anhydrous DMF (1 mL) and anhydrous Et₃N (1 mL) were added via syringe and the reaction was stirred for 16 hours at 100 degrees Celsius. After cooling, the reaction mixture was diluted with 3 mL dichloromethane and filtered through celite, which was then washed with methanol. The solvent was removed from the filtrate via rotary evaporation and the resulting residue was dissolved in 5 mL dichloromethane. The mixture was then poured into diethyl ether, resulting in precipitation of a brown solid. The solid was isolated via vacuum filtration (66 mg, 44%). A small amount of material was purified via RP-HPLC for further characterization. ¹H NMR (900 MHz, DMSO-*d*₆) δ 8.15 (s, 2H), 7.94 (s, 2H), 7.75 (d, *J* = 8.2 Hz, 2H), 7.64 (d, *J* = 8.0 Hz, 2H), 7.50 (d, *J* = 7.9 Hz, 4H), 7.38 (d, 14.1 Hz, 2H), 7.34 (d, *J* = 16.5 Hz, 2H), 7.21 – 7.17 (m, 3H), 7.12 (s, 1H), 7.06 (s, 1H), 3.85 (s, 3H), 3.08 (dd, *J* = 7.3, 4.7 Hz, 4H), 1.16 (t, *J* = 7.3 Hz, 6H). HR-ESI-MS *m/z* for C₄₀H₃₄NO₇S⁻ calcd: 672.2134 found: 672.1844.

HPLC: 254 nm/Ref 700 nm

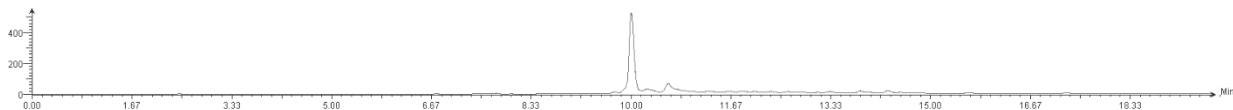


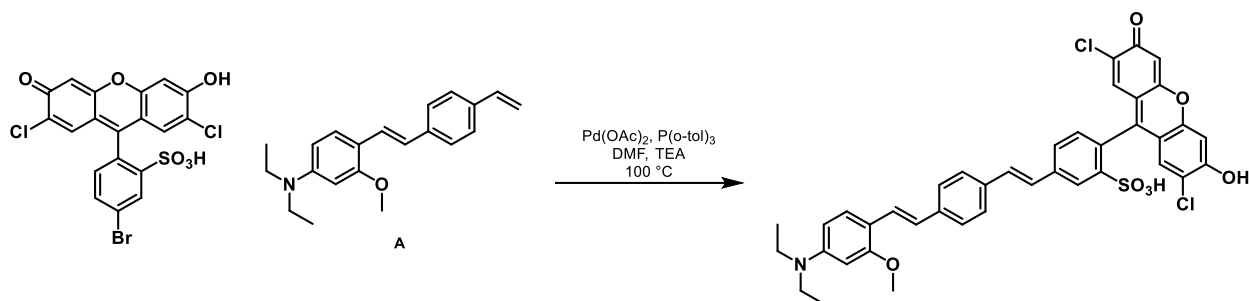


Synthesis of monosulfoVF2.2(OMe).F

5-bromo-2',7'-difluorosulfofluorescein (100 mg, 0.21 mmol), A (83 mg, 0.25 mmol), palladium acetate (1 mg, 0.045 mmol), and P(*o*-tol)₃ (2.7 mg, 0.09 mmol) were placed in an oven-dried Schlenk flask. The flask was sealed and evacuated/backfilled with nitrogen (3x). Anhydrous DMF (1 mL) and anhydrous Et₃N (1 mL) were added via syringe and the reaction was stirred for 16 hours at 100 degrees Celsius. After cooling, the reaction mixture was diluted with 3 mL dichloromethane and filtered through celite, which was then washed with methanol. The solvent was removed from the filtrate via rotary evaporation and the resulting residue was dissolved in 5 mL dichloromethane. The mixture was then poured into diethyl ether, resulting in precipitation of a brown solid. The solid was isolated via vacuum filtration (70 mg, 52%). A small amount of material was purified via RP-HPLC for further characterization. ¹H NMR (900 MHz, DMSO-*d*₆) δ 8.16 (s, 2H), 7.94 (s, 1H), 7.77 (d, *J* = 9.1 Hz, 2H), 7.72 (s, 1H), 7.69 (s, 1H), 7.65 (d, *J* = 8.1 Hz, 2H), 7.49 (m, 2H), 7.41 (d, *J* = 17.9 Hz, 1H), 7.39 – 7.32 (m, 4H), 7.21 (d, *J* = 7.8 Hz, 1H), 6.61 (d, *J* = 11.4 Hz, 2H), 3.85 (s, 3H), 3.09 (p, 4.9 Hz, 4H), 1.11 (t, *J* = 6.5 Hz, 6H). ¹³C NMR (226 MHz, DMSO) δ 157.99, 157.71, 157.57, 138.31, 129.92, 127.91, 127.54, 127.19, 126.38, 125.92, 125.38, 117.55, 116.23, 114.91, 104.19, 55.25, 45.72, 41.34. HR-ESI-MS *m/z* for C₄₀H₃₂F₂NO₇S⁻ calcd: 708.1946 found: 708.1898.

HPLC: 254 nm/Ref 700 nm

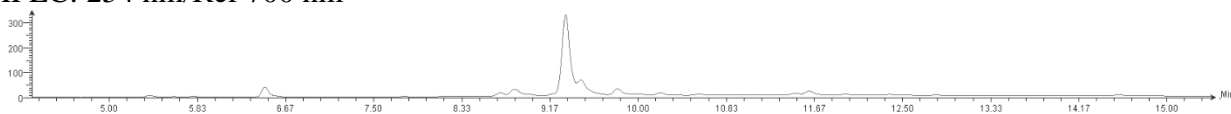


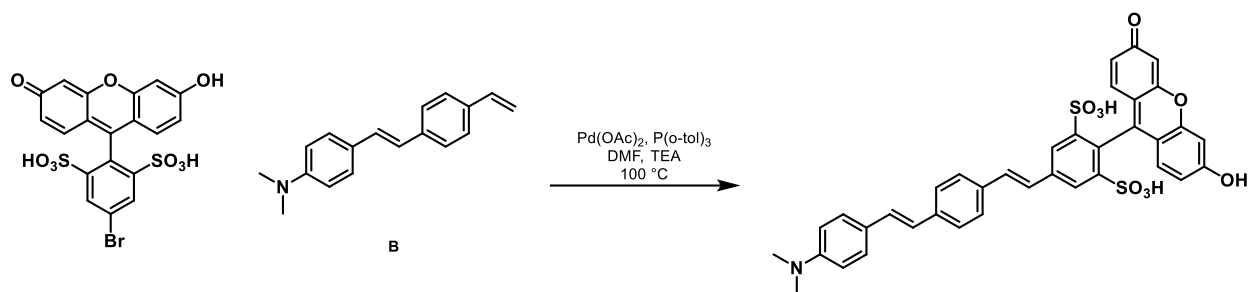


Synthesis of monosulfoVF2.2(OMe).Cl

5-bromo-2',7'-dichlorosulfofluorescein (100 mg, 0.19 mmol), **A** (71 mg, 0.23 mmol), palladium acetate (1 mg, 0.045 mmol), and P(*o*-tol)₃ (2.7 mg, 0.09 mmol) were placed in an oven-dried Schlenk flask. The flask was sealed and evacuated/backfilled with nitrogen (3x). Anhydrous DMF (1 mL) and anhydrous Et₃N (1 mL) were added via syringe and the reaction was stirred for 16 hours at 100 degrees Celsius. After cooling, the reaction mixture was diluted with 3 mL dichloromethane and filtered through celite, which was then washed with methanol. The solvent was removed from the filtrate via rotary evaporation and the resulting residue was dissolved in 5 mL dichloromethane. The mixture was then poured into diethyl ether, resulting in precipitation of a brown solid. The solid was isolated via vacuum filtration (55 mg, 46%). A small amount of material was purified via RP-HPLC for further characterization. ¹H NMR (900 MHz, DMSO-*d*₆) δ 8.22 (s, 2H), 7.71 (d, *J* = 8.1 Hz, 1H), 7.56 (d, *J* = 8.0 Hz, 2H), 7.49 (d, *J* = 16.3 Hz, 1H), 7.45 (d, *J* = 8.4 Hz, 2H), 7.34 (d, *J* = 16.3 Hz, 2H), 7.20 (d, *J* = 16.2 Hz, 1H), 7.15 (s, 1H), 7.07 (m, 1H), 7.00 (d, *J* = 16.5 Hz, 2H), 6.73 (d, *J* = 8.4 Hz, 3H), 3.44 (s, 3H), 3.08 (dd, *J* = 7.2, 4.9 Hz, 4H), 1.16 (t, *J* = 7.3 Hz, 6H). ¹³C NMR (226 MHz, DMSO) δ 157.78, 157.64, 157.51, 149.97, 147.92, 127.61, 127.33, 126.16, 125.61, 118.75, 117.84, 116.52, 115.19, 112.28, 112.25, 100.92, 53.33, 45.70. HR-ESI-MS *m/z* for C₄₀H₃₂Cl₂NO₇S⁻ calcd: 740.1355 found: 740.1322.

HPLC: 254 nm/Ref 700 nm

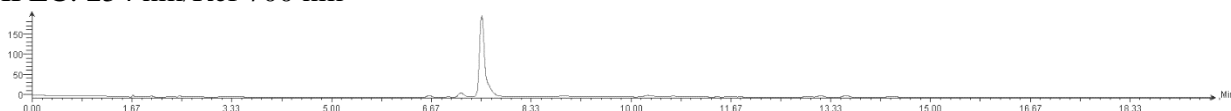


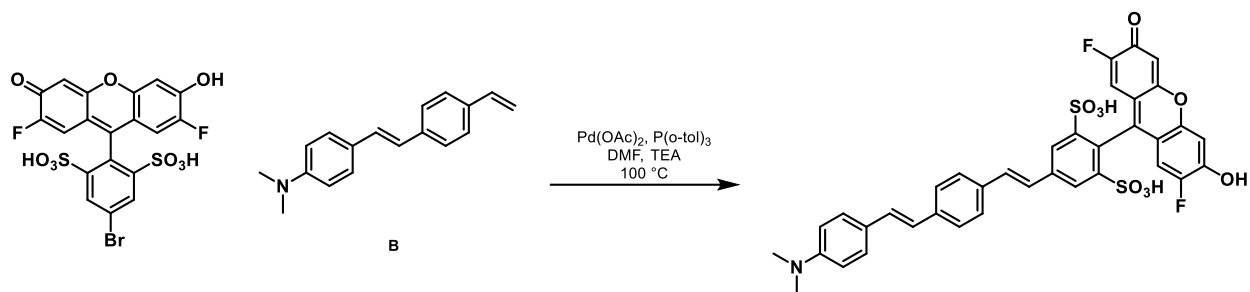


Synthesis of disulfoVF2.1.H

5-bromodisulfofluorescein (100 mg, 0.19 mmol), **B** (56 mg, 0.22 mmol), palladium acetate (1 mg, 0.045 mmol), and P(*o*-tol)₃ (2.7 mg, 0.09 mmol) were placed in an oven-dried Schlenk flask. The flask was sealed and evacuated/backfilled with nitrogen (3x). Anhydrous DMF (1 mL) and anhydrous Et₃N (1 mL) were added via syringe and the reaction was stirred for 16 hours at 100 degrees Celsius. After cooling, the reaction mixture was diluted with 10 mL methanol and filtered through celite, which was then washed with methanol. The solvent was removed from the filtrate via rotary evaporation and the resulting residue was dissolved in 5 mL dichloromethane. The mixture was then poured into diethyl ether, resulting in precipitation of a brown solid. The solid was isolated via vacuum filtration (37 mg, 28%). A small amount of material was purified via RP-HPLC for further characterization. ¹H NMR (900 MHz, DMSO-*d*₆) δ 8.16 (s, 2H), 8.12 (s, 2H), 7.78 (d, *J* = 7.9 Hz, 2H), 7.64 (d, *J* = 7.8 Hz, 2H), 7.54 (d, *J* = 7.6 2H), 7.50 (d, *J* = 7.9 Hz, 2H), 7.40 (d, *J* = 11.5 Hz, 1H), 7.34 (d, *J* = 16.5 Hz, 1H), 7.24 (d, *J* = 7.7 Hz, 1H), 7.15 (s, 1H), 7.09 (s, 2H), 7.04 (s, 2H), 2.88 (s, 6H). HR-ESI-MS *m/z* for C₃₇H₂₈NO₉S₂⁻ calcd: 694.1284 found: 694.1188.

HPLC: 254 nm/Ref 700 nm

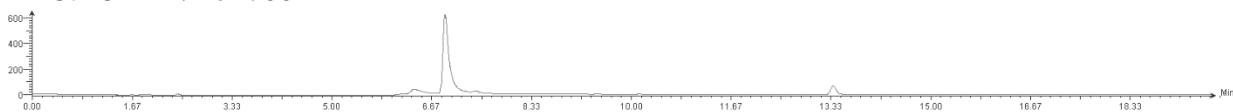


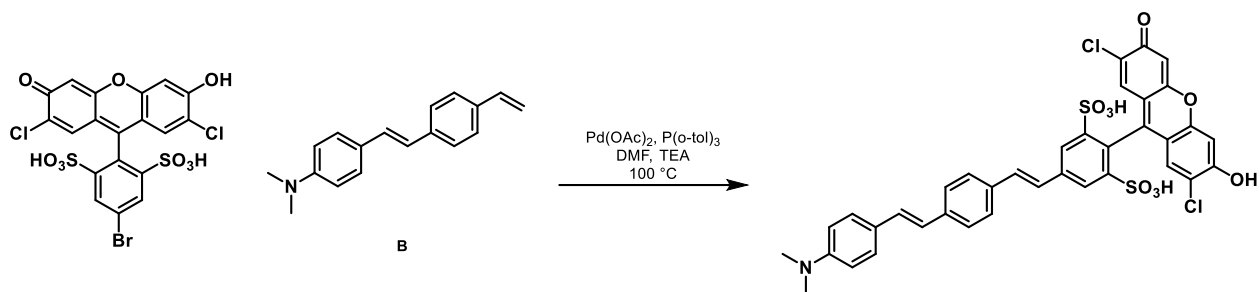


Synthesis of disulfoVF2.1.F

5-bromo-2',7'-difluorodisulfofluorescein (100 mg, 0.19 mmol), **B** (53 mg, 0.21 mmol), palladium acetate (1 mg, 0.045 mmol), and P(*o*-tol)₃ (2.7 mg, 0.09 mmol) were placed in an oven-dried Schlenk flask. The flask was sealed and evacuated/backfilled with nitrogen (3x). Anhydrous DMF (1 mL) and anhydrous Et₃N (1 mL) were added via syringe and the reaction was stirred for 16 hours at 100 degrees Celsius. After cooling, the reaction mixture was diluted with 10 mL methanol and filtered through celite, which was then washed with methanol. The solvent was removed from the filtrate via rotary evaporation and the resulting residue was dissolved in 5 mL dichloromethane. The mixture was then poured into diethyl ether, resulting in precipitation of a brown solid. The solid was isolated via vacuum filtration (30 mg, 23%). A small amount of material was purified via RP-HPLC for further characterization. ¹H NMR (900 MHz, DMSO-*d*₆) δ 7.73 (s, 2H), 7.70 (d, *J* = 8.4 Hz, 2H), 7.56 (s, 2H), 7.53 – 7.49 (m, 1H), 7.45 (d, *J* = 9.0 Hz, 4H), 7.30 (d, *J* = 16.5 Hz, 1H), 7.19 (d, *J* = 18.2 Hz, 1H), 7.00 (d, *J* = 15.8 Hz, 1H), 6.98 – 6.93 (m, 1H), 6.75 – 6.69 (m, 3H), 2.93 (s, 6H). HR-ESI-MS *m/z* for C₃₇H₂₆F₂NO₉S₂⁻ calcd: 730.1905 found: 730.1798.

HPLC: 254 nm/Ref 700 nm

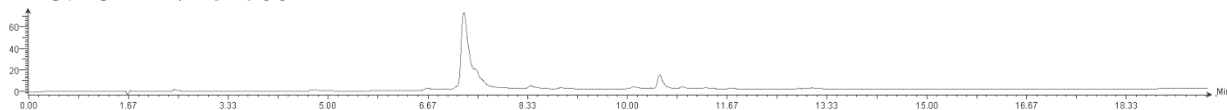


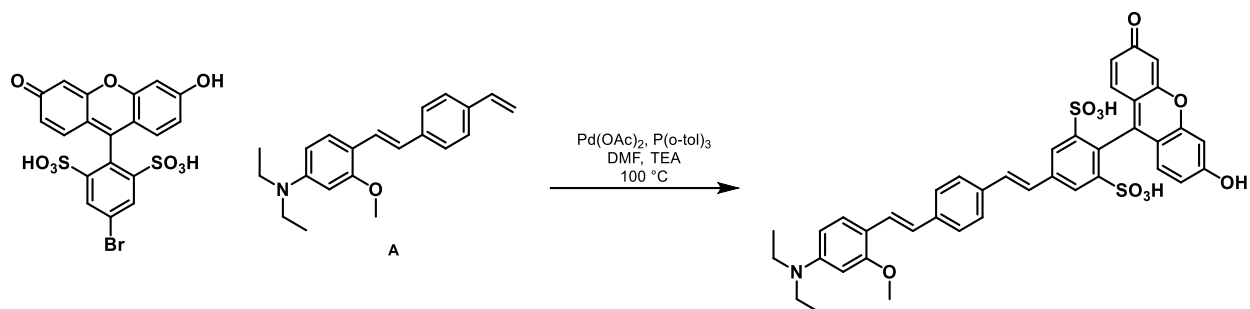


Synthesis of disulfoVF2.1.Cl

5-bromo-2',7'-dichlorodisulfofluorescein (100 mg, 0.17 mmol), **B** (50 mg, 0.20 mmol), palladium acetate (1 mg, 0.045 mmol), and P(*o*-tol)₃ (2.7 mg, 0.09 mmol) were placed in an oven-dried Schlenk flask. The flask was sealed and evacuated/backfilled with nitrogen (3x). Anhydrous DMF (1 mL) and anhydrous Et₃N (1 mL) were added via syringe and the reaction was stirred for 16 hours at 100 degrees Celsius. After cooling, the reaction mixture was diluted with 10 mL methanol and filtered through celite, which was then washed with methanol. The solvent was removed from the filtrate via rotary evaporation and the resulting residue was dissolved in 5 mL dichloromethane. The mixture was then poured into diethyl ether, resulting in precipitation of a brown solid. The solid was isolated via vacuum filtration (48 mg, 38%). A small amount of material was purified via RP-HPLC for further characterization. ¹H NMR (900 MHz, DMSO-*d*₆) δ 8.35 (s, 2H), 8.03 (s, 2H), 7.80 (d, *J* = 8.2 Hz, 2H), 7.68 (d, *J* = 8.2 Hz, 2H), 7.57 (d, *J* = 8.6 Hz, 2H), 7.54 (d, *J* = 16.2 Hz, 1H), 7.46 (d, *J* = 16.4 Hz, 1H), 7.29 (d, *J* = 16.3 Hz, 1H), 7.11 (d, *J* = 16.2 Hz, 1H), 7.01 (s, 2H), 6.84 (d, *J* = 8.7 Hz, 2H), 3.04 (s, 6H). ¹³C NMR (226 MHz, CDCl₃) δ 162.99, 152.00, 150.42, 147.99, 138.21, 136.12, 135.25, 130.63, 129.63, 129.41, 128.04, 126.61, 126.21, 125.23, 124.46, 123.48, 112.62, 41.83. HR-ESI-MS *m/z* for C₃₇H₂₆F₂NO₉S₂⁻ calcd: 762.0504 found: 762.0468.

HPLC: 254 nm/Ref 700 nm

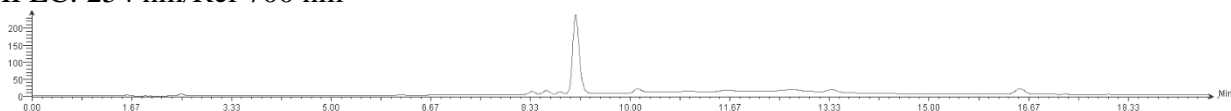


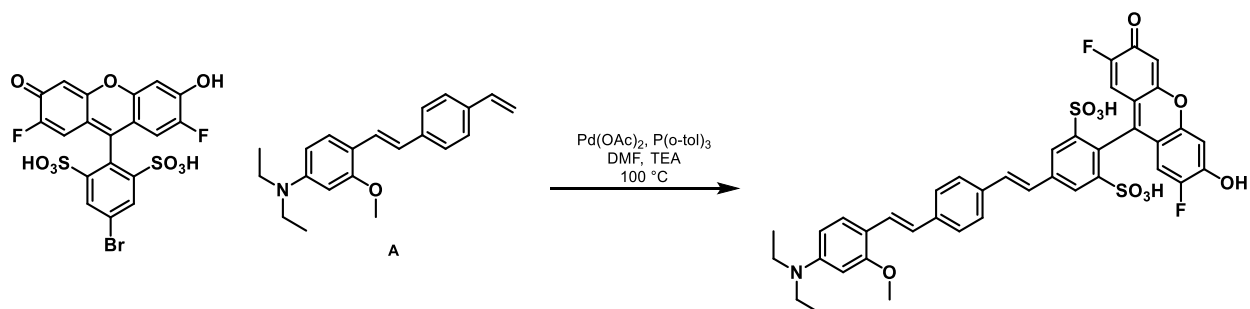


Synthesis of disulfoVF2.2(OMe).H

5-bromodisulfofluorescein (100 mg, 0.19 mmol), **A** (69 mg, 0.23 mmol), palladium acetate (1 mg, 0.045 mmol), and $P(o\text{-tol})_3$ (2.7 mg, 0.09 mmol) were placed in an oven-dried Schlenk flask. The flask was sealed and evacuated/backfilled with nitrogen (3x). Anhydrous DMF (1 mL) and anhydrous Et_3N (1 mL) were added via syringe and the reaction was stirred for 16 hours at 100 degrees Celsius. After cooling, the reaction mixture was diluted with 10 mL methanol and filtered through celite, which was then washed with methanol. The solvent was removed from the filtrate via rotary evaporation and the resulting residue was dissolved in 5 mL dichloromethane. The mixture was then poured into diethyl ether, resulting in precipitation of a brown solid. The solid was isolated via vacuum filtration (52 mg, 37%). A small amount of material was purified via RP-HPLC for further characterization. ^1H NMR (900 MHz, $\text{DMSO-}d_6$) δ 8.19 (s, 1H), 7.67 (d, $J = 7.9$ Hz, 2H), 7.60 – 7.56 (m, 1H), 7.54 – 7.50 (m, 1H), 7.47 (d, $J = 7.5$ Hz, 1H), 7.46 (s, 1H), 7.44 (s, 1H), 7.34 – 7.29 (m, 3H), 7.23 (d, $J = 7.8$ Hz, 1H), 7.13 (s, 1H), 6.97 (s, 3H), 6.84 (d, $J = 9.2$ Hz, 1H), 6.52 (s, 2H), 3.82 (s, 3H), 3.06 (dd, $J = 13.6, 6.3$ Hz, 4H), 1.15 – 1.11 (m, 6H). HR-ESI-MS m/z for $\text{C}_{40}\text{H}_{34}\text{NO}_{10}\text{S}_2^-$ calcd: 752.1702 found: 752.1684.

HPLC: 254 nm/Ref 700 nm

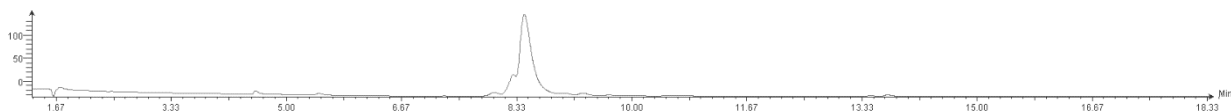


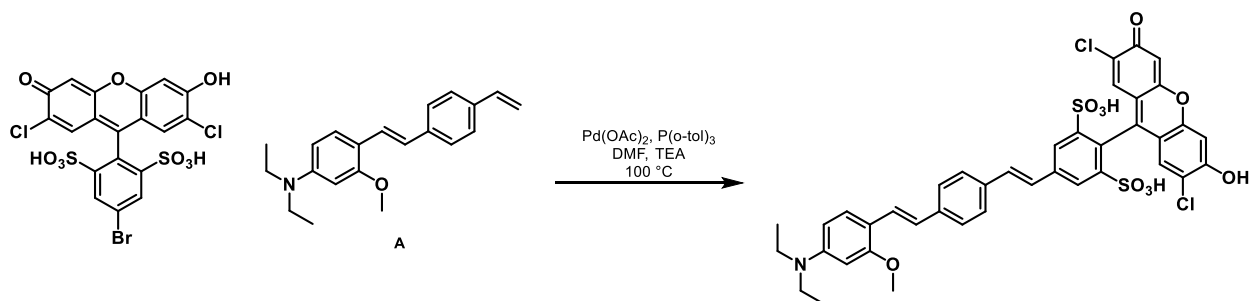


Synthesis of disulfoVF2.2(OMe).F

5-bromo-2',7'-difluorodisulfofluorescein (100 mg, 0.18 mmol), A (65 mg, 0.21 mmol), palladium acetate (1 mg, 0.045 mmol), and P(*o*-tol)₃ (2.7 mg, 0.09 mmol) were placed in an oven-dried Schlenk flask. The flask was sealed and evacuated/backfilled with nitrogen (3x). Anhydrous DMF (1 mL) and anhydrous Et₃N (1 mL) were added via syringe and the reaction was stirred for 16 hours at 100 degrees Celsius. After cooling, the reaction mixture was diluted with 10 mL methanol and filtered through celite, which was then washed with methanol. The solvent was removed from the filtrate via rotary evaporation and the resulting residue was dissolved in 5 mL dichloromethane. The mixture was then poured into diethyl ether, resulting in precipitation of a brown solid. The solid was isolated via vacuum filtration (79 mg, 56%). A small amount of material was purified via RP-HPLC for further characterization. ¹H NMR (900 MHz, DMSO-*d*₆) δ 8.22 (s, 2H), 8.17 (s, 1H), 8.12 (s, 1H), 7.68 (d, *J* = 7.8 Hz, 2H), 7.50 – 7.47 (m, 2H), 7.47 – 7.40 (m, 1H), 7.34 (d, *J* = 16.4 Hz, 1H), 7.29 (d, *J* = 16.6 Hz, 1H), 7.09 (m, 1H), 7.03 – 6.95 (m, 1H), 6.30 (s, 1H), 6.22 (s, 1H), 3.85 (s, 3H), 3.09 (dd, *J* = 7.3, 5.0 Hz, 4H), 1.17 (t, *J* = 7.3 Hz, 6H). HR-ESI-MS *m/z* for C₄₀H₃₂F₂NO₁₀S₂⁻ calcd: 788.1514 found: 788.1394.

HPLC: 254 nm/Ref 700 nm

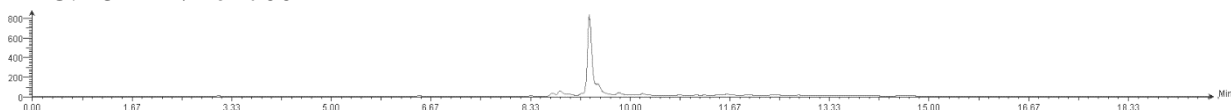




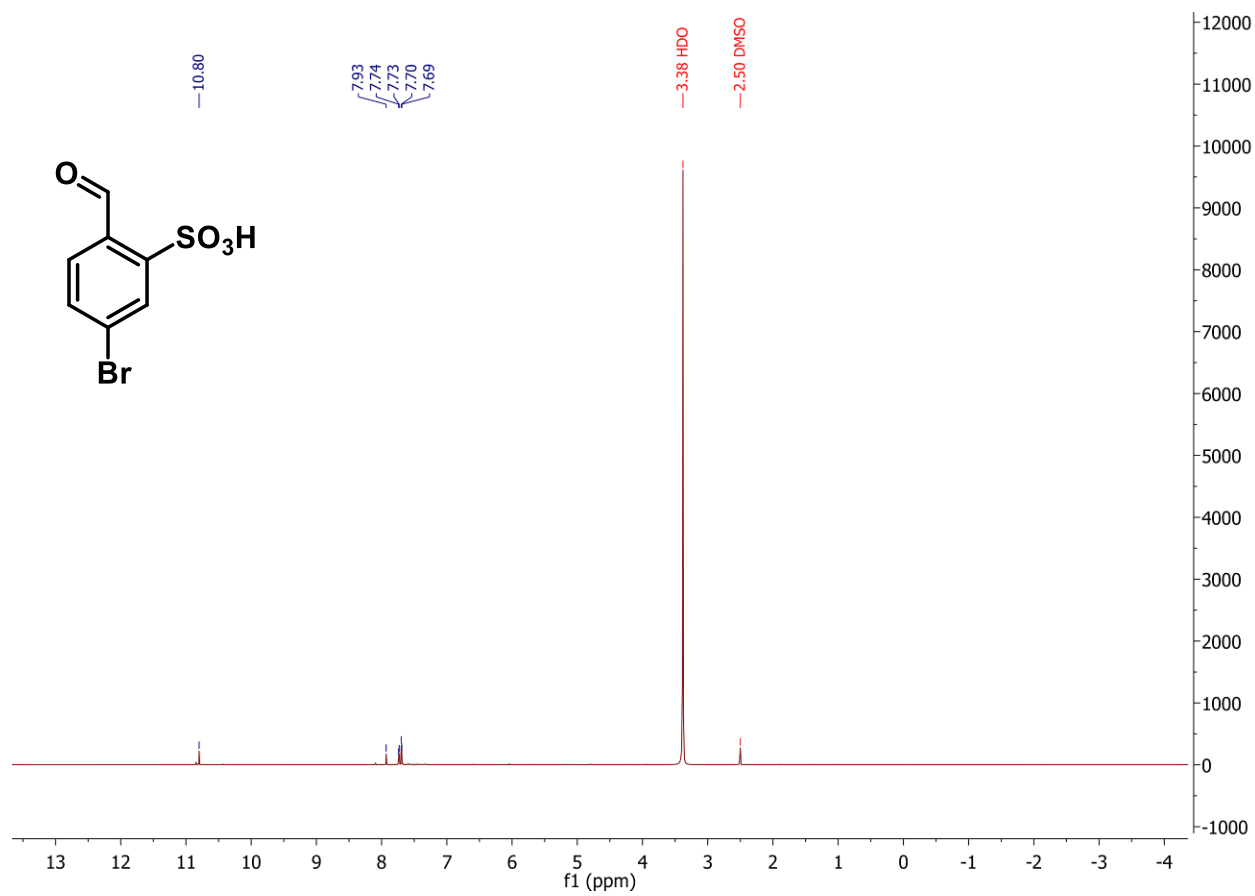
Synthesis of disulfoVF2.2(OMe).Cl

5-bromo-2,7-dichlorodisulfofluorescein (100 mg, 0.18 mmol), **A** (65 mg, 0.21 mmol), palladium acetate (1 mg, 0.045 mmol), and $P(o\text{-tol})_3$ (2.7 mg, 0.09 mmol) were placed in an oven-dried Schlenk flask. The flask was sealed and evacuated/backfilled with nitrogen (3x). Anhydrous DMF (1 mL) and anhydrous Et_3N (1 mL) were added via syringe and the reaction was stirred for 16 hours at 100 degrees Celsius. After cooling, the reaction mixture was diluted with 10 mL methanol and filtered through celite, which was then washed with methanol. The solvent was removed from the filtrate via rotary evaporation and the resulting residue was dissolved in 5 mL dichloromethane. The mixture was then poured into diethyl ether, resulting in precipitation of a brown solid. The solid was isolated via vacuum filtration (79 mg, 56%). A small amount of material was purified via RP-HPLC for further characterization. ^1H NMR (900 MHz, $\text{DMSO-}d_6$) δ 8.24 (s, 1H), 7.95 (d, $J = 8.1$ Hz, 2H), 7.93 – 7.89 (m, 2H), 7.69 (d, $J = 16.4$ Hz, 2H), 7.43 (d, $J = 16.4$ Hz, 2H), 7.11 (s, 2H), 7.05 (s, 1H), 7.00 (s, 1H), 6.85 (s, 1H), 6.75 (s, 2H), 6.61 (s, 1H), 3.83 (s, 3H), 3.08 – 3.03 (m, 4H), 1.13 (t, $J = 7.4$ Hz, 6H). ^{13}C NMR (226 MHz, DMSO) δ 192.94, 162.75, 158.44, 148.62, 143.30, 137.41, 135.74, 131.61, 131.36, 130.43, 130.16, 130.09, 129.37, 127.92, 126.74, 118.54, 118.04, 117.62, 116.31, 115.00, 102.93, 46.17, 41.80, 36.22, 34.80, 31.21. HR-ESI-MS m/z for $\text{C}_{40}\text{H}_{32}\text{Cl}_2\text{NO}_{10}\text{S}_2^-$ calcd: 820.0923 found: 819.9684.

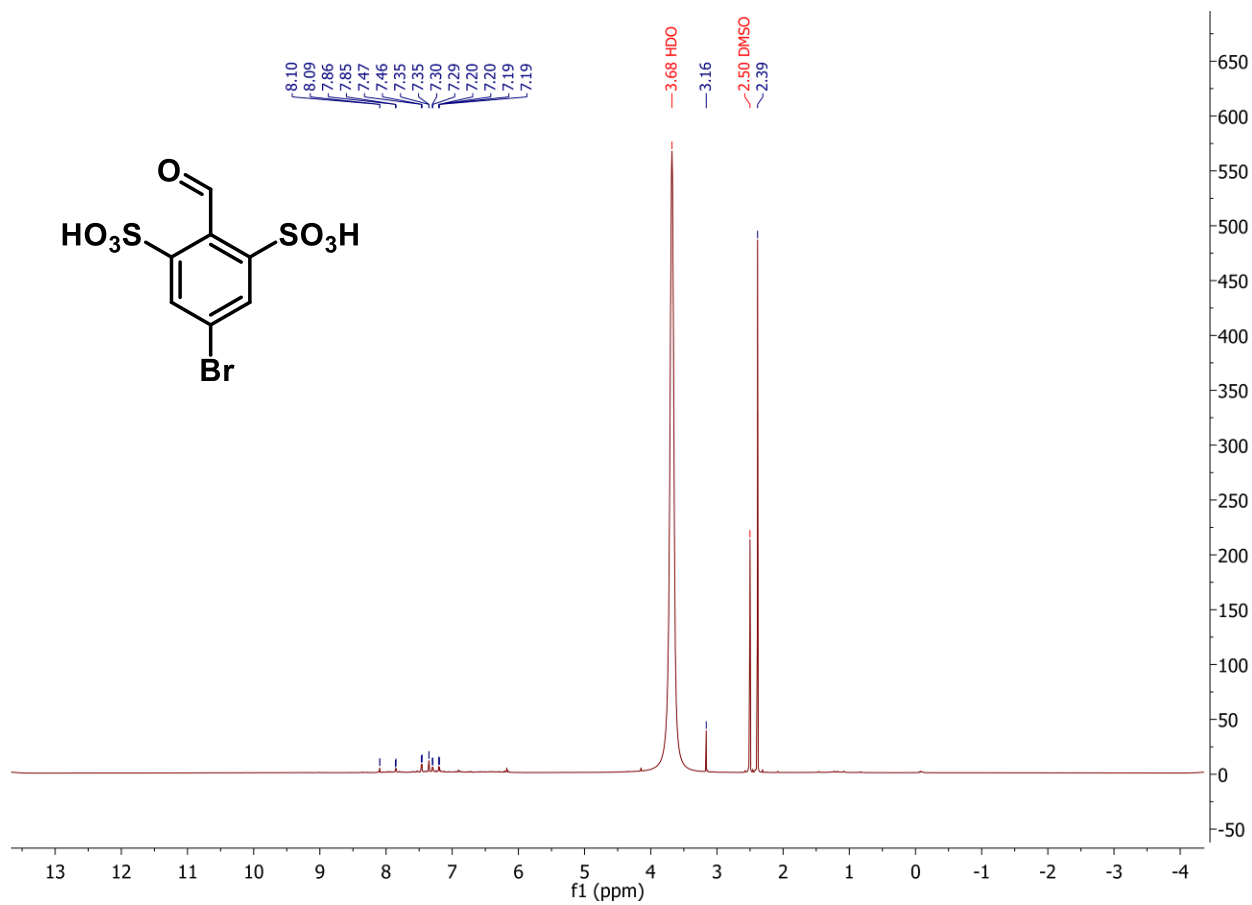
HPLC: 254 nm/Ref 700 nm



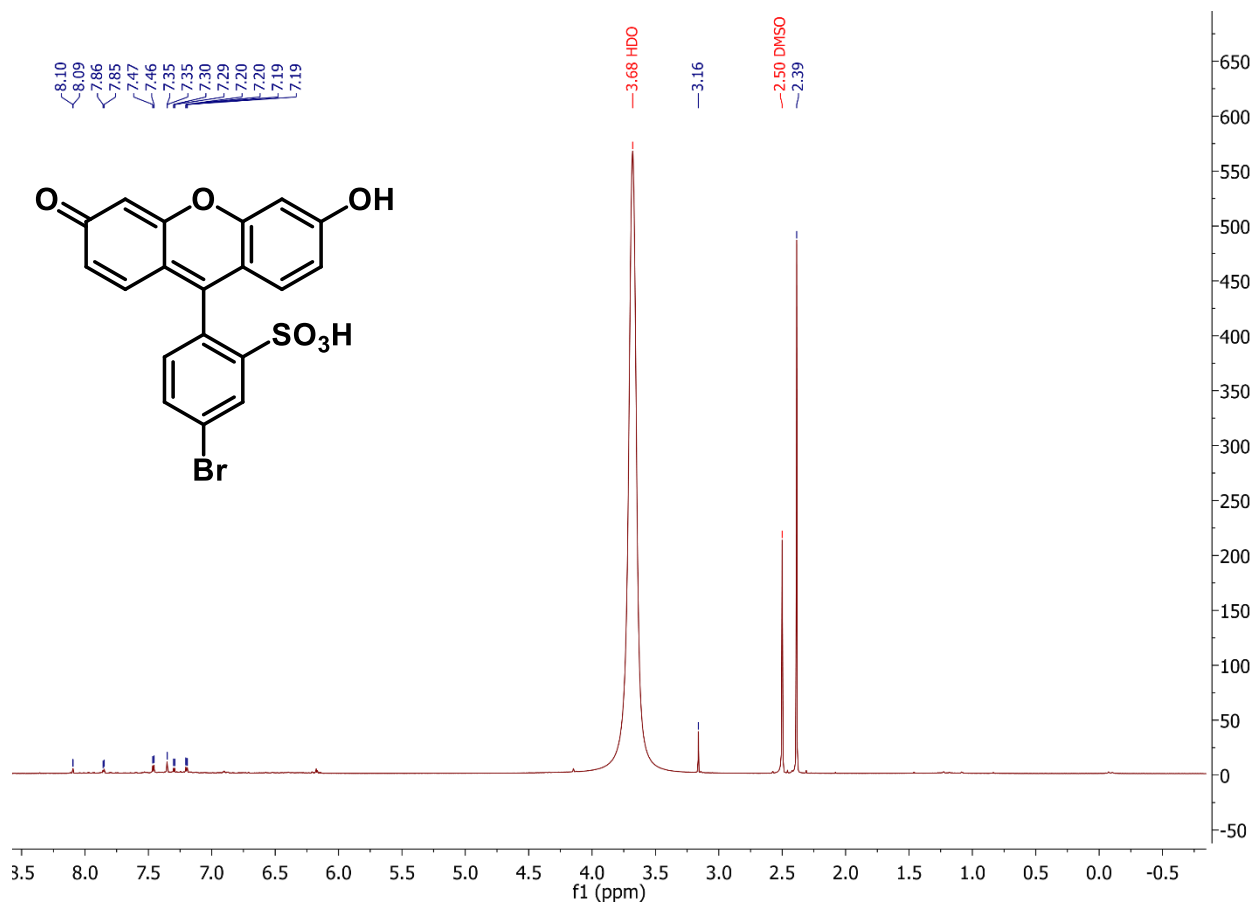
Spectra



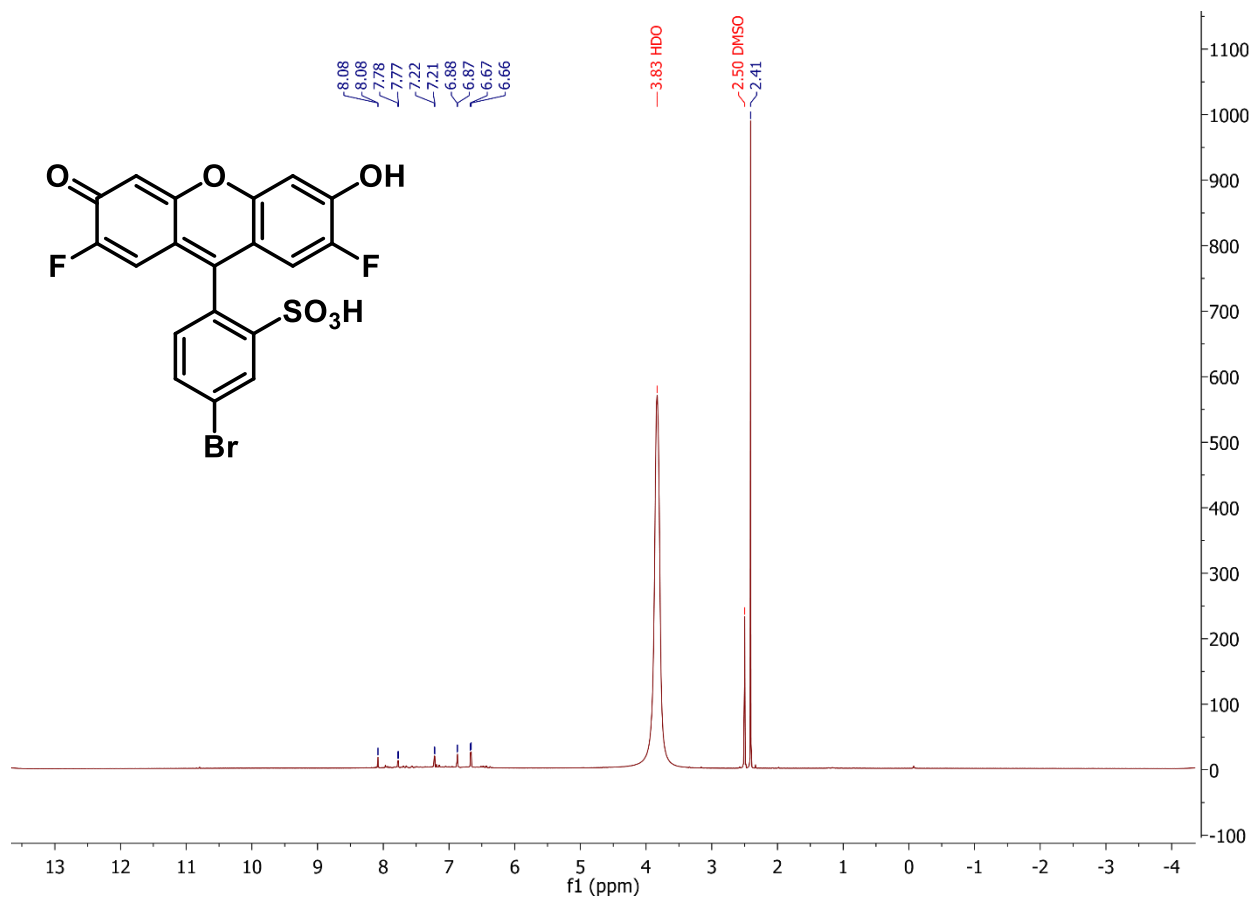
Spectrum 4.1. ¹H NMR of 4-bromo-2-sulfobenzaldehyde



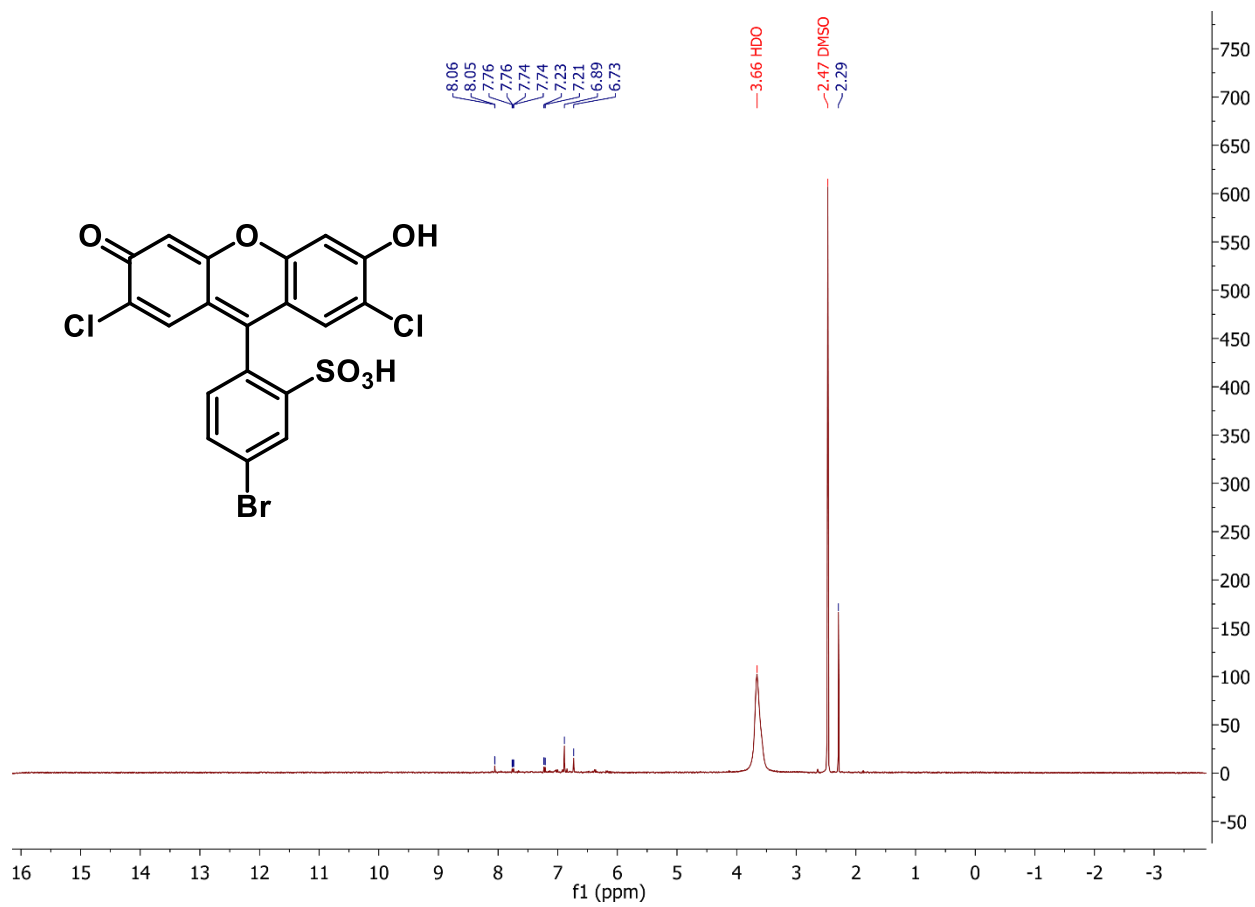
Spectrum 4.2. ¹H NMR of 4-bromo-2,6-disulfobenzaldehyde



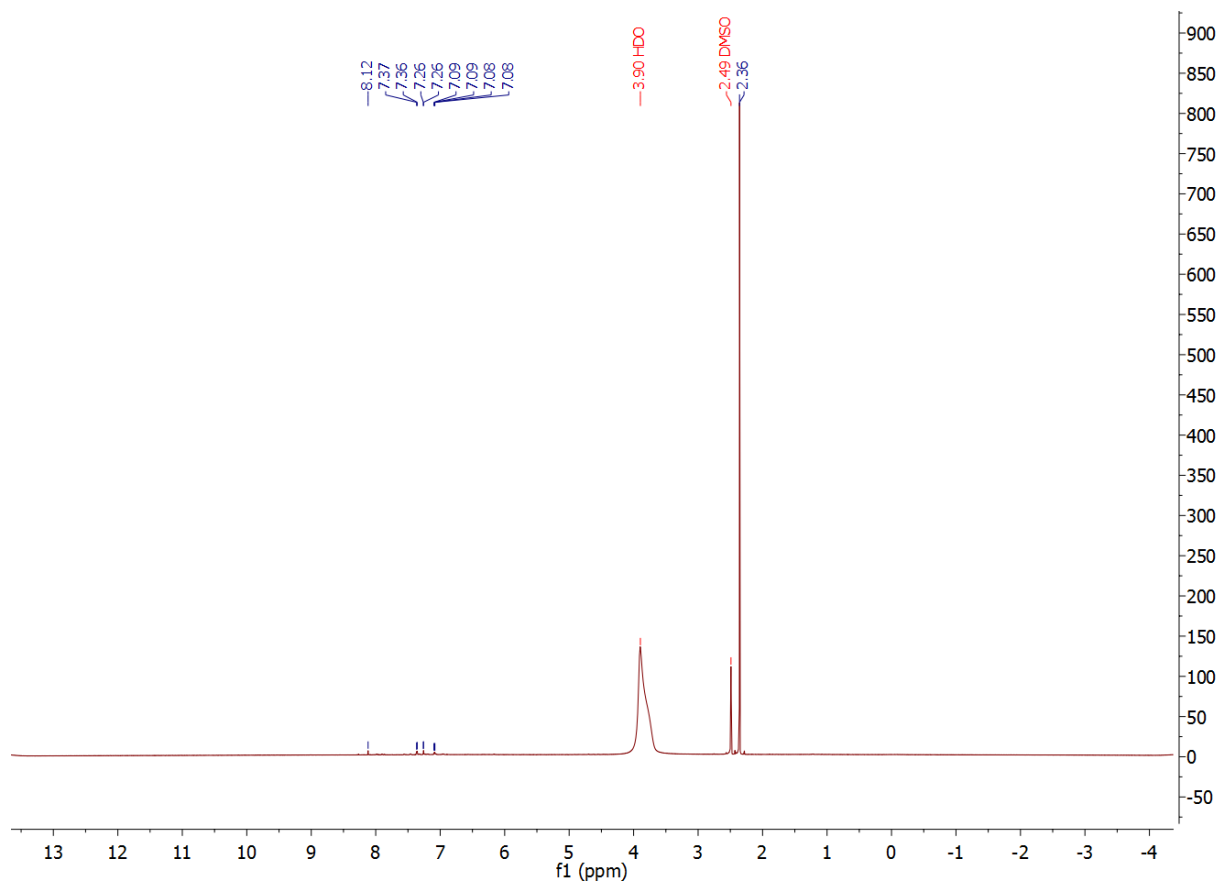
Spectrum 4.3. ¹H NMR of 5-bromosulfofluorescein



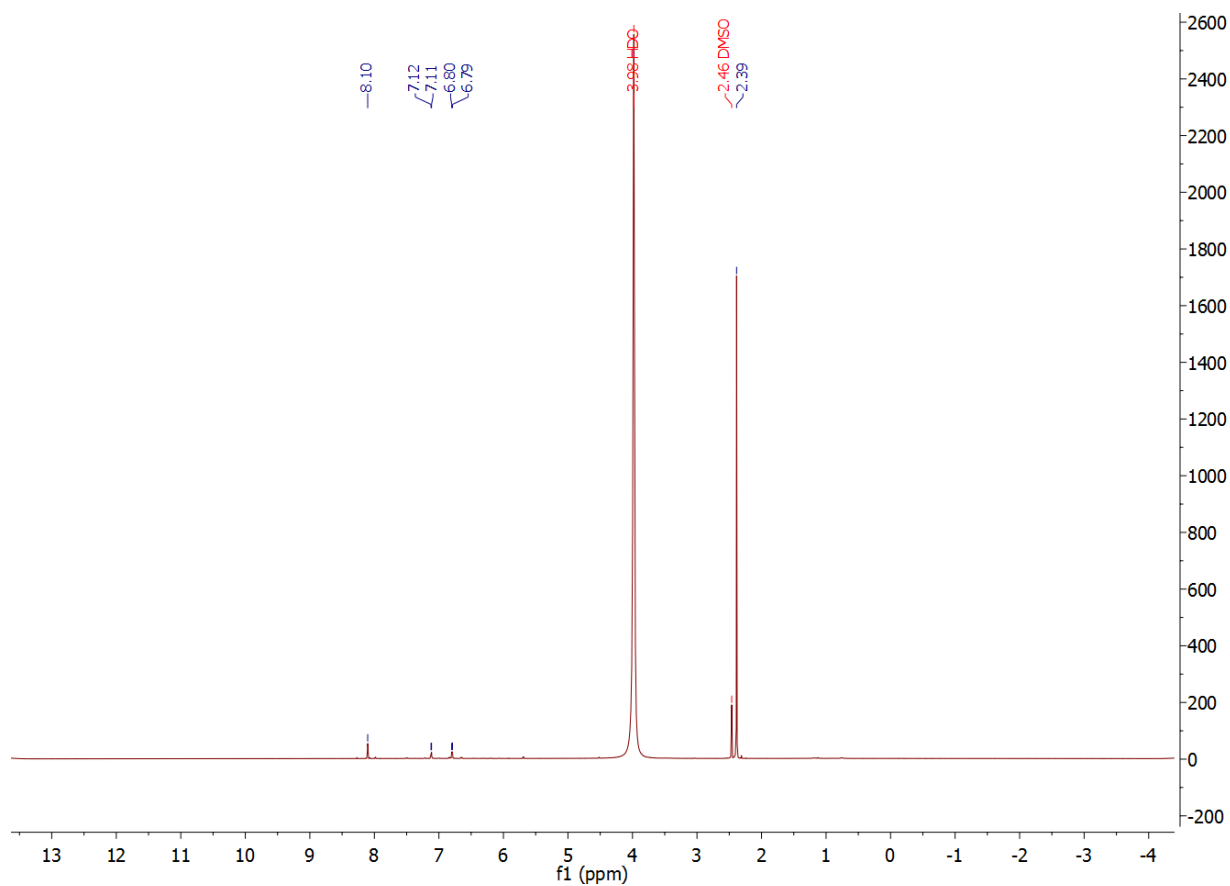
Spectrum 4.4. ¹H NMR of 5-bromo-2',7'-difluorosulfofluorescein



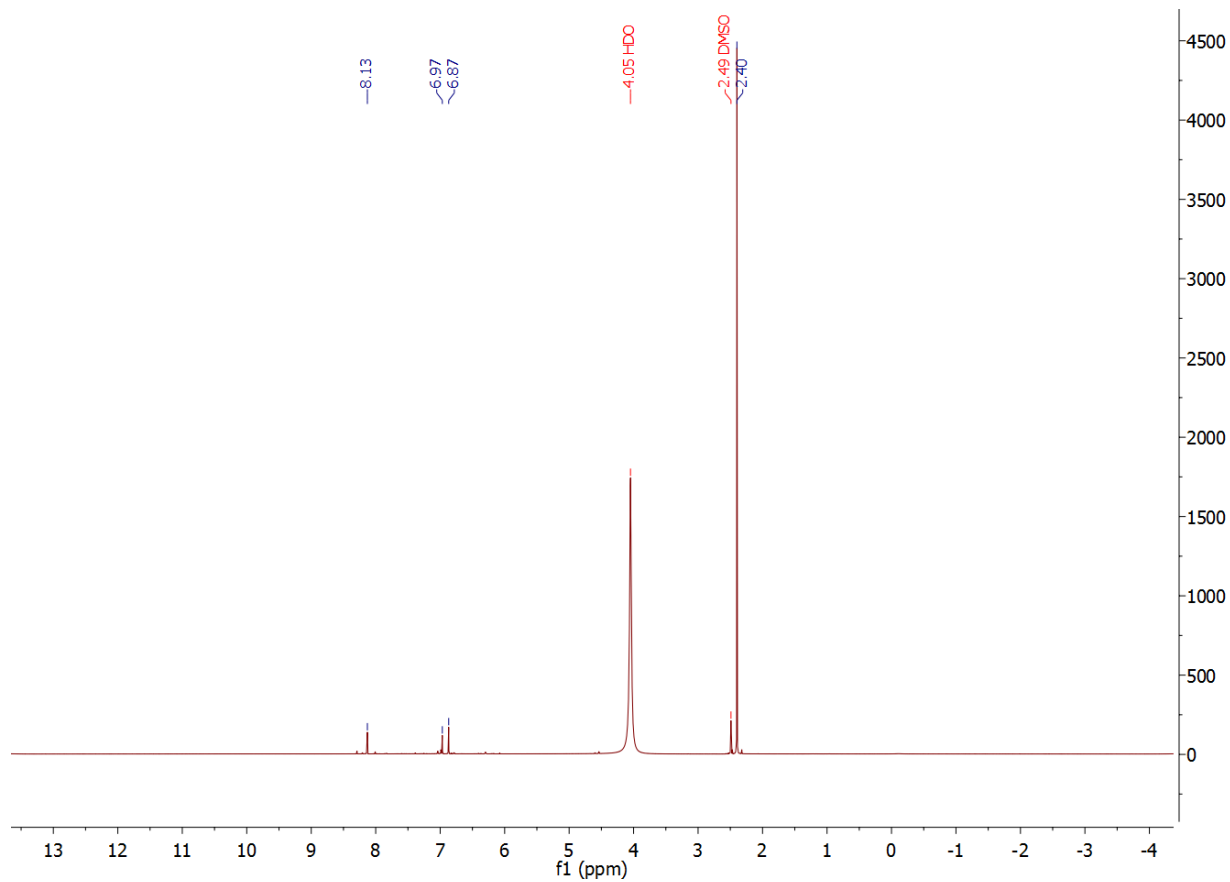
Spectrum 4.5. ¹H NMR of 5-bromo-2',7'-dichlorosulfofluorescein



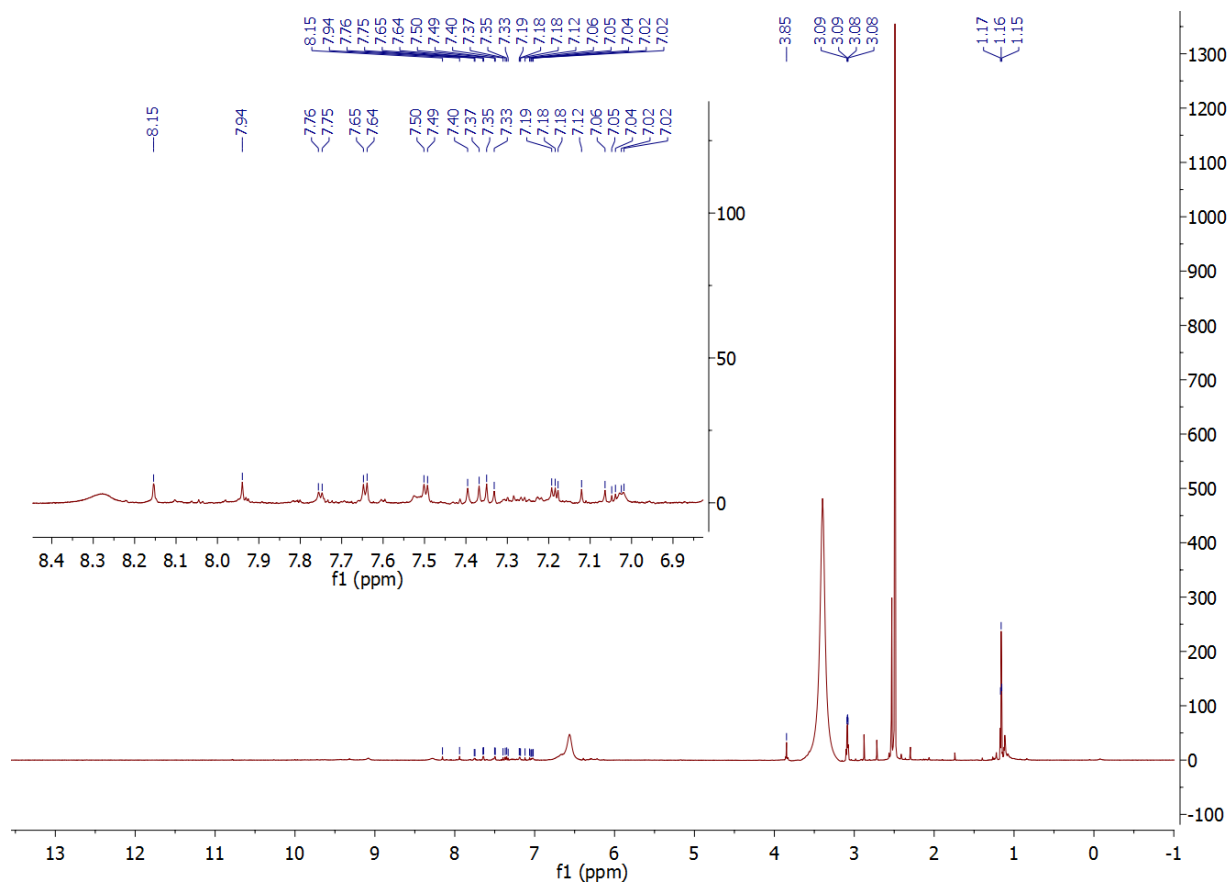
Spectrum 4.6. ^1H NMR of 5-bromodisulfofluorescein



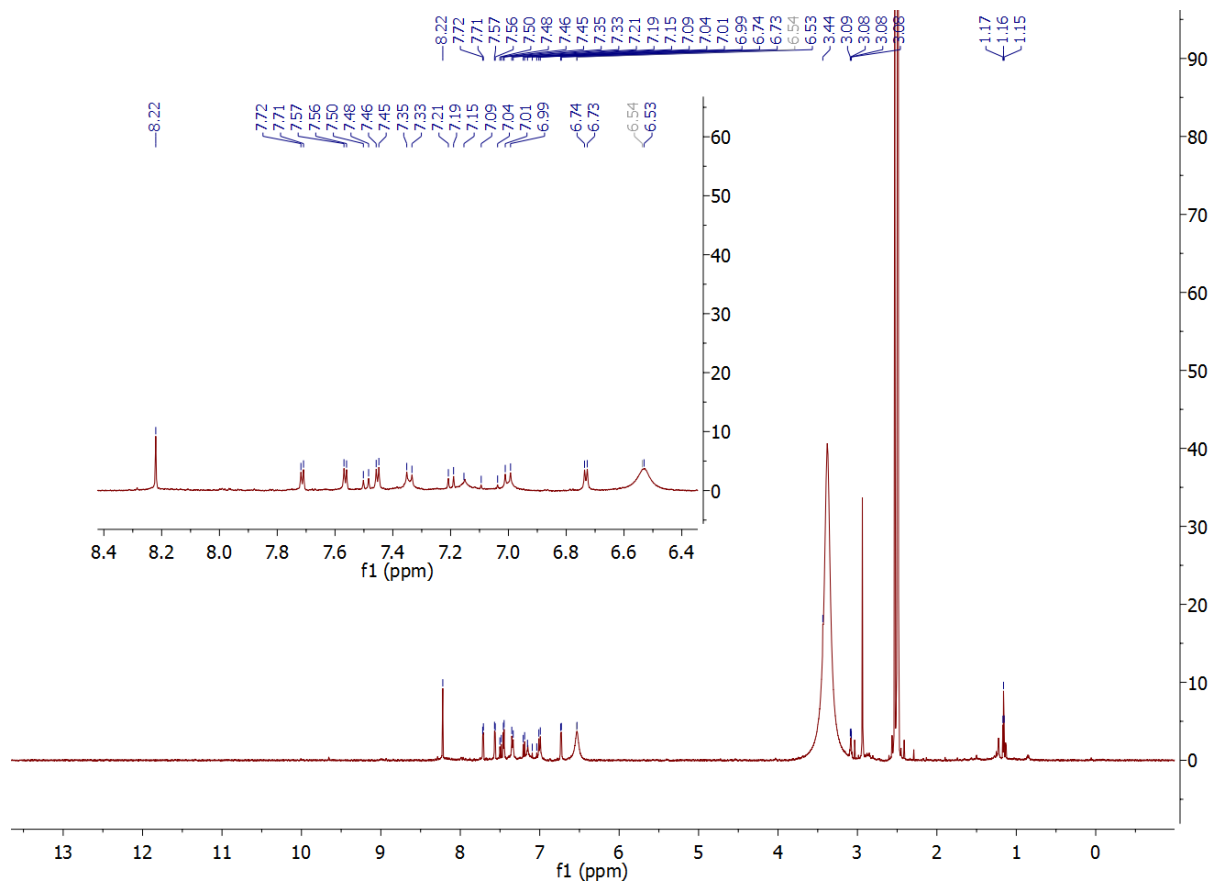
Spectrum 4.7. ¹H NMR of 5-bromo-2',7'-difluorodisulfofluorescein



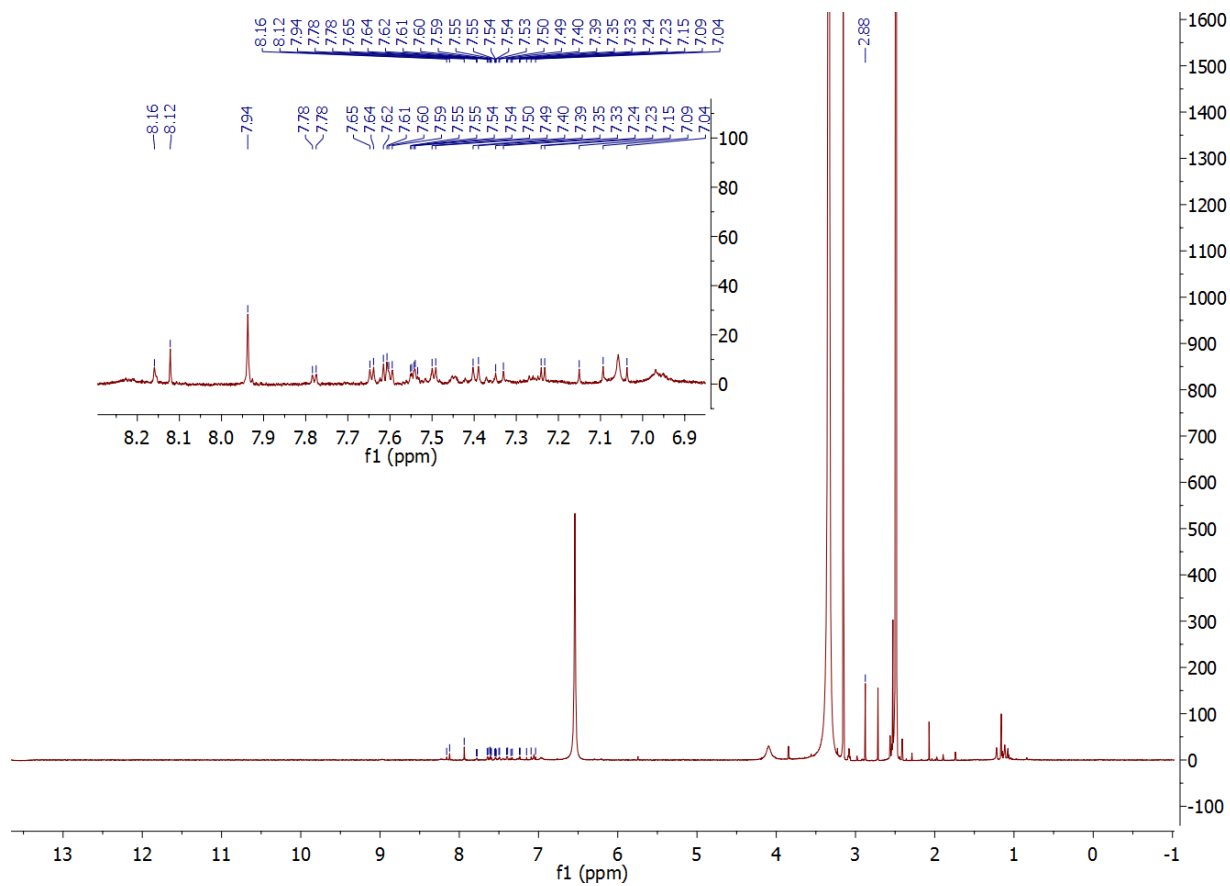
Spectrum 4.8. ^1H NMR of 5-bromo-2',7'-dichlorodisulfofluorescein



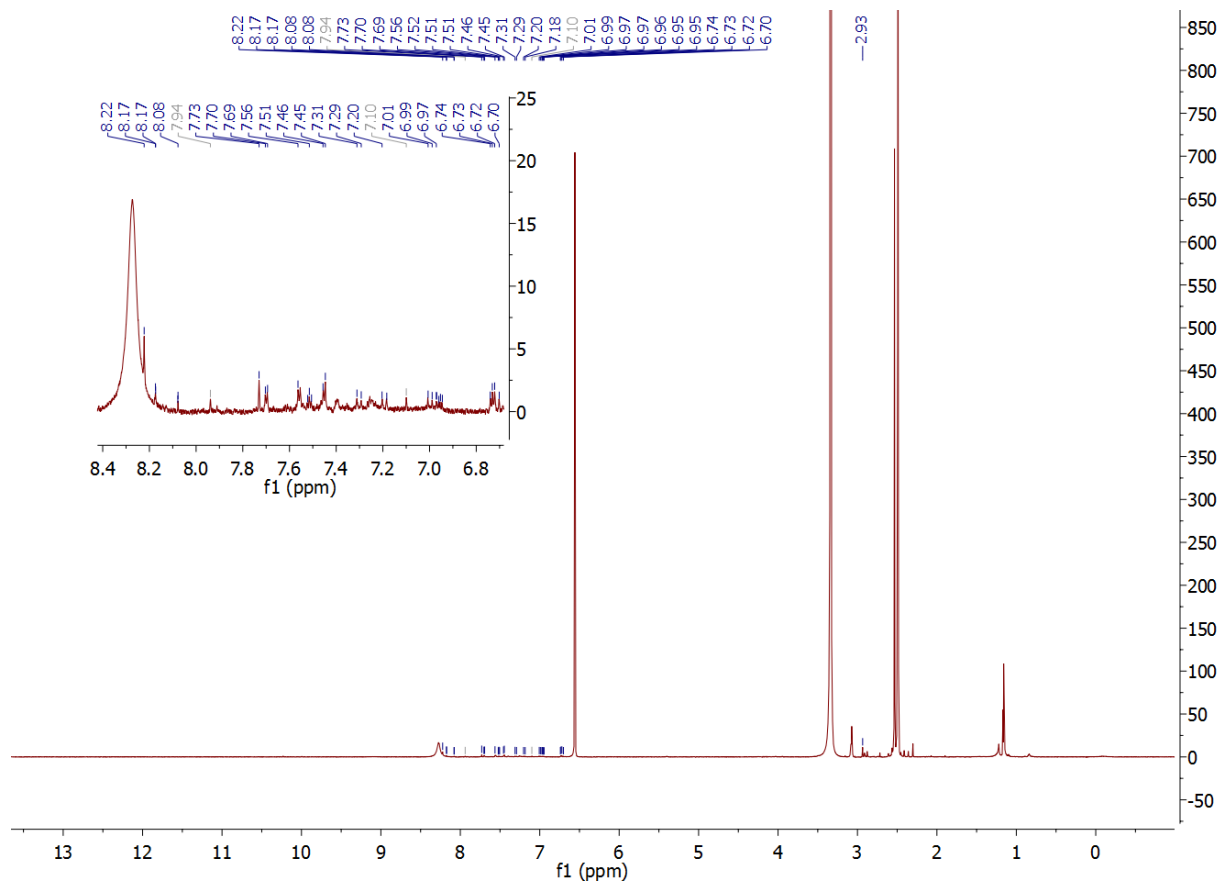
Spectrum 4.9. ^1H NMR of msVF2.2(OMe).H



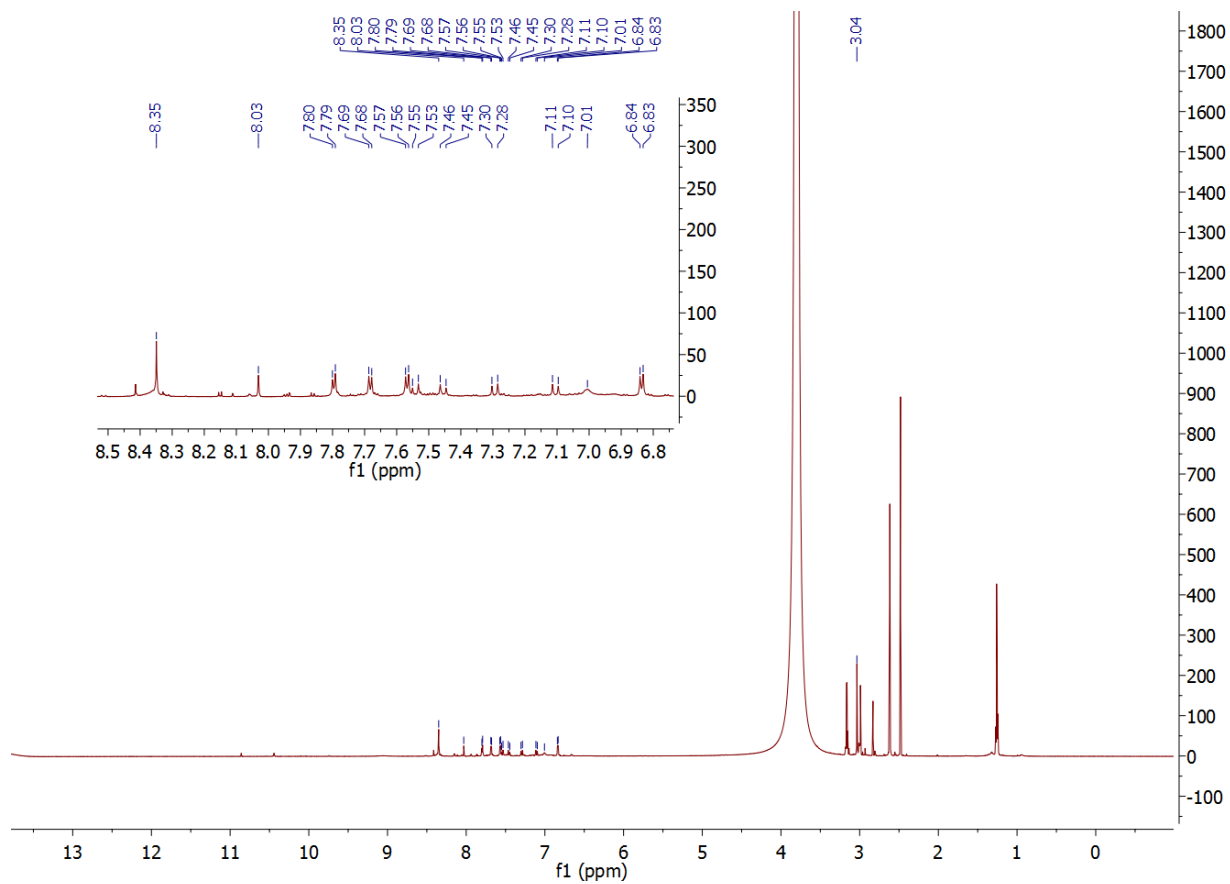
Spectrum 4.11. ^1H NMR of msVF2.2(OMe).Cl



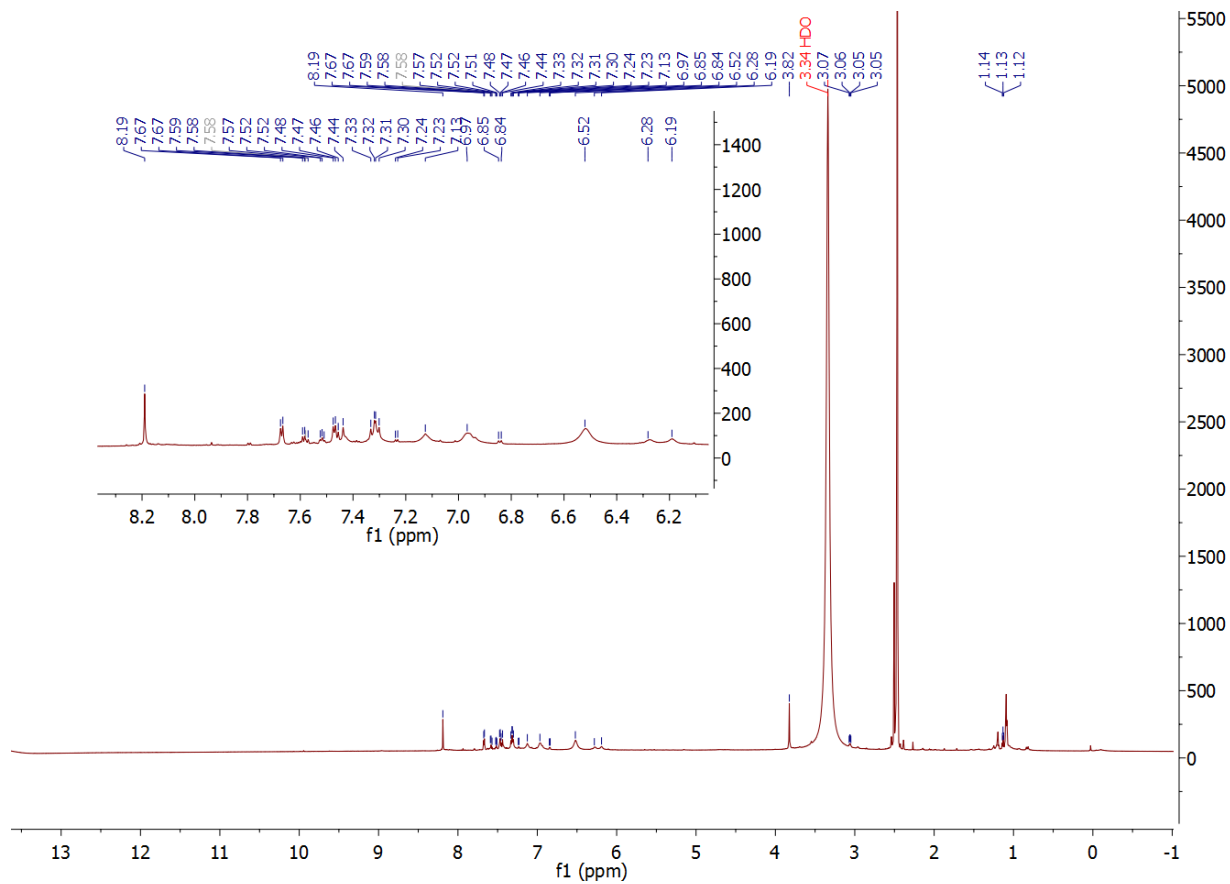
Spectrum 4.12. ^1H NMR of dsVF2.1.H



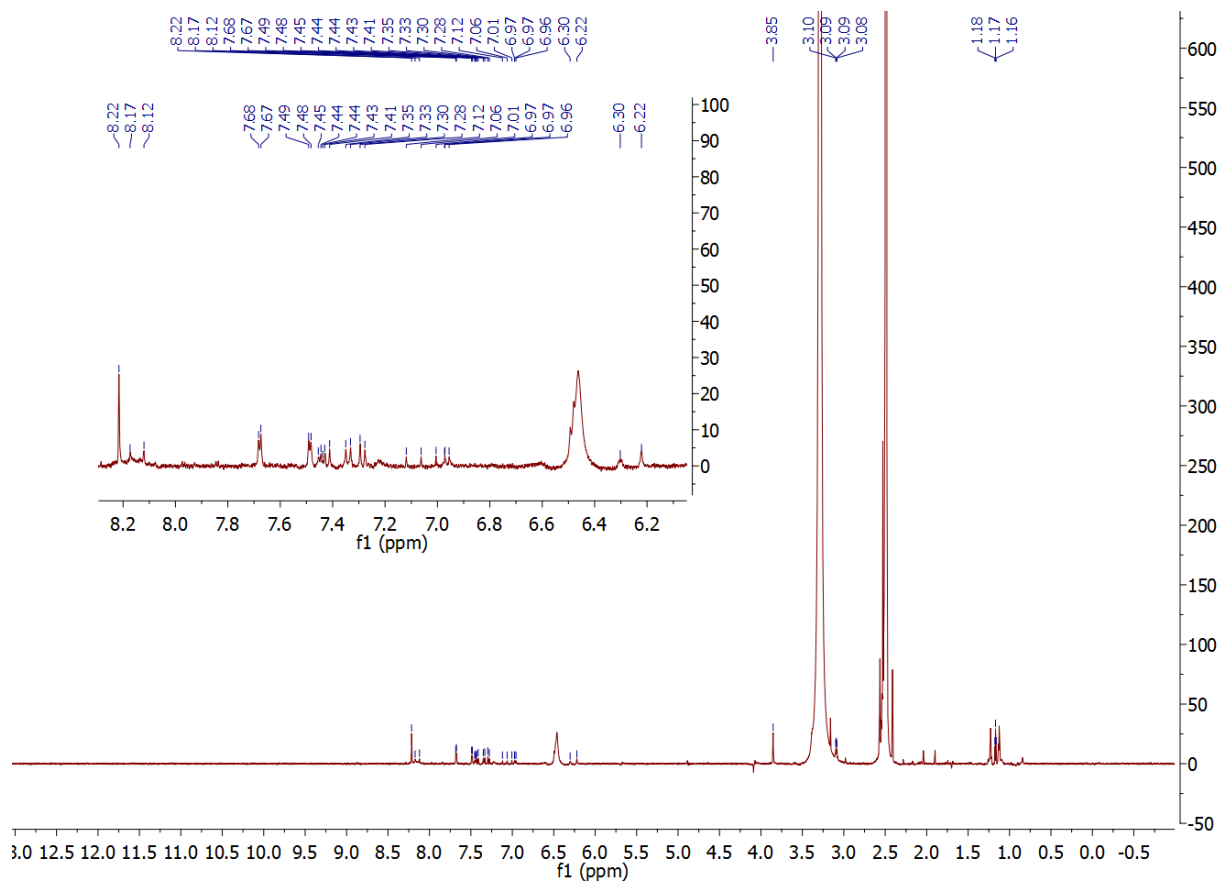
Spectrum 4.13. ^1H NMR of dsVF2.1.F



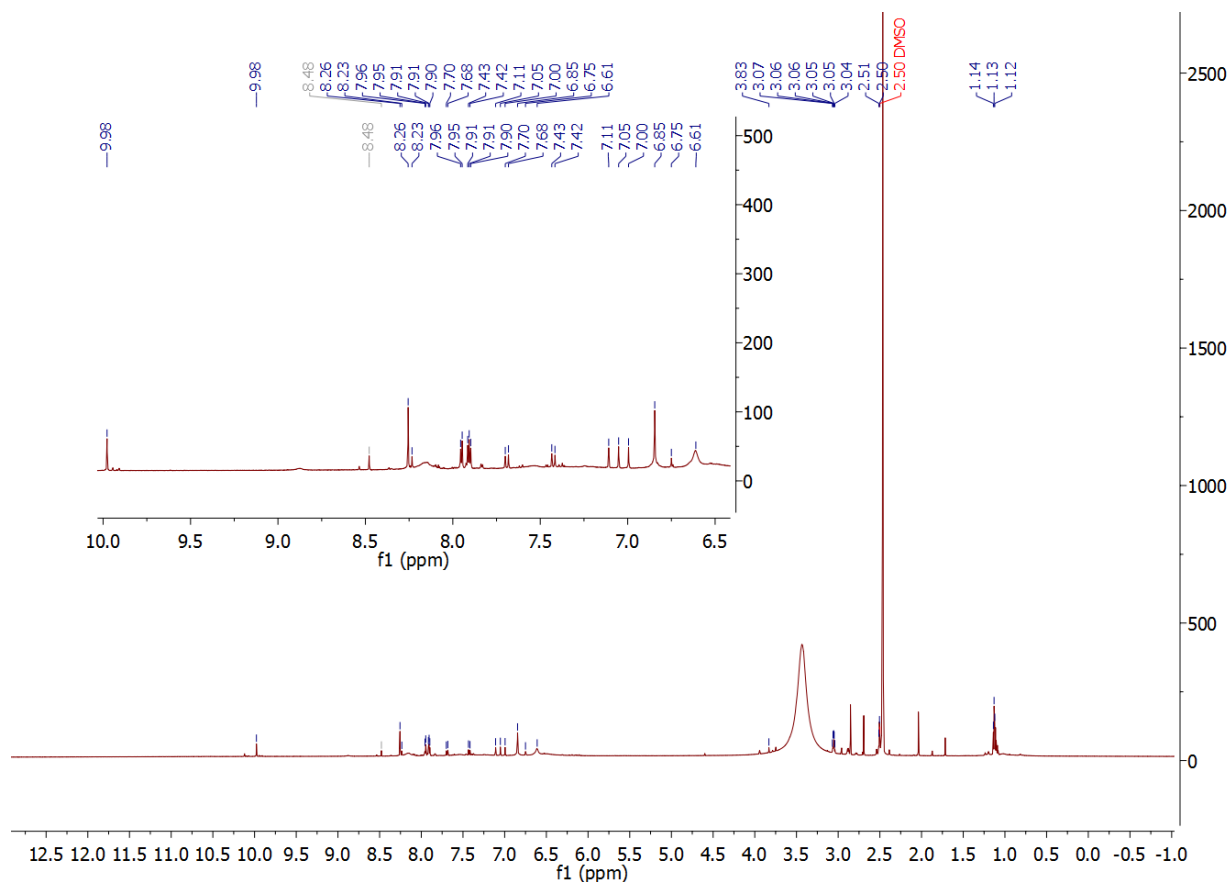
Spectrum 4.14. ^1H NMR of dsVF2.1.Cl



Spectrum 4.15. ^1H NMR of dsVF2.2(OMe).H



Spectrum 4.16. ^1H NMR of dsVF2.2(OMe).F



Spectrum 4.17. ^1H NMR of dsVF2.2(OMe).Cl

4.7 References

1. Grimm, J. B.; English, B. P.; Chen, J. J.; Slaughter, J. P.; Zhang, Z. J.; Revyakin, A.; Patel, R.; Macklin, J. J.; Normanno, D.; Singer, R. H.; Lionnet, T.; Lavis, L. D. *Nat Methods* **2015**, *12*, 244.
2. Lavis, L. D.; Raines, R. T. *Acs Chem Biol* **2014**, *9*, 855.
3. Kushida, Y.; Nagano, T.; Hanaoka, K. *Analyst* **2015**, *140*, 685.
4. Brewer, T. F.; Chang, C. J. *J Am Chem Soc* **2015**, *137*, 10886.
5. Aron, A. T.; Ramos-Torres, K. M.; Cotruvo, J. A.; Chang, C. J. *Accounts Chem Res* **2015**, *48*, 2434.
6. Kobayashi, H.; Ogawa, M.; Alford, R.; Choyke, P. L.; Urano, Y. *Chem Rev* **2010**, *110*, 2620.
7. Lee, H. L. D.; Lord, S. J.; Iwanaga, S.; Zhan, K.; Xie, H. X.; Williams, J. C.; Wang, H.; Bowman, G. R.; Goley, E. D.; Shapiro, L.; Twieg, R. J.; Rao, J. H.; Moerner, W. E. *J Am Chem Soc* **2010**, *132*, 15099.
8. Anzalone, A. V.; Wang, T. Y.; Chen, Z. X.; Cornish, V. W. *Angew Chem Int Edit* **2013**, *52*, 650.
9. Yun, S. W.; Kang, N. Y.; Park, S. J.; Ha, H. H.; Kim, Y. K.; Lee, J. S.; Chang, Y. T. *Accounts Chem Res* **2014**, *47*, 1277.
10. Lukinavicius, G.; Umezawa, K.; Olivier, N.; Honigmann, A.; Yang, G. Y.; Plass, T.; Mueller, V.; Reymond, L.; Correa, I. R.; Luo, Z. G.; Schultz, C.; Lemke, E. A.; Heppenstall, P.; Eggeling, C.; Manley, S.; Johnsson, K. *Nat Chem* **2013**, *5*, 132.

11. Uno, S. N.; Kamiya, M.; Yoshihara, T.; Sugawara, K.; Okabe, K.; Tarhan, M. C.; Fujita, H.; Funatsu, T.; Okada, Y.; Tobita, S.; Urano, Y. *Nat Chem* **2014**, *6*, 681.
12. Lincoln, R.; Greene, L. E.; Krumova, K.; Ding, Z. T.; Cosa, G. *J Phys Chem A* **2014**, *118*, 10622.
13. Huang, Y. L.; Walker, A. S.; Miller, E. W. *J Am Chem Soc* **2015**, *137*, 10767.
14. Grenier, V.; Walker, A. S.; Miller, E. W. *J Am Chem Soc* **2015**, *137*, 10894.
15. Miller, E. W. *Curr Opin Chem Biol* **2016**, *33*, 74.
16. Peterka, D. S.; Takahashi, H.; Yuste, R. *Neuron* **2011**, *69*, 9.
17. Scanziani, M.; Hausser, M. *Nature* **2009**, *461*, 930.
18. Braubach, O.; Cohen, L. B.; Choi, Y. *Adv Exp Med Biol* **2015**, *859*, 3.
19. De Silva, A. P.; Gunaratne, H. Q. N.; Habibiwan, J. L.; Mccoy, C. P.; Rice, T. E.; Soumillion, J. P. *Angew Chem Int Edit* **1995**, *34*, 1728.
20. Li, L. S. *Nano Lett* **2007**, *7*, 2981.
21. Miller, E. W.; Lin, J. Y.; Frady, E. P.; Steinbach, P. A.; Kristan, W. B., Jr.; Tsien, R. Y. *Proc Natl Acad Sci U S A* **2012**, *109*, 2114.
22. Woodford, C. R.; Frady, E. P.; Smith, R. S.; Morey, B.; Canzi, G.; Palida, S. F.; Araneda, R. C.; Kristan, W. B., Jr.; Kubiak, C. P.; Miller, E. W.; Tsien, R. Y. *J Am Chem Soc* **2015**, *137*, 1817.
23. Farsi, Z.; Preobraschenski, J.; van den Bogaart, G.; Riedel, D.; Jahn, R.; Woehler, A. *Science* **2016**, *351*, 981.
24. Wagenaar, D. A. *J Exp Biol* **2015**, *218*, 3353.
25. Frady, E. P.; Kapoor, A.; Horvitz, E.; Kristan, W. B., Jr. *Neural Comput* **2016**, *28*, 1453.
26. Asakura, K.; Hayashi, S.; Ojima, A.; Taniguchi, T.; Miyamoto, N.; Nakamori, C.; Nagasawa, C.; Kitamura, T.; Osada, T.; Honda, Y.; Kasai, C.; Ando, H.; Kanda, Y.; Sekino, Y.; Sawada, K. *J Pharmacol Tox Met* **2015**, *75*, 17.
27. Dempsey, G. T.; Chaudhary, K. W.; Atwater, N.; Nguyen, C.; Brown, B. S.; McNeish, J. D.; Cohen, A. E.; Kralj, J. M. *J Pharmacol Tox Met* **2016**, dx.doi.org/10.1016/j.vascn.2016.05.003.
28. Ceriani, F.; Mammano, F. *Cell Commun Signal* **2013**, *11*, 10.1186/1478.
29. Dolensek, J.; Stozer, A.; Klemen, M. S.; Miller, E. W.; Rupnik, M. S. *Plos One* **2013**, *8*, 10.1371/journal.pone.0082374.
30. Loew, L. M.; Bonneville, G. W.; Surow, J. *Biochemistry-Us* **1978**, *17*, 4065.
31. Loew, L. M. In *Adv Exp Med Biol*; Canepari, M., Zecevic, D., Bernus, O., Eds.; **2015**; *859*, 27.
32. Vanommeslaeghe, K.; Hatcher, E.; Acharya, C.; Kundu, S.; Zhong, S.; Shim, J.; Darian, E.; Guvench, O.; Lopes, P.; Vorobyov, I.; MacKerell, A. D. *J Comput Chem* **2010**, *31*, 671.
33. Hong, C.; Tieleman, D. P.; Wang, Y. *Langmuir* **2014**, *30*, 11993.
34. van Meer, G.; Voelker, D. R.; Feigenson, G. W. *Nat Rev Mol Cell Bio* **2008**, *9*, 112.
35. Jiao, G. S.; Han, J. W.; Burgess, K. *J Org Chem* **2003**, *68*, 8264.
36. Kovi, R.; Nampalli, S.; Tharal, P. X. (*Apicore, LLC, USA*), **2008**, US20080281127A1.
37. Deal, P. E.; Kulkarni, R. U.; Al-Abdullatif, S. H.; Miller, E. W. *J Am Chem Soc* **2016**, *138*, 9085.
38. Kriks, S.; Shim, J. W.; Piao, J. H.; Ganat, Y. M.; Wakeman, D. R.; Xie, Z.; Carrillo-Reid, L.; Auyeung, G.; Antonacci, C.; Buch, A.; Yang, L. C.; Beal, M. F.; Surmeier, D. J.; Kordower, J. H.; Tabar, V.; Studer, L. *Nature* **2011**, *480*, 547.
39. Kriks, S.; Shim, J. W.; Piao, J. H.; Ganat, Y. M.; Wakeman, D. R.; Xie, Z.; Carrillo-Reid, L.; Auyeung, G.; Antonacci, C.; Buch, A.; Yang, L. C.; Beal, M. F.; Surmeier, D. J.; Kordower, J. H.; Tabar, V.; Studer, L. *Nature* **2011**, *480*, 547.

40. Vanommeslaeghe, K.; MacKerell, A. D. *J Chem Inf Model* **2012**, *52*, 3144.
41. Vanommeslaeghe, K.; Raman, E. P.; MacKerell, A. D. *J Chem Inf Model* **2012**, *52*, 3155.
42. Mayne, C. G.; Saam, J.; Schulten, K.; Tajkhorshid, E.; Gumbart, J. C. *J Comput Chem* **2013**, *34*, 2757.
43. Frisch, M. J.; Trucks, G. W.; Schlegel, H. B.; Scuseria, G. E.; Robb, M. A.; Cheeseman, J. R.; Scalmani, G.; Barone, V.; Mennucci, B.; Petersson, G. A.; Nakatsuji, H.; Caricato, M.; Li, X.; Hratchian, H. P.; Izmaylov, A. F.; Bloino, J.; Zheng, G.; Sonnenberg, J. L.; Hada, M.; Ehara, M.; Toyota, K.; Fukuda, R.; Hasegawa, J.; Ishida, M.; Nakajima, T.; Honda, Y.; Kitao, O.; Nakai, H.; Vreven, T.; Montgomery Jr., J. A.; Peralta, J. E.; Ogliaro, F.; Bearpark, M. J.; Heyd, J.; Brothers, E. N.; Kudin, K. N.; Staroverov, V. N.; Kobayashi, R.; Normand, J.; Raghavachari, K.; Rendell, A. P.; Burant, J. C.; Iyengar, S. S.; Tomasi, J.; Cossi, M.; Rega, N.; Millam, N. J.; Klene, M.; Knox, J. E.; Cross, J. B.; Bakken, V.; Adamo, C.; Jaramillo, J.; Gomperts, R.; Stratmann, R. E.; Yazyev, O.; Austin, A. J.; Cammi, R.; Pomelli, C.; Ochterski, J. W.; Martin, R. L.; Morokuma, K.; Zakrzewski, V. G.; Voth, G. A.; Salvador, P.; Dannenberg, J. J.; Dapprich, S.; Daniels, A. D.; Farkas, Ö.; Foresman, J. B.; Ortiz, J. V.; Cioslowski, J.; Fox, D. J.; Gaussian, Inc.: Wallingford, CT, USA, 2009.
44. Vanommeslaeghe, K.; Hatcher, E.; Acharya, C.; Kundu, S.; Zhong, S.; Shim, J.; Darian, E.; Guvench, O.; Lopes, P.; Vorobyov, I.; MacKerell, A. D. *J Comput Chem* **2010**, *31*, 671.
45. Batistela, V. R.; Cedran, J. D.; de Oliveira, H. P. M.; Scarminio, I. S.; Ueno, L. T.; Machado, A. E. H.; Hioka, N. *Dyes Pigments* **2010**, *86*, 15.
46. Hong, C.; Tieleman, D. P.; Wang, Y. *Langmuir* **2014**, *30*, 11993.
47. Shaw, D. E.; Deneroff, M. M.; Dror, R. O.; Kuskin, J. S.; Larson, R. H.; Salmon, J. K.; Young, C.; Batson, B.; Bowers, K. J.; Chao, J. C.; Eastwood, M. P.; Gagliardo, J.; Grossman, J. P.; Ho, C. R.; Ierardi, D. J.; Kolossvary, I.; Klepeis, J. L.; Layman, T.; McLeavey, C.; Moraes, M. A.; Mueller, R.; Priest, E. C.; Shan, Y. B.; Spengler, J.; Theobald, M.; Towles, B.; Wang, S. *C. Conf Proc Int Symp C* **2007**, 1.
48. Humphrey, W.; Dalke, A.; Schulten, K. *J Mol Graph* **1996**, *14*, 33.
49. Phillips, J. C.; Braun, R.; Wang, W.; Gumbart, J.; Tajkhorshid, E.; Villa, E.; Chipot, C.; Skeel, R. D.; Kale, L.; Schulten, K. *J Comput Chem* **2005**, *26*, 1781.
50. Klauda, J. B.; Venable, R. M.; Freites, J. A.; O'Connor, J. W.; Tobias, D. J.; Mondragon-Ramirez, C.; Vorobyov, I.; MacKerell, A. D.; Pastor, R. W. *J Phys Chem B* **2010**, *114*, 7830.
51. Andersen, H. C. *J Comput Phys* **1983**, *52*, 24.
52. Miyamoto, S.; Kollman, P. A. *J Comput Chem* **1992**, *13*, 952.
53. Darden, T.; York, D.; Pedersen, L. *J Chem Phys* **1993**, *98*, 10089.
54. Feller, S. E.; Zhang, Y. H.; Pastor, R. W.; Brooks, B. R. *J Chem Phys* **1995**, *103*, 4613.

Chapter 5

Isomerized Xanthene PeT-Based Chromophores with Increased Brightness and Signal-to-Noise

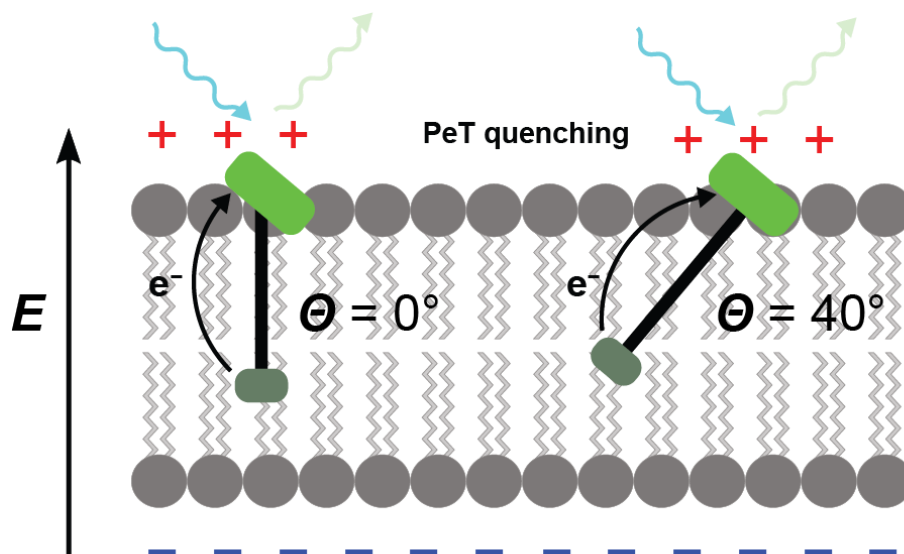
Abstract

Voltage imaging with fluorescent dyes provides a fast and sensitive measure of membrane potential in complex biological preparations. Low sensitivity limits the applicability of these dyes, however. In this chapter, we use molecular dynamics simulations and density functional theory calculations to guide the design of a new, high-brightness fluorescent voltage indicator that uses photoinduced electron transfer as a voltage-sensing mechanism. MD simulations and DFT calculations predict that the new dye should have similar sensitivity, but higher brightness resulting from improvement alignment of the dye with the membrane and a smaller driving force for the PeT mechanism in the resting state. We confirm this theoretical finding by synthesizing isoVF2.2(OMe).Cl and establishing that it possesses a four-fold improvement in signal-to-noise over msVF2.2(OMe).Cl. This outworking of theory and experiment has yielded the highest signal-to-noise dye in the fluorescein family of VoltageFluors. We then use this new indicator to monitor and characterize the differentiation of human embryonic stem cells into medium spiny neurons.

5.1 Dye Membrane Orientation and Donor-Acceptor Energy Matching as a Factor in PeT

While the advent of fluorescent indicators for biological activity has revolutionized our ability to understand the biochemistry and molecular biology of living cells, the rational design and improvement of fluorescent sensors remains an outstanding challenge in the field.¹⁻¹² Our group is currently undertaking a program to build chemical indicators for sensing membrane potential in excitable cells, such as neurons and cardiomyocytes.¹³⁻¹⁵ The traditional approach to monitoring membrane potential relies on electrode-based methods. Voltage imaging with fluorescent indicators promises to circumvent the problems of low-throughput, low spatial resolution, and invasiveness associated with electrophysiology.¹⁶⁻¹⁸ Our lab has recently reported on several high photoinduced electron transfer-based voltage dyes, or VoltageFluors, that possess high signal-to-noise and voltage sensitivity. These previously reported dyes have proven useful for measuring voltage in a variety of biological preparations, including mouse brain slices, cultured rat hippocampal neurons, leech neuronal ganglia, and more. Improvement of these dyes, in theory, requires a better understanding of the biophysical and chemical properties influencing the voltage sensitivity of VoltageFluor dyes. The newest generation of reported VoltageFluor dyes primarily emit in the orange-red and red section of the visible light spectrum and also include new structural innovations that have resulted in up to four-fold increases in signal-to-noise ratio.^{19,20} In order to modernize our blue-green series of VoltageFluors, we aimed to explore the nature of how structural changes affect the voltage sensitivity of VoltageFluor dyes and apply them to our fluorescein-based VoltageFluor scaffold.

Our group recently reported on disulfonated VoltageFluor dyes, which demonstrated a 20% increase in voltage sensitivity due to a reduction in the membrane tilt angle, resulting in better alignment of the dye with the membrane electric field.²¹ While disulfoVoltageFluors are much better than the monosulfonated counterparts, the overall improvement to signal-to-noise is small. By contrast, our recently reported Rhodamine Voltage Reporters, or RhoVRs, explored the movement of the molecular wire from the *para*-position of the meso xanthene ring to the *meta*-position, resulting in a two-fold increase in voltage sensitivity and a four-fold increase to signal-to-noise ratio (SNR).²² We hypothesized that part of the improvement to voltage sensitivity was likely due to the alignment of the direction of electron transfer with the transmembrane electric field, but also that electronic effects associated with the isomerization of the donor portion of the VoltageFluor were resulting in better brightness and sensitivity. We therefore desired to study and explore this effect in greater detail using a mixed computational and experimental approach.



$$\Delta F/F \propto \Delta\mu \cdot E = \|\Delta\mu\| \|E\| \cos(\theta)$$

Scheme 5.1. The orientation of the VoltageFluor within the plasma membrane plays a significant role in voltage sensitivity. In order to properly align the direction of electron transfer with the transmembrane electric field, we proposed moving the molecular wire from the *para* position relative to the xanthene chromophore to the *para* position relative to the sulfonate group.

Our previous work established the hypothesis that VF dyes sense voltage via a PeT-based mechanism in which the transmembrane electric field of the cell increases or decreases the rate of electron transfer from the donor to the acceptor.²¹ As a result, when the membrane is hyperpolarized, the rate of PeT is increased, resulting in quenching of the acceptor, while when the membrane depolarizes, the rate of PeT is decreased, resulting in acceptor fluorescence. Our prior work with disulfonated VoltageFluors demonstrated that the voltage sensitivity of the dye depends on the cosine of the angle between the electron transfer vector and the electric field vector. In that case, reducing the angle by 20 degrees resulting in a 20 percent increase in voltage sensitivity.²¹ Due to loading issues associated with the increased water-solubility of disulfoVF, however, we wished to explore the meta-substituted VoltageFluors we recently reported in further detail (**Scheme 5.1**).²² Our initial assumption was that the tilt angle of the meta-substituted VF dyes would be close to zero degrees, but the electronic structure of the wire would be perturbed by the movement of the sulfonate group from a position *meta* to the aniline donor to a *para* position. To test this hypothesis, we turned to molecular modeling and DFT calculations to measure the tilt angle of isoVF and compare the HOMO energies of the donors and acceptors in isoVF and paraVF. We performed three replicates of 500 ns molecular dynamics simulations of isoVF2.1.Cl in a pure POPC membrane and sampled the tilt angle between the long axis of the molecular wire and the membrane normal every 5 ps using principal component analysis.

5.2 Computational Modeling of isoVF2.2(OMe).Cl

We parameterized isoVF2.1.Cl with the CHARMM force field and then performed molecular dynamics (MD) simulations of the dye embedded in a POPC lipid bilayer to simulate the mammalian cell membrane.²³ We aimed to compare the observed tilt angle between the direction of electron transfer and the direction of the electric field with our previously-derived tilt angles from simulations of the behavior of VF2.1.Cl and disulfoVF2.1.Cl in the same model of the cell membrane.²¹ In concordance with our simulations of VF2.1.Cl and disulfoVF2.1.Cl, the 2' sulfonate group of isoVF2.1.Cl localized to the lipid:water interface and appeared to anchor the dye to the outer leaflet of the plasma membrane. Because the direction of electron transfer is slightly offset from the long axis of the VF dye, however, the overall tilt angle of isoVF2.1.Cl (25.5 degrees) is intermediate to VF2.1.Cl (35 degrees) and dsVF2.1.Cl at 17 degrees (**Figure 5.1b**). Similar to VF2.1.Cl, isoVF2.1.Cl appears “floppy” in the plasma membrane with a tilt angle standard deviation of 13.5 degrees, which we reasoned was due to the single sulfonate group serving as the plasma membrane anchor. We noted that the AryIP angle, which we previously reported to be 30 degrees off parallel in msVF dyes, was significantly straightened in isoVF, consistent with our hypothesis that the sulfonate group plays a dominating role as the membrane anchor (**Figure 5.1a, c**). Due to the lack of a second sulfonate group, however, isoVF remains better embedded in the membrane than disulfoVF (**Figure 5.1d**). An average tilt angle of 25.5 degrees predicts that isoVF2.1.Cl would be 10% more sensitive than VF2.1.Cl and that isoVF2.2(OMe).Cl would have a voltage sensitivity of 59% per 100 millivolts. However, we noted that this structural modification resulted in a much larger improvement to voltage sensitivity in the case of previously reported RhoVR dyes. The movement of the molecular wire from the *para* position to the *meta* position of the meso xanthene ring results in the overall movement of the electron-withdrawing sulfonate group from the *meta* position to the *para* position relative to the aniline portion of the donor. We reasoned that this could result in a substantial change in the energetics of the PeT process and therefore have a large effect on the voltage sensitivity of the final VoltageFluor. To determine the magnitude of these effects, we performed DFT calculations of the energy levels of the VoltageFluor orbitals.

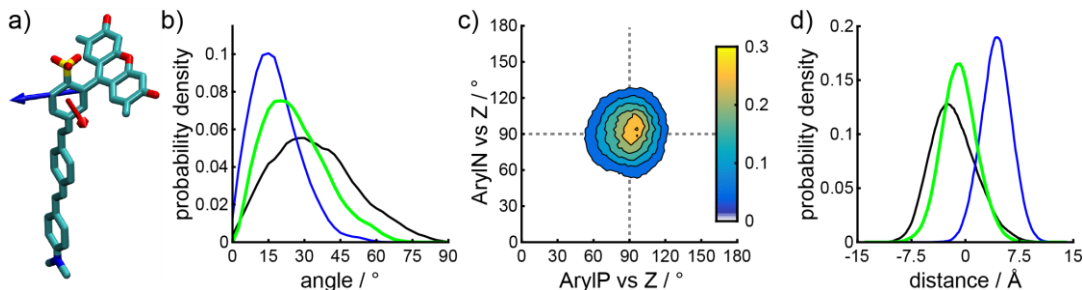


Figure 5.1. Molecular modeling of VoltageFluor dyes. A) Definition of vectors used to examine angles in VF dyes. The blue arrow, “ArylP,” describes the vector parallel to the *meso*-aryl ring, while “ArylN,” the red arrow, represents the vector normal to the plane of the aryl ring. They are compared to “Z,” the membrane normal. B) Plot of probability density vs. angle of displacement between the 3rd principle component (the long axis) of VF dyes and “Z.” The blue trace represents dsVF, the green trace represents isoVF, and the black trace represents msVF. C) Contour plot describes the ArylP vs. Z and ArylN vs. Z for isoVF. D) Plot of probability density vs. the distance of displacement between the xanthene head of VF dyes and the top of the plasma membrane.

We optimized the geometry of VF2.2(OMe).Cl and isoVF2.2(OMe).Cl in Gaussian94 using the wB97X-D functional and the def2-TZVP basis set.²⁴ To determine the energies of the VF molecular orbitals, the def2-TZVPD basis set was used. In order to stabilize the phenolate and sulfonate ions in the simulation, we introduced a sodium atom to counterbalance the charge. The calculated donor HOMO in isoVF2.2(OMe).Cl demonstrated electron density pulled closer to the sulfonate group than the donor HOMO in VF2.2(OMe).Cl, in agreement with our hypothesis that the electronic structure of the donor was significantly perturbed by the relocation of the aniline donor. The resulting HOMO-HOMO gap between the donor and acceptor for isoVF2.2(OMe).Cl was smaller than the gap for VF2.2(OMe).Cl (**Table 5.1**), suggesting that the rate of PeT is decreased in isoVF2.2(OMe).Cl compared to VF2.2(OMe).Cl. A decrease in the overall rate of PeT would result in a brighter dye with lower sensitivity, but we hypothesized that the lower sensitivity due to rate of PeT may be compensated for by the higher sensitivity due to a small tilt angle defect. Based on the MD simulations and DFT calculations, we predicted that isoVF2.2(OMe).Cl would be a brighter dye with a similar voltage sensitivity to VF2.2(OMe).Cl, potentially resulting in a higher signal-to-noise blue-green VoltageFluor.

Table 5.1. Properties of VoltageFluor dyes

Name	Φ_{fl}^a	λ_{abs}^a	λ_{em}^a	$\Delta F/F^b$	SNR ^c	A-D Gap ^d	Predicted Wire Absorption ^e
msVF2.2(OMe).Cl	0.23	518	534	49	17	0.414	351.93 nm
dsVF2.2(OMe).Cl	0.25	520	540	63	43	N/A	N/A
isoVF2.2(OMe).Cl	0.32	512	528	53	92	0.381	361.96 nm

^a Measured in phosphate-buffered saline with 0.1 M NaOH and with 0.1% Triton X-100. ^b per 100 mV. Determined in HEK cells. ^c Measured in terms of a 100 mV step in HEK293T cells. ^d Calculated via DFT in Hartrees. ^e Calculated via TD-DFT.

5.3 Synthesis and Characterization of isoVF2.2(OMe).Cl

To confirm the simulation and calculation results and experimentally test our hypothesis about the sensitivity of isoVF2.2(OMe).Cl, we synthesized isoVF2.2(OMe).Cl (**Scheme 5.2**). The meta-bromo sulfofluorescein chromophore was readily accessible using our previously reported strategy to synthesize sulfonated xanthenes via brominated 2-formylbenzenesulfonic acids.^{21,22} This aldehyde condensed smoothly with 4-chlororesorcinol in methanesulfonic acid to give the sulfofluorescein derivative in good yield (83%). This meta-bromo sulfofluorescein demonstrated absorption and emission profiles similar to the para-bromo sulfofluorescein and also displayed the high quantum yield of fluorescein characteristic of fluorescein derivatives. As methoxy-substituted molecular wires have generally given the best voltage sensitivity in the context of VoltageFluors, we combined the dye head with a N,N-diethyl-3-methoxyaniline molecular wire via a Heck coupling to provide isoVF2.2(OMe).Cl after purification and crystallization. The dye was further purified via preparative HPLC for further analysis and comparison with VF2.2(OMe).Cl and dsVF2.2(OMe).Cl. The fully-assembled VoltageFluor displayed similar absorption and emission profiles to paraVF2.2(OMe).Cl and dsVF2.2(OMe).Cl. However, we noted a slight red-shift in the main wire absorbance peak around 400 nm that corresponded to the likely absorption peak predicted by TD-DFT (**Figure 5.2**). The quantum yield of isoVF2.2(OMe).Cl in basic water is also 1.3-fold higher than paraVF2.2(OMe).Cl, agreement with our hypothesis that the rate of PeT in isoVF is slower, resulting in a higher brightness baseline.

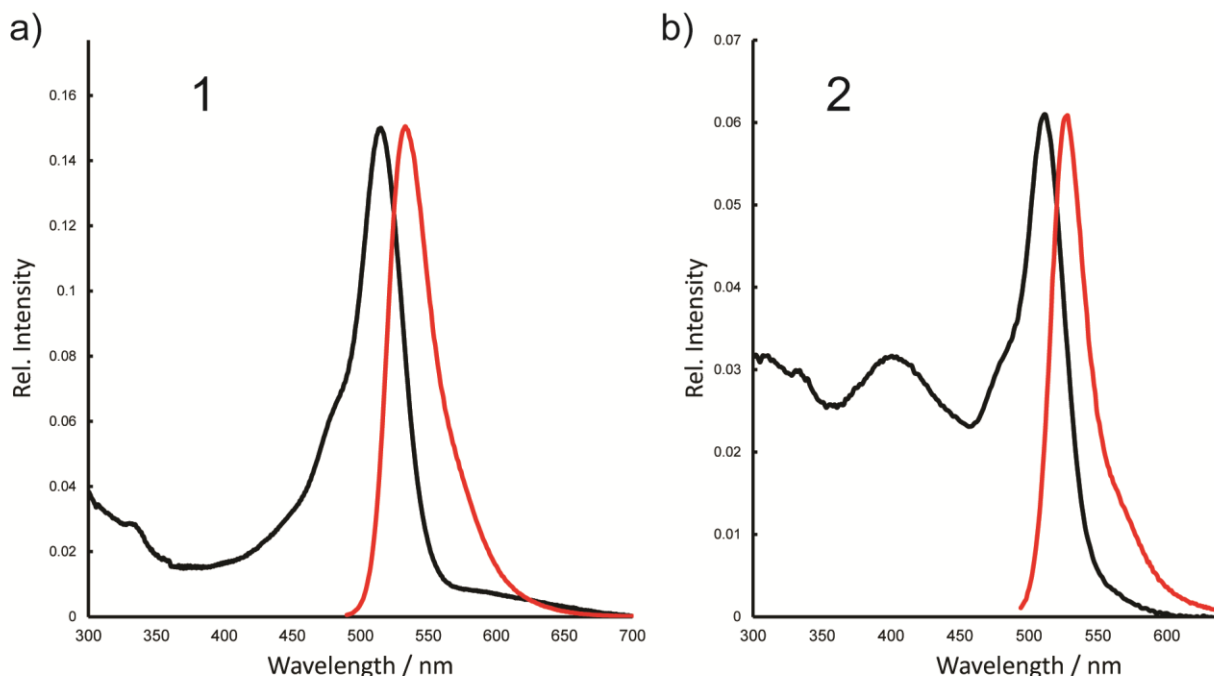
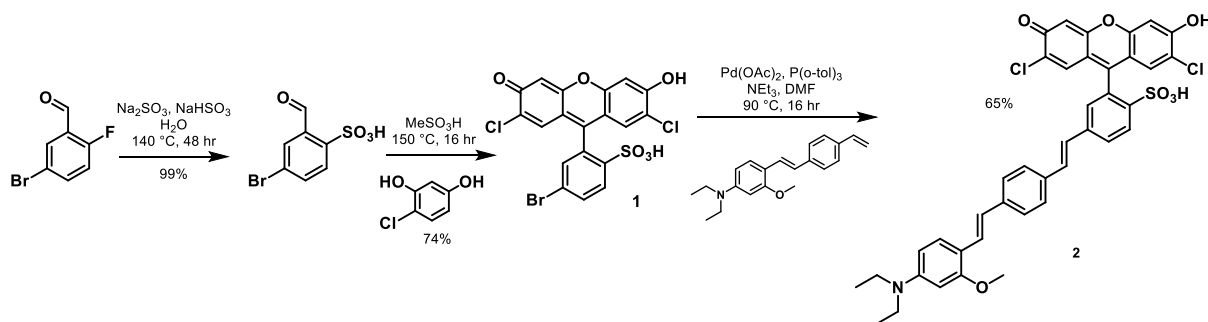


Figure 5.2. Absorption (UV/vis) and fluorescence emission spectra of compounds **1** and **2**. Black lines indicate the UV/vis absorption spectra. Red lines indicate the fluorescence emission spectra. Spectra were acquired in PBS with 0.1 M NaOH. For fluorescence emission spectra, excitation was provided at 10 nm longer wavelength than the respective absorbance maximum.



Scheme 5.2. isoVF2.2(OMe).Cl was synthesized from a regio-isomerically pure bromo-sulfonated fluorescein, which was in turn synthesized from a sulfonated benzaldehyde. This route gives robust yields compared to sulfobenzoic acid-based routes for xanthene synthesis.

In order to determine the voltage sensitivity of isoVF2.2(OMe).Cl, we performed whole-cell voltage clamp electrophysiology on HEK293T cells loaded with 500 nM VF dye (**Figure 5.3a**). The membrane was depolarized in the presence of VF dye and the increase in fluorescence was quantified. We found that isoVF2.2(OMe).Cl had a voltage sensitivity of 45% dF/F per 100 mV (**Figure 5.3b,c**), which is in good agreement with our hypothesis that isoVF2.2(OMe).Cl would have a lower voltage sensitivity than its para-substituted counterparts, msVF2.2(OMe).Cl (53% dF/F per 100 mV) and dsVF2.2(OMe).Cl (63% dF/F per 100 mV). However, we were pleased to observe a 1.4-fold larger baseline brightness for isoVF2.2(OMe).Cl relative to msVF2.2(OMe).Cl,

resulting in a much larger absolute change in brightness per 100 mV for isoVF2.2(OMe).Cl when compared to its *para*-substituted counterparts (Figure 5.4, 5.5). This increase in the change in photons emitted per 100 mV step resulted in isoVF2.2(OMe).Cl (92 SNR) possessing a four-fold higher signal to noise than msVF2.2(OMe).Cl (17 SNR). This matches well with our computationally-derived predictions and validates our simulation methodology for predicting overall trends in VoltageFluor sensitivities and brightness. We further note that our model fails to include effects due to changes in the relative orientation of the donor and acceptor, which has been demonstrated to have substantial effects on the overall rate of PeT. We suspect that in the case of the fluorescein acceptor, the movement of the electron donor from the *para* position to the *meta* position does not cause significant orientation effects, but that they could play a larger role in the behavior of other donor-acceptor pairs.

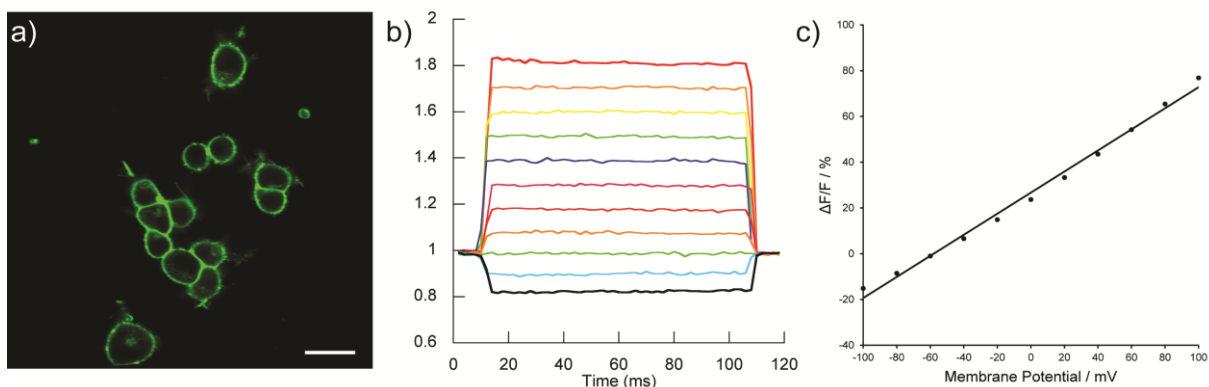


Figure 5.3. Characterization of isoVF2.2(OMe).Cl in HEK293T cells. A) isoVF2.2(OMe).Cl brightly stains the outer membranes of HEK293T cells under one-photon illumination. Scale bar is 20 μm . b) The fractional change in fluorescence is plotted vs. time for 100 millisecond depolarizing and hyperpolarizing steps from a holding potential of -60 mV for a single HEK293T cell under whole-cell voltage-clamp mode. c) A plot of percentage $\Delta F/F$ vs. membrane potential, summarizing the data from five separate cells, revealing an average sensitivity of 45% per 100 mV. Error bars are $\pm\text{SEM}$.

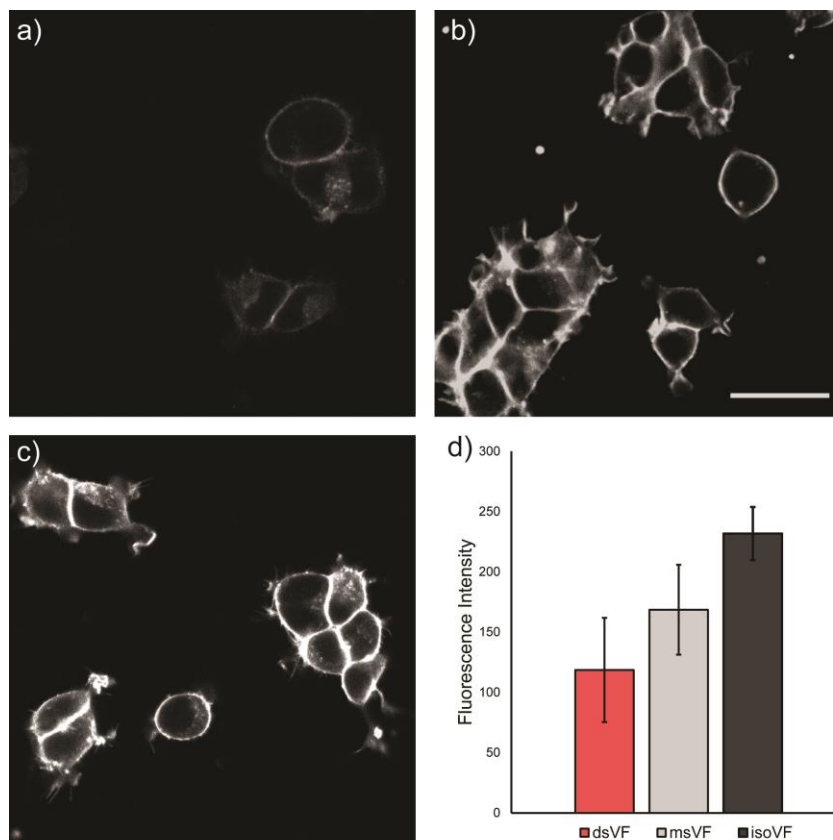


Figure 5.4. Confocal imaging of VF dyes in HEK cells. HEK cells were stained with 500 nM in HBSS dsVF2.2(OMe).Cl (a), msVF2.2(OMe).Cl (b), or isoVF2.2(OMe).Cl for 15 minutes at 37 °C. Cells were transferred to fresh HBSS (without any dye) and imaged via confocal laser scanning microscopy. All imaging parameters are identical. Histogram display values are identical. Scale bar is 20 μ m. The fluorescence intensity of the membrane staining is quantified in panel d). Values represent the mean fluorescence of membrane ROIs containing HEK cells stained with compounds **7-10**. $n = 7$. Error bars are \pm standard deviation.

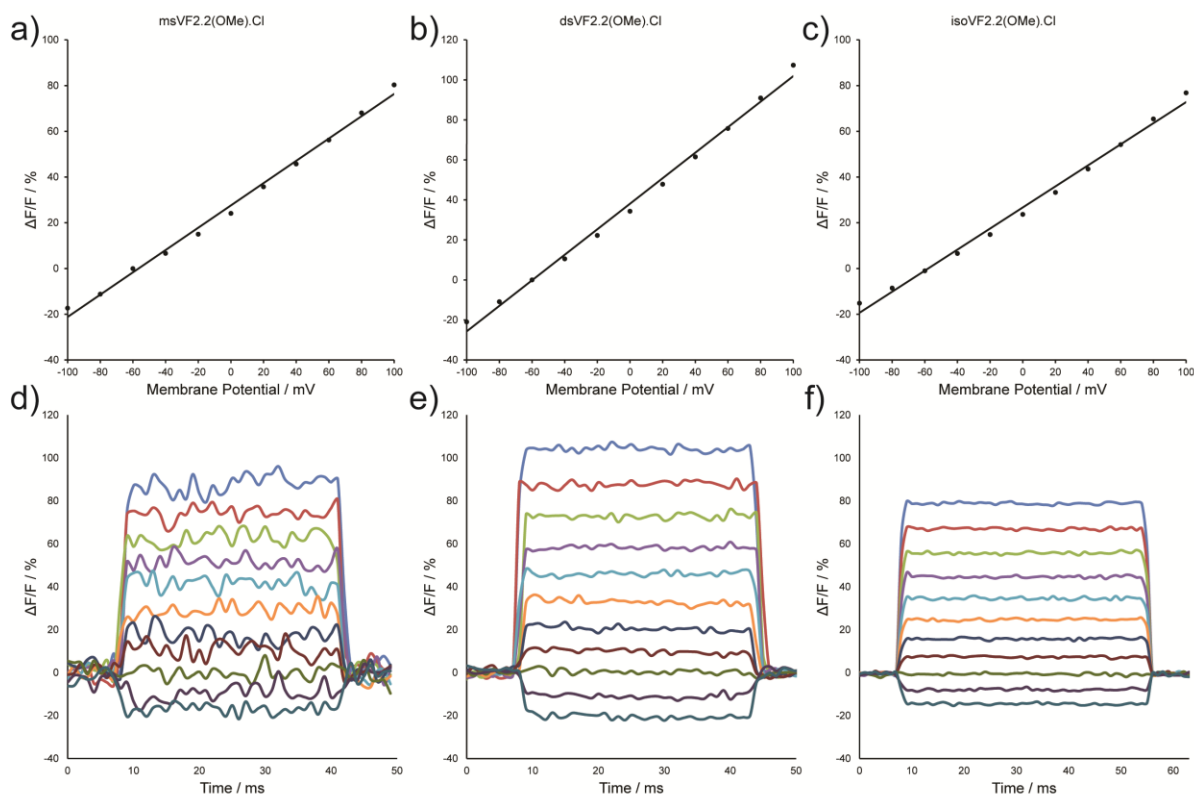


Figure 5.5. Voltage sensitivity of compounds **msVF2.2(OMe).Cl**, **dsVF2.2(OMe).Cl**, and **isoVF2.2(OMe).Cl**, determined by fluorescence microscopy and electrophysiology. Average voltage sensitivity plots of percentage change in fluorescence vs. membrane potential values from whole-cell voltage-clamp electrophysiology of 5 HEK cells for each dye (a), (b), and (c), respectively. Error bars indicate standard error of the mean for $n = 5$ different cells. Summaries reveal average voltage sensitivities of 49%, 64%, and 46%, respectively. Representative traces reveal fractional change in fluorescence vs. time from whole-cell voltage-clamp electrophysiology for each compound (d), (e), and (f).

5.4 Neuronal Imaging with isoVF2.2(OMe).Cl

Due to its exceptional signal-to-noise ratio compared to msVF2.2(OMe).Cl and dsVF2.2(OMe).Cl, we expected that isoVF2.2(OMe).Cl should demonstrate strong utility for observing membrane potential changes in neurons. Cultured rat hippocampal bathed in isoVF2.2(OMe).Cl showed bright membrane staining (**Figure 5.6a**). When activity was evoked via field stimulation, isoVF2.2(OMe).Cl possessed a SNR of 16 per action potential, much higher than that of msVF2.2(OMe).Cl (8.7 SNR). Spontaneous activity imaging of rat hippocampal neurons loaded with isoVF2.2(OMe).Cl readily revealed spiking activity and smaller membrane potential changes (**Figure 5.6b-d**). Comparison of the electrophysiological properties of neurons with and without isoVF2.2(OMe).Cl showed that the meta-substituted VF dye does not significantly perturb membrane properties (**Figure 5.7**). We performed dual optical and electrophysiological recordings to demonstrate that isoVF2.2(OMe).Cl faithfully and rapidly tracks the fast changes in voltage associated with the neuronal action potential (**Figure 5.6e**). Because of the large increase in brightness of isoVF2.2(OMe).Cl over msVF2.2(OMe).Cl, we

hypothesized that isoVF may have sufficient brightness to have utility as a two-photon voltage dye. Despite possessing a lower two-photon absorption cross-section than previously reported VoltageFluors (**Figure 5.8**), bath application of isoVF2.2(OMe).Cl to cultured rat hippocampal neurons demonstrated bright staining under 2P illumination at 800 nm. When a time-lapse recording was performed, spiking behavior was readily distinguishable in the imaged neurons (**Figure 5.9**).

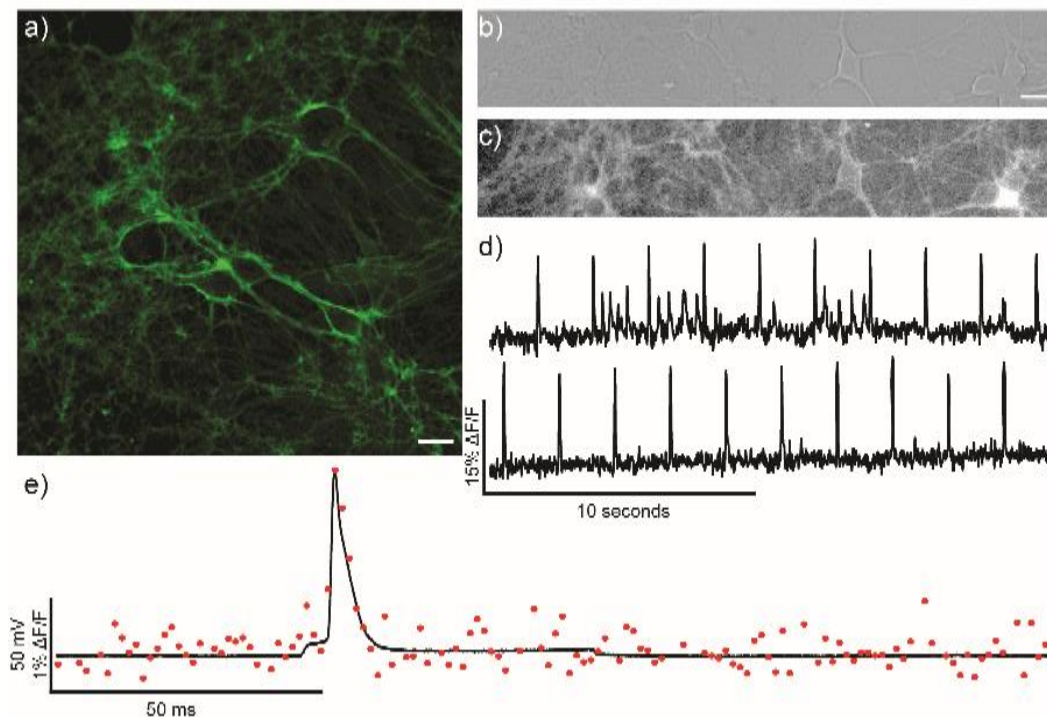


Figure 5.6. Characterization of isoVF2.2(OMe).Cl in dissociated rat hippocampal neurons. A) isoVF2.2(OMe).Cl localizes to the plasma membrane of rat hippocampal neurons. b) and c) Sample brightfield (b) and fluorescence (c) from a spontaneous activity recording of isoVF2.2(OMe).Cl bath applied to cultured rat hippocampal neurons. All error bars are 10 μm . d) Sample optical activity traces from the recording in panels (b) and (c) show both large spikes and smaller membrane activity. e) Dual optical and electrophysiological recording of action potentials in cultured hippocampal neurons. Action potentials were evoked under current clamp mode and recorded electrophysiologically (black trace, 50-kHz sampling rate) and optically (red dots, 1-kHz sampling rate).

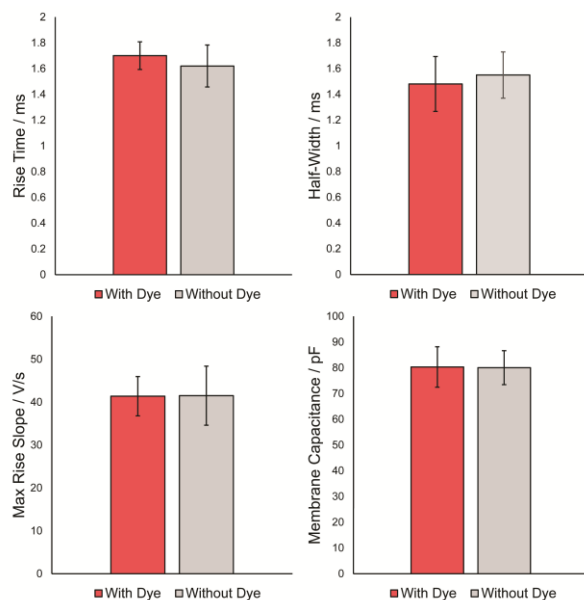


Figure 5.7. Comparison of several action potential kinetic parameters with and without the presence of isoVF2.2(OMe).Cl. Mouse hippocampal neurons were subjected to patch clamp electrophysiology under current clamp mode in whole-cell configuration, with or without the presence of isoVF2.2(OMe).Cl. Trains of action potentials were evoked (10 AP, 20 Hz) via current injection. Values are mean values from $n = 7$ cells for each condition with each cell's average action potential determined from 10 action potentials each. Error bars are \pm SEM and all p values are > 0.05 (Student's t -test, two tailed).

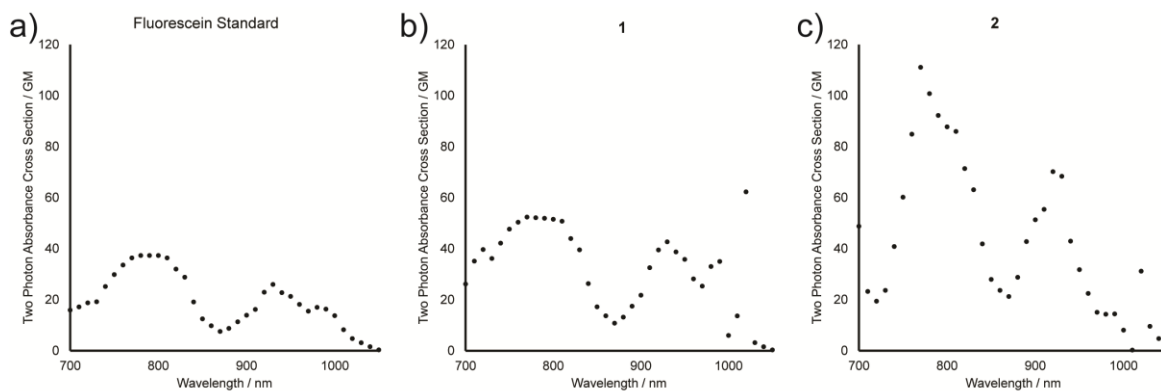


Figure 5.8. Two-photon absorption cross sections of fluorescein (a) sulfluorescein dye head 1 (b) and isoVF2.2(OMe).Cl 2 (c). All spectra were taken in PBS with 0.1 M NaOH.

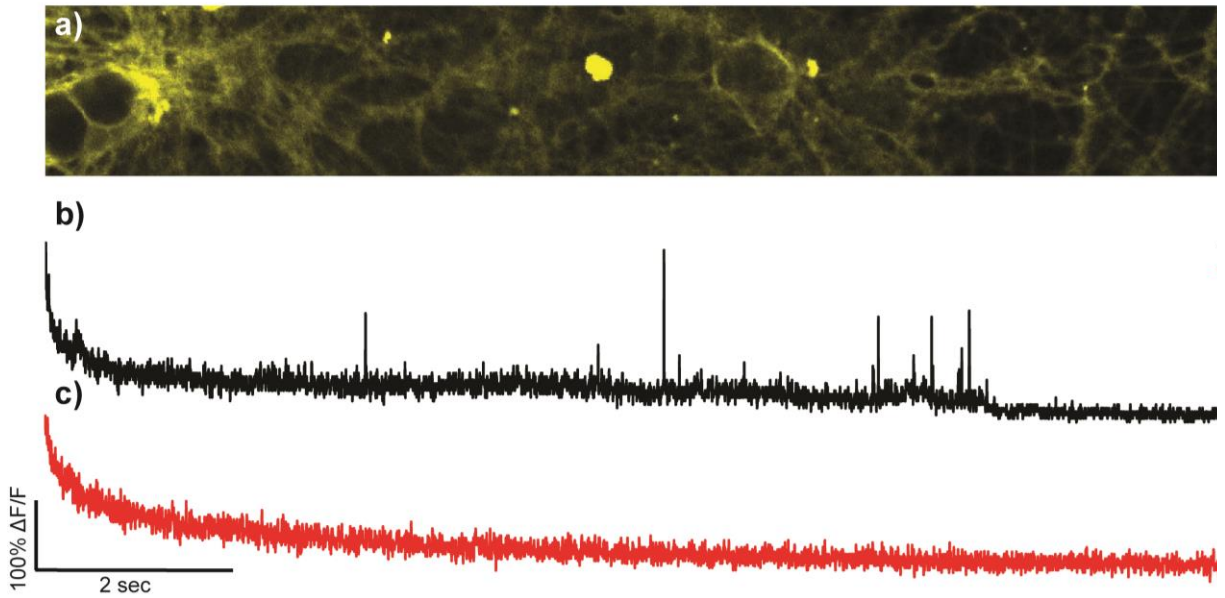


Figure 5.9. 2P imaging of spontaneous activity in cultured mouse neurons with isoVF2.2(OMe).Cl. (a) High-resolution frame from spontaneous activity imaging. (b-c) Robust spontaneous spiking is observed via 2P imaging of isoVF2.2(OMe).Cl. Addition of TTX (1 μ M) abolishes activity. Traces are single trials and are not filtered.

To further demonstrate the utility of isoVF2.2(OMe).Cl for imaging activity in neurons, we used isoVF to track the development of cultured human embryonic stem cells into medium spiny neurons over the course of differentiation (**Figure 5.10**). isoVF2.2(OMe).Cl was able to readily distinguish between a variety of spiking and bursting activities as the cells progressed and developed into neurons on days 35, 58, and 88 of differentiation (**Figure 5.10g-i**). These data suggest a promising role for isoVF2.2(OMe).Cl as a non-invasive diagnostic tool for assuring proper differentiation of stem cell-derived neurons prior to implantation for therapeutic use.

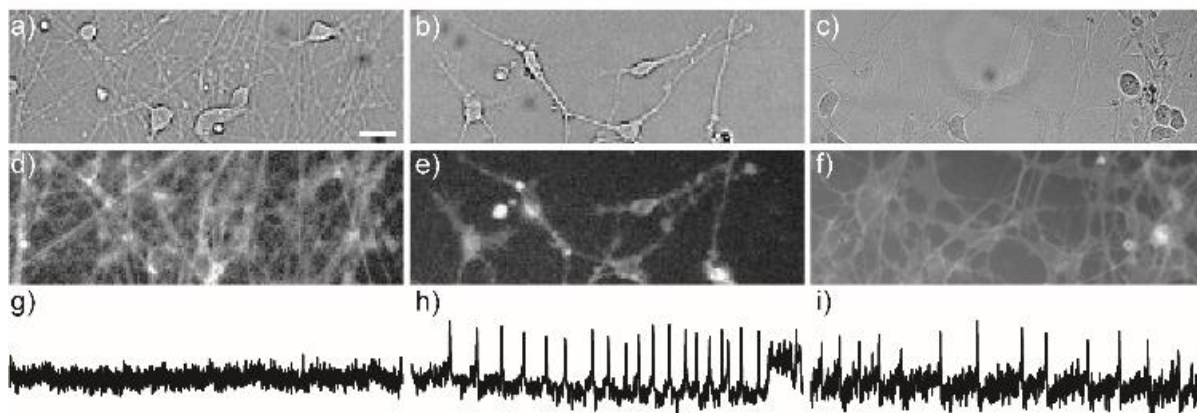


Figure 5.10. Characterization the differentiation of human embryonic stem cells differentiation into midbrain spiny neurons. Panels (a), (b), and (c) show brightfield images of the stem cells at days 35, 58, and 88 of the differentiation protocol. Panels (d), (e), and (f) show isoVF2.2(OMe).Cl bath applied to these cells prior to each imaging session. Cells at day 35 show little activity (g), but as differentiation progresses, robust spiking is readily visible using isoVF2.2(OMe).Cl (h) and (i). Scale bars for all images are 10 μm .

5.5 Conclusions and Future Outlook

In summary, we used a combined computational and experimental approach to optimize the matching of donor and acceptor in a photo-induced electron transfer system and, as a result, propose a structure with enhanced brightness and signal-to-noise over previous generations of VoltageFluor dyes. Based on the molecular dynamics simulations and DFT calculations, we predicted that the resulting isoVF dye would be brighter, but less sensitive than its msVF counterpart.

To validate our predictions, we designed and synthesized meta-bromo sulfofluorescein by taking advantage of our previously reported synthesis of isomerically pure sulfonated xanthene dyes. The meta-bromo sulfofluorescein may represent a useful scaffold for the fluorescent portion of other PeT-based sensors, which may also be improved by placing the PeT donor at the *meta* position of the meso xanthene ring. We used this dye head to synthesize isoVF2.2(OMe).Cl, which demonstrates four-fold higher signal-to-noise over msVF2.2(OMe).Cl in HEK293T cells and two-fold higher SNR for an action potential in cultured rat hippocampal neurons.

These results validate our hypothesis that the donor and the acceptor in the VoltageFluor scaffold must be properly matched to balance sensitivity and brightness. This provides further support for a PeT-based mechanism of voltage sensitivity in VF dyes and demonstrates that a computational approach can be used to fine-tune the acceptor to quench the donor in a manner that results in the highest SNR. The newest VF dye, isoVF2.2(OMe).Cl, shows the highest SNR observed in the fluorescein family of PeT-based voltage sensors thus far and can be readily used to visualize spiking behavior in rat hippocampal neurons and human-derived medium spiny neurons under one-photon and two-photon illumination. The improved SNR of isoVF2.2(OMe).Cl facilitates voltage imaging under suboptimal conditions, such as low-power illumination, complex biological preparations, and long-term imaging. Finally, the meta-substituted VF scaffold has demonstrated

itself to raise SNR by factors of two to four in both fluorescein- and rhodamine-based VF dyes. Efforts are currently underway in our lab to generalize this structural modification to other chromophores, such as silicon-rhodamines and BODIPYs.

5.6 Methods and Materials

General methods for chemical synthesis and characterization

Chemical reagents and anhydrous solvents were purchased from commercial suppliers and used without further purification. All reactions were carried out in oven-dried flasks under an inert atmosphere of N₂. Thin layer chromatography (TLC) (Silicycle, F254, 250 μm) was performed on glass backed plates pre-coated with silica gel and were visualized by fluorescence quenching under UV light. NMR spectra were measured on a Bruker AV-900 MHz, 226 MHz. Chemical shifts are expressed in parts per million (ppm) and are referenced to *d*₆-DMSO, 2.50 ppm. Coupling constants are reported as Hertz (Hz). Splitting patterns are indicated as follows: s, singlet; d, doublet; sep, septet; dd, doublet of doublet; ddd, doublet of doublet of doublet; dt, doublet of triplet; td, triplet of doublet; m, multiplet. High-resolution mass spectra (ESI EI) were measured by the QB3/Chemistry mass spectrometry service at University of California, Berkeley. High performance liquid chromatography (HPLC) and low resolution ESI Mass Spectrometry were performed on an Agilent Infinity 1200 analytical instrument coupled to an Advion CMS-L ESI mass spectrometer. Columns used for the analytical and preparative HPLC were Phenomenex Luna C18(2) (4.6 mm I.D. × 150 mm) and Waters XBridge 10μ C18 (19 mm I.D. × 250 mm) columns with a flow rate of 1.0 and 30.0 mL/min, respectively. The mobile phase were MQ-H₂O with 0.05% trifluoroacetic acid (eluent A) and HPLC grade acetonitrile with 0.05% trifluoroacetic acid (eluent B). Signals were monitored at 254, 350, and 580 nm in 20 min with gradient 10-100% eluent B.

Imaging Parameters

Epifluorescence imaging was performed on an AxioExaminer Z-1 (Zeiss) equipped with a Spectra-X Light engine LED light (Lumencor), controlled with Slidebook (v6, Intelligent Imaging Innovations). Images were acquired with either a W-Plan-Apo 20x/1.0 water objective (20x; Zeiss) or a W-Plan-Apo 63x/1.0 water objective (63x; Zeiss). Images were focused onto either an OrcaFlash4.0 sCMOS camera (sCMOS; Hamamatsu). The sCMOS was used to acquire large fields of view for recording from multiple neurons. Two-photon imaging was performed with a Zeiss LSM 880 NLO AxioExaminer equipped with a Chameleon Ultra I laser (Coherent Inc.) Fluorescence images were acquired using a Zeiss BiG-2 GaAsP detector.

Spectroscopic studies

Stock solutions of VF dyes were prepared in DMSO (1.0–10 mM) and diluted with PBS (100 mM Na₂HPO₄, 0.1 M NaOH). UV-Vis absorbance and fluorescence spectra were recorded using a Shimadzu 2501 Spectrophotometer (Shimadzu) and a Quantmaster Master 4 L-format scanning spectrofluorometer (Photon Technologies International). The fluorometer is equipped with an LPS-220B 75-W xenon lamp and power supply, A-1010B lamp housing with integrated igniter, switchable 814 photon-counting/analog photomultiplier detection unit, and MD5020 motor driver. Samples were measured in 1-cm path length quartz cuvettes (Starna Cells).

Measurement of Two-Photon Cross Section

Two-photon excitation cross section measurements were obtained via comparison to a fluorescein standard, as previously reported.

Cell Culture

All animal procedures were approved by the UC Berkeley Animal Care and Use Committees and conformed to the NIH Guide for the Care and Use of Laboratory Animals and the Public Health Policy. Human embryonic kidney 293T (HEK) cells were passaged and plated onto 12 mm glass coverslips pre-coated with Poly-D Lysine (PDL; 1 mg/ml; Sigma-Aldrich) to provide a confluency of ~15% and 50% for electrophysiology and imaging, respectively. HEK cells were plated and maintained in Dulbecco's modified eagle medium (DMEM) supplemented with 4.5 g/L D-glucose, 10% FBS and 1% Glutamax.

Voltage sensitivity in HEK cells

Functional imaging of VF dyes was performed using a 20x objective paired with image capture from the EMCCD camera at a sampling rate of 0.5 kHz. VF dyes were excited using the 475 nm LED with an intensity of 9.7 W/cm². For initial voltage characterization emission was collected with the QUAD filter (430/32, 508/14, 586/30, 708/98 nm) after passing through a quadruple dichroic mirror (432/38, 509/22, 586/40, 654 nm LP).

Electrophysiology

For electrophysiological experiments, pipettes were pulled from borosilicate glass (Sutter Instruments, BF150-86-10), with a resistance of 5–8 M Ω , and were filled with an internal solution; (in mM) 115 potassium gluconate, 10 BAPTA tetrapotassium salt, 10 HEPES, 5 NaCl, 10 KCl, 2 ATP disodium salt, 0.3 GTP trisodium salt (pH 7.25, 275 mOsm).

Recordings were obtained with an Axopatch 200B amplifier (Molecular Devices) at room temperature. The signals were digitized with Digidata 1332A, sampled at 50 kHz and recorded with pCLAMP 10 software (Molecular Devices) on a PC. Fast capacitance was compensated in the on-cell configuration. For all electrophysiology experiments, recordings were only pursued if series resistance in voltage clamp was less than 30 M Ω . For whole-cell, voltage clamp recordings in HEK 293T cells, cells were held at -60 mV and 100 ms hyper- and de-polarizing steps applied from -100 to +100 mV in 20 mV increments. For whole-cell, following membrane rupture, resting membrane potential was assessed and recorded at $I = 0$ and monitored during the data acquisition. Neurons were switched to current clamp mode if they displayed series resistance in voltage clamp less than 30 megaohms. Pipette tip resistance was corrected by performing a bridge balance compensation.

To test if loading isoVF2.2(OMe).Cl onto the membrane of neurons has any effect on action potential firing, ten 500 ms current steps were injected into neurons in increments of 0.05 pA. The action potentials for each sweep were analyzed in Clampfit 10 software (Molecular Devices) to give amplitude and kinetic data.

Voltage Imaging of Medium Spiny Neurons

D35, 58, or 88 striatal progenitors, which were generated via previously published protocols²⁵, were harvested from 3D gels, seeded as small 50-100 μ m clusters on laminin-coated 12 mm glass coverslips, and cultured using differentiation medium. For experiments monitoring spontaneous neuronal activity, the cells were incubated in 1 μ M isoVF2.2(OMe).Cl in HBSS at 37 degrees

Celsius for 15 minutes. Functional imaging was performed using the above-mentioned 20x water immersion objective under epifluorescence illumination. Images were captured using an ORCA-Flash4.0 camera at a sampling rate of 400 Hz. The VF dye was excited using a 488 nm LED with an intensity of 2.5 W/cm². For image analysis, a custom MATLAB routine (SpikeMapper, available upon request), was employed. Cells were selected by drawing regions of interest in a differential interference contrast image corresponding to the time-series recording and outputting the bleach-corrected trace as an Excel file. The spike times (measured as frames in which the intensity exceeded 3x the standard deviation of the overall trace) were outputted as a text file.

Image analysis

Analysis of voltage sensitivity in HEK cells was performed using custom Python scripts. Briefly, a region of interest (ROI) was selected based on fluorescence intensity and applied as a mask to all image frames. Fluorescence intensity values were calculated at known baseline and voltage step epochs.

Two-Photon Excitation Cross Section Measurement

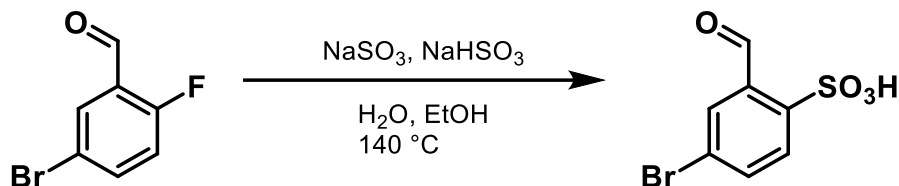
The two-photon excitation (TPE) cross section of isoVF2.2(OMe).Cl was determined according to previously reported procedures. We first measured the fluorescence signal generated by two-photon excitation of a fluorescein standard using a Zeiss BiG-2 GaAsP detector on a Zeiss LSM 880 NLO AxioExaminer equipped with a Chameleon Ultra I laser. We then determined the one-photon quantum yield of the dyes of interest and measured the fluorescence signal generated by two-photon excitation of the dyes of interest. We then calculated the TPE of the dyes of interest via the following equation:

$$\sigma_{TPE\ DYE} = \frac{\varphi_{Rho\ B} * \sigma_{TPE\ Rho\ B}}{\varphi_{DYE}} * \frac{F_{DYE}}{F_{Rho\ B}}$$

Where F_{DYE} and $F_{Rho\ B}$ are the measured fluorescence signal from the dye of interest and rhodamine b, respectively. The values for σ_{TPE} at different wavelengths for rhodamine b were obtained from ref.²⁶

Synthetic Details

Preparation of sulfobenzaldehydes:



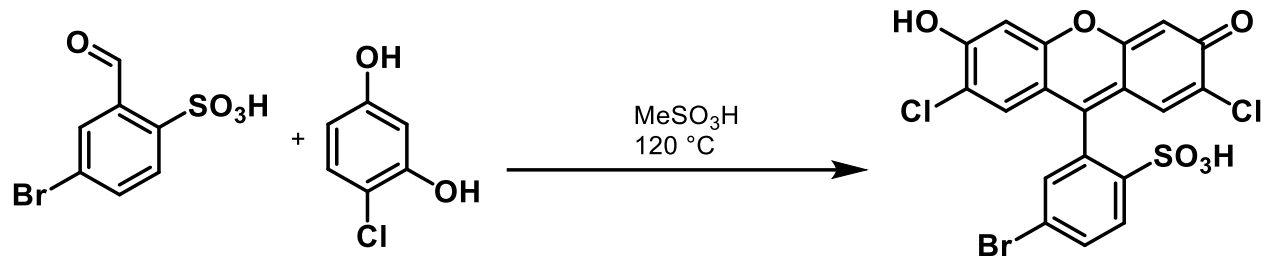
Synthesis of 5-bromo-2-sulfobenzaldehyde

5-bromo-2-fluorobenzaldehyde (3.0 g, 14.78 mmol) was placed in a long-necked bomb flask and dissolved in a 1:1 mixture of ethanol and water. Sodium sulfite (1.49 g, 11.82 mmol) and sodium bisulfite (123 mg, 1.18 mmol) were added and the reaction was stirred for 48 hours at 140 degrees Celsius. The reaction mixture, after cooling, was poured into methanol while stirring so as to make 20% aqueous content of the whole volume. This process precipitated the inorganic salts, which were then removed by vacuum filtration. The solvent from the filtrate was removed under reduced pressure to obtain a solid residue, which was triturated with methanol/ethyl ether to produce a fluffy white solid (3.9 g, 99%).

$^1\text{H NMR}$ (900 MHz, $\text{DMSO-}d_6$) δ 10.80 (s, 1H), 7.83 – 7.82 (m, 2H), 7.76 (d, $J = 8.1$ Hz, 1H).

$^{13}\text{C NMR}$ (226 MHz, $\text{DMSO-}d_6$) δ 192.31, 148.83, 135.64, 134.14, 129.29, 128.91, 122.43.

HR-ESI-MS m/z for $\text{C}_7\text{H}_4\text{BrO}_4\text{S}^-$ calculated: 263.9092 found: 262.9021 (M-H).



Synthesis of *meta*-bromo-sulfo-dichlorofluorescein

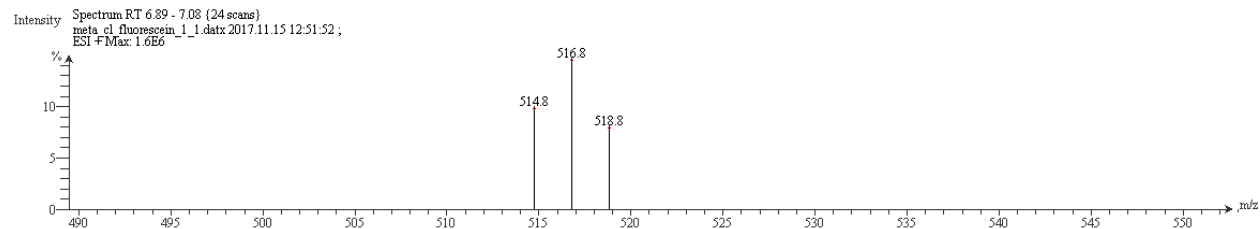
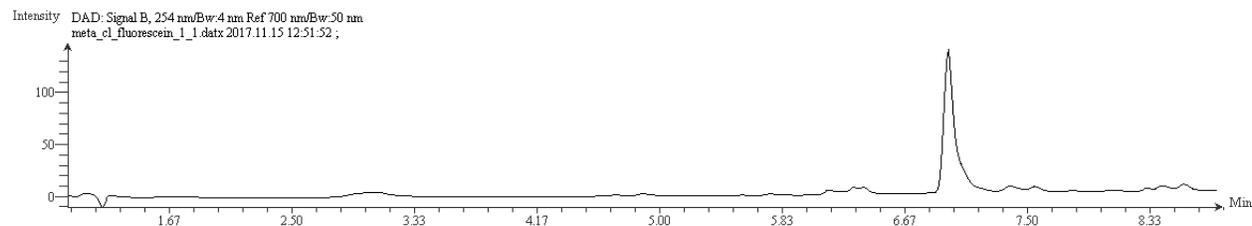
4-bromo-2-sulfobenzaldehyde (300 mg, 1.13 mmol) and 4-chlororesorcinol (327 mg, 2.26 mmol) were placed in a roundbottom flask, dissolved in 3 mL of neat methanesulfonic acid, and stirred for 16 hours at 120 degrees Celsius. After cooling, the reaction mixture was diluted with 30 mL water, resulting in the formation of a dark brown precipitate. The dark brown solid (433 mg, 74%) was collected via vacuum filtration.

¹H NMR (400 MHz, DMSO-*d*₆) δ 7.88 (d, *J* = 8.5 Hz, 1H), 7.80 (dd, *J* = 8.5, 2.0 Hz, 1H), 7.54 (d, *J* = 2.0 Hz, 1H), 6.89 (s, 2H), 6.74 (s, 2H).

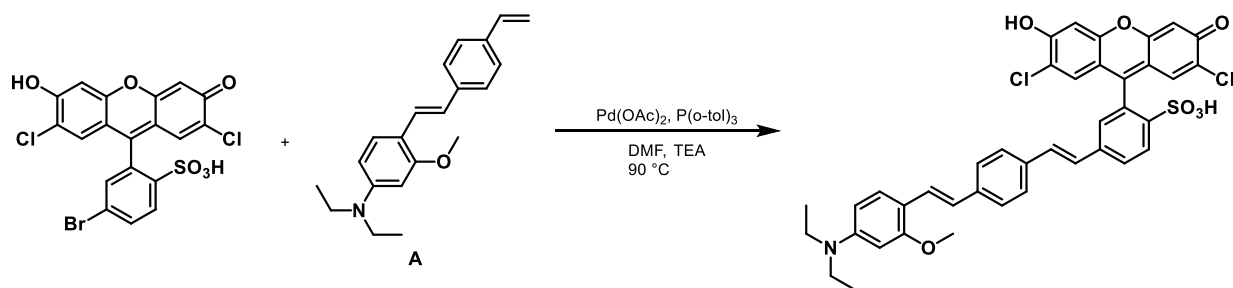
¹³C NMR (201 MHz, DMSO) δ 161.18, 153.09, 149.73, 135.55, 135.01, 134.66, 133.05, 132.64, 125.07, 121.34, 119.83, 115.17, 106.55.

HR-ESI-MS *m/z* for C₁₉H₁₀BrCl₂O₆S⁺ calculated: 514.8680 found: 514.8366 (M+Na).

LR-ESI-MS *m/z* for C₁₉H₁₀BrCl₂O₆S⁺ calculated: 514.9 found: 514.8 (M)



Preparation of SulfoRhoVR dyes:



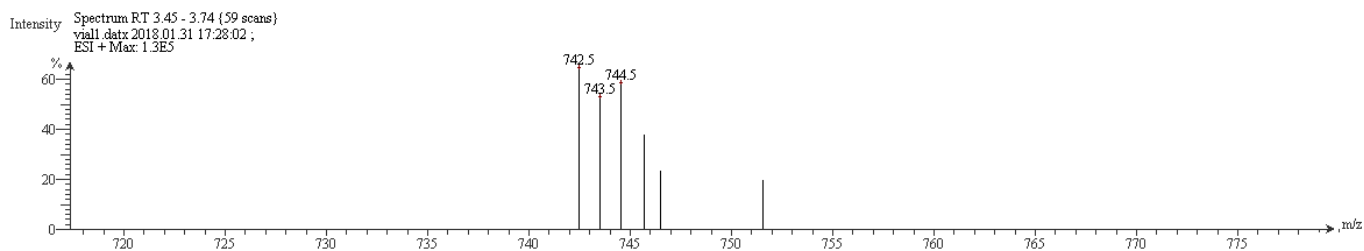
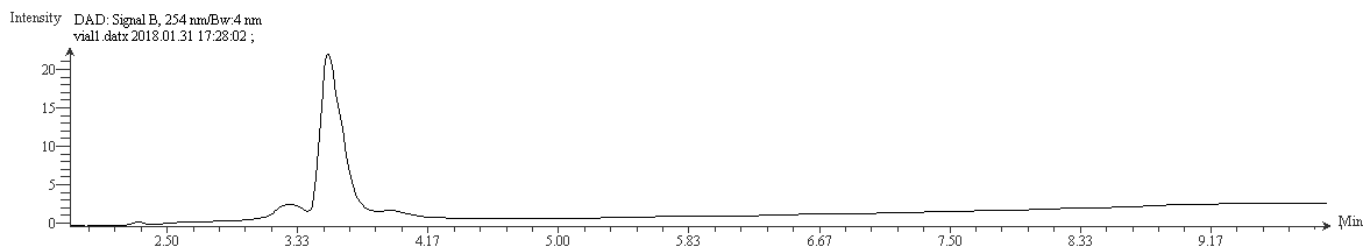
Synthesis of isoVF2.2(OMe).Cl

meta-bromo-sulfo-dichlorofluorescein (100 mg, 0.20 mmol), A (73 mg, 0.24 mmol), palladium acetate (2 mg, 0.008 mmol), and P(*o*-tol)₃ (5.4 mg, 0.018 mmol) were placed in an oven-dried Schlenk flask. The flask was sealed and evacuated/backfilled with nitrogen (3x). Anhydrous DMF (1 mL) and anhydrous Et₃N (1 mL) were added via syringe and the reaction was stirred for 16 hours at 100 degrees Celsius. After cooling, the reaction mixture was diluted with 10 mL dichloromethane and filtered through celite, which was then washed with methanol. The solvent was removed from the filtrate via rotary evaporation and the resulting residue was dissolved in 5 mL dichloromethane. The mixture was then poured into diethyl ether, resulting in precipitation of a violet solid. The crude solid was isolated via vacuum filtration (82 mg, 56%, 85% pure by HPLC). A small amount of material was purified via RP-HPLC for further characterization (12 mg, 8%).

¹H NMR (900 MHz, DMSO-*d*₆) δ 7.96 (d, *J* = 8.2 Hz, 1H), 7.85 – 7.81 (m, 1H), 7.62 (dd, *J* = 11.5, 7.2 Hz, 3H), 7.58 – 7.52 (m, 2H), 7.50 (s, 1H), 7.46 (d, *J* = 8.2 Hz, 2H), 7.43 (d, *J* = 8.1 Hz, 2H), 7.37 (d, *J* = 16.4 Hz, 1H), 7.32 (d, *J* = 16.3 Hz, 1H), 7.28 (s, 1H), 7.26 (s, 1H), 7.23 (s, 1H), 7.18 (s, 1H), 7.12 (s, 1H), 3.83 (s, 3H), 3.09 (dd, *J* = 7.3, 4.8 Hz, 4H), 1.11 (t, *J* = 7.0 Hz, 6H).

HR-ESI-MS *m/z* for C₄₀H₃₂Cl₂NO₇S⁻ calculated: 740.1355 found: 740.1261.

LR-ESI-MS *m/z* for C₄₀H₃₄Cl₂NO₇S⁺ calculated: 742.1 found: 742.5.



5.7 References

55. Grimm, J. B.; English, B. P.; Chen, J. J.; Slaughter, J. P.; Zhang, Z. J.; Revyakin, A.; Patel, R.; Macklin, J. J.; Normanno, D.; Singer, R. H.; Lionnet, T.; Lavis, L. D. *Nat Methods* **2015**, *12*, 244.
56. Lavis, L. D.; Raines, R. T. *Acs Chem Biol* **2014**, *9*, 855.
57. Kushida, Y.; Nagano, T.; Hanaoka, K. *Analyst* **2015**, *140*, 685.
58. Brewer, T. F.; Chang, C. J. *J Am Chem Soc* **2015**, *137*, 10886.
59. Aron, A. T.; Ramos-Torres, K. M.; Cotruvo, J. A.; Chang, C. J. *Accounts Chem Res* **2015**, *48*, 2434.
60. Kobayashi, H.; Ogawa, M.; Alford, R.; Choyke, P. L.; Urano, Y. *Chem Rev* **2010**, *110*, 2620.
61. Lee, H. L. D.; Lord, S. J.; Iwanaga, S.; Zhan, K.; Xie, H. X.; Williams, J. C.; Wang, H.; Bowman, G. R.; Goley, E. D.; Shapiro, L.; Twieg, R. J.; Rao, J. H.; Moerner, W. E. *J Am Chem Soc* **2010**, *132*, 15099.
62. Anzalone, A. V.; Wang, T. Y.; Chen, Z. X.; Cornish, V. W. *Angew Chem Int Edit* **2013**, *52*, 650.
63. Yun, S. W.; Kang, N. Y.; Park, S. J.; Ha, H. H.; Kim, Y. K.; Lee, J. S.; Chang, Y. T. *Accounts Chem Res* **2014**, *47*, 1277.
64. Lukinavicius, G.; Umezawa, K.; Olivier, N.; Honigmann, A.; Yang, G. Y.; Plass, T.; Mueller, V.; Reymond, L.; Correa, I. R.; Luo, Z. G.; Schultz, C.; Lemke, E. A.; Heppenstall, P.; Eggeling, C.; Manley, S.; Johnsson, K. *Nat Chem* **2013**, *5*, 132.
65. Uno, S. N.; Kamiya, M.; Yoshihara, T.; Sugawara, K.; Okabe, K.; Tarhan, M. C.; Fujita, H.; Funatsu, T.; Okada, Y.; Tobita, S.; Urano, Y. *Nat Chem* **2014**, *6*, 681.
66. Lincoln, R.; Greene, L. E.; Krumova, K.; Ding, Z. T.; Cosa, G. *J Phys Chem A* **2014**, *118*, 10622.
67. Huang, Y. L.; Walker, A. S.; Miller, E. W. *J Am Chem Soc* **2015**, *137*, 10767.
68. Grenier, V.; Walker, A. S.; Miller, E. W. *J Am Chem Soc* **2015**, *137*, 10894.
69. Miller, E. W. *Curr Opin Chem Biol* **2016**, *33*, 74.
70. Peterka, D. S.; Takahashi, H.; Yuste, R. *Neuron* **2011**, *69*, 9.
71. Scanziani, M.; Haussler, M. *Nature* **2009**, *461*, 930.
72. Braubach, O.; Cohen, L. B.; Choi, Y. *Adv Exp Med Biol* **2015**, *859*, 3.
73. De Silva, A. P.; Gunaratne, H. Q. N.; Habibiwan, J. L.; McCoy, C. P.; Rice, T. E.; Soumillion, J. P. *Angew Chem Int Edit* **1995**, *34*, 1728.
74. Li, L. S. *Nano Lett* **2007**, *7*, 2981.
75. Kulkarni, R. U.; Yin, H.; Pourmandi, N.; James, F.; Adil, M. M.; Schaffer, D. V.; Wang, Y.; Miller, E. W. *ACS Chemical Biology* **2017**, *12*(2), 407-413.
76. Deal, P. E.; Kulkarni, R. U.; Al-Abdullatif, S. H.; Miller, E. W. *J Am Chem Soc* **2016**, *138*, 9085.
77. Vanommeslaeghe, K.; Hatcher, E.; Acharya, C.; Kundu, S.; Zhong, S.; Shim, J.; Darian, E.; Guvench, O.; Lopes, P.; Vorobyov, I.; MacKerell, A. D. *J Comput Chem* **2010**, *31*, 671.
78. Frisch, M. J.; Trucks, G. W.; Schlegel, H. B.; Scuseria, G. E.; Robb, M. A.; Cheeseman, J. R.; Scalmani, G.; Barone, V.; Mennucci, B.; Petersson, G. A.; Nakatsuji, H.; Caricato, M.; Li, X.; Hratchian, H. P.; Izmaylov, A. F.; Bloino, J.; Zheng, G.; Sonnenberg, J. L.; Hada, M.; Ehara, M.; Toyota, K.; Fukuda, R.; Hasegawa, J.; Ishida, M.; Nakajima, T.; Honda, Y.; Kitao, O.; Nakai, H.; Vreven, T.; Montgomery Jr., J. A.; Peralta, J. E.; Ogliaro, F.; Bearpark, M. J.; Heyd, J.; Brothers, E. N.; Kudin, K. N.; Staroverov, V. N.; Kobayashi, R.; Normand, J.; Raghavachari, K.; Rendell, A. P.; Burant, J. C.; Iyengar, S. S.; Tomasi, J.; Cossi, M.; Rega, N.; Millam, N. J.; Klene, M.; Knox, J. E.; Cross, J. B.; Bakken, V.; Adamo, C.; Jaramillo, J.;

- Gomperts, R.; Stratmann, R. E.; Yazyev, O.; Austin, A. J.; Cammi, R.; Pomelli, C.; Ochterski, J. W.; Martin, R. L.; Morokuma, K.; Zakrzewski, V. G.; Voth, G. A.; Salvador, P.; Dannenberg, J. J.; Dapprich, S.; Daniels, A. D.; Farkas, Ö.; Foresman, J. B.; Ortiz, J. V.; Cioslowski, J.; Fox, D. J.; Gaussian, Inc.: Wallingford, CT, USA, 2009.
79. Adil, MM.; Gaj, T.; Rao, AT.; Kulkarni RU.; Fuentes, CM.; Ramadoss, GN.; Ekman, FK.; Miller, EW.; Schaffer, DV. *Stem Cell Reports*. **2018**. *10*, 1481-1491.
80. Albota MA, Xu C, & Webb WW (1998) Two-photon fluorescence excitation cross sections of biomolecular probes from 690 to 960 nm. *Appl Optics* 37(31):7352-7356.

Appendix 1. Protocol for Two-Photon Voltage Imaging

Two-photon microscopy experiments were performed at the Molecular Imaging Center at UC Berkeley. The primary microscope used was a Zeiss LSM 880 NLO AxioExaminer outfitted with a BiG-2 GaAsP non-descanned detector and a Coherent Chameleon Vision. For some experiments, a Zeiss LSM 880 NLO AxioExaminer outfitted with a BiG-2 GaAsP non-descanned detector and a Coherent Chameleon MPX OPO laser were used.

For cultured neuron imaging, the dye was solubilized in HBSS at a concentration of 500 nM. The neurons were then incubated in this loading solution at 37 degrees Celsius for 15 minutes. After incubation, the neurons were placed in an imaging dish filled with HBSS and imaged without perfusion.

For brain slice imaging, the dye was solubilized in oxygenated artificial CSF at a concentration of 20 mM. The brain slice was then incubated in this loading solution for 30 minutes at room temperature. During incubation, the dye-loading solution was continuously oxygenated in order to maintain slice health. After incubation, the slice was moved to a perfusion chamber and subjected to a continuous flow of oxygenated ACSF at room temperature. In order to minimize motion artifacts, the slice was held down with a small metal harp. For experiments involving drug application to the slice, the source of oxygenated ACSF was switched to ACSF containing the drug of interest.

Dye	Excitation Wavelength	Laser Power (culture)	Laser Power (slice)
RVF5	820 nm	6%	10%
sRhoVR 1	840 nm	5%	8%
isoVF2.2(OMe).Cl	800 nm	5%	N/A

Table 1. Excitation Wavelengths and Laser Power used for Two-Photon Imaging Experiments.

During imaging, the Coherent Chameleon lasers were set to a laser power and excitation wavelength dependent on the dye used for the experiment (**Table 1**). Still-frame acquisition was performed at a resolution of 1024 by 1024 pixels, typically with the water-immersion Objective W Plan-Apochromat 20x/1.0 DIC objective. Exposure time was typically set to the fastest parameters as determined by the Zeiss Zen imaging software. Voltage imaging experiments were performed via the time series functionality in Zen. In order to reach a frame acquisition time of 4.95 milliseconds, the resolution was set to 64 pixels wide by 8 pixels tall. The acquisition mode was also set to bidirectional scanning. Via these settings and the selection of the fastest imaging speed in Zen, spiking activity can be detected using 2P imaging. Using the Zen software, the imaging region was set such that it overlapped with several neurons aligned horizontally. Time series acquisitions were typically 4000 or 8000 frames long (20 or 40 seconds). The image files were extracted as TIFFs for image analysis.

Time series files were typically analyzed using a custom Matlab script due to the large binning factor in a 64x8 video resulting in a single pixel typically encapsulated most of a cell's membrane. To extract each trace, the Matlab script plots the fluorescence intensity of each pixel vs. time and creates an array of plots 64 wide by 8 tall. Pixels of interest can be selected in this three-dimensional plot and exported as Excel worksheets for further analysis.

Appendix 2. Protocol for Density Functional Theory Calculations

Density Functional Theory (DFT) calculations were performed at the Molecular Graphics Computational Facility in the College of Chemistry at UC Berkeley. Gaussian 16 Revision A.03 was used to set up and review calculations.

The molecules were built in GaussView6 and their geometry was optimized by setting up a calculation with Job Type: Optimization and Method: Ground State, DFT, Default Spin, and using the wB97X-D functional. In the Basis Set pulldown, the Custom: def2-TZVP basis set was selected. The Charge option was set to -2 and the Spin option was set to singlet. In the Pop. Tab, the Level of Output was set to Regular and in the Link 0 tab, 16 processors were selected. In order to better model the stabilization that the highly-charged VoltageFluor molecule experiences at the membrane-water interface, a second round of geometry optimization using the same method settings was performed by adding a sodium atom and freezing the motion of the VoltageFluor molecule, thereby attenuating the charge repulsion between the sulfonate group and the xanthene phenolate. Using the same settings, frequency calculations were then performed on the final geometries to determine that they were stationary states.

Energy calculations were then performed on these optimized geometries. Job Type was set to Energy and, in order to account for the role of the sulfonate group *d* orbitals, the def2-TZVPD basis set was used to perform the computations. The resulting output files were viewed in GaussView6 to ensure completion of the calculation and then, the checkpoint files were viewed to determine the energy surfaces of each molecule.

Using the Tools>MOs functionality, a New Gaussian MO was created by using the Load Existing Chk or FChk File command in the Method pulldown. Then, the MOs of interest were selected and then displayed on-screen using the Visualize command. An Isovalue of 0.02 was selected to constrain the size of the MO lobes.

To generate graphics of the MOs, VMD was used. In the GaussView6 window, the Surfaces>Results>Cube Actions window was opened and a New Cube was generated for each of the MOs of interest. Each of these cube files were opened in VMD. The display mode was changed to Orthographic and the molecule was centered and scaled to desired specifications in the display window. In the Graphical Representations Window under the Graphics Tab, the representation of the molecule was changed to CPK for ball-and-stick representation and the coloring was changed to element to differentiate between different atoms. Two new representations were then generated using the Drawing Method: Isosurface and the Coloring Method: ColorID, with Isovalues of 0.02 and -0.02, respectively. The Draw pulldown was changed to Solid Surface to overlay the molecular orbitals over the ball-and-stick model of the molecule. These images were then Rendered as TIFF files for publication.